Beam Dynamics of Proton-Nucleus Collisions in the Large Hadron Collider

Dissertation
zur Erlangung des Doktorgrades
der Naturwissenschaften

vorgelegt beim Fachbereich Physik
der Johann Wolfgang Goethe-Universität
in Frankfurt am Main

von
Marc Andre Jebramcik
aus Essen

Frankfurt am Main 2020
(D 30)

vom Fachbereich Physik der Johann Wolfgang Goethe-Universität als Dissertation angenommen.

Dekan:
Prof. Dr. Michael Lang

Gutachter:
Prof. Dr. Holger Podlech
Priv.-Doz. Dr. Giuliano Franchetti

Datum der Disputation: 20.07.2020

Zusammenfassung

Diese Arbeit diskutiert wichtige Fragestellungen der Strahldynamik im Proton-Blei-Betrieb im Large Hadron Collider (LHC) am CERN in Genf. In diesem Betriebsmodus besteht einer der zwei kollidierenden Teilchenstrahlen aus Protonen und der andere Strahl aus vollständig ionisierten Bleiatomen $^{208}\mathrm{Pb}^{82+}$. Die Operation mit unterschiedlichen Teilchentypen in den jeweiligen Strahlen war im ursprünglichen Design des LHCs nicht vorgesehen [1]. Während zwei Testläufen in den Jahren 2011 und 2012 wurden erstmalig erfolgreich Blei- und Protonenstrahlen zeitgleich beschleunigt und zur Kollision gebracht. Dies erbrachte den Beweis, dass der Proton-Blei-Betrieb im LHC möglich ist [2, 3]. In zwei mehrwöchigen Zeitblöcken in den Jahren 2013 und 2016 konnten seitdem erfolgreich Proton-Blei-Kollisionen im LHC erzeugt und von den Experimenten am LHC genutzt werden [4, 5].

Grund für den Zweifel an der Realisierbarkeit eines Operationsmodus mit verschiedenen Teilchensorten in den beiden Strahlen war die Tatsache, dass die Strahlen aufgrund des Magnetdesigns des LHCs mit derselben magnetischen Steifigkeit $B\rho$ aber unterschiedlichen Umlauffrequenzen f_0 beschleunigt werden müssen. Obwohl beide Strahlen während des Beschleunigungsvorgangs nicht in den Regionen um die Wechselwirkungspunkte kollidieren (Orbits sind mehrere mm von einander getrennt), kommt es dennoch zu einer langreichweitigen Abstoßung zwischen den Strahlen, da sich beide Strahlen um die Wechselwirkungspunkte die Strahlkammer teilen. Als Folge der unterschiedlichen Umlauffrequenzen begegnen die Teilchenpakete aus dem einen Strahl den Teilchenpaketen aus dem anderen Strahl jeden Umlauf an verschobenen Positionen. Dies kann zu resonanter Anregung und zum Anwachsen der transversalen Strahlemittanz führen. Die Befürchtungen, dass die Anregung im LHC möglicherweise stark ausfallen könnte, wurden durch Experimente an den Intersecting Storage Rings (ISR) am CERN [6, 7] und am amerikanischen Relativistic Heavy-Ion Collider (RHIC) am Brookhaven National Laboratory in Upton, New York, motiviert [8]. Die 18-fach höhere Injektionsenergie des LHCs im

Vergleich zu der vom RHIC und der daraus resultierende viel kleinere Geschwindigkeitsunterschied zwischen den Strahlen (schwächere resonante Anregung) war jedoch das Hauptargument für eine erfolgreiche Beschleunigung von Strahlen mit unterschiedlichen Umlauffrequenzen. Auch ist die Abstoßung der Strahlen im LHC schwächer als im RHIC und die Abstoßung fluktuiert weniger stark im LHC aufgrund des kleineren Teilchenpaketabstands im Verhältnis zur Länge der gemeinsamen Strahlkammer um die Wechselwirkungspunkte. Der Future Circular Collider (FCC) wird im Proton-Blei-Betrieb wegen der hohen Injektionsenergie und des großen Umfangs nicht durch fluktuierende Strahl-Strahl-Wechselwirkung beeinflusst werden.

In Kapitel 2 wird ein auf Matrizen basierendes Modell entwickelt, das die lineare Optik des Beschleunigers als Grundlage hat und nichtlineare Elemente wie Sextupol- und Oktupolmagnete vernachlässigt [9]. Das Modell berücksichtigt jedoch die Änderung des Arbeitspunktes durch Sextupol- und Oktupolmagnete bei anwachsenden transversalen Amplituden und durch die Chromatizität mittels künstlicher Veränderung des transversalen Phasenvorschubs. Die linearen Einflüsse der fluktuierenden Strahl-Strahl-Wechselwirkung werden innerhalb des Modells mit der richtigen Zeitstruktur abgebildet. *Tracking*-Simulationen für den LHC, den RHIC und den High-Luminosity Large Hadron Collider (HL-LHC), das voraussichtlich 2026 einsatzbereite Upgrade des LHCs, wurden im Rahmen dieser Arbeit bei Injektionsenergie mit dem genannten Modell durchgeführt. Die Ergebnisse für RHIC zeigen große Anwachsraten der transversalen Emittanzen des Goldstrahls in Gold-Deuteron-Konfiguration für Deuteronstrahlen unterschiedlicher Intensität. Die relativen Anwachsraten der Emittanzen des Goldstrahls im RHIC sind in der Region von $0.1\,\%/\mathrm{s}$ bis $1.5\,\%/\mathrm{s}$ abhängig von der Anzahl der Teilchenpakete des Deuteronstrahls und der transversalen Ebene. Anwachsraten dieser Größenordnung wurden im RHIC experimentell beobachtet [10], was die Ergebnisse der Simulationen grob validiert. Ein Vergleich zu Messdaten ist nicht möglich, da keine kontinuierliche Emittanzmessung im RHIC existiert. Simulationen für den LHC zeigen keinen nennenswerten Emittanzzuwachs des Bleistrahls für unterschiedliche Intensitäten des gegenläufigen Protonenstrahls. Die relativen Anwachsraten der Emittanzen sind teilweise deutlich kleiner als $10^{-3}\,\%/\mathrm{s}$. Diese Simulationsergebnisse bestätigen die gemessene Stabilität der Strahlen im LHC und die Problematik stark anwachsender Emittanzen im RHIC wird reproduziert. Ein weiteres wichtiges Ergebnis der Simulationen ist, dass im HL-LHC ebenfalls kein signifikanter Zuwachs der Emittanz zu erwarten ist, obwohl sich die Protonenstrahlintensität im HL-LHC verdoppeln wird. Selbst Teilchenpaketintensitäten, die äquivalent zu denen in Proton-Proton-Kollisionen sind, führen zu keinem Emittanzzuwachs, der nennenswert wäre.[1]

Ein Grund für den Zweifel an dem erfolgreichen Betrieb in Proton-Blei-Konfiguration war auch die potentiell destruktive Wechselwirkung zwischen den Strahlen, wenn diese in den

[1] Typische Intensitäten der Protonenpakete in Proton-Blei-Kollisionen sind etwa 2.8×10^{10} Protonen pro Teilchenpaket. In Proton-Proton-Kollisionen ist die Intensität mit 1.15×10^{11} Protonen pro Teilchenpaket weit höher.

Detektoren kollidieren. Besonders der unterschiedliche Lorentzfaktor γ für die beiden Strahlen, führt zu deutlich unterschiedlichen geometrischen Strahlgrößen aufgrund der im Falle des Bleis schwächeren und im Falle der Protonen stärkeren adiabatischen Dämpfung der Strahlemittanz. Erfahrungen bei HERA am DESY in Hamburg und beim Sp$\overline{\text{p}}$S am CERN haben gezeigt, dass die Lebensdauer des größeren Strahls rapide abnehmen kann, falls sich die Strahlgrößen der beiden kollidierenden Strahlen stark unterscheiden [11, 12]. In Kapitel 3 wird daher eine sogenannte *Frequency-Map*-Analyse durchgeführt, um potentielle Diffusion des größeren Bleistrahls, der mit dem viel kleineren Protonenstrahl kollidiert, zu untersuchen. Das dazu genutzte Modell gleicht dem zuvor vorgestellten Modell zur Bestimmung der Emittanzzunahme aufgrund fluktuierender Strahl-Strahl-Wechselwirkung bei Injektionsenergie. Eine wichtige Modifikation zum vorherigen Modell ist jedoch die Berücksichtigung aller Nichtlinearitäten der Strahl-Strahl-Abstoßung. Die Ergebnisse der Simulation zeigen keine chaotische Dynamik nahe des Strahlzentrums des, im Verhältnis zum Protonenstrahl, größeren Bleistrahls. Selbst im Falle eines unrealistisch kleinen Protonenstrahls ($\sigma_{\text{Pb}}/\sigma_{\text{p}} \approx 2.1$) ist keine nennenswerte Diffusion des Arbeitspunktes der Teilchen zu beobachten. Dieses Ergebnis unterstützt die experimentelle Beobachtung, dass abgesehen von zusätzlichen Verlusten durch eine erhöhte Luminosität keine stark reduzierte Strahllebensdauer des Bleistrahls zu beobachten ist, wenn dieser mit einem weit kleineren Protonenstrahl kollidiert.

Die Thematik der Strahllebensdauer im Proton-Blei-Betrieb wird auch in Kapitel 4 behandelt. Dazu werden Simulationen durchgeführt, die die Entwicklung der Strahlparameter in einer LHC-Füllung nachbilden. Für diese Simulationen wurde ein Programmcode entwickelt, der gekoppelte Differentialgleichungen löst, die die Luminosität, *Intra-Beam-Scattering* (IBS) und Synchrotronstrahlungsdämpfung für jedes Teilchenpaket beider Teilchenstrahlen berücksichtigen [13]. Die Ergebnisse dieser Studie zeigen, dass die Anwachsraten des Bleistrahls durch IBS überschätzt werden und dass besonders Teilchenpakete des Bleistrahls mehr Intensität verlieren als im Modell angenommen. Diese zusätzlichen Verluste beschränken sich auf Teilchenpakete, die in einem Detektor kollidieren, und die Verlustraten nehmen mit abnehmendem Kreuzungswinkel im Kollisionspunkt zu. Generell sind die zusätzlichen Verlustraten $\alpha_{\text{IP}} = -\frac{\text{d}N_b}{\text{d}t}/N_b$ (N_b ist die Teilchenpaketintensität) an den vier Detektoren des LHCs klein und überschreiten nicht $\alpha_{\text{IP}} \leq 1/34\,\text{h}^{-1}$.

Eine wichtige beschleuniger- und teilchenphysikalische Größe ist der Wirkungsquerschnitt σ der Kollision von Blei mit Protonen im LHC. Der Wirkungsquerschnitt ist eine Größe, die sich mit der Schwerpunktsenergie der Kollision $\sqrt{s_{\text{NN}}}$ ändert. In Kapitel 5 dieser Arbeit werden die Daten von Strahlverlustmonitoren in Kombination mit der Luminosität und der Verlustrate der Strahlintensität aus dem Jahre 2016 genutzt, um den Wirkungsquerschnitt von Proton-Blei-Kollisionen bei $\sqrt{s_{\text{NN}}} = 8.16\,\text{TeV}$ zu bestimmen. Im LHC kann der Wirkungsquerschnitt nicht über Intensitätsverluste in Kombination mit der Luminosität bestimmt wer-

den [14, 15], da substantielle Verluste, die nicht durch den Kollisionsprozess verursacht werden, vorliegen. Die in Kapitel 5 vorgestellte Methode ist mit denen am LHC installierten Strahlverlustmonitoren in der Lage, selbst unter diesen Umständen den Wirkungsquerschnitt von Proton-Blei-Kollisionen zu bestimmen. Der sogenannte effektive Wirkungsquerschnitt $\sigma_{\mathrm{eff}}(t) = -\frac{\mathrm{d}N_{\mathrm{Pb}}(t)/\mathrm{d}t}{\mathcal{L}_{\mathrm{tot}}(t)} = \sigma + \frac{\alpha_{\mathrm{ex}}(t)}{\mathcal{L}_{\mathrm{tot}}(t)}$ ist eine zeitabhängige Größe, die aus der Abnahme der Intensität des Bleistrahls N_{Pb} und der Gesamtluminosität $\mathcal{L}_{\mathrm{tot}}(t)$ berechnet wird. Falls die Verlustrate α_{ex}, die nicht durch Teilchenkollisionen in den Detektoren hervorgerufen wird, verschwindet $\alpha_{\mathrm{ex}} \ll 1$, gleicht der effektive Wirkungsquerschnitt dem Gesamtwirkungsquerschnitt $\sigma_{\mathrm{eff}} = \sigma$. Strahlverlustmonitore, die hauptsächlich Strahlverluste detektieren, die nicht durch den Kollisionsprozess selbst hervorgerufen werden und proportional zu α_{ex} sind, werden genutzt um mittels des Ausdrucks für den effektiven Wirkungsquerschnitt den Gesamtwirkungsquerschnitt via Regression zu bestimmen. Eine Analyse der in 2016 bei der Schwerpunktsenergie von $\sqrt{s_{\mathrm{NN}}} = 8.16\,\mathrm{TeV}$ aufgenommenen Daten ergibt einen Gesamtwirkungsquerschnitt von $\sigma = (2.32 \pm 0.01\,(\mathrm{stat.}) \pm 0.20\,(\mathrm{sys.}))\,\mathrm{b}$. Dies entspricht in etwa einem hadronischen Wirkungsquerschnitt von $\sigma_{\mathrm{had}} = (2.24 \pm 0.01\,(\mathrm{stat.}) \pm 0.21\,(\mathrm{sys.}))\,\mathrm{b}$. Dieser Wert weicht nur um $5.7\,\%$ von dem theoretischen Wert $\sigma_{\mathrm{had}} = (2.12 \pm 0.01)\,\mathrm{b}$ ab [16]. Die Analyse zeigt daher, dass es möglich ist, den Wirkungsquerschnitt unter der Zuhilfenahme beschleunigerphysikalischer Größen und der Luminosität zu bestimmen, auch wenn zusätzlich zur Luminosität andere Verlustmechanismen vorliegen.

Ein weiteres Ziel dieser Arbeit ist die Abschätzung der integrierten Luminosität, die der LHC in einem künftigen vierwöchigen Proton-Blei-Betrieb erzeugen wird. Ein potentieller Betrieb mit Proton-Blei-Kollisionen könnte bereits 2023 stattfinden. Eine genaue Kenntnis der zu erwartenden integrierten Luminosität ist essenziell für die Wissenschaftler an den Experimenten, um wohlüberlegte Strahlzeitanfragen stellen zu können. Der in Kapitel 4 entworfene Simulationscode zur Bestimmung der Strahlentwicklung wird daher im Kapitel 6 genutzt, um die integrierte Luminosität eines zukünftigen einmonatigen Betriebes mit Proton-Blei-Kollisionen abzuschätzen [17, 18]. Die jeweiligen Teilchenstrahlen werden zu diesem Zeitpunkt wahrscheinlich über die doppelte Teilchenpaketanzahl im Vergleich zu 2016 verfügen, da in den kommenden Jahren sogenanntes *Slip-Stacking* im Super Proton Synchrotron (SPS) realisiert werden soll [19, 20]. Das Ergebnis der Studie zeigt, dass in der Zukunft die Luminosität in den Experimenten ATLAS und CMS von $15\,\mathrm{nb}^{-1}$ pro Tag in 2016 auf $30\,\mathrm{nb}^{-1}$ pro Tag anwachsen wird, was eine deutliche Leistungssteigerung ist. Die Experimente ATLAS und CMS (ALICE und LHCb) erhoffen innerhalb von zwei einmonatigen Zeitblöcken mit Proton-Blei-Kollisionen im Zeitraum 2021–2029 eine integrierte Luminosität von $1.2\,\mathrm{pb}^{-1}$ ($0.6\,\mathrm{pb}^{-1}$) zu erreichen. Die Berechnungen zeigen, dass ATLAS und CMS mit $1.4\,\mathrm{pb}^{-1}$ und ALICE mit $0.68\,\mathrm{pb}^{-1}$ ihre gesetzten Ziele in diesem Zeitraum erreichen werden. Damit das LHCb-Experiment das Ziel von $0.6\,\mathrm{pb}^{-1}$ erreicht, ist jedoch die Entwicklung einer neuen Füllstruktur notwendig.

Die Luminosität wurde 2016 durch Teilchenverluste in den dispersionunterdrückenden Regionen bei ATLAS und CMS begrenzt. Die erwähnten Strahlverluste traten nur in Propagationsrichtung des Bleistrahls in etwa $300\,\mathrm{m}$ Entfernung hinter den Kollisionspunkten auf [21]. Die angezeigten Werte der Strahlverlustmonitore an diesen Stellen waren nur knapp unterhalb der erlaubten Grenzwerte. Es ist davon auszugehen, dass es sich bei den Verlusten um Fragmente von Bleiionen, die durch die Wechselwirkung mit Protonen in den Kollisionspunkten gespalten werden, handelt. Im Abstand von $150\,\mathrm{m}$ bis $200\,\mathrm{m}$ hinter den Kollisionspunkten von ATLAS und CMS sind sogenannte TCL-Kollimatoren[2] installiert, die während des Proton-Proton-Betriebs Kollisionsfragmente absorbieren, jedoch im Schwerionenbetrieb nicht im Gebrauch waren (von der Strahlachse zurückgezogen). Eine Analyse in Kapitel 6 zeigt durch Teilchen*tracking*, dass TCL-Kollimatorabstände von $15\sigma_x$ bis $20\sigma_x$ (σ_x ist die horizontale Strahlgröße des Bleistrahls) zur Strahlachse diese Fragmente abfangen. Es ist davon auszugehen, dass nur Teilchen mit Abweichungen der x'-Koordinate um das Vielfache der regulären Standardabweichung die TCL-Kollimatoren umgehen und die kritischen Stellen bei etwa $300\,\mathrm{m}$ erreichen können. Dementsprechend ist die zu erwartende deponierte Leistung bei Gebrauch der TCL-Kollimatoren verschwindend klein. Keine erfolgreiche Kollimation würde Spitzenluminosität im künftigen Proton-Blei-Betrieb verhindern und ein Rückschritt zu den instantanen Luminositäten aus 2016 wäre unumgänglich.

Ein Problem beim Schwerionenbetrieb mit Strahlenergien äquivalent zu denen im RHIC und im LHC ist die höchst periphere Wechselwirkung zwischen den Strahlen in den Kollisionspunkten. Diese Wechselwirkung äußert sich in Form von ladung- und masseverändernden Prozessen, die erheblich zum Gesamtwirkungsquerschnitt beitragen und zu Teilchenverlusten führen. Diese Prozesse skalieren sehr stark mit der Ladung der Kollisionspartner. Eine Reduktion der Ionengröße und damit der Ladung erhöht das Verhältnis des hadronischen Wirkungsquerschnittes zum Gesamtwirkungsquerschnitt deutlich. Kapitel 7 gibt einen Ausblick auf die zu erwartende Luminositätsproduktion im Proton-Nukleus-Betrieb bei Verwendung von Ionenarten, die leichter sind als Blei. Ein Wechsel von Proton-Blei- zu Proton-Argon-Kollisionen würde beispielsweise die integrierte Luminosität innerhalb eines Monats von $0.8\,\mathrm{nb}^{-1}$ auf $9.4\,\mathrm{nb}^{-1}$ in ATLAS und CMS erhöhen. Dies ist eine Steigerung von einer Größenordnung und eine Verbesserung der integrierten Nukleon-Nukleon-Luminosität um den ungefähren Faktor 2. Im Jahr 2023 wird es möglicherweise zu einem Test von Sauerstoff-Sauerstoff- und Proton-Sauerstoff-Kollisionen im LHC kommen [17, 18]. Der Betrieb mit Sauerstoff wird nur wenige Tage andauern und es wird nur mit einer geringen Luminosität operiert werden. In Kapitel 7 wird ebenfalls die zu erwartende Luminosität eines Proton-Sauerstoff-Testlaufs berechnet. Das LHCf-Experiment (LHCb-Experiment) würde entsprechend dieser Studie die angestrebte integrierte Luminosität von $1.5\,\mathrm{nb}^{-1}$ ($2\,\mathrm{nb}^{-1}$) innerhalb von $70\,\mathrm{h}$ ($35\,\mathrm{h}$) Strahlzeit erreichen.

[2] TCL: *Target Collimator Luminosity*

Contents

Symbols and abbreviations

Latin symbols

A	Number of nucleons
A_{IBS}	IBS common factor
a_m	Fourier coefficient of dipole-kick function Θ
A_m	Tune-modulation depth
$a_{x,n}$, $a_{y,n}$	Fourier coefficient of beam-beam kick function $h_{x/y}$
B	Magnetic field strength
$\hat{b}$	Impact parameter
b	Beam-beam encounter function
b_m	Fourier coefficient of beam-beam encounter function b
$B\rho$	Magnetic rigidity
c	speed of light
C	Machine circumference
$\mathcal{C}_{\mathrm{glo},x}$, $\mathcal{C}_{\mathrm{glo},y}$	Global cancellation efficiency
$\mathcal{C}_{\mathrm{IR},x}$, $\mathcal{C}_{\mathrm{IR},y}$	IR cancellation efficiency
$C_{\log}$	Coulomb logarithm
c_{mn}, C_{mn}	Fourier coefficients of Hamiltonian/potential
d	Total transverse beam separation
D	Tune-diffusion coefficient
$\mathcal{D}$	Synchrotron radiation integral
d_b	Beam-beam encounter spacing
d_t	Beam-beam encounter shift
d_x, d_y	Transverse beam separation

D_x, D_y	Transverse dispersion function
e	Elementary charge
E_b	Beam energy
E_{kin}	Kinetic energy
f	Arbitrary function (multiple redefinitions)
$\mathcal{F}$	(Discrete) Fourier transform
f_0	Revolution frequency
f_{RF}	RF frequency
f_s	Synchrotron frequency
f_x, f_y	Projected beam-beam kick function
g	Gain of transverse feedback system
h	Harmonic number
H	Hamiltonian
$\hbar$	Planck's constant ($\hbar = h/(2\pi)$)
H_0	Lie operator of linear motion
H_{b}	Lie operator of beam-beam interaction
H_{oct}	Hamiltonian of infinitesimal short octupole
H_{p}	Lie operator of arbitrary multipole
H_{turn}	Linear one-turn Hamiltonian
h_x, h_y	Long-range beam-beam kick function
$\mathcal{H}_x$, $\mathcal{H}_y$	Dispersion invariant
I_{oct}	LHC octupole current
J_x, J_y	Transverse linear action
$\mathcal{J}_x$, $\mathcal{J}_y$, $\mathcal{J}_z$	Synchrotron radiation partition number
k	Beam-beam constant
k_1	Quadrupole strength
k_2	Sextupole strength
k_3	Octupole strength
k_{b}	Bunch harmonic number
l	Linear correlation coefficient
$\mathcal{L}$	Instantaneous luminosity
$\mathcal{L}_{\mathrm{bb}}$	Bunch-by-bunch luminosity
$\mathcal{L}_{\mathrm{int}}$	Integrated luminosity
$\mathcal{L}_{\mathrm{NN}}$	Instantaneous nucleon-nucleon luminosity
$\mathcal{L}_{\mathrm{NN,int}}$	Integrated nucleon-nucleon luminosity
$\mathcal{L}_{\mathrm{t}}$	Targeted luminosity levelling value
$\mathcal{L}_{\mathrm{tot}}$	Total instantaneous luminosity

m	Particle mass
$\mathbf{M}$	Linear transfer matrix (4×4)
$\mathbf{M}_{\mathrm{b}}$	Linear beam-beam matrix
$\mathbf{M}_{\mathrm{b,coup}}$	Linear beam-beam coupling matrix
m_e	Electron mass
$\mathbf{M}_{\mathrm{IR}}$	Linear transfer matrix through IR
m_{p}	Proton mass
$\mathbf{M}_x$, $\mathbf{M}_y$	Linear transfer matrix (2×2)
n	Index of dipole overlap-knock out resonance
N	Beam intensity
$N(\omega)$	Photon flux
n_b	Number of bunches
N_b	Bunch intensity
n_c	Number of colliding bunch pairs
p	Particle momentum
p_0	Design momentum
Δp	Momentum deviation
p_{p}	Proton momentum
q	Particle charge
Q_s	Synchrotron tune
Q_v	Overlap-knock out resonance tune
Q_x, Q_y	transverse betatron tune
ΔQ_x, ΔQ_y	Transverse betatron-tune shift
r	Transverse radius
R	Nuclear electric radius
$\mathbf{r}$	Transverse phase-space vector
$\mathbf{R}$	Rotation matrix (4×4)
$\hat{r}$	Ratio of geometric beam sizes
r_0	Classical particle radius
r_{p}	Classical proton radius
$\mathbf{R}_x$, $\mathbf{R}_y$	Rotation matrix (2×2)
s	Longitudinal position along reference orbit
$\mathcal{S}_d$	Reduction factor due to transverse separation
$\mathcal{S}_g$	Geometry reduction factor
$\mathcal{S}_h$	Hourglass reduction factor
s_{IP}	Position of IP
$s_{\mathrm{IR}}^{\mathrm{end}}$	Position at end of common beam pipe of IR

$s_{\mathrm{IR}}^{\mathrm{start}}$	Position at start of common beam pipe of IR
$\sqrt{s_{\mathrm{NN}}}$	Nucleon-nucleon centre-of-mass energy
t	Time
$\mathbf{t}$	Transverse coherent kick vector
$\mathbf{T}$	Linear one-turn matrix
T_0	Revolution period
T_b	Beam-beam encounter period
T_m	Recurrence time
T_r	Turnaround time
T_{ramp}	Duration of the energy ramp
u	Arbitrary coordinate
U	Potential
v	Particle velocity
$\mathbf{v}$	Eigenvector of matrix
$\mathbf{V}_x$, $\mathbf{V}_y$	Normalisation matrix
W_0	Energy loss per turn
W_{stored}	Stored beam energy
x	Transverse horizontal coordinate
y	Transverse vertical coordinate
Δy	Rapidity shift
z	Longitudinal coordinate tangential to reference orbit
Z	Atomic number

Greek symbols

α_x, α_y	Twiss α-function
α_{xx}, α_{xy}, α_{yy}	linear detuning parameter
α_{ex}	Loss rate of non-colliding bunches
$\alpha_{\mathrm{IBS},x}$, $\alpha_{\mathrm{IBS},y}$, $\alpha_{\mathrm{IBS},z}$	IBS growth rate
α_c	Momentum-compaction factor
α_{IP}	Extra loss rate at IP
β	Particle velocity in units of the speed of light ($\beta = v/c$)
β_x, β_y	Twiss β-function
β_x^*, β_y^*	β-function at IP
γ	Relativistic Lorentz factor

γ_c	Fixed-target Lorentz factor
Γ_j	Relative position along total phase advance
γ_x, γ_y	Twiss γ-function
$\Delta\beta_x/\beta_x$, $\Delta\beta_y/\beta_y$	Transverse beta beating
δ_{eff}	Effective relative momentum error
δ_p	Relative momentum error $(p - p_0)/p_0$
$\delta_{t,x}$, $\delta_{t,y}$	Normalised net kick remaining after turn
δ_x, δ_y	Normalised net kick remaining after IR
ε_0	Vacuum permittivity
ϵ_x, ϵ_y	Transverse geometric emittance
ε_v	Fractional overlap-knock out resonance tune
$\epsilon_{\text{n}x}$, $\epsilon_{\text{n}x}$	Transverse normalised emittance
η	Slippage factor
θ	Crossing angle
θ_{ext}	External crossing angle
Θ_x, Θ_y	(Long-range beam-beam) dipole kick function
κ	Scaling factor for BFPP and EMD cross section
λ	Eigenvalue (spectrum) of matrix
μ	Pile-up
μ_x, μ_y	Total transverse phase advance
$\xi_{\text{HO}x}$, $\xi_{\text{HO}y}$	(Head-on) beam-beam parameter
$\xi_{\text{LR}x}$, $\xi_{\text{LR}y}$	Long-range beam-beam tune shift
ξ_x, ξ_y	Chromaticity
ρ	Radius of curvature
$\rho(Q_x)$, $\rho(Q_y)$	Density function of transverse tune
$\rho(x, y, z, t)$	Bunch density function
σ	Total cross section
σ_{BFPP}	Total BFPP cross section
$\sigma_{\text{BFPP}m}$	Cross section of order m BFPP process
σ_{EMD}	Total EMD cross section
$\sigma_{\text{EMD}m}$	Cross section of order m EMD process
σ_{had}	Hadronic cross section
σ_k	RMS focusing strength
σ_p	RMS relative momentum error
σ_x, σ_y	RMS beam size
Σ_x, Σ_y	Convoluted RMS beam size
$\tilde{\Sigma}_x$, $\tilde{\Sigma}_y$	RMS size of luminous area

$\sigma_{x'}$, $\sigma_{y'}$	RMS transverse angle
σ_z	RMS bunch length
τ	Intensity lifetime
τ_{ex}	Lifetime of non-colliding bunches
τ_{fill}	Fill duration
$\tau_{\mathrm{IBS},x}$, $\tau_{\mathrm{IBS},y}$, $\tau_{\mathrm{IBS},z}$	IBS growth time
τ_{opt}	Optimum fill duration
ϕ_x, ϕ_y	Transverse betatron phase
Ω	BLM signal
Ω_0	BLM noise floor
Ω_1	BLM scaling factor
ω_b	bunch-encounter angular frequency
$\Omega_{m,n}^{\mathrm{even}\pm}$, $\Omega_{m,n}^{\mathrm{odd}\pm}$	Frequencies of sidebands
ω_x, ω_y	Transverse betatron angular frequency

Acronyms and Abbreviations

ADT	LHC Transverse Damper
AGS	Alternating Gradient Synchrotron
ALICE	A Large Ion-Collider Experiment
ATLAS	A Toroidal LHC Apparatus
BCH	Baker-Campbell-Hausdorff
BFPP	Bound-Free Pair Production
BLM	Beam-Loss Monitor
BNL	Brookhaven National Laboratory
BPM	Beam-Position Monitor
BRAHMS	Broad RAnge Hadron Magnetic Spectrometers
BSRT	Beam Synchrotron Radiation Telescope
CERN	Organisation européenne pour la recherche nucléaire
CIMP	Completely Integrated Modified Piwinski
CMS	Compact Muon Solenoid

CTE	Collider Time Evolution
CTEPY	Collider Time Evolution Python
DC	Direct Current
DCBCT	Direct Current Beam-Current Transformer
DESY	Deutsches Elektronen-Synchrotron
DFT	Discrete Fourier Transformation
DS	Dispersion Suppressor
EBIS	Electron Beam Ion Source
ECR	Electron-Cyclotron Resonance
EMD	Electromagnetic Dissociation
ESPPU	European Strategy Particle Physics Update
FCC	Future Circular Collider
FLUKA	FLUktuierende KAskade
FMA	Frequency-Map Analysis
GDR	Giant Dipole Resonance
HE-LHC	High-Energy Large Hadron Collider
HERA	Hadron-Elektron-Ring-Anlage
HL-LHC	High-Luminosity Large Hadron Collider
HO	Head On
IBS	Intra-Beam Scattering
IP	Interaction Point
IR	Interaction Region
ISR	Intersecting Storage Rings
LEIR	Low Energy Ion Ring
LEP	Large Electron-Positron Collider
LEReC	Low-Energy RHIC electron Cooler
LHC	Large Hadron Collider

LHCb	Large Hadron Collider beauty
LR	Long Range
LS	Long Shutdown
MAD-X	Methodical Accelerator Design X
MKI	Injection Kicker Magnet
NAFF	Numerical Analysis of Fundamental Frequencies
NN	Nucleon-Nucleon
ODE	Ordinary Differential Equation
OKO	Overlap Knock-Out
PHENIX	Pioneering High Energy Nuclear Interaction Experiment
PS	Proton Synchrotron
PSB	Proton Synchrotron Booster
PTC	Polymorphic Tracking Code
QCD	Quantum Chromodynamics
QGP	Quark-Gluon Plasma
RF	Radio Frequency
RFQ	Radio-Frequency Quadrupole
RHIC	Relativistic Heavy-Ion Collider
RMS	Root Mean Square
SD	Standard Deviations
SO	Special Orthogonal Group
Sp$\bar{p}$S	Super Proton-Antiproton Synchrotron
SPS	Super Proton Synchrotron
STAR	Solenoidal Tracker
TCL	Target Collimator Long
TCLA	Target Collimator Long Absorber

TCLD	Target Collimator Long Dispersion Suppressor
TCP	Target Collimator Primary
TCSG	Target Collimator Secondary Graphite
TCT	Target Collimator Tertiary
TPC	Time Projection Chamber
WG	Working Group
ZDC	Zero-Degree Calorimeter

CHAPTER 1

Introduction to high-energy heavy-ion colliders and asymmetric collisions

This chapter describes the physics of heavy-ion collisions and gives an introduction to the two heavy-ion colliders currently in operation. This chapter is also used to put the topics this thesis is dealing with into perspective. Throughout the presentation of the different topics, basic concepts of accelerator physics in synchrotrons will not be recalled. These can be found, e.g., in the references [22–24]. Advanced mechanisms and effects are introduced at the positions they occur.

1.1 Heavy-ion physics and motivation for asymmetric collisions

The focus of this work is on the Large Hadron Collider (LHC) [1] in heavy-ion operation. Before the LHC achieved heavy-ion collisions for the first time in 2010, the Intersecting Storage Rings (ISR) [25] and the Relativistic Heavy-Ion Collider (RHIC) [26] already collided various ion species. RHIC and the LHC are the only heavy-ion colliders currently in operation. An important aim of producing heavy-ion collisions is the investigation of the quark-gluon plasma (QGP). This form of plasma is only generated at energies and densities that can only be achieved by mankind in particle colliders like the LHC which routinely collides $^{208}\mathrm{Pb}^{82+}$ ions in symmetric nucleus-nucleus (A-A) collisions for this purpose. The temperatures and densities in such a collision are sufficient for so-called de-confinement to take place, i.e., the colour neutrality which is generally enforced in quantum chromodynamics (QCD) is overcome and quarks

and gluons move freely. The QGP is expected to be the predominant state of matter in the ms range right after the big bang.

The heavy-ion operation of the LHC is a substantial and essential part of the LHC physics programme. While an important objective of the LHC proton-proton (p-p) physics case was the discovery of the Higgs boson [27, 28], the implication of the Higgs mechanism proposed in the 1960s, the main aim of the heavy-ion programme is the generation of the QGP and to understand its properties and its implications. Experiments at RHIC at Brookhaven National Laboratory (BNL), Upton, USA, already investigated this collective state in 2004/2005 [29–32]. The LHC and RHIC have discovered important features of the QGP, e.g., the suppression of J/Ψ particles [33] and the reduction of the transverse momentum of emerging particles from the collision point (jet quenching) [34, 35]. To understand whether these observed phenomena are caused by the QGP or other parameters, it requires complementary measurements for benchmarking. Obtaining data sets for collisions of protons or deuteron with the respective heavy-ion species (p-A or D-A) is the preferred way to obtain these complementary data sets. Hence, efforts were made early to investigate the feasibility of p-Pb or D-Pb collision in the LHC since this form of operation would become an important pillar of the LHC heavy-ion programme. Initially, the collision of D-Pb was also considered since the central rapidity shift is smaller compared to that in p-Pb collisions; however, the acceleration of deuteron was classified as highly cumbersome and would have required significant resources [36].[1] Short runs with p-Pb and p-p collisions at the equivalent nucleon-nucleon centre-of-mass energy $\sqrt{s_{\mathrm{NN}}}$ as the Pb-Pb collisions were performed over the years to complement the Pb-Pb data sets of the experiments. These runs allowed particle physicists to compare Pb-Pb collisions with those of the presumably cold matter states in p-p and p-Pb collisions. Besides the already mentioned investigation of the QGP, additional effects like light-by-light scattering [37], a process forbidden in Maxwell's theory of electrodynamics, have been observed in heavy-ion collisions at the LHC. This observation was only possible because of the large photon flux generated by the strongly Lorentz contracted electromagnetic fields of the highly charged Pb ions.

1.2 The Large Hadron Collider (LHC)

The LHC is the world's most powerful and largest particle accelerator built in the tunnel of the former Large Electron-Positron Collider (LEP) [38] at CERN, Geneva, Switzerland, in the early 2000s. The most important information regarding the LHC, its layout and the injector chain are given in the LHC design report [1]. The LHC has a clockwise rotating (blue) beam referred to as Beam 1 and a counterclockwise rotating (red) beam referred to as Beam 2. The beams

[1] The acceleration of deuteron would have required a new RF quadrupole and a switch yard in order two quickly switch between ions (Pb) and deuteron.

provide head-on collisions in four large experiments. These four experiments are ATLAS at the interaction point 1 (IP1) [39], ALICE [40] at IP2, CMS [41] at IP5 and LHCb [42] at IP8. Figure 1.1 shows a sketch of the LHC. The LHC only accelerates beams of hadrons with positive charge. The LHC operates with a harmonic number $h = 35640$; however, only every 10th bucket is filled. These 3564 buckets are usually referred to as bunch slots and are spaced by $25\,\mathrm{ns}$ in time, corresponding to $7.5\,\mathrm{m}$ in space.[2] The LHC design study foresaw the feasibility and performance of p-p and Pb-Pb collisions as the two main operation modes. This thesis, however, focusses on the asymmetric case of p-Pb collisions which was not included in the initial design. The feasibility of p-Pb collisions in the LHC was investigated up to the years 2011/2012 when accelerating and colliding protons with Pb ions was successfully achieved for the first time [3]. Until today, the LHC has provided collisions in four different operation modes, namely p-p, Pb-Pb [43–46], p-Pb [3–5] and xenon-xenon (Xe-Xe) [47]. In addition, the LHC was able to accelerate partially stripped Pb ions ($^{208}\mathrm{Pb}^{81+}$-$^{208}\mathrm{Pb}^{81+}$) [48] in the scope of the gamma factory project. It is highly likely that the LHC will accelerate and collide additional ion species in the future (see Sec. 1.2.6).

At injection in the LHC, protons and Pb ions have a magnetic rigidity of $B\rho = 1.5 \times 10^3\,\mathrm{Tm}$ equivalent to a proton momentum of $p_\mathrm{p} = 450\,\mathrm{GeV/c}$. The LHC can accelerate these to a maximum magnetic rigidity of $B\rho = 25 \times 10^3\,\mathrm{Tm}$ equivalent to the proton momentum of $p_\mathrm{p} = 7\,\mathrm{TeV/c}$ according to the design. Since heavy ions have the same magnetic rigidity as protons in the LHC, the notation $p = Zp_\mathrm{p}$ is used with p being the ion momentum, Z being the atomic number of the ion and p_p being the proton momentum at equal rigidity. In the limit of a much larger particle momentum compared to the particle mass ($pc \gg mc^2$), this notation can be extended to the beam energies $E_b = ZE_{b,\mathrm{p}}$ with $E_{b,\mathrm{p}} \approx p_\mathrm{p}c$ referring to the proton energy at the equivalent magnetic rigidity. The LHC has not been operated at its design energy of $E_b = 7Z\,\mathrm{TeV}$ yet. During Run 1 of the LHC (2010–2013), it was operated at $E_b = 3.5Z\,\mathrm{TeV}$ and during Run 2 (2015–2018) at $E_b = 6.5Z\,\mathrm{TeV}$. At this point in time, the second long shutdown (LS2) is ongoing and the design energy is envisaged for Run 3 (2021–2023).

With a circumference of $C = 26\,659\,\mathrm{m}$, the LHC is the largest particle accelerator in terms of circumference in the world. The four experiments are positioned at four out of eight insertions loosely called interaction regions (IRs).[3] At the remaining four positions, the accelerating RF structures (IR4), the beam dumps (IR6) and the two collimation regions (IR3 and IR7) are located. The eight IRs are interconnected by the arcs. The magnetic accelerator lattice in these arcs is made of FODO cells. Most of the LHC magnets are superconducting. All 1232 arc dipoles are superconducting and provide a field strength up to $B = 8.33\,\mathrm{T}$. At the IRs, nor-

[2] With an abort gap of roughly $3\,\mu\mathrm{s}$ and gaps of multiple $100\,\mathrm{ns}$ that result from the LHC injection-kicker rise time, not every single bunch slot out of the 3564 bunch slots accommodates a bunch.

[3] The four IRs not featuring detectors are also called IRs independently of the fact that no particle collisions take place at these points.

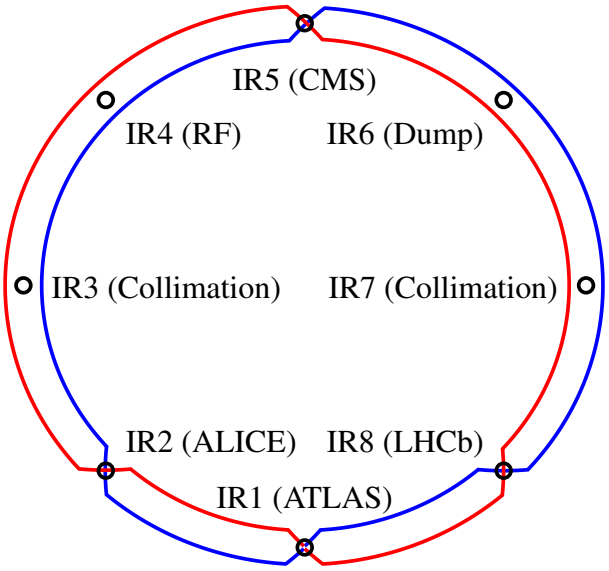

Figure 1.1: A sketch of the LHC layout. The LHC has four experimental and four utility insertions. The two large experiments ATLAS and CMS are diametrically opposed to each other while the smaller experiments ALICE and LHCb are on either side of ATLAS in one eighth of the circumference distance to ATLAS.

mal conducting magnets are occasionally used. This large number of superconducting magnets makes the LHC highly susceptible to beam losses. Small fractions of the particles in a single stored proton or Pb bunch can cause a magnet quench (the loss of superconductivity) if the energy of these particles is deposited in the superconducting coils of such a magnet. Since the LHC accelerates positively charged hadrons, a two-beam-pipe magnet layout is deployed with flipped field directions in the two beam pipes. Such a magnet design reduces the required space in the tunnel, and infrastructure like cryostats can be shared. This so-called two-in-one bending magnet design (see Fig. 1.2) lacks flexibility in the sense the magnetic field is of the same magnitude in both beam pipes.

The LHC is in good approximation eight-fold rotation symmetric, splitting the accelerator in eight octants with roughly similar particle-beam optics. The two detectors ATLAS and CMS are located diametrically opposite (see Fig. 1.1) and are the two high-luminosity experiments. The ALICE and LHCb detectors on either side of ATLAS have significantly smaller read-out rates and therefore demand much less luminosity than ATLAS/CMS. In the context of this thesis, it is important to note ALICE is a dedicated heavy-ion experiment with hardware optimised for the analysis of heavy-ion collisions. ALICE features zero-degree calorimeters (ZDCs) in the high

and low rapidity range to detect spectator nucleons (protons and neutrons not participating in the collision) and the inner detector comprises a time projection chamber (TPC). Furthermore, ALICE features a dedicated muon spectrometer with its dipole being one of the largest normal conducting magnets ever built; however, the spectrometer is positioned asymmetrically with respect to the IP, making ALICE an asymmetric experiment. Because of the asymmetry, ALICE requires a beam-direction reversal in p-Pb collisions to cover a larger rapidity range. ALICE's hardware and event triggers are designed in a way that ALICE requires a low luminosity to avoid multiple simultaneous collisions per bunch crossing, the so-called pile-up (see Sec. 4.1.3). The nominal design luminosity of ALICE in Pb-Pb collisions is at $\mathcal{L} = 10^{27}\,\mathrm{Hz/cm^2}$. This value is orders of magnitude smaller than the usually achieved luminosity of roughly $\mathcal{L} = 2 \times 10^{34}\,\mathrm{Hz/cm^2}$ in the two high-luminosity experiments ATLAS and CMS in p-p operation.

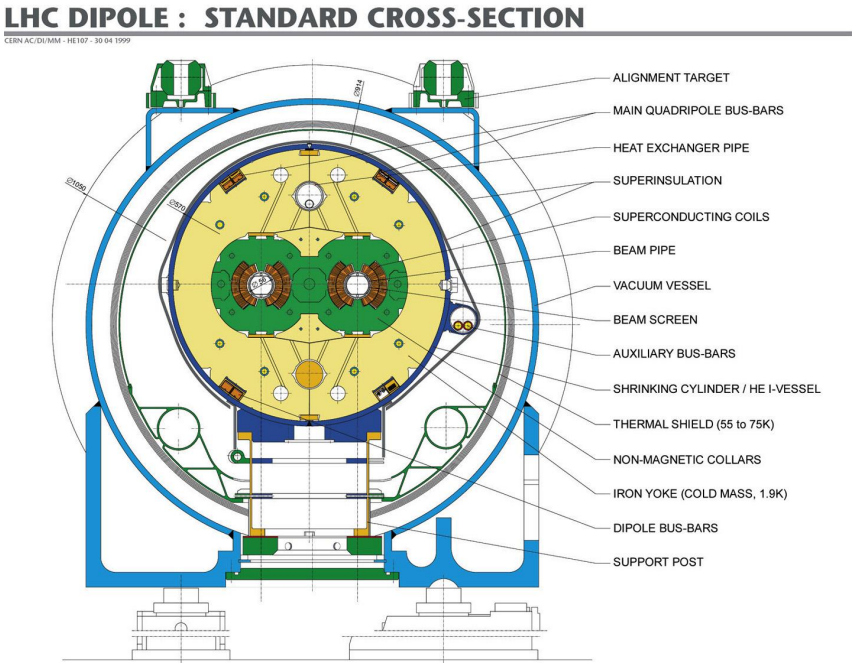

Figure 1.2: Sketch of the LHC dipole cross section. The two-in-one magnet design forces the magnitudes of the fields to be equal within the two beam apertures; however, the field directions are antiparallel. Picture provided by CERN [49].

The LHC collides large numbers of bunches in its four experiments. In p-p operation, a typical number is 2544 bunches per beam with a 25 ns bunch spacing and intensities of $N_b = 1.15 \times 10^{11}$ particles per bunch. Ion bunches cannot be produced with such high bunch intensities and small bunch spacing. The initial design foresaw 592 Pb bunches per beam in Pb-Pb operation (100 ns bunch spacing) with an intensity of $N_b = 7 \times 10^7$ ions per bunch [1]; however, more than 592 Pb bunches were already achieved in 2016 during the second p-Pb

run [5]. The Pb bunch intensities exceeded the design value already in the first Pb-Pb run in 2010 with $N_b = 1.2 \times 10^8$ ions per bunch.

Because of the small bunch spacing, crossing angles at the IPs are applied to avoid parasitic collisions close to the IPs. The ALICE and LHCb experiments have spectrometer magnets that influence the orbits and therefore the crossing angles. Without the influence of the respective spectrometer, corrector magnets on either side of the IP generate a natural crossing angle at the collision point, the external crossing angle. The spectrometer introduces additional distortion of the orbits and modifies the crossing angle. The net crossing angle at the IP is therefore a combination of the external crossing angle and the crossing angle generated by the spectrometer, the internal crossing angle. The proton and Pb bunches are produced by the LHC injector chain, which will be explained in the next section.

1.2.1 Injector chain

The first accelerators of the CERN accelerator complex (see Fig. 1.3) the ion and proton bunches are passing through are different for the two particle types. The last two accelerators of the LHC injector chain, however, are common to the proton and ion bunches. The last accelerator of the injector chain injects both particle types into the LHC. The different kinematic properties of the particles at low energies require different accelerating structures because of, e.g., the particle velocity and space charge. The injector chain for ions and protons is explained in the following.

1.2.1.1 Ion injector chain

An oven provides vaporised Pb to an electron-cyclotron resonance (ECR) ion source. Within the ECR source, plasma electrons in combination with an external RF wave ionise the Pb ions to an intermediate charge state. Oxygen serves as a buffer gas in the ion source to cool the longitudinal motion of the Pb ions to increase the time the Pb ions remain in the ion source. A dipole acting as a spectrometer selects the $^{208}\mathrm{Pb}^{29+}$ ions from the beam after the ion source. These are accelerated in the RF quadrupole (RFQ) and the linear accelerator (linac) Linac3 before a stripping foil increases the charge state to $^{208}\mathrm{Pb}^{54+}$. At injection into the Low Energy Ion Ring (LEIR), the ions have a kinetic energy of $E_{\mathrm{kin}} = 4.2\,\mathrm{MeV/nucleon}$. LEIR usually accumulates seven Linac3 injections in a coasting beam and performs an RF capture to obtain two bunches. LEIR then accelerates these two bunches to a kinetic energy of $E_{\mathrm{kin}} = 72\,\mathrm{MeV/nucleon}$. While the particles are stored in LEIR, electron cooling is applied to reduce the beam size. The bunch volume reaches equilibrium once the damping rate from the cooling and the growth rate caused by intra-beam scattering (IBS) cancel out. The Proton Synchrotron (PS) continues the acceleration of the ions after LEIR. During the 2016 p-Pb run of the LHC, two Pb bunches were accumulated and split into four bunches spaced by $100\,\mathrm{ns}$, a so-called batch, via the sophisti-

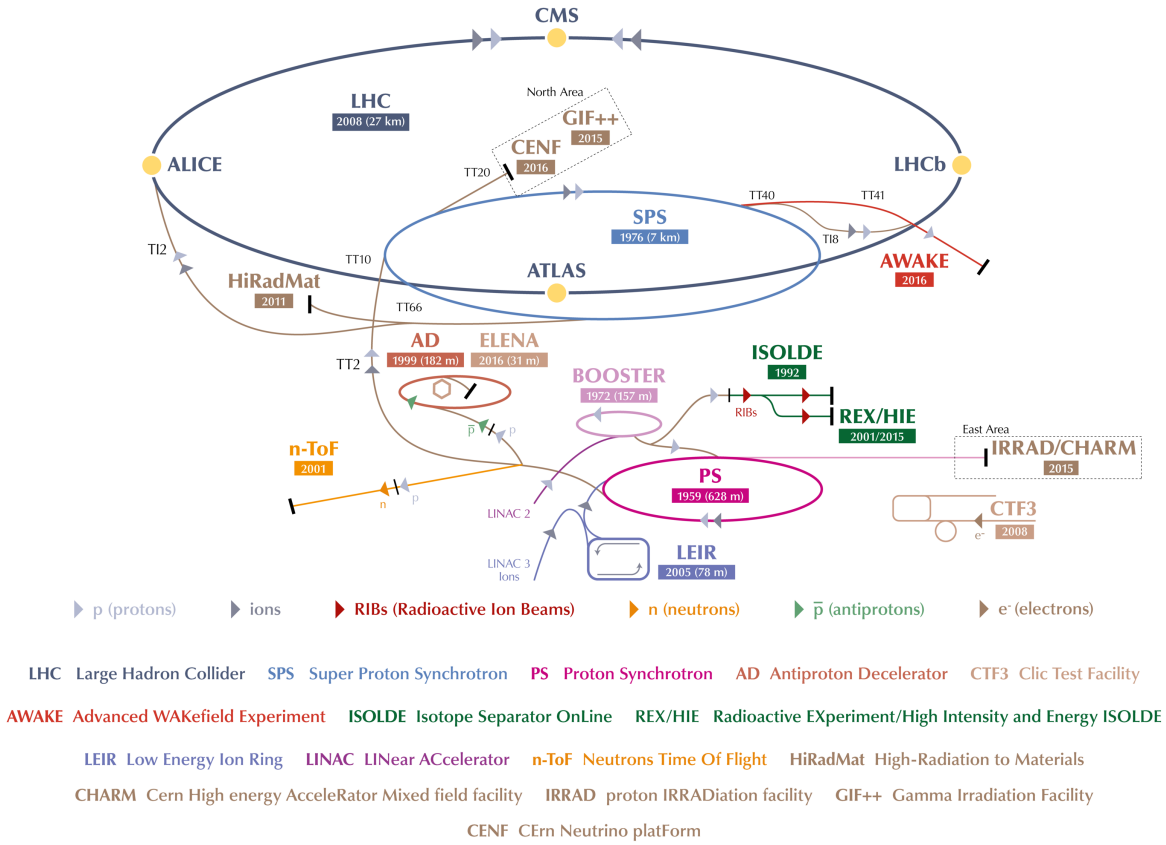

Figure 1.3: Schematic diagram of the CERN accelerator complex. During Run 1 and Run 2 of the LHC, the protons were generated at the Linac2 that was followed by the booster, PS, SPS and finally the LHC. The heavy-ion injector chain starts with the Linac3 followed by LEIR. After LEIR, the ions are injected into the PS and follow the nominal proton chain. The Linac2 decommissioning started towards the end of 2018. Linac4, an H^- accelerator, will replace Linac2 in LHC Run 3 and beyond. Picture provided by CERN [50] (modified).

cated use of three RF systems with three different frequencies in the PS [51]. Figure 1.4 shows a sketch of the bunch and batch production along the ion and proton injector chain as used during the 2016 p-Pb run. The kinetic energy is increased to $E_{\mathrm{kin}} = 5.9\,\mathrm{GeV/nucleon}$ before the particles are extracted from the PS. In the beamline between the PS and the Super Proton Synchrotron (SPS), the next accelerator in the ion injector chain, a last stripping foil strips off the remaining electrons to reach the fully ionised $^{208}\mathrm{Pb}^{82+}$ state. The SPS accumulated up to seven PS batches (28 Pb bunches in total) in 2016. The seven batches were separated by 200 ns as a result of the SPS injection-kicker rise time. The batches injected first into the SPS suffer intensity losses due to space charge and IBS while the remaining batches are injected since the beam energy is unchanged at injection energy during that time span. Space charge and IBS

become insignificant at the SPS top energy of $E_b = 450Z\,\mathrm{GeV} = 177.4A\,\mathrm{GeV}$ with A being the number of nucleons of the ion.

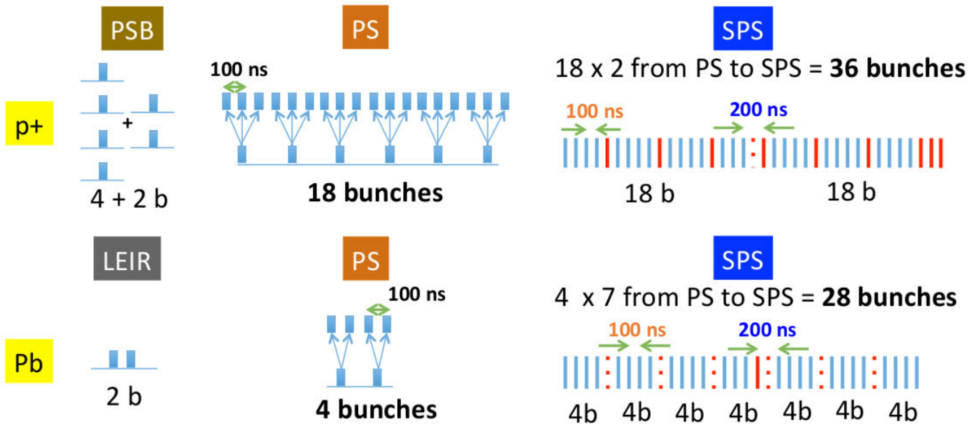

Figure 1.4: Bunch-pattern production scheme throughout the injector chain for the 2016 heavy-ion run of the LHC. With 28 Pb bunches and 36 proton bunches aligned in the LHC, only one Pb bunch is non-colliding. Courtesy of R. Alemany-Fernández. Plot taken from [13].

1.2.1.2 Proton injector chain

The protons do not share the same injector chain with the Pb ions at low energy. The protons are produced in the source and the first stage of acceleration after the RFQ was provided by the Linac2 until 2018. In the upcoming LHC runs, a next-generation linac, the Linac4, will accelerate the protons instead. Linac4 will be fully operational after LS2 and will provide the protons for p-Pb and p-p collisions in Run 3 and beyond. This modern linac has the advantage of being an accelerator of H^- (negatively ionised hydrogen). This allows to inject larger intensities into the Proton Synchrotron Booster (PSB), the synchrotron right after Linac2/4. Larger intensities are possible since the kinetic energy $E_{\mathrm{kin}} = 160\,\mathrm{MeV}$ provided by the Linac4 is roughly three times as large as the Linac2 energy; therefore, significantly increased intensities are accomplished for a given space-charge tune shift in the PSB.

The protons are injected from the proton booster at a kinetic energy of $E_{\mathrm{kin}} = 800\,\mathrm{MeV}$ into the PS. In 2016, six proton bunches from the proton booster were accumulated and split into 18 bunches spaced by 100 ns by overlaying the fundamental RF frequency with its third harmonic. Two of these batches, comprising 18 proton bunches each, were then injected into the SPS with an energy of $E_b = 25\,\mathrm{GeV}$ spaced by 200 ns. After the acceleration in the SPS, the extraction at $E_b = 450\,\mathrm{GeV}$ of the 36 bunches into the LHC took place.

In regular p-p operation, the bunches are separated by 25 ns. In p-Pb operation, however, it is inefficient to produce 25 ns proton bunch trains since the Pb injector chain only provides either 100 ns (2016 p-Pb run [5]) or 75 ns (2018 Pb-Pb run [46]) bunch trains. The number

of bunches injected into the PS and the following bunch split were different during the 2018 Pb-Pb run. In 2018, the operation took place with a bunch spacing of 100 ns during the first part and a bunch spacing of 75 ns during the second part of the run; however, in future p-Pb runs, it is planned to use a 100 ns bunch spacing in the injector chain in order to interleave two batches in the SPS (momentum slip-stacking) to accomplish a 50 ns bunch spacing in the LHC. Section 1.2.6 gives a short description of the momentum slip-stacking.

1.2.2 The LHC cycle

The LHC has to be injected with fresh beams typically two to three times per day since the beam intensities decrease over time due to intensity losses that result from, e.g., collisions of beam particles with those of the counter-rotating beam (luminosity burn-off) or residual gas, non-linearities of the magnetic lattice or faults of the accelerator software and hardware which may cause the dump of the beams. The LHC operation divides itself into so-called fills. Figure 1.5 illustrates the operational cycle of such a fill. A fill starts with the injection of the two beams.

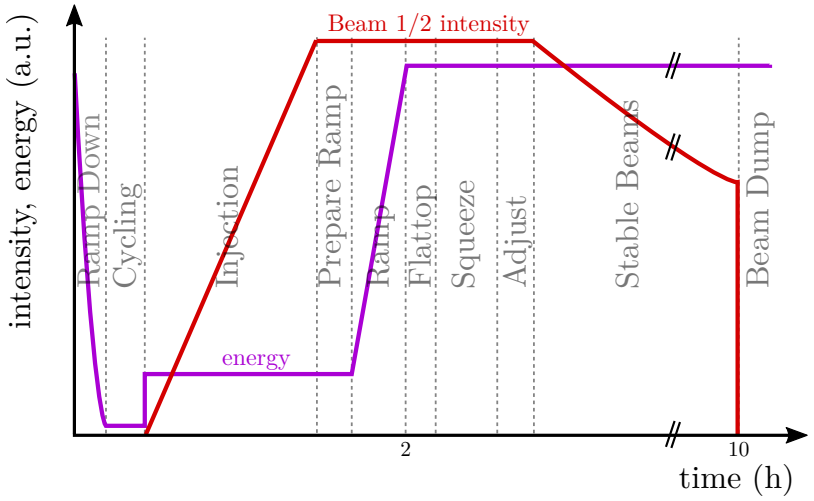

Figure 1.5: Sketch of an example operational cycle of the LHC. The red line is the beam intensity of Beam 1 and Beam 2 and the purple line is the beam energy. The different steps throughout the cycle are given in grey. It may take 2 h to reach top energy after the Beam Dump of the previous fill and Stable Beams condition can be kept easily for 8 hours in most heavy-ion fills.

After the *Injection*, the energy *Ramp* increases the beam energy to the target value. To inject and ramp the new beams can easily take 2 h or longer from the *Ramp Down* of the previous fill and the *Cycling* of the magnets. After the ramp, *Flattop* (top energy) is reached and the *Squeeze* reduces the β^* in the experiments to the collision values. Nowadays, a part of the *Squeeze* is included in the *Ramp* (combined ramp and squeeze). In the *Adjust* phase, the beams are brought

in collisions until finally *Stable Beams* is achieved. After a while in *Stable Beams*, e.g., $8\,\mathrm{h}$, the *Beam Dump* takes place and the next fill is prepared. The time span between the *Beam Dump* of the previous fill and achieving *Stable Beams* is the so-called turnaround time T_r. This value is important for the operation of the LHC. The longer the turnaround time, refilling the LHC becomes more and more uneconomic. The LHC operators therefore use the turnaround time to estimate whether they should extend or shorten respective fills to maximise the integrated luminosity.

1.2.3 The LHC collimation system

Another feature of the operation with Pb ions is the poor collimation efficiency. Collimators are artificial restriction of the physical aperture via the insertion of, e.g., carbon-fibre, copper or tungsten-alloy blocks close to the beam axis. The LHC stores beams with total energies up to $360\,\mathrm{MJ}$ during proton operation. The LHC has therefore dedicated systems like the collimation system to protect the LHC against its own beams since small fractions of the beams can create severe damage to the hardware of the LHC as already mentioned. The collimation system shields the LHC from particles which may diverge from the design orbit for multiple reasons, e.g., residual-gas scattering, de-bunching caused by IBS, optical resonances and many more. These particles have to be intercepted to avoid magnet quenches in superconducting magnets. A magnet quench leads to the immediate dump of the two beams, i.e., the beams are extracted from the LHC and diverted into copper blocks. The recovery after a magnet quench can take hours and easily half a day. The collimation systems comprises roughly 100 collimators, which are distributed in specific locations around the LHC circumference. These collimators fulfil different tasks in the protection of the LHC.

The TCP collimators are the primary collimators located in the IR7 region of the LHC (betatron cleaning) and IR3 region (momentum cleaning). Among all collimators, the TCP collimators are the closest to the beam axis and define the acceptance of the machine. The TCP collimator jaws in IR7 usually approach the beams down to a half gap between 5σ to 6σ of the beam size. Because of the high power of the primary halo[4], the TCPs are made of a carbon-fibre composite. The different TCPs have respectively horizontally, vertically and skew-aligned collimator jaws. The beta-cleaning TCPs are responsible for the scraping of particles with large transverse amplitudes while the momentum-cleaning TCPs are positioned at locations where the horizontal dispersion is large to allow the interception of particles with an increased momentum deviation with respect to the nominal momentum. Figure 1.6 gives a schematic picture describing the functionality of the collimation system.

Heavy ions like Pb may undergo nuclear fission and photonuclear processes or they are elastically scattered at impact on the TCPs. In the first two cases, a shower of fragments and

[4]The halo refers to particles in the tails of the transverse distributions.

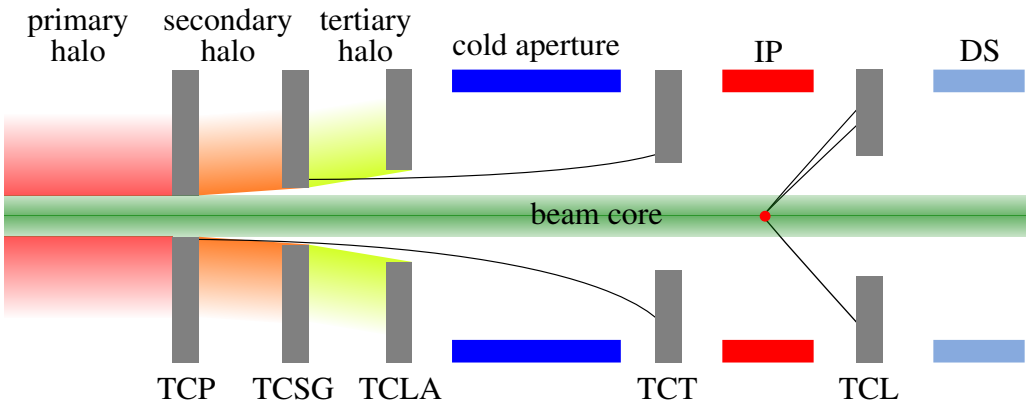

Figure 1.6: Sketch of the multi-stage collimation system of the LHC in the case of protons. The longitudinal proportions of the accelerator layout are altered. The TCSG and TCLA collimators intercept potential halo particles emerging from the TCPs while the TCT and TCL collimators protect the IPs and the dispersion suppressors (DSs), respectively, from collision fragments. During the operation with heavy ions like Pb, larger quantities of particles scattered or produced at the collimator jaws impact the cold (superconducting) aperture. This happens much more often compared to the proton case.

modified particles emerge from the TCP collimators. These fragments continue to propagate along the beam pipe. The distance they travel depends on the rigidity difference to the nominal beam. If a primary particle is elastically scattered, the yet unmodified particle continues its propagation, however, with a changed transverse angle. The secondary collimators (TCSGs) are positioned downstream of the TCPs to intercept these particles/fragments. The TCSGs are retracted by a few σ compared to the TCPs to avoid damage on the TCSG collimator jaws. Downstream of the TCSGs, TCLA absorbers are installed to intercept a potential tertiary halo and particles which might have passed by the TCSGs. The tertiary collimators (TCTs) are installed just before each detector to protect the detector hardware. Special collimators are installed downstream of the high-luminosity experiments ATLAS and CMS since fragments from the collisions also pose threats to the superconducting arcs of the LHC. These collimators are the TCLs which are not available at ALICE and LHCb.

Because of the fragmentation of heavy-ions at impact on the collimators, the Pb collimation efficiency is much worse compared to protons. In other words, the ratio of collimation losses to the losses in the cold region of the collider is much larger for protons than for Pb ions. In particular, the dispersion suppressors at IR7 are of constant concern since all fragments which were produced at the collimators of IR7 and were not intercepted yet are deposited in the dispersion suppressors. This behaviour happens naturally because the first peak of the dispersion function is located in the dispersion suppressors. To protect the dispersion suppressors, additional collimators, TCLDs, are going to be installed on either side of IR7.

TCLD collimators will also be installed on both sides of the ALICE IR to protect the ALICE dispersion suppressors from secondary beams. Heavy-ion collisions feature secondary beams coming out of the collision points. Ultra-peripheral collisions of the colliding ions may generate electron-positron pairs with electrons being in bound states of the participating ions. For a Pb ion colliding with an arbitrary ion A, the so-called bound-free pair production (BFPP) process reads

$$A + {}^{208}\mathrm{Pb}^{82+} \rightarrow A + {}^{208}\mathrm{Pb}^{81+} + e^{+}\,. \tag{1.1}$$

BFPP causes a secondary beam of ${}^{208}\mathrm{Pb}^{81+}$ ions with slightly different magnetic rigidity compared to the nominal beam particles to emerge out of the collision point. Ultra-peripheral collisions may also excite Pb nuclei that end up emitting a neutron during the relaxation process

$$A + {}^{208}\mathrm{Pb}^{82+} \rightarrow A + {}^{207}\mathrm{Pb}^{82+} + \mathrm{n}\,. \tag{1.2}$$

This process is so-called electromagnetic dissociation (EMD). Section 4.1.4 gives a detailed description of the BFPP and EMD processes. At the two high-luminosity experiments ATLAS and CMS, the secondary beams resulting from BFPP in Pb-Pb collisions may cause magnet quenches if not mitigated. This mitigation is achieved by guiding the location the BFPP beam impacts the physical aperture via orbit bumps to the position of a connection cryostat in the dispersion suppressors at which a dipole is *missing* to suppress the dispersion function [52]. Such measures do not have to be taken in p-Pb operation since the power of the secondary beams is orders of magnitudes smaller compared to the symmetric Pb-Pb case. Because of the quadrupole polarity at ALICE, the mitigation via orbit bumps is not feasible. This makes the installation of TCLD collimators in the ALICE dispersion suppressors the only effective way to remove luminosity restrictions in future Pb-Pb runs.

1.2.4 The feasibility of the LHC ever colliding p-Pb

The feasibility of colliding p-Pb in the LHC was not investigated in the LHC design [1] as already mentioned. One way to accelerate Pb ions and protons simultaneously is to accelerate them with the same momentum per charge $p/Z = B\rho$. Although the momentum per charge is equal for the proton and Pb beams, the energy per nucleon and consequently the relativistic Lorentz factors $\gamma = E_b/(mc^2)$ are unequal. This also implies that besides the velocities $v = c\sqrt{1 - 1/\gamma^2}$ also the revolution frequencies f_0 of the two beams are different. At the four experimental IPs, both beams share the same beam pipe for at least $200\,\mathrm{m}$ as is shown in Fig. 1.7. While a bunch is passing through these IRs, potential interactions between the bunch and the bunches of the counter-rotating beam can occur (beam-beam effect). Although the beams are separated via orbit bumps that create parallel separations in the IRs to avoid unwanted head-on

collisions during the energy ramp, long-range beam-beam interactions still occur. In symmetric p-p or Pb-Pb operation, these long-range beam-beam interactions always occur at the same positions; however, in p-Pb operation at injection energy, the velocity difference between the two beams causes a shift of all potential long-range beam-beam encounter locations by $15\,\mathrm{cm}$ per turn.[5] This shift is considerably smaller compared to the length of the common beam pipe in the IRs. Previous experience at the ISR [6, 7] and RHIC [8] has shown that unequal revolution frequencies of the beams may lead to rapid emittance growth and intensity losses. The excitation of specific transverse betatron tunes resulting from different revolution frequencies among the beams was called overlap knock-out (OKO) resonance. Section 2.1.8 explains this effect in detail. In RHIC, the switch to an acceleration scheme with the same f_0 and unequal $B\rho$ avoided moving long-range beam-beam encounters in the IPs; however, such a scheme is not applicable in the LHC since it would require unequal magnetic field strengths for the two beams. Attempting the energy ramp with locked RF frequencies and consequently fixed long-range beam-beam encounter points is also no option in the LHC. Although locked RF frequencies would equalise the f_0 of the two beams, it also induces large relative momentum shifts $\delta_p = (p - p_0)/p_0$ on both beams with p_0 being the nominal momentum. The momentum shift δ_p is positive (negative) for the faster (slower) beam.[6] The combination of δ_p with dispersion in the LHC arcs drives the Pb and proton orbits outside the aperture of the LHC at injection energy. An RF lock is only possible at intermediate energies $E_b \geq 2.73Z\,\mathrm{TeV}$ [53]. The orbit excursions are smaller than $1\,\mathrm{mm}$ in the arc quadrupoles at these energies. Because of the lack of a viable alternative, the energy ramp with unequal f_0 and moving long-range beam-beam encounters is forced in the LHC. The experience made at RHIC caused concerns regarding the operability of the LHC when attempting the injection and energy ramp in the presence of moving long-range beam-beam encounters. The concerns vanished once a test with p-Pb beams in 2011 showed the feasibility of injecting a handful Pb bunches in the presence of multiple hundred proton bunches into the LHC and collisions of a few Pb and proton bunches were established in 2012. The 2013 run gave the final confirmation of the feasibility of p-Pb operation with nominal bunch numbers. Since then, it is clear that proton and Pb beams can be injected into the LHC and collisions can be established without facing losses like those observed in RHIC. After the initial tests in 2011/2012, the LHC was operated in p-Pb configuration twice (2013 and 2016). Although the feasibility of colliding p-Pb was proven experimentally, a complete model to show the stability of the LHC in this configuration is still due.

The collision of proton and Pb beams in the LHC implies the collisions of beams of a very different beam size. Previous experience at HERA [11], DESY, Germany, and the SPS [12] has shown the major reduction of the beam lifetime of the beam with the larger transverse

[5] The value of $15\,\mathrm{cm}$ applies at LHC injection energy. The shift becomes smaller towards higher energies.

[6] This assumes a positive slippage factor like in the LHC at injection.

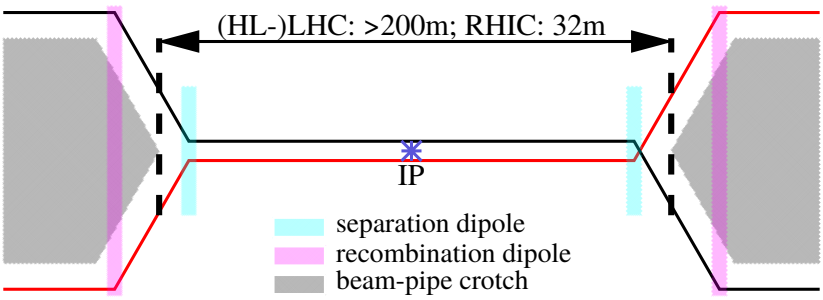

Figure 1.7: General layout of the interaction region in heavy-ion colliders in the horizontal plane. The beams are separated by a few mm (in this case in the horizontal plane) at the IP. The dipoles guiding the two beams together are referred to as the separation and recombination dipoles. The distance between the beam-pipe crotches L is more than $200\,\mathrm{m}$ in the LHC and roughly $32\,\mathrm{m}$ in RHIC. (Strongly exaggerated ratio between longitudinal and horizontal dimension.)

beam size because of the collision with the smaller beam. Because of these observations, the feasibility of p-Pb collisions had been questioned since the Pb beam size is often $70\,\%$ larger than that of the proton beam. It was observed in HERA and the SPS that the beam lifetime decreased rapidly with an increasing ratio of the two geometric emittances ϵ of the two beams. The geometric beam emittance is $\epsilon = \epsilon_\mathrm{n}/(\gamma\beta)$ with ϵ_n being the normalised emittance and $\beta = v/c$. The geometric emittance therefore shrinks with increasing beam energy. This process is called adiabatic damping. In the LHC, the geometric-emittance difference is partly a result of the injector chain but also due to the smaller relativistic Lorentz factor of the Pb ions $\gamma_\mathrm{Pb} = Z_\mathrm{Pb}\gamma_\mathrm{p}m_\mathrm{p}/m_\mathrm{Pb} \approx 0.39\gamma_\mathrm{p}$ and the resulting weaker adiabatic damping for Pb ions. During the p-Pb runs of the LHC, unaccounted beam intensity losses were observed. It is unclear whether these are a consequence of colliding beams of different size. A larger fraction of Pb ions are at transverse actions at around 1σ to 2σ of the smaller proton beam at which the non-linear components of the beam-beam force are the strongest (see Sec. 2.1.4). It is speculated that this behaviour causes diffusion of more Pb ions than in the symmetric case.

This section gave the two main reasons the successful operation of the LHC in p-Pb configuration was initially doubted. These critical topics are objectives of this thesis:

- **Objective 1** (Chapter 2) The influence of moving long-range beam-beam encounters on the LHC beams during p-Pb operation is mostly unknown and insufficiently analysed. A model that describes the influence on the beams and reproduces the today's LHC in p-Pb operation as stable is highly desirable at this point in time.

- **Objective 2** (Chapter 3) The influence of colliding Pb and proton beams of significantly different geometric beam sizes is insufficiently known, and it is not clear if this form

of collisions influences the beam lifetime negatively. An analysis with respect to these questions is required.

1.2.5 Previous heavy-ion runs of the LHC

The LHC has been operated with heavy ions a substantial fraction of its operational time. With six full one-month runs, the LHC has concluded its Run 1 and Run 2. A short account of the different Pb-Pb and p-Pb runs is given in the following.

1.2.5.1 Previous Pb-Pb runs

The LHC has finished four Pb-Pb runs with a combined duration of roughly 13.5 weeks. The first two Pb-Pb runs in 2010 and 2011 in LHC Run 1 were operated at a beam energy of $E_b = 3.5Z\,\mathrm{TeV}$. Table 1.1 gives a reduced parameter list of the respective runs. The Pb-Pb runs (2015 and 2018) in Run 2 of the LHC were operated at $E_b = 6.5Z\,\mathrm{TeV}$. Besides the higher beam energy, the bunch numbers n_b and bunch intensities N_b, in particular, were improved over time. While only 137 bunches per beam ($500\,\mathrm{ns}$ bunch spacing) with $N_b = 1.22 \times 10^8$ particles per bunch were collided in the first Pb-Pb run in 2010 [43], the bunch intensity was improved to $N_b = 2.2 \times 10^8$ particles per bunch and a bunch spacing of $75\,\mathrm{ns}$ was achieved in 2018 [46]. This small bunch spacing allowed a maximum of 733 stored bunches per beam. The design luminosity of $\mathcal{L} = 10^{27}\,\mathrm{Hz/cm^2}$ was achieved for the first time in 2015 [45]. The largest luminosity achieved during that run was $\mathcal{L} = 3.6 \times 10^{27}\,\mathrm{Hz/cm^{-2}}$. Over time, the β-function at the interactions points, the β^*, became substantially smaller. The target of $\beta^* = 0.5\,\mathrm{m}$ was achieved in 2018 for the first time. ATLAS, ALICE and CMS were all operated at $\beta^* = 0.5\,\mathrm{m}$ and LHCb at $\beta^* = 1.5\,\mathrm{m}$. These were the smallest β^* ever achieved in ALICE and LHCb including p-p operation. The peak luminosity until this point was achieved in 2018 with $\mathcal{L} = 6.1 \times 10^{27}\,\mathrm{Hz/cm^{-2}}$ (6.1 times larger than the design value) in ATLAS and CMS. The integrated luminosity increased rapidly among the different Pb-Pb runs. While the 2018 run delivered roughly $900\,\mu\mathrm{b}^{-1}$ to ALICE and $1.8\,\mathrm{nb}^{-1}$ to ATLAS and CMS, the 2011 run delivered *only* $160\,\mu\mathrm{b}^{-1}$ per experiment in the same time span.

1.2.5.2 Previous p-Pb runs

Besides the p-Pb pilot run in 2012 that featured the first p-Pb collisions, the LHC has performed two full one-month p-Pb runs. The combined duration of the p-Pb runs is roughly 6 weeks. In the following, a brief account of the first tests in 2011/2012 and of the two one-month runs is given.

Table 1.1: List of Pb-Pb runs during LHC Run 1 and Run 2. The parameters improved rapidly among the different runs with the 2018 Pb-Pb run achieving a peak luminosity 6.1 times larger than the design value and an integrated luminosity of $1.8\,\mathrm{nb}^{-1}$ in ATLAS and CMS. In 2015, the bunches had an alternating bunch spacing (100 ns and 150 ns) [54]. At the start of the 2015 run, it was an alternating 100 ns / 225 s bunch spacing although not listed here [45]. In 2018, the first part of the run was performed with a 100 ns and the second part with a 75 ns bunch spacing. Parameters that exceed their respective design value for the first time are underlined. Table adapted from [17, 55].

Year		Run 1 '10 [43]	Run 1 '11 [44]	Run 2 '15 [45]	Run 2 '18 [46]	Design [1]
Beam energy E_b	Z TeV	3.5	3.5	6.37	6.37	7
Collision energy $\sqrt{s_{\mathrm{NN}}}$	TeV	2.51	2.51	5.02	5.02	5.52
Run duration	weeks	4	3.5	2.5	3.5	-
Bunch spacing	ns	500	200	100 / 150	100, 75	100
Number of bunches n_b	1	137	338	518	733	592
Pb bunch intensity N_b	10^8	1.2	1.14	2.0	2.2	0.7
Normalised emittance ϵ_{n}	μm	2	2	2.1	2	1.5
Minimum β^* at the IP	m	3.5	1.0	0.8	0.5	0.5
Peak luminosity $\mathcal{L}$	$10^{27}\,\frac{\mathrm{Hz}}{\mathrm{cm}^2}$	0.03	0.5	3.6	6.1	1
IP1/5 int. luminosity $\int \mathcal{L}$	$\mu\mathrm{b}^{-1}$	9	160	585	1800	1000

First injection and ramp with p-Pb beams in 2011 In 2011, a test of injecting a few Pb bunches in the presence of roughly 300 proton bunches with the beams having unequal revolution frequencies was performed [2]. This test proved the insignificance of moving long-range beam-beam encounters in the case of the LHC with an injection energy of $E_b = 450Z\,\mathrm{GeV}$. No unaccounted emittance growth that could have been caused by moving beam-beam encounters was observed. During the test, the energy ramp to a target energy of $E_b = 3.5Z\,\mathrm{TeV}$ was performed. Figure 1.8 shows a screenshot of the RF frequencies and beam intensities. Before the ramp, a small intensity decay of the Pb beam is visible, but the loss rate decreased during the ramp. The beams reached the target energy and the RF lock (cogging procedure) was performed to the central RF frequency. The resulting relative momentum shift was $\delta_p = \pm 0.03\,\%$ (positive for the proton beam, negative for the Pb beam; see Chapter 2) and created excursions on the scale of 1 mm as is shown by the beam-position monitor (BPM) measurement of the orbit excursion of the Pb beam in Fig. 1.9. After the RF lock, the collision point of the first bunches of the proton and Pb beam which was supposed to centred in the ATLAS IP was shifted by 9 km from that position. This occurred because the cogging process did not take place the moment the first bunches were colliding in ATLAS and instead when the collision point was shifted mul-

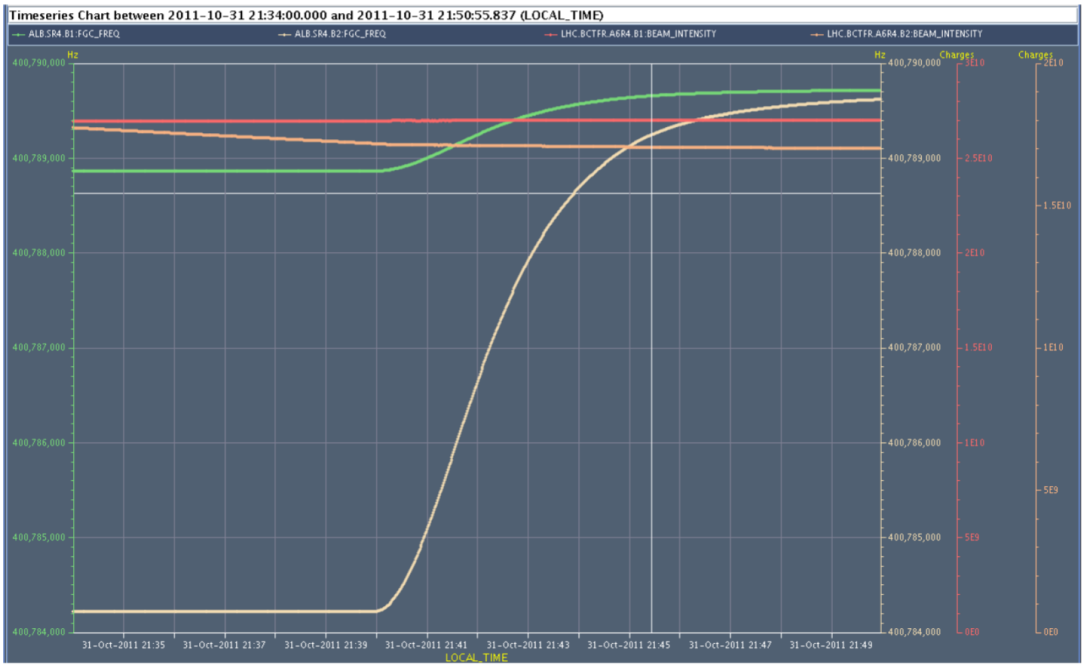

Figure 1.8: The ramp of the RF frequencies and the evolution of the beam intensities. The two RF frequencies are approaching each other during the ramp. Minor Pb beam losses are observed before and during the ramp. Plot taken from [2].

tiple km from the ATLAS IP. In the wake of that test, an automatic RF cogging and re-phasing procedure was developed (tested with protons) to ensure the correct phase between the two RF systems and the IPs being longitudinally centred in the experiments [4].

First p-Pb collisions in 2012 The p-Pb pilot run took place during the night of 12/13 September 2012 [3]. Both beams comprised only 13 bunches, providing eight collisions to each experiment. The bunch intensities were low ($N_b = 8.5 \times 10^7$ Pb ions per bunch and $N_b = 1.2 \times 10^{10}$ protons per bunch) to minimise the amount of required loss maps which have to be taken to ensure safe operation.[7] To avoid the injection of new beams after taking momentum loss maps requiring the blow-up of the transverse emittances with the transverse damper (ADT), three non-colliding bunches were included in the filling schemes of the two beams. These bunches were meant for off-momentum loss maps at top energy. After the validation of the collimator settings, the beams were lost during the first attempt to ramp the beam energy. A second fill with different collimator settings was then successfully ramped to the target energy. After the RF lock, the beams were brought in collision with unsqueezed β^*. The β^* in ATLAS and CMS

[7]Loss maps are measurements which comprise the artificial creation of beam losses to investigate the locations of impact with the aperture or collimators. Loss maps are used to validate that the collimators are sufficiently protecting the superconducting sections of the LHC against different types of beam losses.

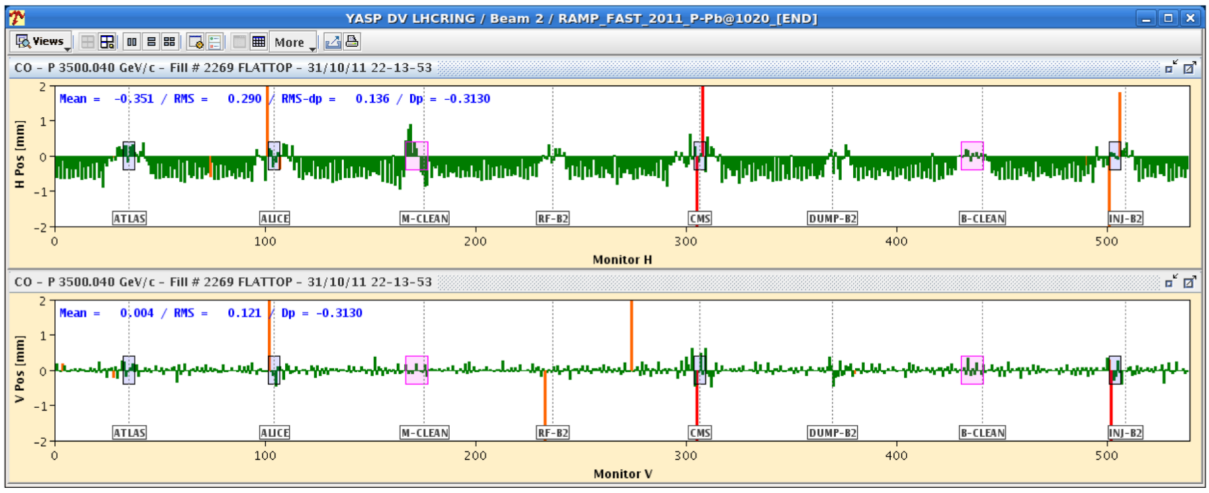

Figure 1.9: The orbit of the Pb beam in the horizontal plane (top) and vertical plane (bottom) after the RF lock measured by the BPMs. The intrinsic momentum shift δ_p due to the RF lock drives out the orbit in the LHC arcs to values slightly smaller than $1\,\mathrm{mm}$. The shift along the orbit is mostly negative because of a negative δ_p and positive dispersion in the arcs. Plot taken from [2].

was $\beta^* = 11\,\mathrm{m}$ while it was $\beta^* = 10\,\mathrm{m}$ in ALICE and LHCb. Stable Beams conditions were kept for roughly $9\,\mathrm{h}$ before the beam dump took place.

During the test, the transverse emittances were closely monitored at injection energy to see potential effects of moving long-range beam-beam encounters on the emittances. The dedicated Collider Time Evolution (CTE) computer code [56] to simulate the beam evolution in hadron colliders (see Chapter 4) produced good results for the emittance evolution by only considering IBS and radiation damping as emittance influencing effects (see Fig. 1.10). Additional emittance growth was only observed in the vertical plane. This, however, can also be caused by slightly coupled IBS growth rates between the vertical plane and the two other planes (horizontal and longitudinal).[8] The p-Pb pilot run confirmed a second time that emittance growth due to moving long-range beam-beam encounters is negligible (in low proton-intensity conditions in this case). Luminosities in the $\mathcal{L} \approx 10^{26}\,\mathrm{Hz/cm^2}$ were achieved, and the integrated luminosity was sufficient for first important findings by the experiments. This p-Pb pilot run which was optimised for an extremely short setup time was used as a guideline for the Xe-Xe [47] and partially stripped Pb-Pb pilot runs [48] in 2017 and 2018, respectively. It was also the first heavy-ion run in which LHCb took part.

[8] Chapter 4 illustrates the difficulty of reproducing the emittance evolution of Pb ions to a high degree even at much larger beam energies than the LHC injection energy.

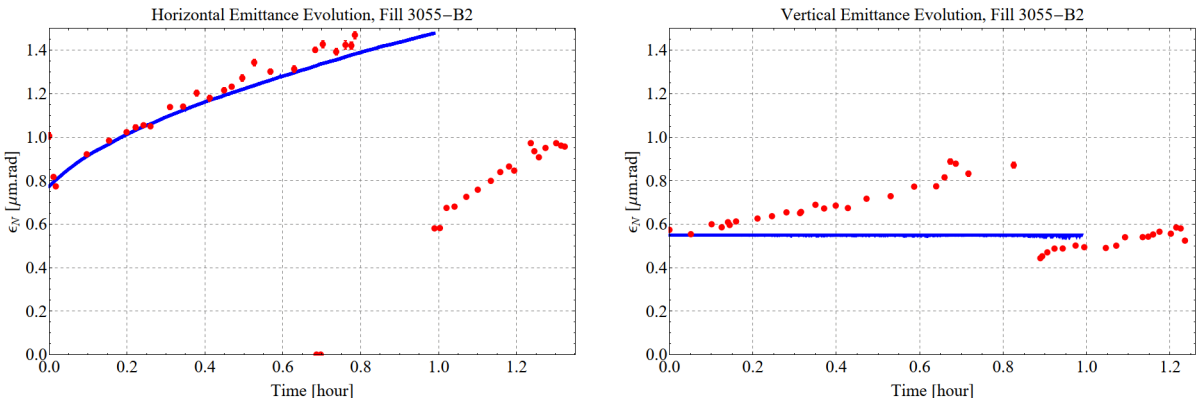

Figure 1.10: The evolution of the horizontal (left) and the vertical (right) normalised emittance of the Pb beam measured via wire scanners (red dots). The CTE simulation (blue line) reproduces the horizontal emittance evolution to a high degree. The discontinuity in the data is caused by the injection of new bunches. Better agreement in the vertical plane would be achieved if coupling of IBS growth rates is introduced. Courtesy of M. Schaumann. Plot taken from [3].

The 2013 p-Pb run The 2013 p-Pb run of the LHC lasted 3 weeks and was operated at a collision energy of $\sqrt{s_{\mathrm{NN}}} = 5.02\,\mathrm{TeV}$ [4]. The negligible effects of moving long-range beam-beam encounters on the LHC beams in high-intensity multiple-bunch conditions were confirmed early into the run. While the 2012 pilot run was conducted with unsqueezed β^* at the IPs, it was at $\beta^* = 0.8\,\mathrm{m}$ in ATLAS, ALICE and CMS; and at $\beta^* = 2\,\mathrm{m}$ in LHCb in 2013. The bunch intensities N_b were significantly increased with $N_b = 1.2 \times 10^8$ particles per bunch for the Pb and $N_b = 1.6 \times 10^{10}$ particles for the proton bunches compared to the pilot run. The luminosity in ATLAS and CMS was roughly $\mathcal{L} = 1.15 \times 10^{29}\,\mathrm{Hz/cm^2}$ while ALICE was levelled at $\mathcal{L} = 10^{29}\,\mathrm{Hz/cm^2}$ for the most time of the run. To cover a wider rapidity range, ALICE requested a beam direction reversal, i.e., the proton beams initially injected in Beam 1 (p-Pb) were switched into Beam 2 (Pb-p) and the Pb beams switched from Beam 2 into Beam 1. ALICE also changed the muon spectrometer polarity to correct for potential systematic uncertainties while LHC operation had to keep the crossing angle within ZDC constrains.

During the run, the intensity lifetimes of the bunches varied over a wide range of values caused by different collision schedules of the bunches.[9] It is not entirely clear if the collision of two beams of different geometric sizes influences the beam lifetime negatively and if it is the case, to which extent. Another issue that was faced during the run was the frequent dumping of the beams. Because of the bunch intensity difference between the Pb and proton beam, Pb bunches dropped out of the dynamic range of common interlock BPMs and caused beam

[9] Bunches do not necessarily collide in all four IPs (see Sec. 4.1.5). Depending on the filling patterns of the two beams, different bunches of the same beam may miss out collisions in different experiments.

dumps as a result. Hence, the proton intensity was limited throughout the run. Table 1.2 lists the parameters of the 2013 p-Pb run.

Table 1.2: Parameter list of the 2013 and 2016 p-Pb runs in comparison to the design and the envisaged HL-LHC values. In 2013, the bunch spacing was alternating 200 ns / 225 ns [57]. The HL-LHC values are calculated in Chapter 6 and are given here for completeness. The HL-LHC parameters are listed in [58, 59]. Parameters that achieved their respective design value for the first time are underlined.

Year		Run 1 '13 [4]	Run 2 '16 [5]	Design [36]	HL-LHC [58, 59]
Beam energy E_b	Z TeV	4	4, 6.5	7	7
Collision energy $\sqrt{s_{\mathrm{NN}}}$	TeV	5.02	5.02, 8.16	8.79	8.79
Run duration	weeks	3	1, 2	-	3.5
Bunch spacing	ns	200/225	<u>100</u>	100	50
Number of bunches n_b	1	358	540	592	1232
Pb bunch intensity N_b	10^8	<u>1.2</u>	2.1	0.7	1.8
Normalised emittance ϵ_{n}	μm	2	<u>1.5</u>	1.5	1.65
Minimum β^* at the IP	m	0.8	10, 0.6	0.5	0.5
Peak luminosity $\mathcal{L}$	$10^{29}\,\frac{\mathrm{Hz}}{\mathrm{cm}^2}$	1.16	<u>8.9</u>	1.5	22
IP1/5 int. luminosity $\int \mathcal{L}$	nb^{-1}	32	<u>190</u>	100	840

The 2016 p-Pb run Chapter 4 gives a complete description of the 2016 p-Pb run [5]. This run was conducted at the beam energies $E_b = 4Z$ TeV (1 week) and $E_b = 6.5Z$ TeV (2 weeks). With a 100 ns bunch spacing and much improved proton and Pb bunch intensities (2.1×10^8 particles per ion bunch and peak proton bunch intensities of 2.8×10^{10} particles per bunch), a peak luminosity of $\mathcal{L} = 8.9 \times 10^{29}\,\mathrm{Hz/cm^2}$ was achieved and integrated luminosities of $190\,\mathrm{nb}^{-1}$ in ATLAS/CMS and $43\,\mathrm{nb}^{-1}$ in ALICE. The run was highly successful and premature beam dumps like in 2013 were successfully avoided.

Throughout the run, different lifetimes among bunches and beam losses exceeding the luminosity burn-off were observed and again the question of the effect of colliding beams of different geometric size arose. Although the issue of beam dumps caused by the dynamic range of the interlock BPMs was solved by sophisticated gating of the BPMs (see Chapter 4), another performance-restricting effect showed up: Fragments from the particle collisions in the IPs generated substantial beam-loss monitor (BLM) signals close to the high-luminosity experiments ATLAS and CMS in the propagation direction of the Pb beam. These signals nearly caused beam dumps and were the reason the proton bunch intensities had to be limited to $N_b = 2.9 \times 10^{10}$ protons per bunch.

These observed effects give rise to two other objectives of this work:

- **Objective 3** (Chapter 4) In order to understand the different intensity lifetimes among the Pb bunches, a beam-evolution study is performed in this thesis. Such a study will show whether extra losses besides luminosity burn-off are present.

- **Objective 4** (Chapter 5) Another goal of the thesis is to determine the total p-Pb cross section. This would enhance the understanding of the observed intensity decay. It would also be the first experimentally determined estimate of the p-Pb cross section at $\sqrt{s_{\mathrm{NN}}} = 8.16\,\mathrm{TeV}$ since it has not been determined by the LHC detectors yet.

1.2.6 The High-Luminosity Large Hadron Collider (HL-LHC)

The High-Luminosity Large Hadron Collider (HL-LHC) [59] is the upgrade of the LHC to achieve much larger integrated luminosities in the future. The HL-LHC is expected to be operational in LHC Run 4 (2027–2029) and beyond. The HL-LHC comprises mostly upgrades significant for p-p operation. A few of these upgrades are new triplets and crab cavities in the ATLAS and CMS IRs. The triplets are the quadrupoles responsible to achieve small β-functions at the IPs while crab cavities improve the beam overlap as the crossing angles at the IPs will be much larger in p-p operation compared to the nominal LHC. The redesign of the ATLAS and CMS IRs reduces the length of the common beam pipe by roughly $15\,\mathrm{m}$ on both sides of the IPs. This is an important change in the context of moving long-range beam-beam encounters (see Chapter 2). In terms of heavy-ion operation, one of the most important upgrades is the insertion of additional TCLD collimators (see Sec. 1.2.3) in the dispersion suppressors downstream of the ALICE IR (no ALICE luminosity limit by intercepting secondary beams coming out of the IP) and the collimation section at IR7 (no limit by fragments generated in the collimation section). The largest performance enhancement in heavy-ion operation is expected from longitudinal momentum slip-stacking [60, 61] in the SPS to reduce the Pb bunch spacing. Longitudinal slip-stacking would allow the reduction of a $100\,\mathrm{ns}$ bunch spacing of the Pb bunches to a $50\,\mathrm{ns}$ bunch spacing. This is achieved by letting two Pb batches slip with respect to each other in longitudinal momentum space in the SPS [19, 20]. The two batches are captured by two different travelling-wave cavities [62] during this process. Once the two Pb batches interleave, a recapture of the bunches is performed to reduce the $100\,\mathrm{ns}$ bunch spacing of the individual Pb batches to an effective $50\,\mathrm{ns}$ bunch spacing of the interleaved batches. Figure 1.11 gives a sketch of this procedure. The slip-stacking in the SPS is going to be commissioned in 2021 or, if necessary, in 2022.[10] If the next p-Pb run takes place in 2023 (not yet confirmed; p-Pb run definitely in 2028), the HL-LHC p-Pb performance will mostly be achieved in LHC Run 3.

[10] If the commissioning of the slip-stacking in the SPS is unsuccessful, the bunch spacing will be $75\,\mathrm{ns}$ as during the 2018 Pb-Pb run.

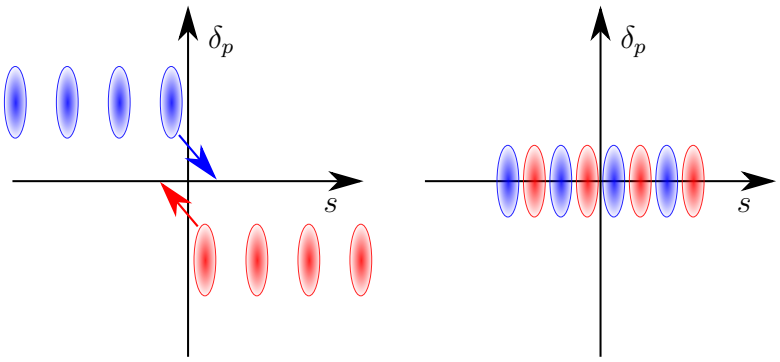

Figure 1.11: Left: Two bunch trains captured by different RF families slip longitudinal in space while separated in momentum. Right: Once the two bunch trains interleave in space, the trains are recaptured. The resulting bunch separation is half of the initial bunch separation, e.g., the bunch spacing will be reduced from $100\,\mathrm{ns}$ to $50\,\mathrm{ns}$ in the SPS.

It is unclear at this point if doubled proton bunch numbers in the LHC will cause problems in terms of emittance growth caused by moving long-range beam-beam encounters. Doubling the proton beam intensity may have a significant effect on the Pb bunches at injection in the LHC.

The cross section in Pb-Pb is dominated by ultra-peripheral effects like BFPP and EMD. The hadronic cross section is much smaller compared to the cross sections of BFPP and EMD. As a result, only a small fraction of the luminosity burn-off is caused by the hadronic interaction. One way to mitigate such effects is to reduce the ion charge. Different ion species are considered in A-A collisions to enhance the nucleon-nucleon luminosity $\mathcal{L}_{\mathrm{NN}}$ in LHC Run 5 and beyond. An analysis of the potential performance of the HL-LHC for future A-A collisions with different ion species is presented in [17]. To complement the A-A data, respective p-A data will be required. The potential performance of such a p-A run has not been evaluated in detail but are required by the experiments to optimise their beam-time request for heavy-ion operation. Furthermore, an oxygen-oxygen (O-O) and a p-O pilot run is possibly going to be scheduled for 2023. Reason for a p-O pilot run is mainly cosmic-ray physics.

Based on the raised issues, the following objectives will be discussed later on:

- **Objective 1 (cont.)** (Chapter 2) It is unclear in which way the doubling of the number of proton bunches and consequently the proton beam intensity will affect the dynamics of moving long-range beam-beam encounters. Whether emittance growth and/or beam losses of the Pb beam are expected has to be investigated.

- **Objective 5** (Chapter 6) The 2016 p-Pb run has shown that the performance-limiting effect are collisions fragments ending up in the ATLAS/CMS dispersion suppressors. One question is whether these losses can be mitigated using the TCL collimators. A second unknown is the performance improvement expected from a future p-Pb run in the LHC Run 3/HL-LHC era. Such an outlook is important for the experiments to request sufficient beam time for the respective collision type.

- **Objective 6** (Chapter 7) It is requested by the experiments to have A-A collisions of ions of intermediate mass in LHC Run 5. While the performance of the symmetric A-A case has already been estimated in [17], the performance in respective p-A collisions is not known yet. Besides the performance of a monthly p-A run, also the performance of a potential p-O pilot run in 2023 is investigated.

1.3 The Relativistic Heavy-Ion Collider (RHIC)

RHIC is besides the LHC the only currently operating hadron collider which is also occasionally operated with asymmetric beams. RHIC started operation in 2000 and explored the collective QGP state. The findings at RHIC had a large influence on the LHC physics programme. RHIC is $C = 3.834\,\mathrm{km}$ in circumference and roughly six-fold symmetric as shown in Fig. 1.12. Even though not all straight sections accommodate experiments, the utility IRs, e.g., the RF section, have the same beam optics as experimental IRs in contrast to the LHC. Hence, the beams share the same beam pipe at all six IRs while this is the case only in four out of eight IRs in the LHC. RHIC has undergone significant changes and upgrades since its start of operation. The BRAHMS experiment has been removed at IR2 and instead accommodates the Low-Energy RHIC electron Cooler (LEReC) [63].[11] Instead of the PHOBOS experiment at IR10, RHIC now features electron lenses to compensate the beam-beam tune shift [66, 67]. In today's RHIC, the STAR and PHENIX experiments are still operating. In contrast to the LHC, RHIC also features stochastic cooling [68–70] which reduces the non-luminous losses[12] substantially. Hence, the luminosity burn-off is almost the only loss mechanism in RHIC. This feature allows to estimate the total collision cross section by just comparing the intensity decay with the luminosity data [14, 15]. This feature becomes important in the context of deriving the p-Pb cross section in the LHC (see Chapter 5).

RHIC comprises two autonomous rings, allowing different magnitudes of the magnetic fields acting on the two beams. The superconducting bending magnets of RHIC reach field strengths of up to $B = 3.46\,\mathrm{T}$, allowing beams with a maximum rigidity $B\rho = 850\,\mathrm{Tm}$ to be

[11] The LEReC was commissioned at the start of 2019 in Au-Au configuration at $E_b = 3.85\,\mathrm{GeV/nucleon} \approx 9.6Z\,\mathrm{GeV}$ [64, 65].

[12] Non-luminous losses are intensity losses not caused by the luminosity burn-off in the experiments.

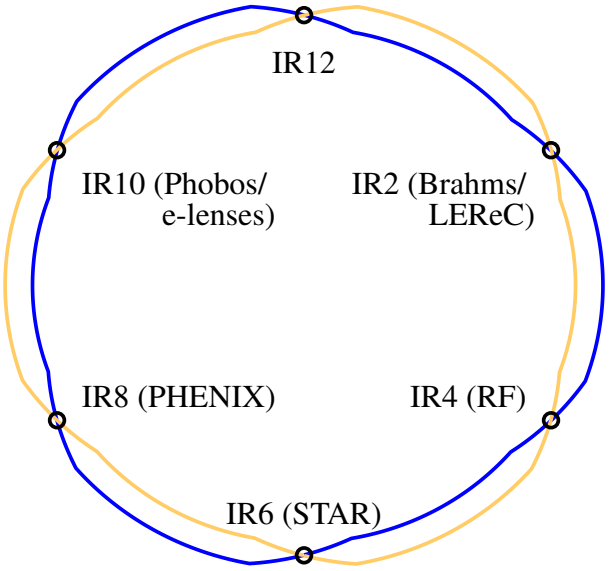

Figure 1.12: Simplified sketch of the RHIC layout. RHIC has six insertion regions which have the same layout independent of whether it is an experimental or utility insertion. The blue beam rotates clockwise while the yellow beam rotates counterclockwise.

stored. RHIC collides around 110 bunches per beam with a bunch spacing of roughly $107\,\mathrm{ns}$ and achieves a peak luminosity in gold-gold (Au-Au) collisions (RHIC's predominant operation mode) in the $\mathcal{L} = 2 \times 10^{26}\,\mathrm{Hz/cm^2}$ range [71]. A wide range of symmetric systems were successfully collided over the years in RHIC [64], e.g., p-p, Au-Au, copper-copper (Cu-Cu), uranium-uranium (U-U) and others. The Electron Beam Ion Source (EBIS) produces the ion beams nowadays; however, the ions were produced by the tandem accelerator when RHIC started operation in 2000. From the EBIS, the ions pass through an RFQ into the Booster Synchrotron. The protons are generated in a different source which produces polarised protons, i.e., the spin is aligned with respect to the longitudinal momentum. The polarised protons are then accelerated in a $200\,\mathrm{MeV}$ linac before being injected into the booster. Protons and ions share the same injector chain from that point on. From the booster, the particles are injected into the Alternating Gradient Synchrotron (AGS) and from there finally into RHIC. To keep the protons polarised, Siberian Snakes are installed in RHIC [72, 73]. These are required since the proton beams pass through numerous depolarising resonances during the energy ramp.

The first attempt to accelerate asymmetric beams was made in 2003 [8]. The initial commissioning of gold-deuteron (Au-D) was attempted with equal rigidities and unequal revolution frequencies. Achieving collisions after the ramp with unequal f_0 succeeded, but the performance

was significantly limited due to the strong deterioration of the beams that took place during the energy ramp. After switching to an acceleration scheme with unequal $B\rho$ and equal f_0, a much improved performance was achieved. After successful Au-D collisions, RHIC also operated in the asymmetric configurations aluminium-proton (Al-p), Au-p and helium-gold (He-Au).

1.3.1 Attempts to accelerate with equal magnetic rigidity

In the following, the observations that were made during the two attempts to accelerate the beams with different revolution frequencies in RHIC are recalled. After the commissioning of Au-D in 2002/2003, an acceleration scheme comprising equal f_0 to accelerate two different ion species simultaneously was regularly used. The attempt to accelerate Al-p with unequal f_0 in 2015 was performed as a confirmation of the negative influence of moving long-range beam-beam encounters on the performance years after the initial Au-D commissioning with unequal revolution frequencies f_0.

2001/2002 Au-D commissioning The initial Au-D commissioning was attempted with equal rigidities [8]. This had the advantage of not having to change any optics as the beams behave identically to the symmetric A-A case. The parallel separations of the beams in the IRs were at $\pm 5\,\mathrm{mm}$; however, with deuteron intensities of 1.2×10^{11} particles per bunch and Au intensities of 0.7×10^9 ions per bunch, the beams started to lose intensity rapidly right after the injection of the second beam. At the injection energies of roughly $E_b = 24.4Z\,\mathrm{GeV}$, the shift of the moving long-range beam-beam encounters is roughly $3\,\mathrm{m}$, which is close to $10\,\%$ of the length of the common beam pipe (see Fig. 1.7). Because of this large shift, it is more likely compared to the LHC to excite low order OKO resonances, e.g., dipole or quadrupole resonances, which overlap with the betatron spectra of the beam (see Chapter 2). Even after increasing the parallel separations to $\pm 8\,\mathrm{mm}$, reliable operation of the collider was still not possible despite decreased losses. An acceleration scheme with equal f_0 was applied in RHIC after the unsatisfactory attempts to do the commissioning with equal rigidities. A technique usually applied in RHIC to ramp different ion species successfully to target energy is the acceleration of the slower particle beam (the beam comprising the ion species with a smaller charge-to-mass ratio) to an intermediate energy in a first step that the revolution-frequency difference is negligible once the second (faster) beam is injected [74, 75].

The test with unequal revolution frequencies proved RHIC as inoperable in these kinds of conditions. A very simplified model treating the moving long-range beam-beam encounters as random dipole noise was developed and reproduced an emittance doubling time of $1\,\mathrm{min}$ which was consistent with observations [10].

2015 Al-p test Another test with unequal revolution frequencies was conducted in 2015 [76] in Al-p configuration [75]. With an even larger charge-to-mass ratio difference, the shift of moving long-range beam-beam encounter locations was roughly $4.6\,\mathrm{m}$. Even the implementation of even larger parallel separations at the IPs did not lead to a successful energy ramp. The intensity evolution of an attempt to accelerate Al-p is shown in Fig. 1.13. The fill is lost within $40\,\mathrm{s}$. During the ramp, it was tried to only ramp the Al beam while the proton beam remained at injection energy [77].

Although the acceleration with fixed moving beam-beam encounters mitigates the beam losses during the energy ramp, operating with equal revolution frequencies (unequal rigidities) has downsides: If RHIC is operated with asymmetric beams with one beam being protons, the separation dipoles in the IRs have to be moved multiple cm to gain aperture because the beam trajectories pass through the IRs at an angle. The separation dipoles are the only magnets common to the two beams; therefore, the two beams are bent by a different angle since the beam rigidities are unequal. This causes the orbits in the IRs to be slightly tilted with respect to the reference orbit in the horizontal plane. The largest effect occurs with protons in one beam and ions with a much smaller charge-to-mass ratio in the other beam. As an example, the separation magnets were moved by more than $2\,\mathrm{cm}$ during the 2015 p-Au run of RHIC [78] to gain more aperture due to the tilted orbits in the horizontal plane.

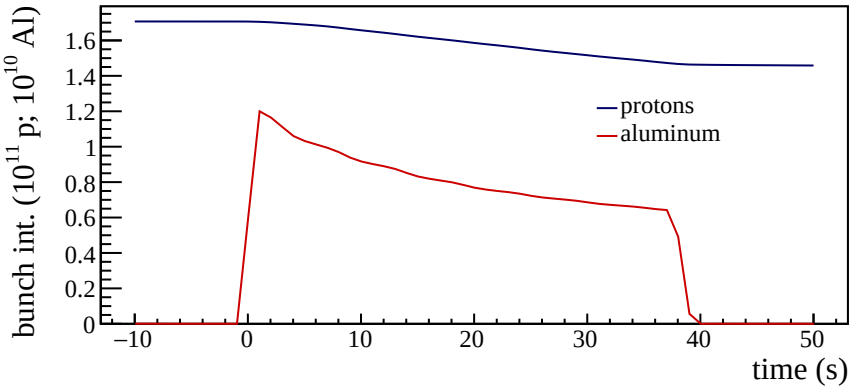

Figure 1.13: Average bunch intensity of the proton beam (blue) and the aluminium bunch (red) versus time. Both beams drastically lose intensity after the injection of the aluminium bunch at $t = 0$. The aluminium bunch is lost at $t = 38\,\mathrm{s}$.

- **Objective 1 (cont.)** (Chapter 2) In order to benchmark potential findings for the LHC and HL-LHC in terms of emittance evolution and intensity losses because of moving long-range beam-beam encounters, a code should be able to reproduce RHIC in Au-D and Al-p configuration as unstable.

1.4 The Future Circular Collider (FCC)

The design study of a roughly $100\,\mathrm{km}$ hadron collider has been conducted over the past several years which concluded towards the end of 2018 with a report as input to the European Particle Physics Strategy Update 2018-2020 [79]. If built, this future collider, also referred to as the

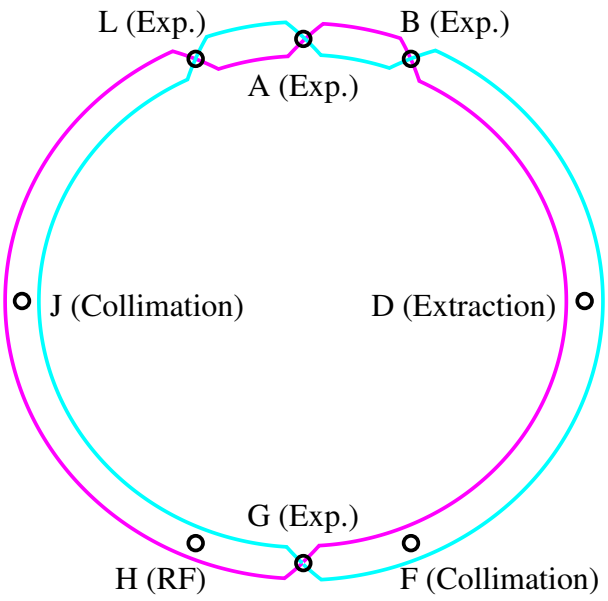

Figure 1.14: Sketch of the potential future collider FCC. The rough positions of the four experiments are comparable to those of the LHC. (Exp.: "Experiment")

Future Circular Collider (FCC), would push the energy frontier much further than the LHC and would cover a much wider energy range, hoping to find evidence of the yet unanswered questions of modern particle physics, e.g., the existence of super-symmetry and dark matter. Such a collider would start operation as a lepton collider (FCC-ee) [80] and then would be replaced by a hadron collider (FCC-hh) [81] in the same tunnel. A lepton collider does not depend on the development of a novel magnet technology and can therefore be realised earlier. The hadron collider version of the FCC would require $16\,\mathrm{T}$ niobium-tin (Nb_3Sn) technology to provide sufficient bending of the envisaged $E_b = 100Z\,\mathrm{TeV}$ hadron beams. It is highly likely that an accelerator like the FCC will also collide heavy ions. The potential performance of the FCC during Pb-Pb, p-Pb and p-p operation has already been studied in detail [82, 83].

The FCC would feature four experimental IRs (see Fig. 1.14) in which both beams share a common beam pipe. Since the injection energy of $E_b = 3.3Z\,\mathrm{TeV}$ is over seven times larger than that of the LHC, the shift of moving long-range beam-beam encounters is only $1\,\mathrm{cm}$ per

turn in p-Pb operation. The FCC will not face issues in terms of emittance blow-up caused by modulated long-range beam-beam encounters because the positional shift of the encounters is very small. Chapter 2 gives more arguments for the unimportance of moving long-range beam-beam encounters in the FCC. The operation of the FCC in p-Pb configuration is therefore not a subject of this work.

CHAPTER 2

Moving long-range beam-beam encounters in heavy-ion colliders

Chapter 1 already gave the historic background and motivation for asymmetric p-A collisions in the LHC. The main issues of an acceleration scheme with unequal revolution frequencies have been explained and introduced in Sec. 1.2.4. Moving beam-beam encounters and the resulting effects are not a heavily investigated topic in accelerator physics since only a handful of accelerators has ever faced this form of beam dynamics. Moving beam-beam encounters and the resulting so-called overlap-knock out resonances have been studied for the first time in the scope of the ISR at CERN [6, 7]; however, the ISR case is not fully comparable to that of the LHC since the interaction in the ISR took place between a bunched and a stacked coasting beam that had a relative energy spread of $2\,\%$ (large tune and velocity spread). Since the commissioning of Au-D collisions in RHIC in the early 2000s, the topic became more relevant since RHIC proved inoperable when the acceleration of the two beams with unequal revolution frequencies $f_{0,\mathrm{Au}} \neq f_{0,\mathrm{D}}$ was attempted [8]. During the energy ramp, the beam orbits in the IRs of RHIC were separated by multiple mm to avoid unwanted head-on collisions. Even the increase from $10\,\mathrm{mm}$ total parallel separation in the IRs to $16\,\mathrm{mm}$ did not adequately mitigate the losses caused by the moving long-range beam-beam encounters. Although the losses during the ramp decreased due to the increased parallel separation, the deterioration of the beams still led to an unacceptable performance in collisions. Conditions with good performance were only achieved after changing to an acceleration scheme with equal revolution frequencies and fixed long-range encounter locations. The discussion of moving long-range encounters in p-Pb

operation in the LHC started at the 2005 workshop on p-Pb operation[1] that took place years before the first p-Pb test in 2011 that demonstrated the injection and energy ramp with different revolution frequencies in the LHC [3]. During the discussion, it was not entirely unambiguous whether the LHC will face similar issues like RHIC when trying to ramp protons and Pb ions with different revolution frequencies. A negative outcome of the p-Pb pilot run in 2011 would have been critical since the LHC magnet design (see Sec. 1.2 and Fig. 1.2) does not allow alternative acceleration schemes with unequal rigidities $B\rho$ and equal revolution frequencies f_0. After the successful test of p-Pb collisions in 2012 and the first one-month p-Pb run of the LHC in 2013, the acceleration with unequal revolution frequencies was once again tested in RHIC with Al-p beams in 2015. This attempt was unsuccessful and confirmed the findings made during the Au-D commissioning years earlier [76]. The attempts to accelerate asymmetric beams with unequal revolution frequencies in the LHC and RHIC were not preceded by detailed simulations indicating the most likely positive or negative outcome of potential tests. This chapter will introduce a model capable of reproducing the beam dynamics when accelerating with unequal revolution frequencies.

The much larger injection energy of the LHC of $E_b = 450Z\,\mathrm{GeV}$ equivalent to the magnetic rigidity $B\rho = 1.5 \times 10^3\,\mathrm{Tm}$ leads to a much smaller frequency difference Δf_0 between the beams compared to RHIC. Besides the much smaller injection energy of RHIC at roughly $E_b = 24.4Z\,\mathrm{GeV}$ equivalent to $B\rho = 81\,\mathrm{Tm}$, the much smaller circumference also leads to a faster emittance growth rate in RHIC. Some scientists were therefore confident that the emittance blow-up and other influences of moving beam-beam encounters on the beams are much weaker in the LHC than in RHIC. First models only considered the coherent dipole kicks of the long-range encounters as random normally distributed noise, and acceptable results were achieved with these assumptions [10]; however, the actual correlation between kicks and also potential tune oscillations were neglected in these models. Another downside of assuming the kicks as normally distributed is that cancellation between kicks is also random, whereas the cancellation between kicks is partially a direct result of the beam optics in the IRs and the accelerator in general. Thus, this type of model yields a too pessimistic emittance evolution for the LHC. Having a model at disposal which takes the filling pattern of the counter-rotating beam, the correct phase advance between the beam-beam interactions, tune oscillations and the correct position-dependent kick strength into account is highly desirable. Being able to analyse different filling patterns is crucial, since gaps along the bunch trains and especially the long abort gap at the end of each bunch train influence the frequency spectrum. Implementing variable beam-beam encounter positions in existing tracking software is not easily performed since these programs are set up to have constant element positions and one-turn maps.

[1] The workshop produced the initial report regarding the physics case that was published years later in 2011 [36].

The first section of this chapter (Sec. 2.1) presents the theoretical concepts and techniques relevant with respect to moving long-range beam-beam encounters. At a second stage (Sec. 2.2), a linear analysis of the long-range beam-beam encounters for the LHC, HL-LHC and RHIC is conducted. This analysis is only based on the linear accelerator model and does not require tracking. This analysis is meant to confirm the theoretical understanding of the underlying dynamics of moving beam-beam encounters. At a third stage (Sec. 2.3), a simplified non-linear tracking routine is presented and used to simulate the emittance evolution. The model is based on the linear beam dynamics of the accelerator; however, the linear model is supplemented with amplitude detuning. The analyses in this chapter focus on Pb-p operation in the (HL-)LHC and Au-D operation in RHIC. In these configurations, the Pb beam in the LHC and the Au beam in RHIC face stronger excitation by the opposing beams than the proton and deuteron beams. This behaviour results from the smaller charge-to-mass ratio of the Pb and Au bunches. Hence, most considerations are made for the slower of the two colliding ion beams which happen to be the Pb beam in the LHC and the Au beam in RHIC.

2.1 Concepts and techniques

This section explains the concepts of moving beam-beam encounter locations, the physics of the beam-beam effect as well as its linearisation and the effects of dipole and quadrupole noise (as it is generated by moving long-range encounters) on the beams. These concepts are applicable to RHIC, the LHC and the HL-LHC.

2.1.1 Energy ramp with unequal revolution frequencies in the LHC

The momentum per charge $p/q = B\rho$ is the magnetic rigidity that is equal for both beams at all times in the LHC independently of the particle types. The momentum of the particles in the LHC is $p = Zp_\mathrm{p}$ with Z being the atomic number of the respective ion species and p_p being the proton momentum at the equivalent rigidity p_p/e. Although the magnetic rigidity is equal for both beams, the velocities of the beams are different in asymmetric p-Pb operation. The expression for the velocities is

$$v_i = c\sqrt{1-\frac{1}{\gamma_i^2}} \approx c\left(1-\frac{c^2 m_i^2}{2Z_i^2 p_\mathrm{p}^2}\right) . \tag{2.1}$$

Here, the index i refers to either of the two beams and m is the particle mass. The velocity v_i yields the revolution frequency $f_{0,i} = C/v_i$ and consequently the RF frequency $f_{\mathrm{RF},i} = hC/v_i$ with the harmonic number h. The RF frequencies of the two beams in p-Pb operation are not equal during acceleration. A small revolution-frequency difference of $\Delta f_0 = 6.3 \times 10^{-4}\,\mathrm{Hz}$ still remains at the target energy of $E_b = 6.5Z\,\mathrm{TeV}$. This small frequency difference still leads

to slowly moving interaction points. At $E_b = 6.5Z\,\mathrm{TeV}$, the encounter positions move with a velocity close to $40\,\mathrm{km/h}$. At least one RF frequency has to be changed to force both beams to have the same revolution frequency f_0. This procedure fixes the collision points at the nominal IPs. By locking both RF frequencies to the middle frequency $\langle f_{\mathrm{RF}} \rangle = \frac{1}{2}(f_{\mathrm{RF},1} + f_{\mathrm{RF},2})$ the momentum shift

$$\delta_{p1} = -\delta_{p2} = \frac{1}{\eta_i} \frac{f_{\mathrm{RF},1} - f_{\mathrm{RF},2}}{f_{\mathrm{RF},1} + f_{\mathrm{RF},2}} \approx \frac{1}{\eta} \frac{c^2}{4p_{\mathrm{p}}^2} \left(\frac{m_1^2}{Z_1^2} - \frac{m_2^2}{Z_2^2} \right) \tag{2.2}$$

is equally distributed on both beams with the relative momentum shift $\delta_p = (p - p_0)/p_0$, p_0 being the nominal momentum and $\eta = \alpha_c - 1/\gamma^2$ being the slippage factor. In this context, α_c is the momentum-compaction factor. The momentum shift δ_p is positive for the faster beam while it is negative for the slower beam if $\alpha_c > 0$ applies like in the LHC. The RF lock can only be performed at large enough energies. At too low energies, the horizontal dispersion D_x would drive the beams outside the beam pipe. At the LHC injection energy of $E_b = 450Z\,\mathrm{GeV}$, the relative momentum offset is $\delta_p = \pm 1.84\,\%$. The horizontal dispersion function is $D_x \approx 2\,\mathrm{m}$ in the horizontally focusing quadrupoles in the LHC arcs. Thus, the orbits are offset by $D_x \delta_p = \pm 3.68\,\mathrm{cm}$ and end up beyond the physical beam pipe. This is ultimately the reason the energy ramp cannot be performed with locked RF frequencies right from the start. As already mentioned in Sec. 1.2.4, at energies of $E_b \geq 2.73Z\,\mathrm{TeV}$, the orbit excursions due to dispersion are acceptable and smaller than $1\,\mathrm{mm}$ in the focusing arc quadrupoles. Figure 2.1 shows the RF

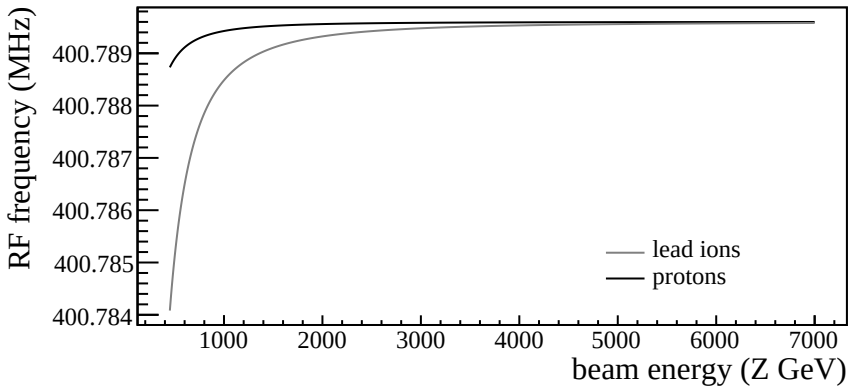

Figure 2.1: Displayed are the RF frequencies of the Pb and proton beam in the LHC as functions of the beam energy E_b. At $E_b = 6.5Z\,\mathrm{TeV}$, the frequency difference is $22\,\mathrm{Hz}$, while the difference is $4.65\,\mathrm{kHz}$ at injection.

frequency's dependence on the beam energy. At injection, the difference in RF frequencies is at around $\Delta f_{\mathrm{RF}} = 4.65\,\mathrm{kHz}$ with the Pb beam having the smaller frequency. At the two 2016 beam energies $E_b = 4\,\mathrm{Z\,TeV}$ and $E_b = 6.5Z\,\mathrm{TeV}$, the RF frequency difference is at $\Delta f_{\mathrm{RF}} = 59\,\mathrm{Hz}$ and $\Delta f_{\mathrm{RF}} = 22\,\mathrm{Hz}$, respectively. Besides technical reasons, it is important to align the

first bunch slots of the two beams at the ATLAS IP when locking the RF frequencies since the filling patterns are optimised to give the correct number of collisions to each experiment. The absolute momentum offset of the beams after the cogging process is shown in Fig. 2.2. At $E_b = 4Z\,\mathrm{TeV}$ and $E_b = 6.5Z\,\mathrm{TeV}$, the momentum shifts are $\delta_p = \pm 2.3 \times 10^{-2}\,\%$ and $\delta_p = \pm 8.7 \times 10^{-3}\,\%$, respectively. These momentum shifts cause orbit excursions smaller than $0.5\,\mathrm{mm}$ ($E_b = 4Z\,\mathrm{TeV}$) and $0.2\,\mathrm{mm}$ ($E_b = 6.5Z\,\mathrm{TeV}$) in the arc quadrupoles.

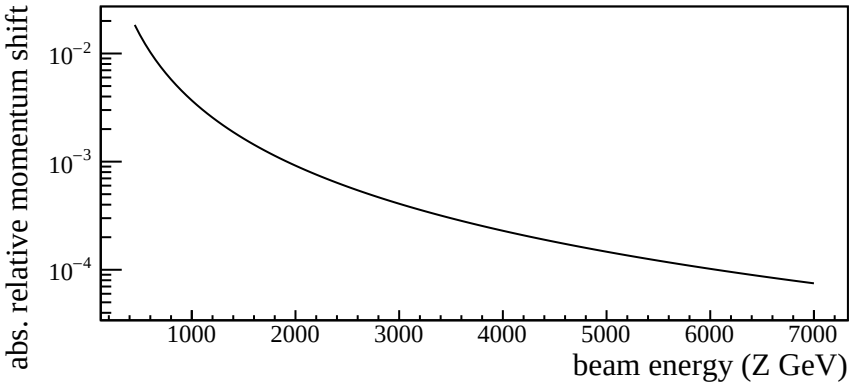

Figure 2.2: The absolute momentum shift $|\delta_p|$ if the RF lock would be performed at the respective beam energy E_b.

The off-momentum operation results in dispersive closed orbits in the arcs, beta beating and a shift of the tunes. Beta beating is the relative change with respect to nominal β-function $\Delta\beta_u(s)/\beta_u(s)$ caused by the variation of the focusing strength for beams with higher or lower energy compared to the design energy [84, 85]. Assuming an ideal lattice (no field and alignment errors), the beta beating due to the momentum shift reads

$$\frac{\Delta\beta_u}{\beta_u}(s_0) = -\frac{\delta_p}{2\sin\mu_u}\oint_C \beta_u(s)\left[k_1(s) - k_2(s)D_x(s)\right]\cos\left(2\left|\phi_u(s) - \phi_u(s_0)\right| - \mu_u\right)\mathrm{d}s\,. \quad (2.3)$$

Here, u is either x or y, μ is the total phase advance, β is the nominal β-function, k_1 is the quadrupole strength, k_2 is the sextupole strength, D_x is the horizontal dispersion function and ϕ is the betatron phase. Quadrupole corrections are applied to reduce the beta beating while leaving the nominal tune as unperturbed as possible [85, 86]. In 2013, the beta beating without corrections was $10\,\%$ and corrections reduced it by another $5\,\%$. These values are small, but beta beating at the IPs is undesirable as the luminosity is possibly reduced. In 2016, the beta beating was small enough that special corrections were not required.

Since the revolution frequencies differ, the encounter locations shift by

$$d_t = C\frac{v_1 - v_2}{v_1 + v_2} \approx C\frac{c^2}{4p_\mathrm{p}^2}\left(\frac{m_1^2}{Z_1^2} - \frac{m_2^2}{Z_2^2}\right) \quad (2.4)$$

every turn. The shift d_t is negative for the slower beam, while it is positive for the faster beam. Figure 2.3 shows the turn-by-turn shift of the encounter locations for the full energy range of the

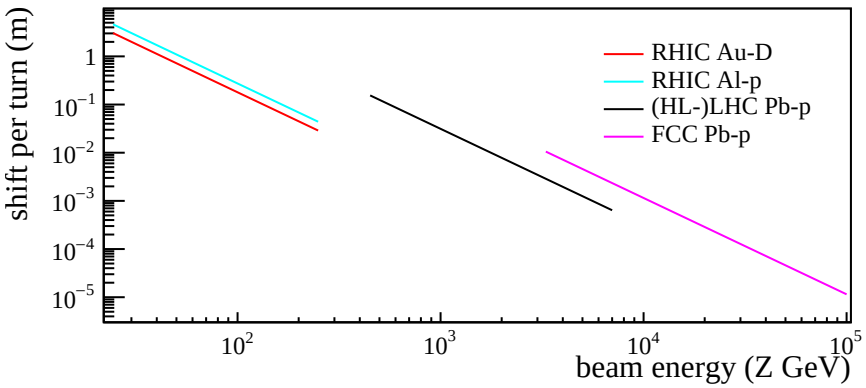

Figure 2.3: Beam-beam encounter shift per turn as a function of the beam energy for RHIC, the (HL-)LHC and the FCC. Since the energy range of the nominal LHC and the HL-LHC is the same, the beam-beam shift behaves identically in these two colliders.

LHC, HL-LHC, FCC and RHIC. Because of the high injection energy compared to RHIC, the shift of approximately $15\,\mathrm{cm}$ per turn in the LHC is much smaller compared to RHIC with a shift between 2–4 m, depending on the collision system. Hence, the encounter locations move easily with velocities in the $\mathrm{km/s}$ range at injection energy in RHIC. A bunch encounters bunches of the opposing beam with a spacing that depends on the velocity of both beams. A bunch in the first beam experiences an encounter spacing of

$$d_b = d_s \frac{v_1}{v_1 + v_2} \tag{2.5}$$

with $d_s = C/k_\mathrm{b}$ being the bunch spacing of the opposing beam in the laboratory frame and k_b being the bunch harmonic. The bunch harmonic k_b does not consider unevenness along the bunch train and therefore neglects gaps. A bunch encounters the same bunch of the opposing beam twice per turn at the positions s and $(s + k_\mathrm{b} d_b) \bmod C$. The reference bunch of the slower beam (index 1) encounters the same bunch of the faster beam (index 2) at the same position after

$$T_m = \frac{v_1}{v_2 - v_1} \qquad (v_1 < v_2) \tag{2.6}$$

turns (assuming T_m being close to an integer). The faster beam encounters the same bunch of the slower beam one turn later $T_m + 1 = v_2/(v_2 - v_1)$ with $v_2 > v_1$; however, the cases that are considered in the following sections are exclusively dealing with the slower of the two beams. Hence, the definition of T_m in Eq. 2.6 is used throughout this thesis. The quantity T_m is referred to as the recurrence time. The recurrence time is not necessarily an integer, but it is a useful quantity to indicate periodicity when analysing non-uniform filling patterns. If the filling pattern is uniform, periodicity is already achieved after d_b/d_t turns or integer multiples of d_b/d_t depending on whether the result is sufficiently close to an integer.

2.1.2 Normalised transverse phase space

Investigating beam dynamics in a frame of normalised coordinates often simplifies matters since normalisation removes dependences on local parameters except the local phase advance. The matrix of the linear transverse motion in two dimensions is

$$\mathbf{M}(s_0, s_1) = \begin{pmatrix} \mathbf{M}_x(s_0, s_1) & \\ & \mathbf{M}_y(s_0, s_1) \end{pmatrix} . \tag{2.7}$$

The matrices $\mathbf{M}_u(s_0, s_1)$ are 2×2 matrices of the form

$$\mathbf{M}_u = \begin{pmatrix} \sqrt{\frac{\beta_u(s_1)}{\beta_u(s_0)}} \left(\cos\Delta\phi_u + \alpha_u(s_0)\sin\Delta\phi_u\right) & \sqrt{\beta_u(s_1)\beta_u(s_0)}\sin\Delta\phi_u \\ \frac{(\alpha_u(s_0)-\alpha_u(s_1))\cos\Delta\phi_u - (1+\alpha_u(s_0)\alpha_u(s_1))\sin\Delta\phi_u}{\sqrt{\beta_u(s_0)\beta_u(s_1)}} & \sqrt{\frac{\beta_u(s_0)}{\beta_u(s_1)}} \left(\cos\Delta\phi_u - \alpha_u(s_0)\sin\Delta\phi_u\right) \end{pmatrix} \tag{2.8}$$

with the linear phase advance difference $\Delta\phi_u = \phi_u(s_1) - \phi_u(s_0)$ and the well known Twiss functions β_u and α_u. Here, s_0 is the initial and s_1 the final position of the covered section. The matrices $\mathbf{M}_x$ and $\mathbf{M}_u$ can be decomposed according to

$$\mathbf{M}_u(s_0, s_1) = \mathbf{V}_u^{-1}(s_1)\mathbf{R}(\Delta\phi_u)\mathbf{V}_u(s_0) . \tag{2.9}$$

The respective matrices in Eq. 2.9 are

$$\mathbf{V}_u(s) = \begin{pmatrix} \frac{1}{\sqrt{\beta_u(s)}} & 0 \\ \frac{\alpha_u(s)}{\sqrt{\beta_u(s)}} & \sqrt{\beta}_u(s) \end{pmatrix} , \qquad \mathbf{R}_u(\Delta\phi_u) = \begin{pmatrix} \cos(\Delta\phi_u) & \sin(\Delta\phi_u) \\ -\sin(\Delta\phi_u) & \cos(\Delta\phi_u) \end{pmatrix} . \tag{2.10}$$

A normalisation of the coordinates

$$\begin{pmatrix} \tilde{u}(s) \\ \tilde{u}'(s) \end{pmatrix} = \mathbf{V}_u(s) \begin{pmatrix} u(s) \\ u'(s) \end{pmatrix} \tag{2.11}$$

simplifies the linear transfer to a simple rotation matrix $\mathbf{M}_u \to \mathbf{R}_u$. In action-angle variables, the normalised motion along the orbit is simply

$$\begin{pmatrix} \tilde{u}(s) \\ \tilde{u}'(s) \end{pmatrix} = \sqrt{2J_u} \begin{pmatrix} \cos(\phi_u(s) + \phi_{u0}) \\ -\sin(\phi_u(s) + \phi_{u0}) \end{pmatrix} \qquad \text{with} \qquad J_u = \frac{1}{2}\left(\tilde{u}^2 + \tilde{u}'^2\right) \tag{2.12}$$

with ϕ_{u0} being an arbitrary initial phase of the linear phase advance $\phi_u(s)$. The linear action J_u is location independent. The underlying Hamiltonian

$$H(J_x, J_y, s) = \frac{J_x}{\beta_x(s)} + \frac{J_y}{\beta_y(s)} \tag{2.13}$$

depends on the positions s because of the non-constant phase advance along the orbit. The corresponding Hamilton equations

$$J'_u(s) = -\frac{\partial H(J_x, J_y, s)}{\partial \phi_u} = 0 \qquad \text{and} \qquad \phi'_u(s) = \frac{\partial H(J_x, J_y, s)}{\partial J_u} = \frac{1}{\beta_u(s)} \tag{2.14}$$

give the well-known relation between the β-function and phase advance. The prime indicates the derivative with respect to the time-like variable $s = vt$. The equation of motion is obtained via integration. The one-turn Hamiltonian then is

$$H_{\mathrm{turn}}(J_x, J_y) = \oint_C H(J_x, J_y, s)\mathrm{d}s = 2\pi(Q_x J_x + Q_y J_y) = \mu_x J_x + \mu_y J_y \,. \tag{2.15}$$

Normalised momentum kick If an infinitesimally short kick by, e.g., a magnet or beam-beam interaction influences a particle in the accelerator, the phase-space coordinates of this particle modify according to

$$\begin{pmatrix} u \\ u' \end{pmatrix}^* = \begin{pmatrix} u \\ u' + f(u) \end{pmatrix} \tag{2.16}$$

with the star indicating the coordinate vector after the kick and f being an arbitrary kick function depending on transverse coordinate at position s_0 of the kick. In the normalised coordinate frame, the kick reads

$$\begin{pmatrix} \tilde{u} \\ \tilde{u}' \end{pmatrix}^* = \begin{pmatrix} \tilde{u} \\ \tilde{u}' + \sqrt{\beta}_u(s_0) f(u(\tilde{u}, \tilde{u}')) \end{pmatrix} . \tag{2.17}$$

The concept of normalised kicks is used throughout this chapter since it allows easier comparison between kicks of different magnitudes at positions of different β-functions.

One-turn transfer matrix The one-turn transfer matrix describes the linear dynamics of a full turn in the accelerator. This matrix contains information on the stability of the linear motion, tunes and potential betatron coupling. The one-turn transfer matrix is a position-dependent matrix; however, it is similar in mathematical sense to a common rotation matrix $\mathbf{R}(\mu_x, \mu_y)$ at all positions s along the orbit. The one-turn transfer matrix is obtained by the multiplication of all N linear elements

$$\mathbf{T}(s) = \prod_{i=0}^{N-1} \mathbf{M}(s_i, s_{i+1}) = \mathbf{M}(s, s + C \bmod C) \,. \tag{2.18}$$

Similarly to Eq. 2.9, the matrix $\mathbf{T}$ can be decomposed into a form

$$\mathbf{T}(s) = \mathbf{V}^{-1}(s)\mathbf{R}(\mu_x, \mu_y)\mathbf{V}(s) \tag{2.19}$$

with $\mu_u = 2\pi Q_u$, Q being the tune, $\mathbf{V}(s) = \mathrm{diag}(\mathbf{V}_x(s), \mathbf{V}_y(s))$ and the rotation matrix $\mathbf{R}(\mu_x, \mu_y) = \mathrm{diag}(\mathbf{R}(\mu_x), \mathbf{R}(\mu_y))$ in the uncoupled case. Note that the two matrices $\mathbf{V}$ in Eq. 2.19 are evaluated at the same s, since the matrix covers the full turn. Because of this feature, $\mathbf{T}(s)$ is a similarity transform of $\mathbf{R}(\mu_x, \mu_y)$, leaving the eigenvalues invariant. The rotation matrix $\mathbf{R}(\mu_x, \mu_y)$ is an element of the four-dimensional special orthogonal group (SO). Matrices of SO(4) have eigenvalues in complex-conjugated pairs on the complex unit circle. Hence, the spectrum of any $\mathbf{T}(s)$ is the set

$$\lambda(\mathbf{T}) = \{\mathrm{e}^{i\mu_x}, \mathrm{e}^{-i\mu_x}, \mathrm{e}^{i\mu_y}, \mathrm{e}^{-i\mu_y}\}\,. \tag{2.20}$$

The transverse tunes $Q_u = \mu_u/(2\pi)$ are obtained from the arguments of the eigenvalues.

Betatron coupling Betatron coupling may have many sources. Besides magnetic field errors and misalignments of potential magnets, sextupoles, octupoles and the beam-beam effect also lead to coupling. Coupling means that the eigenmodes are rotated out of their original plane. This causes problems as potential orbit corrections and beam parameter measurements lose their effectiveness and accuracy. Coupling is also a local phenomenon. Hence, local coupling correction schemes are applied in large-scale colliders like the LHC. The one-turn map is not block diagonal when the motion is coupled

$$\mathbf{T}(s) = \begin{pmatrix} \mathbf{A} & \mathbf{C}_{12} \\ \mathbf{C}_{21} & \mathbf{B} \end{pmatrix}\,. \tag{2.21}$$

The matrices $\mathbf{A}$ and $\mathbf{B}$ are not necessarily similar to rotation matrices in this context. The one-turn matrix can still be decomposed (assuming symplecticity) in a slightly more complicated manner $\mathbf{T} = \mathbf{W}\mathbf{R}(\mu_1, \mu_2)\mathbf{W}^{-1}$. The eigenmodes are no longer fully embedded in either the x-x' or y-y' plane.

There are two widely used parameterisation forms. One has been developed by Edwards-Teng [87] and the other one by Ripken-Mais [88]. Throughout this thesis, it will not be necessary to apply either of the two decompositions. The coupling is in general small and the modes can easily be associated with the original horizontal and vertical modes.

2.1.3 Non-linear dynamics and effects

The topic of non-linear dynamics and effects is of great importance as most circular accelerators or storage rings are operated with at least the lowest-order non-linear magnet type, namely sextupoles. Sextupoles are important to control the chromaticity, i.e., the energy dependence of the tunes of the particles. This is important because a negative chromaticity may lead to the excitation of head-tail instabilities in a synchrotron running above transition energy. The non-linear nature of the sextupoles restricts the maximum transverse amplitudes since chaotic

behaviour sets in at a certain threshold, and the particles are in risk of being lost in successive turns. This threshold is the so-called dynamic aperture which is usually determined in numerical studies. Besides limiting the maximum transverse actions, sextupoles introduce amplitude detuning, i.e., a tune shift depending on the transverse actions. The effect is rather small for sextupoles because the detuning is only of second order in the sextupole strength. The detuning due to octupoles is much stronger with a dependence of first order on the octupole strength. Octupoles are therefore the elements of choice to introduce a larger tune spread (the range of variation of the tunes) within the beams that enhances Landau damping.

2.1.3.1 Amplitude detuning

Amplitude detuning is the change of the transverse tunes with increasing transverse actions due to the non-linear nature of an underlying potential. All non-linear elements in an accelerator create amplitude detuning; however, the contribution of the different magnet types to the linear detuning is not necessarily a first-order effect. Assuming a Hamiltonian which has successfully been transformed to its normal form (no dependence on angles θ_u), the Hamiltonian is

$$H(J_x, J_y) = \mu_x J_x + \mu_y J_y + f(J_x, J_y) \tag{2.22}$$

The modified tunes are

$$2\pi Q_u(J_x, J_y) = \mu_u + \frac{\partial f}{\partial J_u}(J_x, J_y) = \mu_u + 2\pi \Delta Q_u(J_x, J_y)\,. \tag{2.23}$$

Often, the amplitude detuning is expanded up to first order in the respective actions at the origin $J_x = J_y = 0$, leading to the notation

$$\Delta Q_x = \alpha_{xx} J_x + \alpha_{xy} J_y\,, \qquad \Delta Q_y = \alpha_{yy} J_y + \alpha_{yx} J_x \tag{2.24}$$

with the linear detuning parameters α_{mn} and the relation $\alpha_{xy} = \alpha_{yx}$. The amplitude detuning in a collider like the LHC is mainly generated by the beam-beam effect and octupoles. Sextupoles contribute only weakly to the overall amplitude detuning (second-order effect). The head-on beam-beam effect is the largest detuning source in the LHC. Octupoles contribute in first order in terms of their strength to the amplitude detuning; therefore, octupoles are used in the LHC to generate additional tune spread. The detuning is an important parameter which has to be controlled carefully. A too large detuning shifts particles towards optical resonances in tune space and may cause intensity losses. On the other hand, a small tune spread makes the beam susceptible to external noise and impedances since the stabilising effect of Landau damping is not present. Landau damping occurs if a spread of the transverse betatron tunes is present and is the absence of instability in the presence of impedances or an external force.

Amplitude detuning has a stabilising effect on particles close to a resonance in tune space. Figure 2.4 shows the dynamics of particles close to a resonance that is generated by a dipole.

The dipole kick is modulated with a sinusoid of the fractional tune $Q = 0.315$. If the tune spread is frozen, i.e., the particle tunes are constant throughout the simulation, the amplitudes of the particles close to the resonance grow uncontrolled. With active detuning, the excited particles start to detune once their amplitudes start to grow. The amplitude growth then stabilises.

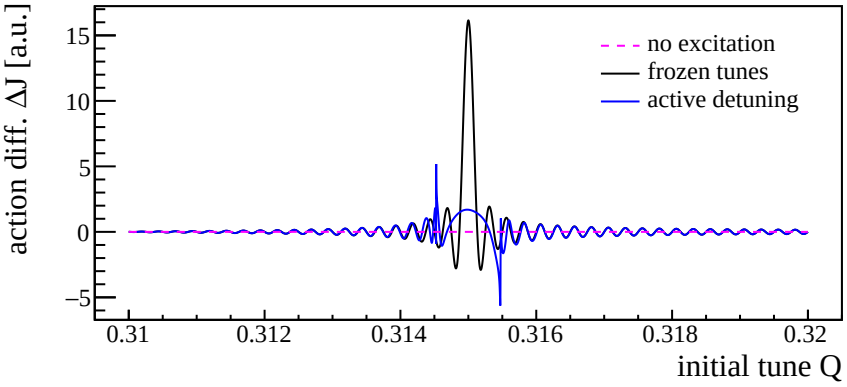

Figure 2.4: Difference between the final and initial action ΔJ versus the initial tune. The sinusoidal dipole kick creates excitation at the tune $Q = 0.315$. Without the excitation (magenta), the action difference ΔJ vanishes. With frozen tunes (black), strong excitation at the resonance tune is observed. Active detuning leads to the stabilisation of the amplitude growth (blue).

2.1.4 The beam-beam effect

The beam-beam effect is the main source of detuning in a collider like the LHC. Since the working point of the collider is close to the difference resonance, the tune footprint resulting from octupoles and beam-beam encounters has to be large enough to supply sufficient Landau damping but has to be small enough to avoid destructive optical resonances. The beam-beam effect is a heavily investigated effect. The derivation of the beam-beam kick can be found in standard literature [89–91] and is beyond the scope of this work. The beam-beam effect can be categorised in terms of whether the bunches are colliding head-on or the bunches are just grazing each other (long-range beam-beam effect), i.e., the beam barycentres are separated at the position at which the beam-beam encounter occurs. Figure 2.5 shows a sketch of the different beam-beam interaction types. The beam-beam effect is an important effect since the head-on tune shift ultimately may limit the collider performance. The long-range interactions excite uneven resonances and influence the dynamic aperture and also shift the closed orbit due to their coherent kick on the beam barycentre. Because of unevenness along the filling pattern, certain bunches may miss out head-on or long-range encounters. These bunches are so-called pacman bunches. Pacman bunches may have different orbits and coherent tunes. Switches of crossing and separation plane among the IPs is an effective tool to suppress at least partially

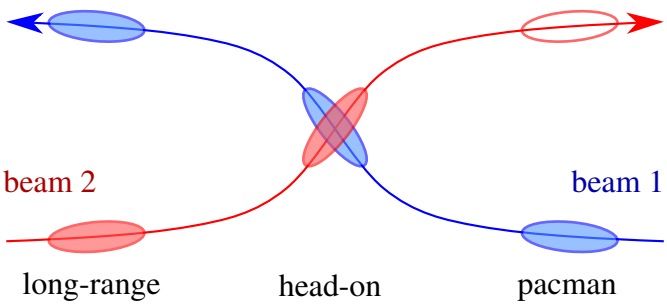

Figure 2.5: The different types of beam-beam interactions. The crossing angle and the beam separation are strongly exaggerated. The long-range interaction (left) occurs when two bunches pass each other with a small separation. Because of unevenness in the filling patterns, a bunch may miss out a long-range or head-on interaction (right). These bunches are so-called pacman bunches.

the effects on pacman bunches. Such a scheme is not necessarily beneficial for the dynamic aperture, but it mitigates strong tune variations along the bunch trains.

The radial kick of a round infinitesimal short bunch on the counter-rotating beam reads

$$\Delta r' = k\frac{1}{r}\left(1-\exp\left(-\frac{r^2}{2\sigma_2^2}\right)\right), \qquad k=\frac{2N_{b2}r_\mathrm{p}m_\mathrm{p}Z_1Z_2}{m_1\gamma_1}, \qquad r=\sqrt{x^2+y^2}. \tag{2.25}$$

Here, the index 1 refers to the witness particle and the index 2 to the source bunch. The quantity N_b is the bunch intensity, Z is the charge number, m_p is the proton mass and m is the particle mass. Also, the classical proton radius $r_\mathrm{p} = e^2/(4\pi\varepsilon_0 m_\mathrm{p}c^2)$ is used with the vacuum permittivity ε_0. For convenience, the scalar constant is substituted by k in the following. Figure 2.6 shows the plot of Eq. 2.25 for a repulsive force between the beams. The corresponding kick in Eq. 2.25 projected into the horizontal and vertical plane reads

$$(\Delta x',\,\Delta y') = k\frac{(x,\,y)}{r^2}\left(1-\exp\left(-\frac{r^2}{2\sigma_2^2}\right)\right). \tag{2.26}$$

The expression in Eq. 2.26 depends on both particle coordinates. Thus, the beam-beam effect introduces coupling between the two transverse planes as long as one coordinate is not strictly zero.

2.1.4.1 Beam-beam potential

A Hamiltonian treatment of the beam-beam effect requires the determination of the beam-beam potential. With the radial kick for round beams given in Eq. 2.25, the beam-beam potential becomes

$$U(x,y) = -\,k\int_0^R \frac{1}{r}\left(1-\exp\left(-\frac{r^2}{2\sigma_2^2}\right)\right)\mathrm{d}r\Big|_{R=\sqrt{x^2+y^2}}. \tag{2.27}$$

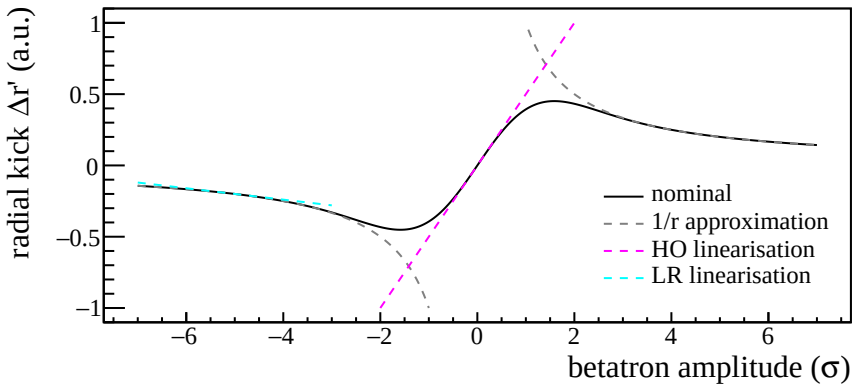

Figure 2.6: Plot of the radial beam-beam kick according to Eq. 2.25 for a repulsive force. Besides the nominal beam-beam kick (solid black), a potential $1/r$ approximation for long-range encounters is given (dashed grey) and also the linearisation for head-on (dashed magenta) and long-range collisions (dashed cyan), allowing a handy matrix representation, is displayed.

There is an analytic expression for the integral making use of the incomplete gamma function $\Gamma(a,x)$ [92]; however, a series expansion may also turn out useful in the limit of small amplitudes. These expressions are (scalar constant dropped)

$$U(x,y) = -\frac{k}{2}\left(\Gamma\left(0, \frac{x^2+y^2}{2\sigma^2}\right) + \log\left(\frac{x^2+y^2}{2\sigma^2}\right)\right) \tag{2.28}$$

$$= -k\sum_{j=1}^{\infty} \frac{(-1)^{j+1}(x^2+y^2)^j}{2j\cdot 2^j\cdot \sigma_2^{2j}\cdot j!}\,. \tag{2.29}$$

In the approximation of a vanishing beam size, the potential simplifies to

$$U(x,y) \approx -\frac{k}{2}\log\left(x^2+y^2\right)\,. \tag{2.30}$$

With the substitutions

$$x = d_x + \sqrt{2J_x\beta_x}\cos\phi_x \qquad \text{and} \qquad y = d_y + \sqrt{2J_y\beta_y}\cos\phi_y\,, \tag{2.31}$$

a transformation into action-angle variables is achieved (required in Sec. 2.1.4.3) with d_u representing the separation of the beam central orbits in the coordinate u and $d = \sqrt{d_x^2+d_y^2}$ being the total separation. The potential is expressible in terms of a Fourier series with the substitutions in Eq. 2.31

$$U(J_x,J_y,\phi_x,\phi_y,d_x,d_y) = \sum_{m,n=-\infty}^{\infty} c_{mn}e^{i(m\phi_x+n\phi_y)} \tag{2.32}$$

with

$$c_{mn} = \frac{1}{4\pi^2}\oint\oint U\left(x(d_x,J_x,\phi_x), y(d_y,J_y,\phi_y)\right)e^{-i(m\phi_x+n\phi_y)}\mathrm{d}\phi_x\mathrm{d}\phi_y\,. \tag{2.33}$$

If there is no separation (head-on), i.e., $(d_x, d_y) = (0, 0)$ and one dimension vanishes (either $J_x = 0$ or $J_y = 0$), this expression simplifies dramatically and c_{mn} has an analytic expression [93]. In all other cases, the evaluation of the different c_{mn} has to be performed numerically.

2.1.4.2 Linear treatment

A linear treatment, i.e., neglecting the higher order non-linear terms, is convenient as a first approach to analyse the beam-beam effect. A linear matrix $\mathrm{M_b}$ that embeds the beam-beam effect into the well-known matrix formalism gives useful insight into important beam dynamics caused by the beam-beam effect. This treatment is valid for head-on collisions at small transverse amplitudes but also for long-range encounters if the beam-beam interaction is mostly of coherent nature (see Fig. 2.6).

Head-on collision A basic approach to modelling the beam-beam interaction is by considering only small amplitudes for the particles of the witness bunch. A matrix representation $\mathrm{M_b}$ of the head-on beam-beam interaction simply is

$$\begin{pmatrix} x \\ x' \\ y \\ y' \end{pmatrix}^* = \begin{pmatrix} 1 & 0 & 0 & 0 \\ k/(2\sigma_2^2) & 1 & 0 & 0 \\ 0 & 0 & 1 & 0 \\ 0 & 0 & k/(2\sigma_2^2) & 1 \end{pmatrix} \begin{pmatrix} x \\ x' \\ y \\ y' \end{pmatrix} . \tag{2.34}$$

The head-on interaction therefore has the same effect on small amplitude particles as a thin quadrupole, except it focuses or defocuses in both planes simultaneously. The tune shift resulting from the interaction can easily be computed by multiplying the matrix $\mathrm{M_b}$ with the linear one-turn map $\mathbf{T}$ followed by the extraction of the arguments of the eigenvalues of the matrix as presented in Eq. 2.20.

Long-range interaction A comparable linear matrix formalism can be used to describe the beam-beam effect with separated beam orbits (long-range encounter). The coherent kick on the bunch (dipole component) can be treated in different ways. One may simply treat it additively, i.e., $\mathbf{r}^* = \mathrm{M_b}\mathbf{r} + \mathbf{t}$ with the coherent kick $\mathbf{t}$ and the phase space vector $\mathbf{r}$ (star indicates modified vector); however, this is cumbersome, and it is inconvenient to obtain the closed orbit shift. Throughout this work, an affine matrix formalism is used to treat the coherent kick. This is performed by extending the standard 4D transverse phase space by a scalar dimension

$$\mathbf{r} = (x, x', y, y', 1)^{\mathrm{T}} . \tag{2.35}$$

Assuming a large separation ($d \geq 5\sigma$), the beam-beam force can be approximated as (see Fig. 2.6)

$$\Delta r' \approx k\frac{1}{r} . \tag{2.36}$$

In terms of the affine matrix formalism, the linearisation for long-range interactions in matrix form then is [9]

$$\mathbf{M}_{\mathrm{b}} = \begin{pmatrix} 1 & 0 & 0 & 0 & 0 \\ \frac{\partial \Delta x'(d_x,d_y)}{\partial x} & 1 & \frac{\partial \Delta x'(d_x,d_y)}{\partial y} & 0 & \Delta x'(d_x,d_y) \\ 0 & 0 & 1 & 0 & 0 \\ \frac{\partial \Delta y'(d_x,d_y)}{\partial x} & 0 & \frac{\partial \Delta y'(d_x,d_y)}{\partial y} & 1 & \Delta y'(d_x,d_y) \\ 0 & 0 & 0 & 0 & 1 \end{pmatrix} . \tag{2.37}$$

The matrix makes use of the expressions

$$(\Delta x',\, \Delta y')(x,y) = k\frac{(x,\, y)}{r^2}\,, \tag{2.38}$$

$$\left(\frac{\partial \Delta x'}{\partial x},\, \frac{\partial \Delta y'}{\partial y}\right)(x,y) = k\left[\frac{1}{r^2} - \frac{2(x^2,\, y^2)}{r^4}\right]\,, \tag{2.39}$$

$$\left(\frac{\partial \Delta x'}{\partial y},\, \frac{\partial \Delta y'}{\partial x}\right)(x,y) = k\frac{-2xy}{r^4}\,. \tag{2.40}$$

The matrix responsible for the linear transfer between potential beam-beam encounter as introduced in Eq. 2.7 modifies to

$$\mathbf{M}(s_0,s_1)\begin{pmatrix} \mathbf{M}_x(s_0,s_1) & & \\ & \mathbf{M}_y(s_0,s_1) & \\ & & 1 \end{pmatrix} \tag{2.41}$$

in the framework of an affine-matrix formalism. The one-turn transfer matrix with no beam-beam interactions is $\mathbf{T} = \mathbf{M}(s_0, s_0+C)$. If there is a single long-range encounter at position s_0, the one-turn matrix becomes $\mathbf{T} = \mathbf{M}(s_0, s_0+C)\mathbf{M}_{\mathrm{b}}$. An eigenvalue calculation for $\mathbf{T}$ yields the tune shift created by the long-range interaction. Since the matrix contains a fifth dimension to enable translation, an additional eigenvalue $\lambda_5 = 1$ that corresponds to a tune of $Q_5 = n \in \mathbb{Z}$ is found. The eigenvector

$$\mathbf{v}_5(s_0) = (x_s, x'_s, y_s, y'_s, 1)^{\mathrm{T}} \tag{2.42}$$

corresponding to the eigenvalue λ_5 contains the closed-orbit shift at the position s_0 of the beam-beam encounter. The concept of a closed orbit only applies if the beam-beam encounter is of constant strength and takes place at a fixed position every revolution. A long-range beam-beam encounter creates coupling between the two transverse planes, i.e., the kicks in both momenta depend on both coordinates if the separation is not only in one plane.

2.1.4.3 Lie-algebraic treatment

The insertion of non-linear magnets or beam-beam interactions causes the particle motion to be non-integrable. The reason for this is not necessarily the non-linear nature of the magnet itself,

but the fact the magnet is localised and its Hamiltonian is not continuously applied along the machine circumference. While the motion of a particle in a continuous octupole is integrable and can be expressed in terms of elliptical functions, the motion with localised octupoles is only quasi integrable in the vicinity of the origin $J_x \approx J_y \approx 0$. In the following, a Lie algebraic approach is used to derive an effective Hamiltonian in the presence of arbitrary beam-beam encounters in the accelerator lattice. This approach is explained in detail in [91, 93, 94] and in Appendix A. A Lie map is applied to the particle vector $\mathbf{r} = (x, x', y, y')$ like $e^{:Lh:}\mathbf{r}$ with L being the length of the element with the constant Hamiltonian $H = -h$. The Poisson operator $:h:a = [h, a]$ applies the Poisson brackets to the element on the right side of it, in this case a. In the following and in Appendix A, the integrated form is used, i.e., $h = -HL$. This way, the step size (the element length) is moved onto the Hamiltonian. Thus, the integration length is unity independently of the element length $e^{:h:}\mathbf{r}$.

The Lie operator of the linear transfer between two non-linear elements reads

$$H_0(s_0, s_1) = -(\phi_x(s_1) - \phi_x(s_0))J_x - (\phi_y(s_1) - \phi_y(s_0))J_y \,. \tag{2.43}$$

The Lie operator of an infinitesimal short beam-beam interaction is[2] (cf. Eq. 2.32)

$$H_\mathrm{b}(J_x, J_y, \phi_x, \phi_y) = -\sum_{m,n=-\infty}^{\infty} c_{mn}(J_x, J_y, d_x, d_y)e^{i(m\phi_x + n\phi_y)} \,. \tag{2.44}$$

The one-turn map is then obtained by alternately multiplying linear transfer maps and the maps of the beam-beam encounters

$$e^{:h:} = e^{:H_0(0,s_1):}e^{:H_\mathrm{b}(s_1):}e^{:H_0(s_1,s_2):} \ldots e^{:H_\mathrm{b}(s_{N-1}):}e^{:H_0(s_{N-1},s_N):}e^{:H_\mathrm{b}(s_N):}e^{:H_0(s_N,C):} \,. \tag{2.45}$$

Following the derivation presented in the Appendix A, the final result is the approximation of the one-turn Hamiltonian $H = -h$ with arbitrary beam-beam encounters

$$\begin{aligned} H(J_x, J_y, \phi_x, \phi_y, d_x, d_y) =& \mu_x J_x + \mu_y J_y + \sum_{m,n=-\infty}^{\infty} C_{mn} \frac{m\mu_x + n\mu_y}{2\sin\left(\frac{m\mu_x + n\mu_y}{2}\right)} \\ & \times \exp\left[im\left(-\frac{\mu_x}{2} + \phi_x\right) + in\left(-\frac{\mu_y}{2} + \phi_y\right)\right] \,. \end{aligned} \tag{2.46}$$

The coefficients read

$$C_{mn}(J_x, J_y, d_x, d_y) = \sum_{p=1}^{N} c_{mn}(J_x, J_y, d_x, d_y, s_p)e^{i(m\phi_x(s_p) + n\phi_n(s_p))} \tag{2.47}$$

with c_{mn} given in Eq. 2.33.

[2] Equation 2.26 already contains the integrated beam-beam force, i.e., the total kick applied by the opposing bunch is effectively compressed into an infinitesimal short kick.

Head-on collision For a particle close to the origin $J_x \approx J_y \approx 0$, the Hamiltonian reduces to

$$H = \mu_x J_x + \mu_y J_y + c_{00}(J_x, J_y) \tag{2.48}$$

assuming round beams and no resonance close by. The tune shift can simply be obtained via

$$\xi_{\mathrm{HO}u} = \frac{1}{2\pi} \frac{\partial c_{00}(J_x, J_y)}{\partial J_x}\bigg|_{J_x=J_y=0} \qquad \text{with} \qquad c_{00} = -k\frac{(J_x + J_y)}{4\epsilon_2} \tag{2.49}$$

and ϵ_2 being the geometric emittance of the source bunch. This yields the final expression for the tune shift, the so-called beam-beam parameter

$$\xi_{\mathrm{HO}u} = -\frac{k}{8\pi\epsilon_2}\,. \tag{2.50}$$

Long-range interaction The long range beam-beam potential is assumed to be

$$U \approx -\frac{k}{2}\log\left((d_x + x)^2 + (d_y + y)^2\right) \tag{2.51}$$

Taylor expanding up to second order in d_u leads to

$$U \approx -\frac{k}{2}\left(\log\left(d^2\right) + \frac{2d_y}{d^2}y + \frac{d_x^2 - d_y^2}{d^4}y^2 + \frac{2d_x}{d^2}x + \frac{d_y^2 - d_x^2}{d^4}x^2 - \frac{4d_x d_y}{d^4}xy\right)\,. \tag{2.52}$$

The next step is substituting x and y by action-angle coordinates and take the average in terms of angles to obtain

$$c_{00}(J_x, J_y) = \frac{k(d_x^2 - d_y^2)(\beta_x J_x - \beta_y J_y) - d^4\log(d^2))}{2d^4}\,. \tag{2.53}$$

The tune shift of the reference particle $\xi_{\mathrm{LR}u} = \partial c_{00}(J_x, J_y)/(2\pi\partial J_u)|_{J_x=J_y=0}$ then reads [95]

$$(\xi_{\mathrm{LR}x}, \xi_{\mathrm{LR}y}) = (\beta_x, -\beta_y)\frac{k}{4\pi}\frac{d_x^2 - d_y^2}{d^4}\,. \tag{2.54}$$

The sign of separation does not have any influence on the tune shift. Cancellation of the detuning can only be achieved by changing the separation plane of the long-range encounters. Figure 2.7 shows a sketch of the tune footprints for head-on collisions and long-range interactions. The sketch illustrates the direction of the tune shift in tune space for the different types of beam-beam interactions.

2.1.4.4 Coherent beam-beam modes

Coherent beam-beam modes can occur due to head-on or long-range beam-beam interactions. The beam-beam force couples the interacting bunches and, depending on the filling pattern, different numbers of bunches are influenced by each other. Coherent beam-beam modes have been

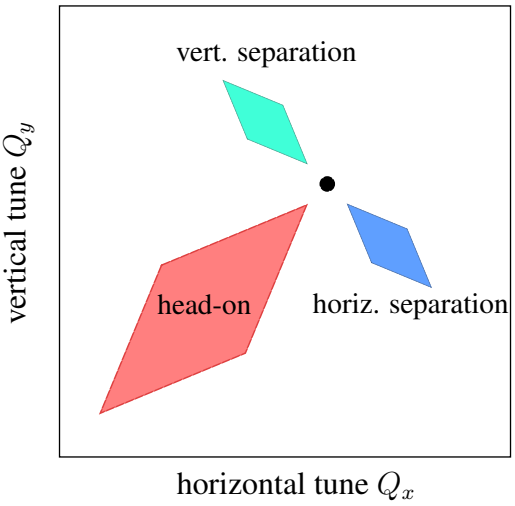

Figure 2.7: Sketch of the tune footprints for the head-on beam-beam effect and for long-range interactions with a vertical and horizontal separation. The tune footprints embed the horizontal and vertical tunes for different transverse actions into tune space.

investigated for p-p collisions by various authors [96, 97]. In particular, the Landau damping due to the head-on interactions in the IPs and also the presence of a transverse feedback system ensure the absence of coherent beam-beam modes. The question arises whether moving long-range beam-beam encounters excite coherent modes among the bunches of the two beams. The main reason coherent modes caused by moving encounter locations are not analysed in the following is the fact the two beams have different transverse tunes. The phrase *different tunes* does not necessarily mean that the betatron tunes of the beams are actually different in this context. Here, it refers to the fact that if the beam-beam encounters become periodic at one point in time, periodicity is achieved in the Nth turn of the slower beam. This corresponds to the $(N+1)$th turn of the faster beam. Hence, the total phase advance is not equal $N\mu_u \neq (N+1)\mu_u$ assuming $\mu_u = 2\pi Q_u$ is equal for both beams like in the LHC. This effective tune difference should provide some level of suppression of coherent modes. For better understanding, the following paragraphs will discuss simple examples of fixed and moving encounter locations.

Single static beam-beam encounter The analysis of coherent beam-beam modes for only one bunch per beam and a single static long-range interaction in a single IP is easily performed. In the following, a single IP with one long-range encounter at a location with a horizontal separation $d_x \neq 0$ is assumed. In addition, the first beam contains a single Pb bunch and the second beam a proton bunch. The beam-beam constants are assumed to follow the values in

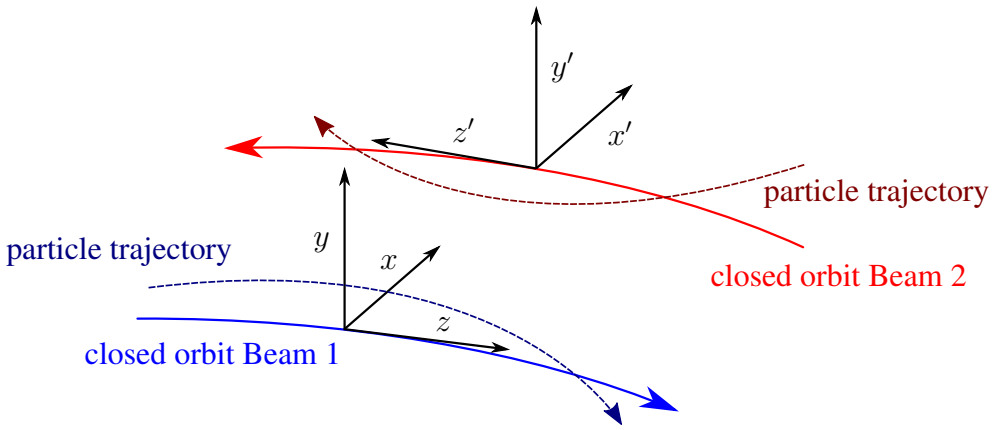

Figure 2.8: The coordinate systems of the clockwise rotating Beam 1 (blue) and counterclockwise rotating Beam 2 (red). The coordinate system of Beam 1 is right-handed, while the primed system of Beam 2 is left-handed.

Tab. 2.1 for the LHC. If one restricts the analysis to the horizontal plane, the phase-space vector of the system is

$$\mathbf{r} = (x_1, x'_1, x_2, x'_2, 1)^{\mathrm{T}} . \tag{2.55}$$

The index 1 refers to the Pb bunch in the first beam, and the second index refers to the proton bunch in the second beam. The fifth dimension is again used to include translations as already introduced in Eq. 2.37. Following the coordinate convention displayed in Fig. 2.8, the beam-beam matrix coupling the two bunches reads in the long-range approximation

$$\mathbf{M}_{\mathrm{b,coup}} \approx \begin{pmatrix} 1 & 0 & 0 & 0 & 0 \\ -k_1/d_x^2 & 1 & k_1/d_x^2 & 0 & -k_1/d_x \\ 0 & 0 & 1 & 0 & 0 \\ k_2/d_x^2 & 0 & -k_2/d_x^2 & 1 & k_2/d_x \\ 0 & 0 & 0 & 0 & 1 \end{pmatrix} . \tag{2.56}$$

The constant k is different for the two beams. The linear map for the rest of the machine is (index x dropped)

$$\mathbf{M} = \begin{pmatrix} \mathbf{R}(2\pi Q) & & \\ & \mathbf{R}(2\pi Q) & \\ & & 1 \end{pmatrix} \tag{2.57}$$

assuming $\alpha_x = 0$ (symmetry point) besides $\beta^* = 1\,\mathrm{m}$ for both beams. This results in the one-turn map $\mathbf{T} = \mathbf{M}\mathbf{M}_{\mathrm{b,coup}}$. The coherent tunes and eigenmodes are easily obtained via eigendecomposition. The two modes are the σ-mode and π-mode. The tune of the σ-mode

is equal to the natural betatron tune $Q_0 = Q$, whereas the π-mode is shifted by the sum of the long-range detuning parameters $Q_\pi = Q + \xi_{\mathrm{LR1}} + \xi_{\mathrm{LR2}}$ given in Eq. 2.54.[3] The σ-mode is responsible for in-phase oscillation of the two bunches while the π-mode represents out-of-phase oscillation.

Single moving beam-beam encounter The question remains whether coherent modes develop due to the moving encounters. To simplify matters, the IR lengths is assumed to be infinitesimal short or at least much smaller than the bunch spacing. The recurrence time T_m of the Pb bunch is exactly $T_m = N$ turns, i.e., the Pb bunch and proton bunch influence each other during the first turn and a second time in turn N ($N + 1$) of the Pb (proton) bunch. No additional interactions occur in the meantime. The faster proton bunch has performed one more turn than the Pb bunch in the same time. Thus, the linear transfer between the two beam-beam interactions modifies to

$$\mathbf{M} = \begin{pmatrix} \mathbf{R}(N2\pi Q) & & \\ & \mathbf{R}((N+1)2\pi Q) & \\ & & 1 \end{pmatrix} . \tag{2.58}$$

The eigendecomposition of $\mathbf{T} = \mathbf{M}\mathbf{M}_{\mathrm{b,coup}}$ shows no coherent modes developing at fractional tunes comparable to the LHC tunes. The eigenmodes reduce to the original orthogonal modes and the betatron tunes are shifted by the long-range linear detuning parameter of the respective bunch $nQ_1 = nQ + \xi_{\mathrm{LR},1}$ and $(n+1)Q_2 = (n+1)Q + \xi_{\mathrm{LR},2}$. This example shows that the development of coherent beam-beam modes is highly unlikely besides the fact that also Landau damping, the transverse feedback system, synchrotron motion, fluctuating bunch intensities and symmetric phase advances between the IPs suppress coherent modes [96–100]. Also, potential coherent modes would extend to all bunches of both beams because of the slippage of the filling patterns with respect to each other, i.e., no disjoint clusters exist and the properties of each bunch become relevant instead. Based on these considerations and the presence of the transverse feedback system, it does not seem necessary to analyse coherent beam-beam modes.

2.1.5 Dipole noise

Dipole errors result from field errors, misalignments of magnets (feed-down effect) and beam-beam interactions with offsets (long-range encounters). In particular, the last-mentioned long-range interaction is the reason dipole noise is discussed here. Moving long-range encounters

[3] In the limit of long-range beam-beam interactions, the coherent tune shift is twice the single-particle tune shift or the sum of the two linear tune shifts if the beams are asymmetric. If the beams collide head-on, the coherent beam-beam force is a factor $1/2$ smaller than the usual single-particle force at the origin, i.e., the coherent tune shift is therefore not twice as large as the single-particle tune shift.

create time-modulated dipole kicks that influence the beams. A general description of dipole noise and its effects on the beam dynamics is given in this section.

Dipole errors cause different effects in a synchrotron. A constant dipole error causes the closed orbit to shift and yields instability at integer tunes (integer resonance). The calculation of the orbit offset was already discussed in the context of the long-range beam-beam effect in Sec. 2.1.4.2 and it can also be found in the standard literature [22–24]. Fluctuating dipole errors create emittance growth in contrast to constant dipole errors. Figure 2.9 shows this behaviour: An instantaneous kick moves the particle ensemble (bunch) in phase space along the momentum axis. This offset translates into an increased emittance due to a distribution of betatron tunes among the particles of the bunch (filamentation). The correlation or Fourier spectrum of these kicks are of great importance since multiple kicks may cancel or amplify each other's effect.

With N dipole-noise sources that behave fully randomly (vanishing autocorrelation and cross-correlation) at the locations s_i, the growth of the normalised emittance is given by

$$\epsilon_{u,n+1} = \epsilon_{u,n} + \frac{1}{2}\sum_{i=1}^{N} \beta_u(s_i)\left\langle \Delta u_i'^2 \right\rangle , \qquad \dot{\epsilon} = f_0 \frac{1}{2}\sum_{i=1}^{N} \beta(s_i)\left\langle \Delta u_i'^2 \right\rangle . \tag{2.59}$$

with $\Delta u'$ being the deflection angle in u and $\langle \bullet \rangle$ indicating the average value. If a noise source is correlated to itself or to another source, the emittance growth rate in Eq. 2.59 potentially modifies. Moving long-range encounter locations do not behave fully randomly and have specific time structures, i.e., the formulas in Eqs. 2.59 become inaccurate. The next paragraph considers an arbitrary number of sources that have arbitrary correlations.

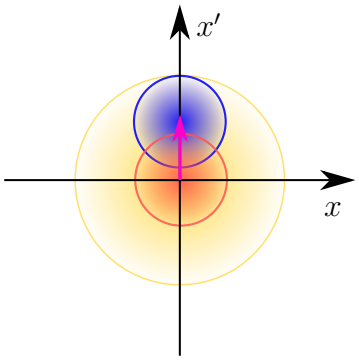

Figure 2.9: The sketch illustrates the principle of filamentation. The particle ensemble (red) experiences a coherent momentum kick $\Delta x'$ (magenta arrow). Filamentation causes the kicked ensemble (blue) to fill out a much larger area in phase space after a while (yellow).

2.1.5.1 Arbitrary dipole noise

Approximating the dipole kicks as fully random dipole-noise sources is a pessimistic approximation because of correlations between the kicks. In the following, a treatment of arbitrary

dipole noise of an arbitrary number of sources is presented. Sometimes it is convenient to summarise multiple kicks of a specific section in the accelerator into a single kick (neglecting detuning between the different kicks) that modifies the momenta x' and y' but also the coordinates x and y because of the phase advance between the kicks and the location of observation (the location the effective kick is applied). During the later stages of this chapter, the regions that are summarised into a single kick will be the IRs of the collider. Summarising multiple kicks into a single kick, however, requires that the kick is also partly applied in the coordinate as previously mentioned. If one considers kicks in the momentum according to the function $\mathcal{G}(t)$ and kicks in the coordinate according to a different function $\mathcal{H}(t)$, the underlying Hamiltonian in one plane and in normalised coordinates has the form

$$H = \frac{\omega_u}{2}(\tilde{u}^2 + \tilde{u}'^2) - \tilde{u}\mathcal{G}(t) + \tilde{u}'\mathcal{H}(t) \qquad \text{with} \qquad \omega_u = \frac{2\pi Q_u}{T_0} = \frac{\mu_u}{T_0}\,. \tag{2.60}$$

The two functions $\mathcal{G}$ and $\mathcal{H}$ are of the form

$$\mathcal{G}(t) = g(t) \sum_{m=-\infty}^{\infty} \delta(t - mT_0)\,. \tag{2.61}$$

Equation 2.61 contains δ-functions of a one-turn periodicity to indicate a kick that is applied every turn at the same position. The strength of the kick is modulated by the noise function $g(t)$. If there are multiple noise sources N_s, the functions are expressed as

$$\mathcal{G}(t) = \sum_{m=-\infty}^{\infty} \sum_{j=1}^{N_\mathrm{s}} g_j(t)\delta(t - mT_0 - \Gamma_j T_0) \qquad \text{with} \qquad \Gamma_j = \frac{\phi_u(s_j)}{2\pi Q_u} \in [0;\, 1)\,. \tag{2.62}$$

The parameter Γ_j is a measure of the location of a noise source along the circumference projected into the $[0;\, 1)$ interval. The differential equation for the coordinate $\tilde{u}$ obtained from the Hamilton equations is

$$\ddot{\tilde{u}} + \omega_u^2 \tilde{u} = \omega_u \mathcal{G}(t) + \dot{\mathcal{H}}(t)\,. \tag{2.63}$$

The inhomogeneous part is zero except during the moment of one of the kicks. The inhomogeneous part $\mathcal{W}(t) = \omega_u\mathcal{G}(t) + \dot{\mathcal{H}}(t)$ is expandable into a Fourier series. If one assumes the knowledge of the kicks up to the Nth turn, the Fourier series then simply reads

$$\mathcal{W}(t) = \sum_{n=-\infty}^{\infty} W_n \exp(in\omega_0 t/N)\,. \tag{2.64}$$

with the Fourier coefficients

$$W_n = \frac{1}{NT_0} \int_0^{NT_0} \sum_{m=-\infty}^{\infty} \sum_{j=1}^{N_s} w_j(t)\delta(t - mT_0 - \Gamma_j T_0) \exp(-it\omega_0 n/N) dt \tag{2.65}$$

$$= \frac{1}{NT_0} \sum_{j=1}^{N_s} \mathcal{F}[w_j](n) \exp(-i2\pi\Gamma_j n/N)\,. \tag{2.66}$$

The notation $\mathcal{F}[w](n) = \sum_{k=0}^{N-1} w_k \exp(-i2\pi kn/N)$ refers to the nth coefficient of the discrete Fourier transform (DFT) $\mathcal{F}$ of the values of w. Hence, the coefficient W_n gives a measure of the excitation at the transverse tune $Q_u = n/N$ and a potential growth rate of a particle located at that specific tune in tune space can be inferred. The emittance ϵ, a quantity proportional to the square of the amplitude, evolves like [101]

$$\dot{\epsilon} \propto |W_n|^2 \, \rho(n\omega_0/N) \tag{2.67}$$

if there is a single excitation at the frequency $n\omega_0/N$. Here, $\rho(Q)$ is the density function of the transverse betatron tunes. Without proof, additional frequency components of the noise are assumed to contribute linearly to the emittance evolution, i.e., $\dot{\epsilon} \propto \sum_n |W_n|^2 \, \rho(n\omega_0/N)$.[4] The formulas for the emittance growth are only valid if the transverse tune distributions are frozen. If active detuning is present, the emittance growth is only obtainable via particle tracking.

2.1.5.2 Transverse feedback system

A transverse feedback system is vital to counteract emittance growth and orbit shifts. A feedback system is based on the idea of measuring the beam offset with a pick-up at position A and correcting that specific offset at position B with preferably a fractional phase advance of $\pm\pi/2$, i.e., the offset in the coordinate has fully shifted into the momentum. A feedback system works differently compared to stochastic cooling. Stochastic cooling is based on *phase mixing*, i.e., because of a finite tune spread of the particles within a bunch, small barycentre displacements appear regularly since the particle distribution is not entirely continuous. These small displacements are corrected by the cooling system over a long time period and ultimately emittance shrinkage is achieved. A feedback system, on the other hand, corrects orbit errors as fast as possible to prevent filamentation (see Fig. 2.9). It is not advantageous to correct the entire offset in a single kick since a potential error of the pick-up is then strongly amplified and may cause emittance growth. Hence, it is advisable to correct the offset over multiple turns. In normalised phase-space coordinates $(\tilde{u}, \tilde{u}')$ in the plane u, a simplified one-turn map that includes the effect of a feedback system on a single particle or rigid bunch is

$$\begin{pmatrix} \tilde{u} \\ \tilde{u}' \end{pmatrix}_{n+1} = \mathbf{R}_u(\mu_u) \begin{pmatrix} \tilde{u}_n \\ \tilde{u}'_n(1-g) \end{pmatrix} . \tag{2.68}$$

The variable $g \leq 1$ is the gain of the feedback system. The linear map in Eq. 2.68 has two eigenvalues. The absolute values of these eigenvalues are[5]

$$|\lambda_{1,2}| \approx \sqrt{1-g} \, . \tag{2.69}$$

[4] This is based on the assumption that terms containing mixed frequencies do not contribute time independently to the emittance growth.

[5] A small gain $g \ll 1$ and a fractional tune close to that of the LHC tune is assumed.

In the limit of applying the map in Eq. 2.68 multiple times in succession with a small gain g, the two eigenmodes damp according to $\exp(-gf_0t/2)$ in time. The action, however, damps twice as fast

$$J_u(t) = J_u(0)e^{-gf_0t} \tag{2.70}$$

since it depends quadratically on both phase space coordinates $J_u = (\tilde{u}^2 + \tilde{u}'^2)/2$. The damping time of the transverse amplitude is $\tau = T_0/g$. It is not too easy to simulate the effect of a feedback system on the particle ensemble because the number of particles in simulations is limited. Thus, a transverse feedback system may act like a stochastic cooling on the beam and the transverse emittances shrink.

Feedback in the presence of dipole noise A transverse feedback system is highly efficient to suppress emittance growth due to dipole noise. The idea is to correct the barycentre offset created by the dipole noise before filamentation (see Fig. 2.9) sets in. The derivation of the emittance growth in the presence of dipole noise and an active feedback system is given in [102] and only the final result is stated here. The derivation, however, assumes constant betatron tunes of the particles. This means that particles do not change tunes if their transverse actions grow or shrink, and the particles do not oscillate in energy. With this limitation, the emittance growth in the presence of an active feedback reads

$$\dot{\epsilon}_u = \dot{\epsilon}_{u,0} \int_{-\infty}^{\infty} \rho(\Delta Q_u) \frac{4\pi^2(1-g/2)^2\Delta Q_u^2}{4\pi^2(1-g/2)\Delta Q_u^2 + (g/2)^2} \mathrm{d}\Delta Q_u \,. \tag{2.71}$$

Here, $\dot{\epsilon}_{u,0}$ is the emittance growth due to the dipole noise without the presence of the feedback system, and ΔQ_u refers to the tune deviation of the particles from the average tune. Equation 2.71 is a good tool to estimate the reduction of the growth rate by a feedback system since a tracking approach comes with difficulties.

2.1.6 Quadrupole noise and tune modulation

Quadrupole noise is different compared to dipole noise in terms of emittance growth. Quadrupole noise results again either from misalignments, field error, feed-down effects but also from beam-beam encounters (head on and long range). In the context of this thesis, moving long-range encounters introduce quadrupole noise on the beam and can cause emittance growth. Additionally, a periodic tune modulation as generated by the synchrotron motion in combination with chromaticity introduces sidebands to optical resonances and especially to the resonances of the dipole noise caused by long-range encounters. Hence, sidebands of these resonances may approach the betatron tune footprint. In the next sections, a description of emittance growth caused by quadrupole noise is given and the formalism for sidebands resulting from a periodic tune modulation is derived.

2.1.6.1 Quadrupole Noise

Assuming a quadrupole that features a normally distributed focusing error, the kick of the quadrupole is $\Delta u' = k_1 u$ with a vanishing DC contribution $\langle k_1 \rangle = 0$ and $\mathrm{Var}(k_1) = \sigma_k^2$.[6] The emittance growth can be expressed as

$$\epsilon_{u,n+1} = \epsilon_{u,n} \left(1 + \frac{\beta_u(s)\sigma_k^2}{2} \right) , \qquad \dot{\epsilon}_u = \epsilon_u f_0 \frac{\beta_u(s)\sigma_k^2}{2} . \tag{2.72}$$

Hence, the emittance evolves like the exponential function

$$\epsilon_u(t) = \epsilon_u(0) \exp \left(f_0 \frac{\beta_u(s)\sigma_k^2}{2} t \right) . \tag{2.73}$$

The growth rate decreases if the values of k_1 obey an exponentially decreasing auto-correlation function

$$\langle k_{1,n}, k_{1,n+m} \rangle = \sigma_k^2 e^{-\alpha|m|} \qquad \text{with} \qquad \alpha \in \mathbb{R}^+ . \tag{2.74}$$

Then, the emittance evolution modifies to [103]

$$\epsilon_u(t) = \epsilon_u(0) \exp \left[f_0 \frac{\beta_u(s)\sigma_k^2}{2} \left(\frac{1 - e^{-2\alpha}}{1 + e^{-2\alpha} - 2\cos(4\pi Q) e^{-\alpha}} \right) t \right] . \tag{2.75}$$

Multiple quadrupole-noise sources modify Eq. 2.75 to

$$\epsilon_u(t) = \epsilon_u(0) \exp \left[f_0 \sum_{i=1}^{N} \frac{\beta_u(s_i)\sigma_{k,i}^2}{2} \left(\frac{1 - e^{-2\alpha_i}}{1 + e^{-2\alpha_i} - 2\cos(4\pi Q) e^{-\alpha_i}} \right) t \right] . \tag{2.76}$$

If the correlation time vanishes, the emittance evolution reads

$$\epsilon(t) = \epsilon(0) \exp \left(f_0 \sum_{i=1}^{N} \frac{\beta(s_i)\sigma_{k,i}^2}{2} t \right) . \tag{2.77}$$

It is obvious that the emittance growth from dipole noise and quadrupole noise follows different patterns. Quadrupole noise is a self-amplifying effect since the kick depends on the transverse amplitude, while dipole noise acts additively. On a short time scale, dipole noise contributes more strongly to emittance growth than quadrupole noise, whereas quadrupole noise is dominating on longer time scales.

2.1.6.2 Tune oscillation

A periodic tune oscillation creates sidebands separated by integer multiples of the modulation frequency ω_s (later on the synchrotron frequency) from the original resonance/excitation in tune

[6] Here, k_1 is the integrated quadrupole strength.

space. Such a tune oscillation is generated by the synchrotron motion in combination with the chromaticity ξ. In the context of long-range beam-beam encounters, sidebands to the tunes that are excited by the beam-beam encounters may approach the transverse tune footprint of the particles in the beam and may cause excitation. The amplitudes of the sidebands in the presence of dipole noise are derived in the following for the longitudinal synchrotron motion.

The simplified Hamiltonian in normalised coordinates and in one plane[7] is

$$H(\tilde{u},\tilde{u}',t) = \frac{\omega + A_m \sin(\omega_s t)}{2}(\tilde{u}^2+\tilde{u}'^2) - \tilde{u}\Theta(t) \qquad \text{with} \qquad \omega = 2\pi Q/T_0\,. \tag{2.78}$$

The Hamiltonian H includes a tune oscillation with the modulation depth $A_m = 2\pi\xi\delta_p$ and the dipole-kick function $\Theta(t)$ (cf. $\mathcal{G}(t)$ in Eq. 2.60). Via the normalised action-angle coordinates

$$\tilde{u} = \sqrt{2J}\cos\phi \qquad \text{and} \qquad \tilde{u}' = -\sqrt{2J}\sin\phi \tag{2.79}$$

that are obtained from the generating function of first kind $F_1(\tilde{u},\phi) = -\tilde{u}^2/2\tan\phi$, the Hamiltonian is expressed as

$$H(J,\phi,t) = (\omega + A_m\sin(\omega_s t))J - \sqrt{2J}\cos\phi\cdot\Theta(t)\,. \tag{2.80}$$

The generating function of second kind $F_2(\phi,\overline{J}) = \phi\overline{J} + A_m/\omega_s\cos(\omega_s t)\overline{J}$ can further be used to obtain the coordinate substitutions

$$J = \overline{J} \qquad \text{and} \qquad \phi = \overline{\phi} - \frac{A_m}{\omega_s}\cos\omega_s t\,. \tag{2.81}$$

These substitutions cause the removal of the explicit dependence on time of the unperturbed Hamiltonian. The Hamiltonian in Eq. 2.80 then is

$$\begin{aligned} H(\overline{J},\overline{\phi},t) &= (\omega + A_m\sin(\omega_s t))\overline{J} - \sqrt{2\overline{J}}\cos\left(\overline{\phi} - \frac{A_m}{\omega_s}\cos\omega_s t\right)\Theta(t) + \frac{\partial F_2}{\partial t} \\ &= \omega\overline{J} - \sqrt{2\overline{J}}\Theta(t)\left[\cos\overline{\phi}\cos\left(\frac{A_m}{\omega_s}\cos\omega_s t\right) - \sin\overline{\phi}\sin\left(\frac{A_m}{\omega_s}\cos\omega_s t\right)\right]\,. \end{aligned} \tag{2.82}$$

The time dependence of the unperturbed Hamiltonian has been eliminated and was successfully shifted onto the perturbation term. With a transformation back into rotating Cartesian coordinates

$$\overline{u} = \sqrt{2\overline{J}}\cos\overline{\phi}\,, \qquad \overline{u}' = -\sqrt{2\overline{J}}\sin\overline{\phi} \tag{2.83}$$

the Hamiltonian coincides with that of a driven harmonic oscillator

$$H(\overline{u},\overline{u}',t) = \frac{\omega}{2}\left(\overline{u}^2+\overline{u}'^2\right) - \overline{u}\cos\left(\frac{A_m}{\omega_s}\cos\omega_s t\right)\Theta(t) + \overline{u}'\sin\left(\frac{A_m}{\omega_s}\cos\omega_s t\right)\Theta(t)\,. \tag{2.84}$$

[7] The index u indicating an arbitrary transverse coordinate is dropped. The formalism is applicable to either of the two transverse planes.

The Jacobi-Anger expansion [104] is now used to express the nested trigonometric functions in terms of Bessel functions J_i

$$H(\overline{u},\overline{u}',t) = \frac{\omega}{2}(\overline{u}^2+\overline{u}'^2) - \overline{u}J_0\left(\frac{A_m}{\omega_s}\right)\Theta(t) - 2\overline{u}\sum_{n=1}^{\infty}(-1)^n J_{2n}\left(\frac{A_m}{\omega_s}\right)\cos(2n\omega_s t)\Theta(t) \\ - 2\overline{u}'\sum_{n=1}^{\infty}(-1)^n J_{2n-1}\left(\frac{A_m}{\omega_s}\right)\cos([2n-1]\,\omega_s t)\Theta(t)\,. \tag{2.85}$$

By expanding the dipole perturbation into the Fourier series

$$\Theta(t) = \sum_{m=0}^{\infty} a_m \cos(m\omega_0 t + \varphi_m)\,, \tag{2.86}$$

the sideband amplitudes are obtained following the insertion of Eq. 2.86 into Eq. 2.85

$$H(\overline{u},\overline{u}',t) = \frac{\omega}{2}\left(\overline{u}^2+\overline{u}'^2\right) - \overline{u}\sum_{m=0}^{\infty} a_m J_0\left(\frac{A_m}{\omega_s}\right)\cos(m\omega_0 t+\varphi_m) \\ -\overline{u}\sum_{\substack{n=1\\m=0}}^{\infty}(-1)^n a_m J_{2n}\left(\frac{A_m}{\omega_s}\right)\left[\cos\left(\Omega_{m,n}^{\text{even}-}t+\varphi_m\right)+\cos\left(\Omega_{m,n}^{\text{even}+}t+\varphi_m\right)\right] \\ -\overline{u}'\sum_{\substack{n=1\\m=0}}^{\infty}(-1)^n a_m J_{2n-1}\left(\frac{A_m}{\omega_s}\right)\left[\cos\left(\Omega_{m,n}^{\text{odd}-}t+\varphi_m\right)+\cos\left(\Omega_{m,n}^{\text{odd}+}t+\varphi_m\right)\right] \tag{2.87}$$

with the angular frequencies

$$\Omega_{m,n}^{\text{even}\pm} = m\omega_0 \pm 2n\omega_s\,, \qquad \Omega_{m,n}^{\text{odd}\pm} = m\omega_0 \pm (2n-1)\omega_s\,. \tag{2.88}$$

The kick is now no longer only in the momentum but effectively also in the coordinate. As already mentioned, the explicit time dependence of the unperturbed Hamiltonian was successfully shifted onto the perturbation. Each existing frequency component has an infinite number of sidebands spaced by $r\omega_s$ with $r \in \mathbb{Z}$. The amplitudes of the frequency components are modulated by Bessel functions. The modulation depth A_m is here of importance since it determines the strength of each sideband. A large modulation may cause higher-order Bessel functions to carry the integral amplitude. Figure 2.10 illustrates the sideband amplitudes $J_n(2\pi\xi\delta_p/\omega_s)$ as a function of the order n for different momentum offsets δ_p using LHC parameters. Simulating the tune oscillation caused by the synchrotron motion is consequently important since particles with larger energy deviations may experience excitation, whereas particles at nominal energy are not influenced.

2.1.7 Multiple Long-range interactions

The kicks of long-range interactions in an IR add up differently in the two transverse planes since the parallel separation is in one plane (separation plane) and the crossing is in the other

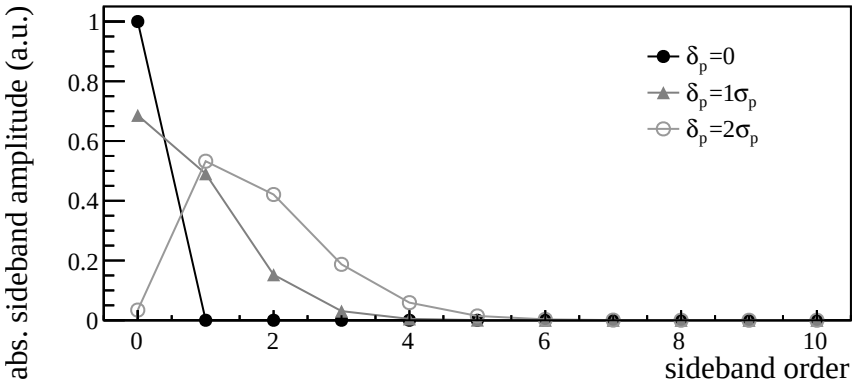

Figure 2.10: Sideband amplitudes as a function of the sideband order for three different energy offsets. This calculation assumes a synchrotron tune of $Q_s = \omega_s/\omega_0 = 0.005$, a relative momentum spread of $\sigma_p = 3.9 \times 10^{-4}$ and a chromaticity $\xi = 15$. With no energy offset, no sidebands exist (full dots), while the sidebands increase in amplitude for larger momentum offsets. For an energy offset of $\delta_p = 2\sigma_p$ (circles), the first sideband is even stronger than the original amplitude.

plane (crossing plane).[8] Thus, there are different phase advances between the long-range interactions in the two planes, and the signs and magnitude of the separation between the two orbits behave differently in the two planes.

The normalised net kick that remains after the IR projected to the start position of the IR $s_{\mathrm{IR}}^{\mathrm{start}}$ (beginning of the common beam pipe) is

$$\delta_u = \Delta\tilde{u}' + i\Delta\tilde{u} = \sum_{j\in\mathrm{enc.}} f_u(s_j) \qquad \text{with} \tag{2.89}$$

$$f_u(s_j) = e^{-i(\phi_u(s_j)-\phi_u(s_{\mathrm{IR}}^{\mathrm{start}}))}\sqrt{\beta}_u(s_j)k\frac{d_u(s_j)}{d^2(s_j)}\,. \tag{2.90}$$

The index j covers the set of long-range beam-beam encounters and s_j is the encounter position along the orbit. Equations 2.89–2.90 neglect coupling terms of the matrix in Eq. 2.37. Depending on the phase advance ϕ_u, the separation d_u and the value of $d^2 = d_x^2 + d_y^2$, certain amplification or cancellation of the kicks in the two planes takes place. If the bunch spacing is large compared to the IR length as in RHIC, kicks in a single IR cannot cancel out because only a single beam-beam interaction occurs in the region of the common beam pipe. If the number of bunches is large and multiple kicks during the passage through the IR take place, the kicks cancel out much better. The cancellation is better in the separation plane than in the crossing plane. This is because of the rapid phase advance at the IP and the switch of the sign of the separation in the crossing plane.

[8] The beams are separated in the *separation plane* to avoid unwanted head-on collisions during the energy ramp.

In the following, two parameters are defined to quantify the cancellation between multiple beam-beam kicks. The *cancellation efficiency* of an IR is defined as

$$\mathcal{C}_{\mathrm{IR},u} = 1 - \left| \sum_{j\in\mathrm{enc.}} f_u(s_j) \right| / \sum_{j\in\mathrm{enc.}} |f_u(s_j)| = 1 - |\delta_u| / \sum_{j\in\mathrm{enc.}} |f_u(s_j)| \ . \tag{2.91}$$

This quantity is $\mathcal{C}_{\mathrm{IR},u} = 1$ if perfect cancellation is observed (no residual kick remains), and $\mathcal{C}_{\mathrm{IR},u} = 0$ holds if the kicks add up exactly in phase. An example is given in Fig. 2.11 for the 2016 p-Pb LHC optics at the CMS IR (IR5) with a total separation of $d_y = 4\,\mathrm{mm}$ in the vertical (separation) plane.

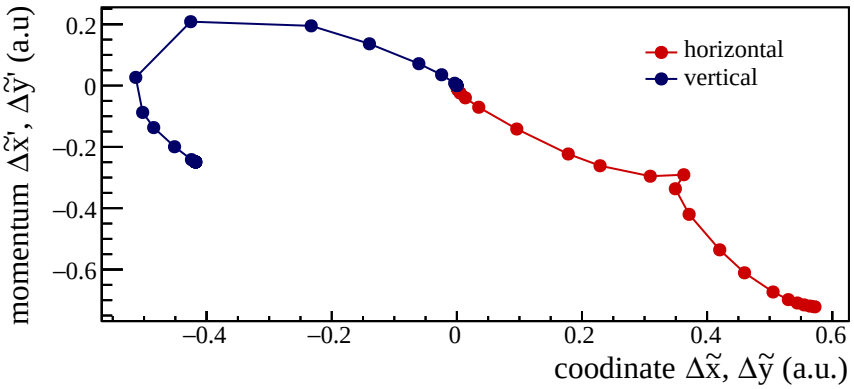

Figure 2.11: The kick contributions of 20 long-range beam-beam encounters (encounter locations are space by 50 ns) in the CMS IR (2016 injection optics) to the net kick remaining after the IR $|\delta_u|$. A variation of Eq. 2.91 is plotted for the horizontal (red) and vertical (blue) plane for each r of the sum $\left|\sum_{j=1}^{r} f_u(s_j)\right| / \sum_{j=1}^{20} |f_u(s_j)|$ with $r \in [1, 20]$. While the kicks build up in the horizontal (crossing) plane ($\mathcal{C}_{\mathrm{IR5},x} = 0.08$; 8 % of the total kick strength was compensated.), the kicks cancel out partially in the vertical (separation) plane ($\mathcal{C}_{\mathrm{IR5},x} = 0.51$; 51 % of the total kick strength was compensated).

Kicks can cancel out not only within but also between IRs. To quantify the cancellation between IRs, the concept of Eq. 2.91 is extended. If multiple IRs are present, the cancellation of the net kicks δ_u that remain after each IR is measured by the cancellation efficiency between the IRs

$$\mathcal{C}_{\mathrm{glo},u} = 1 - \left| \sum_{j\in\mathrm{IRs}} e^{-i\phi_u(s_{\mathrm{IR}j}^{\mathrm{start}})} \delta_{u,j} \right| / \sum_{j\in\mathrm{IRs}} |\delta_{u,j}| = 1 - |\delta_{t,u}| / \sum_{j\in\mathrm{IRs}} |\delta_{u,j}| \ . \tag{2.92}$$

Analogously to the dipole kicks, one may also define the cancellation of the tune shift created by the beam-beam encounters. Appropriate definitions comparable to Eqs. 2.91–2.92 are omitted. In the LHC, one may roughly assume the beam-beam tune shifts between ATLAS and CMS cancel out while those of ALICE and LHCb cancel out. Hence, good cancellation can be

assumed because of the regular switch of the separation and crossing plane among IRs. In the case of RHIC, no cancellation is assumed as the separation plane is always vertical, i.e., each IR contributes more or less equally to the tune shift if the amplitudes of the separation are the same in each IR.

2.1.8 Overlap knock-out resonances

The longitudinal modulation of the encounter locations may lead to the excitation of so-called overlap knock-out (OKO) resonances [6, 7] if the frequency components of the modulation overlap with the transverse frequency spectrum of the beam. The OKO resonance condition is

$$pQ_x + qQ_y = n + mQ_v \tag{2.93}$$

with $m,\ n,\ p,\ q \in \mathbb{Z}$ and the resonance order $\mathcal{O} = |p| + |q|$. In this form, the well-known optical resonance condition $pQ_x + qQ_y = n$ is extended by sidebands spaced by integer multiples of

$$Q_v = \frac{C}{d_b} = k_\mathrm{b}\frac{v_1 + v_2}{v_1}\,. \tag{2.94}$$

The integer k_b is the bunch harmonic (uniform filling pattern assumed). The first order resonances $\mathcal{O} = |p| + |q| = 1$ may easily approach the betatron tune of the collider; however, this requires a large n. These resonances of $\mathcal{O} = 1$ (dipole resonances) are analysed in detail in the following.

Uniform filling pattern The function $h_u(t)$ represents the normalised dipole-like kicks due to the beam-beam force during a revolution in the accelerator

$$h_u(t) = k\ \sqrt{\beta}_u(s)\frac{d_u(s)}{d_x^2(s) + d_y^2(s)}\bigg|_{s=v_1 ct} \tag{2.95}$$

with $d_u(s)$ being the beam separation in either x or y at position s. For simplicity, the conversion from s to t was performed via $s = tv_1$ with v_1 being the velocity of the slower test beam ($v_1 < v_2$). The function $h_u(t)$ has a Fourier series of the form

$$h_u(t) = \sum_{n=-\infty}^{\infty} a_{u,n}\mathrm{e}^{in\omega_0 t} \tag{2.96}$$

resulting from the condition $h_u(t) = h_u(t + T_0)$. The coefficients $a_{u,n}$ depend on the IR layout and location along the linear phase advance. If there is only a single IR that is short compared to the machine circumference, an approximation of the function $h_u(t)$ with a square pulse can be performed, i.e., the coefficients behave roughly $|a_{u,n}| \propto |\sin(n\omega_f)/n|$ with $\omega_f = \pi L/C$ being determined by the quotient of common beam-pipe length L and circumference C. Assuming

the test bunch in the slower beam is experiencing the kicks of an uniform filling pattern of the counter-rotating beam, the encounters take place in time intervals of $T_b = d_b/v_1$, resulting in the angular frequency $\omega_b = 2\pi/T_b = \omega_0 Q_v$. The Dirac comb representing this behaviour is

$$b(t) = \frac{1}{T_b} \sum_{m=-\infty}^{\infty} \mathrm{e}^{im\omega_b t} \,. \tag{2.97}$$

The time-dependent dipole kicks are given by the product

$$\Theta_u(t) = h_u(t)b(t) = \frac{1}{T_b} \sum_{n,m=-\infty}^{\infty} a_{u,n} \mathrm{e}^{i(n\omega_0 + m\omega_b)t} \,. \tag{2.98}$$

The Fourier transform $\mathcal{F}$ of the acquired function is simply

$$\mathcal{F}[\Theta_u(t)](\omega) = \frac{a_{u,n}}{T_b} \delta(\omega - n\omega_0 - m\omega_b) \tag{2.99}$$

leading to resonances at

$$Q_u = n + mQ_v \,. \tag{2.100}$$

The last simplification, however, assumes a constant phase advance along the machine $1/\beta_u(s) = \mathrm{const}$. The resonance condition in Eq. 2.100 naturally coincides with the $\mathcal{O} = 1$ condition of Eq. 2.93. If $h(t)$ is roughly square-pulse shaped, the resonance strength decreases approximately with $|a_{u,n}| \propto 1/|n|$; however, this behaviour is not necessarily monotone. The behaviour of a_n with increasing n depends on factors like the positioning of the IRs along the circumference, the phase advance within the IRs and the signs and smoothness of the separations. Although a large integer tune gives rise to higher orders of $|n|$, the value of Q_v in Eq. 2.100 is the most crucial parameter. Rewriting Q_v in terms of an integer and fractional part results in

$$Q_v = k_\mathrm{b} \frac{v_1 + v_2}{v_1} = 2k_\mathrm{b} + k_\mathrm{b}\varepsilon_v \qquad \text{with} \qquad \varepsilon_v = \frac{v_2 - v_1}{v_1} = \frac{1}{T_m} \approx \frac{c^2}{2p_\mathrm{p}^2} \left(\frac{m_1^2}{Z_1^2} - \frac{m_2^2}{Z_2^2} \right) \tag{2.101}$$

and $2k_\mathrm{b} \in \mathbb{Z}$. The fractional part $k_\mathrm{b}\varepsilon_v$ determines how quickly a fractional betatron tune of $Q_u = 0.27$–0.31 (typical for the LHC and RHIC) is approached in terms of n.

Non-uniform filling patterns A feature that was not considered yet is the effect of a potential non-uniform filling pattern as is usually the case in RHIC and the LHC. In the following, a bunch harmonic of k_b is assumed, but bunch slots may be empty or, more generally, the bunch intensity may fluctuate among the bunch slots. Empty slots are usually present in a heavy-ion collider like the LHC and RHIC as a result of the rise time of the injection kickers (gaps

between batches) or the extraction kicker (abort gap at end of bunch train). If the filling pattern is non-uniform, the Fourier coefficients b_m are unequal to $1/T_b$, i.e., Eq. 2.97 modifies to

$$b(t) = \sum_{m=-\infty}^{\infty} b_m \mathrm{e}^{im\omega_b/k_\mathrm{b}t} \qquad (b_m = b_{m+k_\mathrm{b}}) \tag{2.102}$$

with $\omega_b/k_\mathrm{b} = \omega_0 Q_v/k_\mathrm{b}$. Figure 2.12 shows example filling patterns with their corresponding Fourier coefficients. Non-uniform filling patterns cause all Fourier coefficients to be non-zero. The first order OKO resonance condition is then written as

$$Q_u = n + \frac{m}{k_\mathrm{b}} Q_v \tag{2.103}$$

which means in the case of a non-uniform filling pattern, the frequency spectrum is denser, i.e., more frequencies are being excited. The resulting frequency spectrum now displays an additional dependence on the Fourier coefficients b_m of the bunch train

$$\mathcal{F}[\Theta_u(t)](\omega) = a_{u,n} b_m \delta\left(\omega - n\omega_0 - \frac{m}{k_\mathrm{b}}\omega_b\right) . \tag{2.104}$$

The total amplitude $a_{u,n}b_m$ therefore depends on n and m. While $|a_{u,n}|$ is mostly decreasing the larger $|n|$ becomes, the coefficients b_m are periodic $b_{m+k_\mathrm{b}} = b_m$.

For small revolution-frequency differences between the beams like in the LHC, unevenness along the filling pattern causes an excitation that is very dense in tune space. When the revolution frequencies differ by a larger margin like in RHIC, these resonances appear as distinct and well separated lines in the frequency spectrum of the first order OKO resonances as is shown later on. At a given energy E_b, resonance lines appear at certain tunes. These tunes may either be strongly or weakly excited and a potential change of the nominal working point may lead to some level of mitigation, i.e., the tune footprint is positioned in a way it does not intersect strong resonance lines; however, this form of mitigation may only work for a singular energy as the resonant tunes move and an energy change of only fractions of a $1\,\mathrm{GeV}$ may cause a strong dipole OKO resonance to shift to the footprint centre. Hence, an adjustment of the nominal tune is inefficient and therefore not considered as a reliable mitigation technique.

OKO resonance condition in the presence of a tune oscillation In the presence of a tune oscillation from the synchrotron motion (see Sec. 2.1.6.2), the general OKO resonance condition (non-uniform filling pattern) reads

$$pQ_x + qQ_y = n + \frac{m}{k_\mathrm{b}} Q_v + rQ_s \qquad \text{with} \qquad p,\, q,\, n,\, m,\, r \in \mathbb{Z} . \tag{2.105}$$

The amplitude of the frequency component at $\omega_u(n,m,r) = \omega_0\left(n + \frac{m}{k_\mathrm{b}}Q_v + rQ_s\right)$ of the dipole OKO resonance scales roughly like (cf. Eq. 2.87)

$$|\mathcal{F}[\Theta_u(t)](\omega(n,m,r))| \propto \left|\frac{b_m}{n} J_r\left(\frac{\xi_u \delta_p}{Q_s}\right)\right| . \tag{2.106}$$

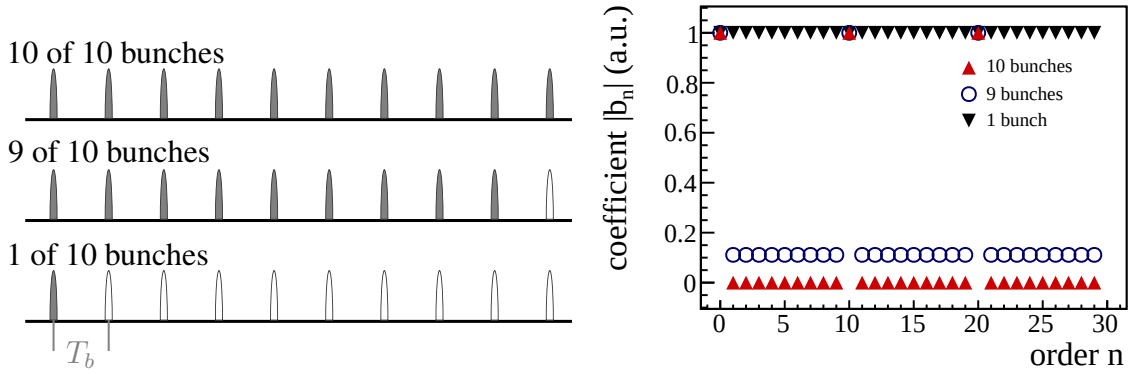

Figure 2.12: Left: Sketch of three different bunch patterns. Two filling patterns are uniform with ten out of ten bunches and one out of ten bunches, respectively. One filling pattern is non-uniform with nine bunches (hole at the end of bunch train as required for abort gap). Right: Absolute values of the Fourier coefficients b_n (normalised to maximum) at the frequencies $\omega(n) = n\omega_b/k_\mathrm{b} = n\omega_b/10$. A bunch pattern with a single bunch (black triangles) generates coefficients of every order n. The filling pattern with ten bunches (red triangles) is only non-zero at $n = 10r$ with $r \in \mathbb{Z}$. The filling pattern with nine bunches (blue circles) has non-zero coefficients for every n; however, it also has the largest coefficients at $n = 10r$ with $r \in \mathbb{Z}$. Unevenness along the filling pattern therefore excites all frequencies.

An easy way to estimate the n that is required for a dipole OKO resonance to approach the transverse betatron tune spread is to neglect the integer part of the betatron tune Q_u to obtain the approximation

$$n \approx 2\frac{Q_u}{\varepsilon_v} \approx \frac{4Q_u p_\mathrm{p}^2}{c^2}\left(\frac{m_1^2}{Z_1^2} - \frac{m_2^2}{Z_2^2}\right)^{-1} . \tag{2.107}$$

This formula, however, assumes all harmonics being present like it results from having either a single bunch ($k_\mathrm{b} = 1$) or a non-uniform filling pattern (see Fig. 2.12) and $Q_u \in [0;\, 0.5)$. Furthermore, the integer part of Q_u is assumed to be small compared to the resulting n. With the simple calculations presented in this section, it is already possible to make comparisons between the different colliders. In the following section, basic calculations for the LHC, HL-LHC, FCC and RHIC are performed based on these findings.

2.2 Linear analysis for the LHC, HL-LHC and RHIC

In this section, the effects of moving beam-beam encounters are analysed. This analysis only considers the linear model of the accelerator, and it therefore uses the linearised long-range beam-beam force. The analysis covers p-Pb operation in the LHC and the LHC upgrade HL-LHC, whereas Au-D operation is analysed for RHIC. Initially, a few calculations are also

demonstrated for p-Pb operation in the FCC; however, these calculations show quickly that a potential FCC will not face any issues caused by moving encounter points and a detailed analysis is therefore omitted. Table 2.1 lists the parameters which are assumed for the different ion colliders. RHIC has successfully collided multiple different asymmetric beam configurations in the past. This analysis is restricted to Au-D collisions since these beam types were present during the first attempt to accelerate beams with unequal revolution frequencies in 2002/2003. Other beam systems like Al-p have even larger charge-to-mass ratio differences between the beams; however, if deterioration of the beams is found in Au-D configuration, the likelihood of similar effects in Al-p configuration is presumably high. The linear analysis in this chapter is performed only at injection energy of the respective collider since the effects of moving beam-beam encounters are expected to be strongest at the lowest beam energy.

2.2.1 IR layout and ring symmetry

In the following, the IR layout and the ring symmetry of the (HL-)LHC and RHIC is discussed. Table 2.2 gives the optics settings at injection energy.

2.2.1.1 LHC 2016 Pb-p optics

The LHC is designed for large bunch numbers and the collisions in the IPs therefore take place with crossing angles to avoid parasitic head-on collisions. The IR design is roughly the same in all four IRs; however, the crossing and separation planes change to suppress tune shifts from long-range beam-beam encounters (see Eq. 2.54). Figure 2.13 presents the optical functions and the kick functions $h_u(s)$ (see Eq. 2.96) of a single IR of the LHC. The LHC IRs have a different length with the ATLAS/CMS IR having a crotch-to-crotch distance (see Fig. 1.7) of $L = 286\,\mathrm{m}$ and the ALICE/LHCb IR having a length of $L = 225\,\mathrm{m}$. This results in up to 16 (ALICE/LHCb) and 19 (ATLAS/CMS) long-range beam-beam encounters per IR with a bunch spacing of $100\,\mathrm{ns}$ (equivalent to a $50\,\mathrm{ns}$ encounter spacing in the IRs). Figure 2.14 shows the amplitudes of the Fourier coefficients $|a_{u,n}|$ of the kick functions $h_u(s)/k$. The envelopes of the coefficients $|a_{u,n}|$ are roughly given by $|a_{u,n}| \propto 1/|n|$. The ALICE and LHCb experiments have orbit bumps very close to the IPs. The spectrometer magnets of the detectors generate these bumps. The orbit bumps are present throughout the whole LHC cycle at a constant strength. Hence, the crossing angles in the two IPs are functions of the beam energy E_b. The bumps are in different planes since the crossing is in the vertical plane in ALICE and in the horizontal plane in LHCb. Besides that, the magnitudes are different. The internal crossing angle generated by the ALICE spectrometer is

$$\frac{\theta}{2} = 490\,\mu\mathrm{rad}\frac{7Z\,\mathrm{GeV}}{E_b} \tag{2.108}$$

Table 2.1: List of the most important optics parameters for the (HL-)LHC, RHIC and the FCC at injection energy. The LHC parameters are those of the 2016 p-Pb run. For RHIC, the Au-D parameters comparable to the parameters during the Au-D commissioning in 2002/2003. Also, the table lists the 2015 Al-p parameters of RHIC.

parameter		LHC, HL–LHC	RHIC		FCC
		(Pb, p)	(Au, D)	(Al, p)	(Pb, p)
Injection energy E_0	Z GeV	450	24.4	24.1	3300
Circumference C	m	26658.88	3833.85	3833.85	97749.39
Revolution frequency f_0	kHz	(11245.3, 11245.3)	(77842, 77964)	(77950, 78136)	(3066.95, 3066.95)
Relativistic Lorentz factor γ	1	(191, 480)	(10.52, 13.00)	(12.62, 25.38)	(1397, 3517)
Normalised horiz. emittance ϵ_{nx}	μm	(2.0, 1.0)	(2.2, 2.2)	(3.0, 2.5)	(2.0, 1.0)
Normalised vert. emittance ϵ_{ny}	μm	(1.5, 1.0)	(2.2, 2.2)	(3.0, 2.5)	(1.5, 1.0)
Horizontal tune Q_x	1	64.28, 62.27	28.277	(28.234, 29.695)	109.28
Vertical tune Q_y	1	59.31, 60.295	29.287	(29.228, 30.692)	107.31
Horiz. & vert. chromaticity $\xi_{x,y}$	1	15	-5	$(-5, 2)$	15
Rel. momentum spread σ_p	1	3.9×10^{-4}	13×10^{-4}	12.5×10^{-4}	1×10^{-4}
Particles per bunch N	10^8	(2.1, 280)	(7, 1200)	(120, 1710)	(2.1, 280)
Beam-beam constant k	10^{-10}	(1.79, 1.10)	(141, 65.3)	(213, 189)	(0.244, 0.150)
Rev.-frequency difference Δf_0	Hz	0.130473	122.5	185.1	6.6×10^{-4}
Shift per turn d_t	m	0.15	3.01	4.55	0.01
Fractional OKO tune ε_v	1	1.16×10^{-5}	1.57×10^{-3}	2.37×10^{-3}	2.157×10^{-7}
Recurrence time $T_m = 1/\varepsilon_v$	turns	86189	636	421	4635156

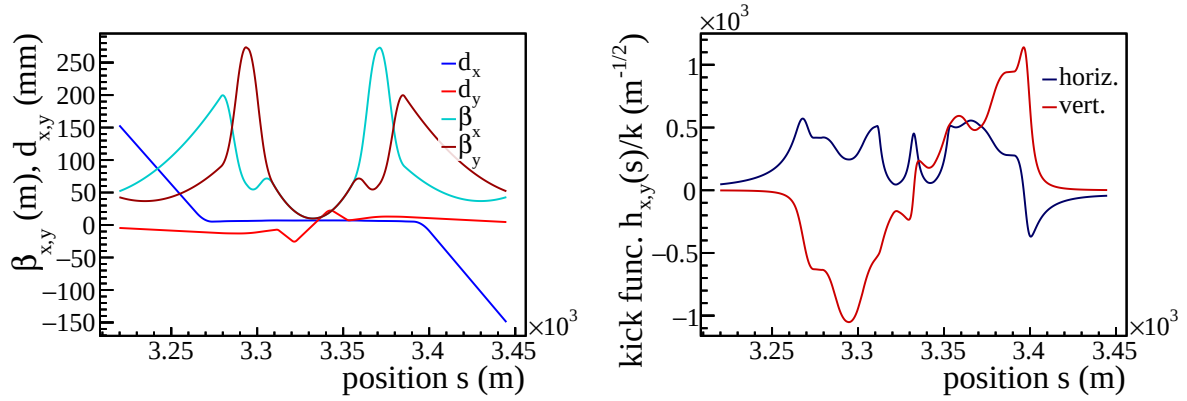

Figure 2.13: Left: Plot of the β-function in the horizontal (teal) and vertical (dark red) plane as well as the horizontal (blue) and vertical separation (red) in the ALICE IR at injection during the 2016 p-Pb run. Right: The horizontal (blue) and vertical (red) normalised kick function $h_u(s)/k$. The kick functions drop to zero on both sides of the plotted area (outside common beam pipe).

while the internal crossing angle in LHCb is

$$\frac{\theta}{2} = 944\,\mu\text{rad}\frac{7Z\,\text{GeV}}{E_b}\,. \tag{2.109}$$

The net crossing angles are the sum of the external crossing angles generated by corrector magnets on both sides of the IRs and the internal crossing angles as given in Eqs. 2.108–2.109. Table 2.2 also lists the external and net crossing angles at injection energy as used during the 2016 run.

For the HL-LHC, the layout and IR design deviates only slightly from that of the nominal LHC. The redesign of IR1 and IR5 reduces the length of the common beam pipe to $254\,\text{m}$. The IR2 and IR8 crotch-to-crotch distance remains unchanged. Overall, the most important change will be the number of bunches stored in the HL-LHC.

2.2.1.2 RHIC 2002/2003 Au-D optics

The RHIC optics is highly symmetrical in terms of the optical functions and separations in the IRs. Figure 2.15 shows this behaviour. The β-functions in both planes are virtually identical (same β^* in both planes), and the separation in y is more or less constant $d_y = \text{const.}$ in the boundaries of the common beam pipe (four-corrector vertical beam bump). Because of the constant separation, the kick function $h_y(s)$ in the vertical plane is to some degree square-pulse shaped (see right plot of Fig. 2.15), i.e., a sinc function gives the behaviour of the underlying Fourier coefficients $a_{y,n}$. In the horizontal plane, the function $h_x(s)$ has two peaks at a distance of roughly $13\,\text{m}$ on either side of the IP and is otherwise small. Since the optics at the experimental and utility IRs are the same at injection energy, $h_u(s)$ is highly three-fold rotation

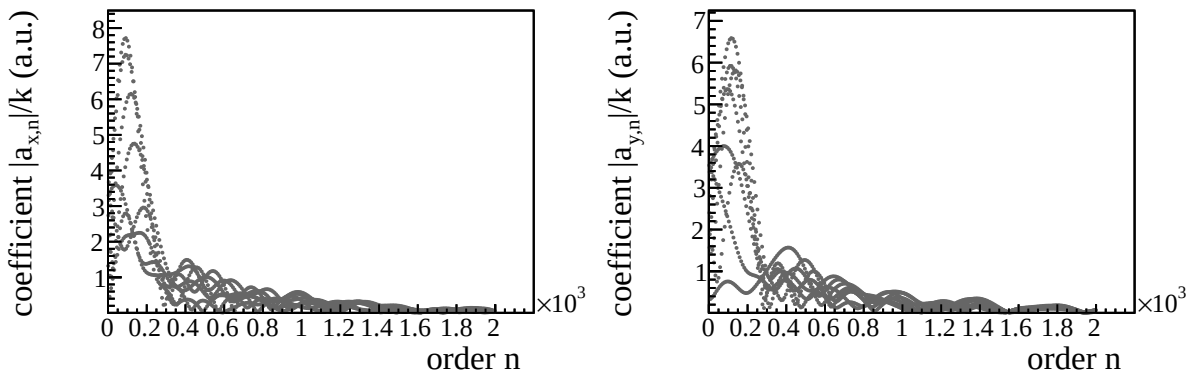

Figure 2.14: The absolute values $|a_{u,n}|/k$ of the functions $h_u(t)$ in the LHC at injection energy for the horizontal (left) and vertical (right) plane as a function of the order n. The DC components $|a_{u,0}|/k$ are not displayed. Because of the asymmetric IR positioning, the coefficients do not behave predictably but decay approximately like $|a_{u,n}| \propto 1/|n|$.

symmetric in RHIC since the separation is always in the vertical plane and of the same magnitude in each IR. Only the sign of the separation alternates between the IRs. The kick functions are therefore periodic $h_u(s) \approx h_u(s \pm C/3)$. The Fourier coefficients behave like a sinc function with two out of three consecutive coefficients having a much smaller absolute value than the third coefficient. If the symmetry between the IRs is broken by applying an asymmetric separation scheme like during the Al-p test in 2015 (see Tab. 2.2), two out of three consecutive coefficients are no longer close to zero.

2.2.2 Dipole OKO resonance strength

As already mentioned, the most important OKO order is that generated by the dipole kicks of the long-range encounters, i.e., $Q_u = n + mQ_v/k$. At large separations ($\sigma_u \ll d$), the derivatives of the beam-beam kick with respect to the transverse coordinates are negligible compared to the dipole component. Hence, a potential tune modulation resulting from the long-range beam-beam encounters is neglected and only the dipole kicks are considered in a first step. The magnitude of the positional shift of the beam-beam encounters d_t during the energy ramp varies significantly between the LHC, RHIC and the FCC as is shown in Fig. 2.3. While the shift in the LHC at injection energy is only $d_t = 15\,\mathrm{cm}$ per turn, the shift is much larger in RHIC with $d_t = 3.0\,\mathrm{m}$ and $d_t = 4.6\,\mathrm{m}$ in Au-D and Al-p operation, respectively. The shift of $d_t = 1\,\mathrm{cm}$ in the FCC at the injection energy of $E_b = 3.3Z\,\mathrm{TeV}$ is even smaller than that of the LHC. Because of the larger d_t, the recurrence time $T_m = 1/\varepsilon_v$, is much shorter for RHIC with $T_m = 636$ in Au-D configuration and $T_m = 421$ in Al-p configuration compared to the LHC with $T_m = 8.6 \times 10^4$ and the FCC with $T_m = 4.6 \times 10^6$ in p-Pb configuration. Table 2.1

Table 2.2: The table gives the optics parameters at the IRs of the LHC, HL-LHC and RHIC. In case of the LHC, it lists the 2016 p-Pb injection parameters. IR1 and IR5 feature slightly different IP-to-beam-pipe-crotch distances $L/2$ (see Fig. 1.7) than in the HL-LHC. Since ALICE and LHCb have spectrometers which influence the beams at the IPs, the external and net crossing angles are both given for ALICE and LHCb (external / internal). The signs of the crossing angles and separations refer to the Beam 1 coordinate frame. Values for the HL-LHC are given in grey if values differ from those of the nominal LHC. The separation scheme that was used during the Al-p test in RHIC in 2015 is also given in grey; however, this separation scheme is not analysed later on. The maximal number of encounters in the IRs is given for a $100\,\mathrm{ns}$ bunch spacing in the LHC, a $50\,\mathrm{ns}$ bunch spacing in the HL-LHC and for 110 bunches in RHIC.

IR	Cros. / sep. plane	Tot. separation d (mm)	IP-to-crotch distance $L/2$ (m)	β-function β^* (m)	Half crossing angle $\theta/2$ (μrad)	Max. encounters
			LHC (HL-LHC) p-Pb			
IR1	vert. / horiz.	-4	142.75 (127.13)	11	-170 (-295)	19 (31)
IR2	vert. / horiz.	$+7$	112.58	10	170 / -919	16 (28)
IR5	horiz. / vert.	$+4$	142.75 (127.13)	11	170 (295)	19 (31)
IR8	horiz. / vert.	-7	112.58	10	-170 / -2270	16 (28)
			RHIC Au-D (Al-p)			
IR6	horiz. / vert.	-10 ($+15$)	31.4	10	0	2
IR8	horiz. / vert.	$+10$ (-15)	31.4	10	0	2
IR10	horiz. / vert.	-10 ($+19$)	31.4	10	0	2
IR12	horiz. / vert.	$+10$ ($+19$)	31.4	10	0	2
IR2	horiz. / vert.	-10 ($+19$)	31.4	10	0	2
IR4	horiz. / vert.	$+10$ ($+19$)	31.4	10	0	2

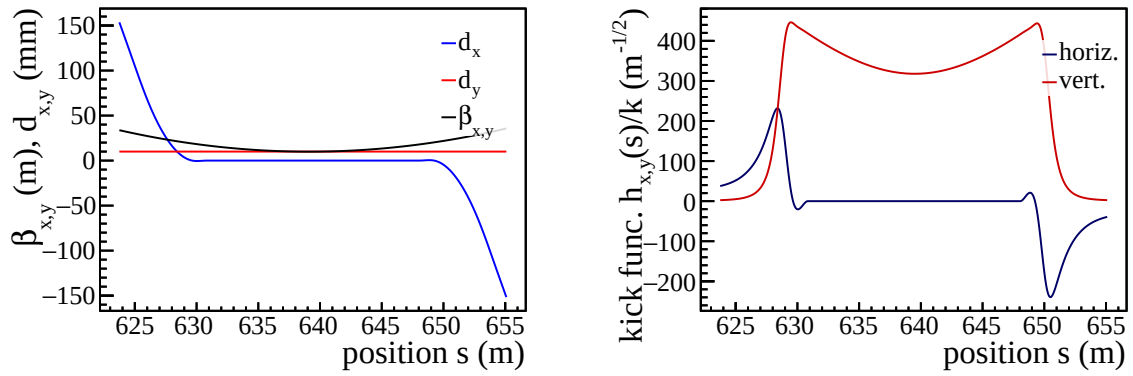

Figure 2.15: Left: Plots of the β-function in the horizontal and vertical plane (black) as well as the horizontal (blue) and vertical separation (red) of IR8 of RHIC at injection during the 2002/2003 Au-D run. Right: The horizontal (blue) and vertical (red) normalised kick function $h_u(s)/k$. The kick functions drop to zero on both sides of the plotted area (outside common beam pipe).

gives the different values of T_m and ε_v. The lowest order of the integer n of the dipole OKO resonances that approach the transverse betatron tunes of the different colliders is calculated in the following. This calculation is based on Eq. 2.107 and the parameters in Tab. 2.1. A non-uniform filling pattern or a one-bunch filling pattern is assumed ($k_\mathrm{b} = 1$), i.e., all b_m in Eq. 2.102 are non-zero.

(HL-)LHC Since the HL-LHC and the nominal LHC are operated at the same beam energy at injection and the circumference remains unchanged, the considerations that follow are valid for the nominal LHC and HL-LHC. The fractional tunes are in the range $Q_u = 0.28$–0.31. Hence, one expects the lowest order resonance to be close to $|n| \approx 4.8 \times 10^4$ with $\varepsilon_v = 1.16 \times 10^{-5}$. A larger integer tune pushes $|n|$ only by a small amount towards larger numbers. The actual fractional part ε_v is much more crucial. The Fourier coefficients $a_{u,n}$ are expected to be very close to $|a_{u,n}| \approx 0$ for such large n. Figure 2.18 presents plots of $1/|n|$ for the LHC at injection energy for the horizontal and vertical betatron tunes. These plots give insight via $1/|n| \propto |a_{u,n}|$ into the magnitude of the Fourier coefficients $a_{u,n}$ that lead to excitation. The excitation in the transverse tune space is broad, i.e., all tunes are getting excited by roughly the same amount and no distinct resonance lines are visible. Compared to RHIC (next paragraph), $1/|n|$ is much smaller in the LHC. Although the HL-LHC has slightly different betatron tunes compared to the nominal LHC, the plots in Fig. 2.18 are virtually the same for the HL-LHC and LHC. There are notable differences in terms of the order of n.

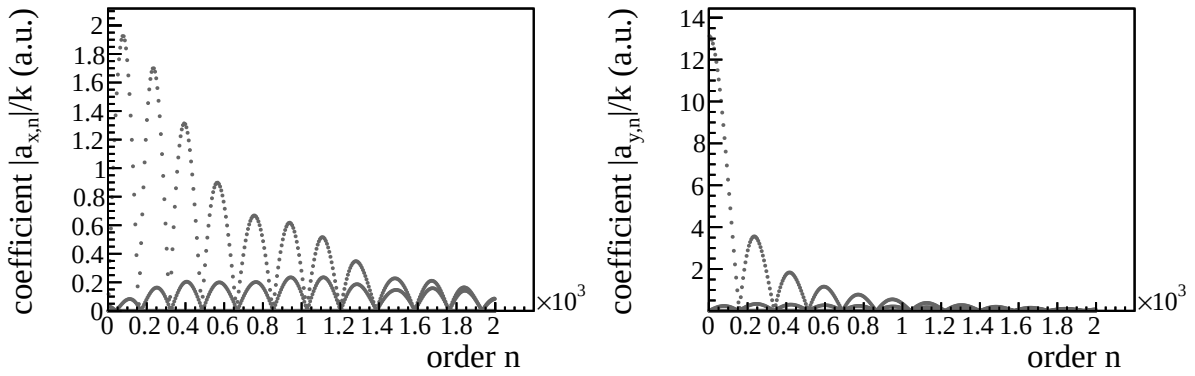

Figure 2.16: The absolute values $|a_{u,n}|/k$ of the functions $h_u(t)$ in RHIC at injection energy for the horizontal (left) and vertical (right) plane in the 2002/2003 Au-D configuration. The DC components $|a_{u,0}|/k$ are not displayed. Because of the high degree of symmetry, every third coefficient is much larger than the previous two. The coefficients behave clearly like the absolute value of a sinc function in the vertical plane in particular.

RHIC The fractional part ε_v is significantly larger than for the LHC, resulting from the much lower injection energy and consequently larder d_t. This means that the fractional betatron tunes are approached by dipole OKO resonances with smaller $|n|$. The lowest $|n|$ of any dipole OKO resonance close to the betatron tunes is at $|n| \approx 350$ in Au-D configuration. Figure 2.18 shows the order of magnitude of $|n|$ that is two orders smaller compared to the LHC. In contrast to the (HL-)LHC, excitation occurs at rather distinct tunes. The distances in tune space between these resonances is too small to accommodate the full tune footprint in a single gap.

During Al-p operation, an even smaller $|n| \approx 230$ is expected due to the larger shift d_t of the beam-beam encounters. Considering the smaller circumference and a larger beam-beam constant k than in the LHC, the emittance growth can easily be multiple orders of magnitudes faster compared to the LHC.

FCC The injection energy is so large that the fractional part of the OKO tune is only $\varepsilon_v = 2.2 \times 10^{-7}$. In combination with very large integer parts of the tunes compared to the other colliders, the required $|n| \approx 2.7 \times 10^6$ to reach the nominal betatron tune is very large. In fact, it is roughly 4 orders of magnitude larger than that of RHIC in Au-D operation. The large integer parts of the tunes also push the order of $|n|$ to even larger numbers. The excitation is again rather broad and dense in frequency space and $1/|n|$ is a factor 0.02 smaller than in the (HL-)LHC. Since the beam-beam constant k is a factor 7 and the revolution frequency is a factor 3 smaller than that of the LHC, it is not necessary to analyse potential emittance growth in the FCC. The emittance growth is already small in the LHC as will be shown later on, and the FCC growth rate should be at least 3 orders of magnitudes smaller than that of the LHC.

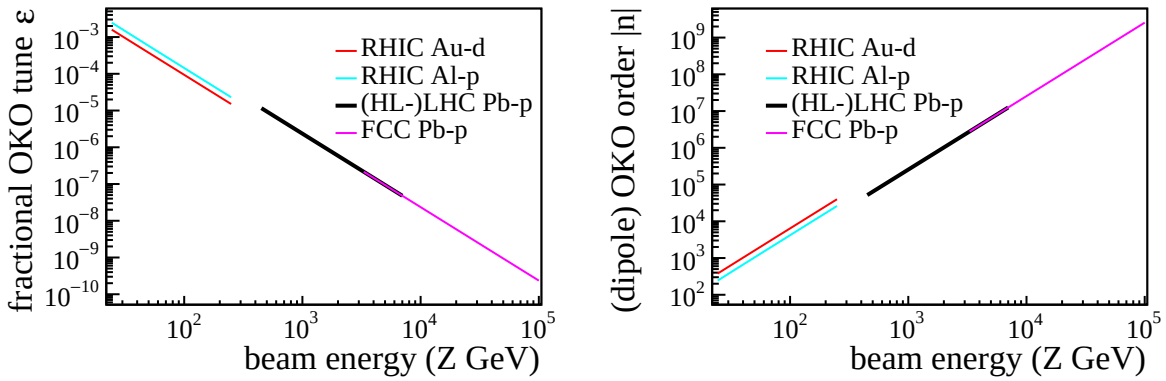

Figure 2.17: Left: Fractional OKO tune ε_v as a function of the beam energy E_b. Since p-Pb operation is assumed for the (HL-)LHC and FCC, both curves overlap. Right: Estimated order $|n|$ that is required for dipole OKO resonances to reach the fractional betatron tunes of $Q_u = 0.3$ in the respective collider (integer parts neglected).

From now on, the FCC is neglected in further calculations and simulations since the effects of moving long-range beam-beam encounters are fully negligible in this future machine.

2.2.3 Linear matrix model

The previous sections introduced a linear matrix formalism for the beam-beam effect, which is used in the following to analyse the effects of moving long-range beam-beam encounters at injection energy in the LHC, HL-LHC and RHIC. Linearising the beam-beam force restricts all findings to dipole and quadrupole effects. This approximation suffices as a first step since the dynamic aperture at injection energy is large and the separation between the beams should be large enough to ignore the higher-order derivatives of the beam-beam force.

The most important feature of the moving encounter points is that the transfer matrices describing the beam dynamics are not constant and change every turn. By assuming strictly linear motion and therefore no detuning in the IRs, the transfer through an IR can be summarised in a single transfer matrix

$$\mathbf{M}_{\mathrm{IR}} = \prod_{r \in \mathrm{enc.}} \mathbf{M}_{\mathrm{b}}(s_r)\mathbf{M}(s_{r-1}, s_r)\,. \tag{2.110}$$

The position $s_0 = s_{\mathrm{IR}}^{\mathrm{start}}$ is the start of the IR (start of the common beam pipe). An additional rotation matrix covering the linear transfer between the last beam-beam encounter and the beam-pipe crotch at $s_{\mathrm{IR}}^{\mathrm{end}}$ (end of the common beam pipe) is applied if the last beam-beam encounter does not take place at $s_{\mathrm{IR}}^{\mathrm{end}}$. This way, $\mathbf{M}_{\mathrm{IR}}$ always covers the same length in the accelerator (section of the common beam pipe). Neglecting detuning in the IRs is a fair assumption since the number of non-linear elements is small in these regions (only sextupoles and no octupoles

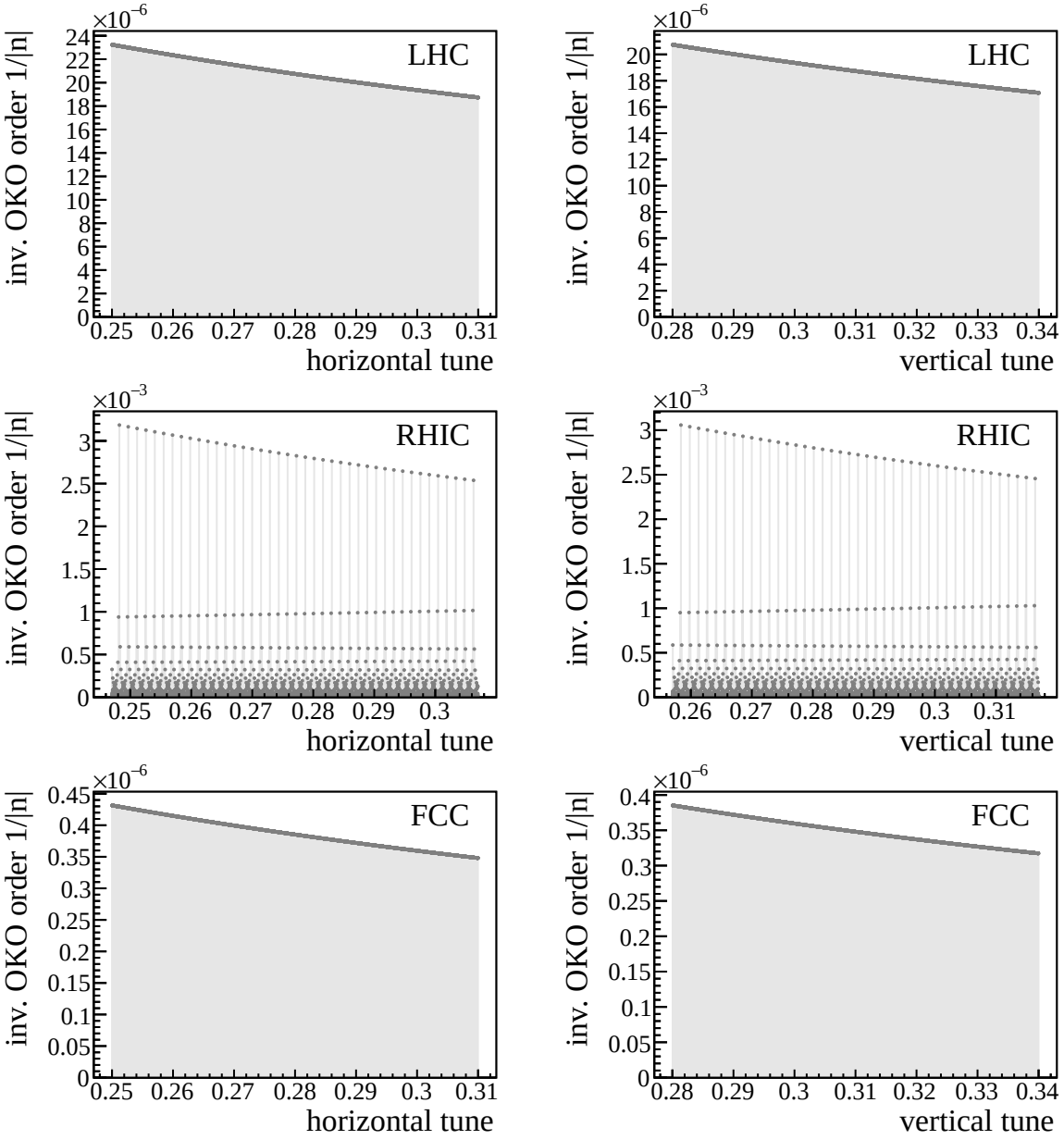

Figure 2.18: Top: The values of $1/|n|$ are shown for the horizontal (left) and vertical (right) tunes of the LHC at injection energy in p-Pb operation. The integer parts of the tunes are not plotted. Centre: The analogous plots for RHIC at injection in Au-D operation. The values are two orders of magnitude larger than in the LHC. Bottom: In the case of the FCC in p-Pb operation, $1/|n|$ is roughly a factor 0.02 smaller than in the LHC because of the much larger FCC circumference and injection energy.

in the IRs) and the IRs are short compared to the full collider length (only a small fraction of the chromatic tune shift is generated in the IRs).

Because the beam-beam encounter positions shift by d_t every turn, the matrices $\mathbf{M}_{\mathrm{IR}}$ and consequently the one-turn transfer matrix

$$\mathbf{T} = \prod_{i \in \mathrm{IPs}} \mathbf{M}(s_{\mathrm{IR}i}^{\mathrm{end}}, s_{\mathrm{IR}i+1}^{\mathrm{start}}) \mathbf{M}_{\mathrm{IR}i} \tag{2.111}$$

have to be re-evaluated every turn. The counter-rotating beam is rigid and not influenced by the long-range interactions.

The fifth column of the IR matrices $\mathbf{M}_{\mathrm{IR}}$ treats the coherent net kick that remains after the particles have passed through the IR; however, it has entries in the momenta x' and y' as well as in the positions x and y because of the phase advance between the beam-beam kicks and the end of the common beam pipe. The coordinates $\Delta\tilde{u}$ and $\Delta\tilde{u}'$ are obtained by normalising the fifth column of the IR matrix $\mathbf{M}_{\mathrm{IR},i5} = (\Delta x, \Delta x', \Delta y, \Delta y', 1)^{\mathrm{T}}$ with the matrix $\mathbf{V}(\mathbf{s})$ (see Eqs. 2.9–2.11) at the position the common beam pipe of the IR ends $s_{\mathrm{IR}}^{\mathrm{end}}$, i.e.,

$$\mathbf{V}(s_{\mathrm{IR}}^{\mathrm{end}}) \mathbf{M}_{\mathrm{IR},i5} = (\Delta\tilde{x}, \Delta\tilde{x}', \Delta\tilde{y}, \Delta\tilde{y}', 1)^{\mathrm{T}} \,. \tag{2.112}$$

By assuming no tune deviation within the IRs, the frequency spectrum of the dipole-like kicks is obtained by adding the DFTs of the net kicks $\delta_u = \Delta\tilde{u} - i\Delta\tilde{u}'$ of the different IR matrices.[9] In order to obtain the DFTs of δ_x and δ_y, the IR matrices are calculated for numerous turns N to obtain vectors of δ_x and δ_y for each IR. The DFT for the coherent net kick δ_u of a single IR i in plane u is $\mathcal{F}[\delta_{u,i}]$. The DFTs of multiple IRs are then combined using Eq. 2.66

$$\mathcal{F}[\delta_u](n) = \sum_{i \in \mathrm{IPs}} \mathcal{F}[\delta_{u,i}](n) \exp\left(-2\pi \frac{n}{N} \frac{\phi_u(s_{\mathrm{IP}i})}{\mu_u}\right) \tag{2.113}$$

with s_{IP} being the position of the respective IP. The DFT $\mathcal{F}[\delta_u](n)$ carries information at the tunes $Q_u = n/N$. Equation 2.113 is an approximation since $\mathcal{F}[\delta_u](n)$ indicates the resonances for particles with non-nominal tunes under the assumption the tune difference ΔQ_u to the nominal tune is equally distributed along the linear phase advance, i.e., $\mathrm{d}\Delta Q_u(s)/\mathrm{d}s \propto 1/\beta_u(s)$. Since the calculation of the IR matrices did not include detuning between the beam-beam encounters within the IRs, the DFT $\mathcal{F}[\delta_u]$ in Eq. 2.113 is only valid if no detuning takes place in the IRs but only in the arcs connecting them.

The fifth column of the one-turn matrix $\mathbf{T}$ contains information regarding the closed-orbit shift. By performing the analogous normalisation as presented in Eq. 2.112, the normalised residual kick $(\Delta\tilde{x}_t, \Delta\tilde{x}_t', \Delta\tilde{y}_t, \Delta\tilde{y}_t', 1)^{\mathrm{T}}$ after one turn is obtained. The average kick in one plane

[9] Choosing the imaginary part of δ_u as the negative momentum causes the phase space angle to rotate in mathematical positive direction.

$\langle \delta_{t,u} \rangle = \langle \Delta\tilde{u}_t - i\Delta\tilde{u}'_t \rangle$ is calculated for many turns. From that, the magnitude of the closed-orbit shift $|\langle \delta_{t,u} \rangle|/(2\sin(\pi Q_u))$ in $\tilde{u}$–$\tilde{u}'$ space is obtained at the position the one-turn matrix is calculated. The shift may also be in the momentum and not only in the coordinate; however, at one point during the passage through the arcs, the momentum component is fully rotated into the coordinate. The scalar factor is roughly $1/(2\sin(\pi Q_u)) \approx 0.6$ for the typical tunes of the considered accelerators.

The cancellation efficiencies $\mathcal{C}_{\mathrm{IR}}$ can be easily calculated from the IR matrices since $|\delta_u|$ is in very good approximation equal to $|\sum_i f_u(s_i)|$ (cf. Eq. 2.91) if one assumes the tune shift due to the beam-beam encounters to be small. The cancellation efficiencies $\mathcal{C}_{\mathrm{IR},u} = |\delta_u| \,/\, \sum_i |f_u(s_i)|$ are quickly calculated if the values of $\sum_i |f_u(s_i)|$ are stored during the calculation of the IR matrices. The global cancellation efficiency $\mathcal{C}_{\mathrm{glo},u}$ is calculated by just comparing the coherent kick component of the one-turn matrix $\delta_{t,u}$ that remains after one turn with the values of the coherent kicks δ_u that remains after the passage through the IRs, i.e., the expression for the global cancellation efficiency reads $\mathcal{C}_{\mathrm{glo},u} = |\delta_{t,u}| \,/\, \sum_i |\delta_{u,i}|$ (cf. Eq. 2.92).

By calculating the one-turn transfer matrix $\mathbf{T}$ (see Eq. 2.111) every turn, the tune of the nominal particle also has to be determined turn-by-turn. The beam-beam force introduces coupling into the one-turn map $\mathbf{T}$ (see Eqs. 2.54 & 2.21). By ignoring coupling and associating the eigenmodes with the nominal unperturbed modes, the tunes are obtained from the arguments of the eigenvalues of $\mathbf{T}$ (see Eq. 2.20).

In the following analysis of the LHC and RHIC, the weak beam is assumed to rotate clockwise. A respective analysis with the weak beam in the counterclockwise rotating beam is omitted. The phase advance between the IRs is roughly the same in both beam directions; therefore, the DFT of the dipole kicks only changes in terms of the complex phases but remains unchanged in magnitude. Also, the tune shift caused by the long-range encounters remains the same. Based on these considerations, the expected emittance growth should be independent of the beam directions. At the start of each simulation, the test bunch of the weak beam collides with the bunch in the first slot of the counter-rotating strong beam at the IP of either ATLAS (LHC) or STAR (RHIC) independently of whether the first slot is filled. The starting position of each turn (the position the one-turn matrix is calculated at) is set to the position the common beam pipe of the ATLAS/STAR IR starts, i.e., it is shifted upstream by the distance between the beam-pipe crotch and the IP $L/2$ (see Tab. 2.2) of the ATLAS/STAR IP.

2.2.4 Results for various filling schemes at injection in RHIC and LHC

The dynamics of a nominal particle, i.e., no transverse excursion and no energy deviation, is calculated using the linear matrix formalism previously introduced. It is important to consider different filling patterns for the counter-rotating beam, since the filling pattern influences the frequency spectrum of the dipole kicks and the induced tune modulation. Three different filling

patterns with different numbers of bunches are considered for each collider. As previously mentioned, the analysis is restricted to the Pb beam in p-Pb operation in the LHC and to the Au beam in Au-D operation in RHIC at injection energy.

The goal of this section is to investigate the way the moving beam-beam encounters influence the linear model of the accelerator. Important quantities are the DFTs $\mathcal{F}[\delta_x]$ and $\mathcal{F}[\delta_y]$ of the dipole kicks obtained via combining the DFTs of the coherent kick components of the IR matrices (see Eq. 2.113). The amplitudes of the DFTs define the linear growth rate of the emittances in the absence of amplitude detuning. The residual (net) kicks remaining after a full turn in the accelerator $\delta_{t,u}$ are also important during the analysis. The time structure of $\delta_{t,u}$ is already partially included in the DFT $\mathcal{F}[\delta_u]$ of the dipole kicks. Nevertheless, a constant component $|\langle\delta_{t,u}\rangle|$ causes a closed-orbit shift. The magnitude of the orbit shift in terms of the beam size is approximated by $0.6|\langle\delta_{t,u}\rangle|/\sqrt{\epsilon_u}$.[10] Although, the analysis of the DFTs indicates the excitation of the betatron tunes in a linear model, the standard deviation (SD) $\sigma(\delta_{t,u}) = \sqrt{\sigma(\Delta\tilde{u}_t)^2 + \sigma(\Delta\tilde{u}_t')^2}$ as a measure of fluctuations also indicates whether fast or slow emittance growth is expected for a given filling scheme in the context of Eq. 2.67. In a real machine, the parameter $\sigma(\delta_{t,u})$ is potentially a better indicator for emittance growth than considering the amplitudes of the DFTs of the dipole kicks at certain tunes since the tunes of the particles are not constant due to detuning.[11] Emittance growth can be inferred from the amplitudes of the DFTs $\mathcal{F}[\delta_x]$ and $\mathcal{F}[\delta_y]$ only in the presence of constant tunes; however, lattice non-linearities and the longitudinal motion in combination with the chromaticity cause oscillating and amplitude-dependent tune variations.

Another key quantity is the tune oscillation caused by the moving beam-beam encounters. Equation 2.72 describes an exponential emittance growth if the focusing strength varies in an accelerator. A constant tune offset $\langle\Delta Q_u\rangle$ is simply mitigated by correcting the tunes using dedicated quadrupoles. Strong tune oscillations, however, are indicators of exponential emittance growth. The interest is therefore on the standard deviation of the tune oscillation $\sigma(\Delta Q_u)$ as it measures (to some degree) the fluctuation of the tune.

Important parameters for each collider are also the cancellation efficiencies. The cancellation efficiencies in the IRs $\mathcal{C}_{\mathrm{IR}}$ and of the whole accelerator $\mathcal{C}_{\mathrm{glo}}$ may change drastically between filling patterns and give an idea of whether the IR and accelerator design enhance or suppress the influence of moving encounters on the beams.

[10] This is the maximum orbit shift in the arc as its implies the momentum (the imaginary part of δ_u) has fully rotated into the coordinate. Also, no beam-size increase due to dispersion is considered.

[11] The particle tunes are non-constant for long durations of, e.g., 10^6 turns and the correlation time of the kicks is reduced by detuning.

2.2.4.1 RHIC – Au-D operation

In this section, the focus is on Au-D operation in RHIC with the parameters of the 2002/2003 run. Section 2.2.1 presents the optics parameters, and Tab. 2.2 lists the IR settings. By considering the beam-beam constants k, it becomes obvious that the kick of the deuteron beam on the Au beam is much stronger than the other way around. Hence, this analysis considers the counter-rotating deuteron beam as strong and rigid. The weak Au beam is the Blue Beam (clockwise) and the strong deuteron beam is the Yellow Beam (counterclockwise).

Multiple filling patterns are analysed to investigate different time structures of the long-range beam-beam encounters. The first filling pattern that is considered in the following contains a single deuteron bunch (R1) that interacts with the test Au bunch.[12] Figure 2.19 displays the three filling patterns. A common filling pattern during the 2002/2003 Au-D run was a deuteron bunch train of 55 bunches (R2). RHIC's harmonic number is 360; therefore, a filling pattern with 55 bunches features a bunch at every sixth bucket and five bunches are missing at the end of the bunch train to accommodate the extraction-kicker rise time (pink vertical line in Fig. 2.19). The third filling pattern comprises 110 deuteron bunches (R3). This filling pattern had the maximum deuteron intensity during the Au-D run in 2002/2003. The intensity of the deuteron bunches is in all cases at $N_b = 1.2 \times 10^{11}$ ions per bunch.

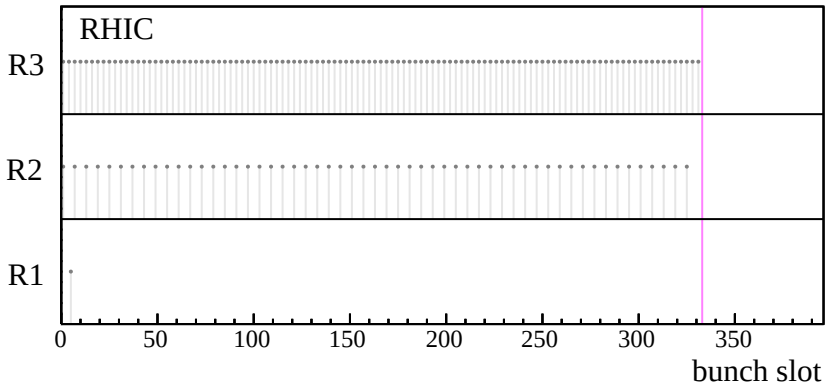

Figure 2.19: The three filling patterns that are analysed for RHIC in Au-D collisions. The filling pattern R1 features a single bunch while the patterns R2 and R3 feature 55 bunches and 110 bunches, respectively. The magenta line indicates the start of the abort gap that is required to accommodate the extraction-kicker rise time.

Intermediate beam intensity – 55 deuteron bunches To avoid the sequential and partially repetitive description of the results for three different filling patterns per collider, the results for a single filling pattern of each collider are explained in detail and the key results of the other

[12] The three analysed filling patterns are labelled R1, R2 and R3 for simplicity.

Table 2.3: The top part of the table specifies the parameters of the counter-rotating deuteron beam of the filling patterns R1, R2 and R3 for RHIC in Au-D operation. The bottom part shows key results obtained from the linear calculations.

Filling pattern		R1	R2	R3
Number of bunches n_b	1	1	55	110
Bunch spacing d_b	ns	12788	213.1	106.6
Bunch harmonic k_b	1	1	60	120
Deuteron bunch intensity N_b	10^{11}	1.2	1.2	1.2
Constant horizontal tune shift $\langle \Delta Q_x \rangle$	10^{-3}	-9.9×10^{-3}	-0.55	-1.1
Constant vertical tune shift $\langle \Delta Q_y \rangle$	10^{-3}	1.0×10^{-2}	0.55	1.1
SD horizontal tune shift $\sigma(Q_x)$	10^{-4}	5.4×10^{-2}	4.1	6.0
SD vertical tune shift $\sigma(Q_y)$	10^{-4}	5.5×10^{-2}	4.1	6.0
Constant horizontal kick $\lvert\langle \delta_{t,x} \rangle\rvert$	$10^{-7}\sqrt{\mathrm{m}}$	6.1×10^{-2}	3.4	6.7
Constant vertical kick $\lvert\langle \delta_{t,y} \rangle\rvert$	$10^{-5}\sqrt{\mathrm{m}}$	1.2×10^{-2}	0.65	1.3
SD horizontal kick $\sigma(\delta_{t,x})$	$10^{-6}\sqrt{\mathrm{m}}$	0.41	1.3	1.8
SD vertical kick $\sigma(\delta_{t,y})$	$10^{-6}\sqrt{\mathrm{m}}$	0.85	5.7	6.5

two filling patterns are then compared to that filling pattern. The Tables 2.3, 2.4 & 2.5 compare the key outcomes of all filling patterns for each collider.

The linear results for the R2 filling pattern are elaborated on in the following. The filling pattern R2 contains 55 deuteron bunches, i.e., the pattern comprises five empty bunch slots at the end of the bunch train. This filling pattern is of intermediate beam intensity compared to the R1 and R3 filling patterns. Table 2.3 lists the key parameters for this filling pattern and the R1 and R3 filling patterns, and the plots of the results for R1 and R3 are given in Appendix B.1 in Figs. B.1 & B.2 for completeness. The top left and right plots of Fig. 2.20 show the absolute DFT amplitudes $|\mathcal{F}[\delta_u]|$ in the horizontal and vertical plane for the relevant betatron tune range. The two DFTs are obtained on the basis of 10^6 turns. Besides the data of $\mathcal{F}[\delta_u]$, the plots also contain the $1/|n|$ approximation of the kick spectrum (see Eq. 2.106 with $b_m = \mathrm{const.}$ and $\delta_p = 0$) and the Gaussian-shaped tune distribution generated by the chromaticity ξ_u in combination with the relative momentum spread σ_p of the particles (red). The maximum amplitude of the DFTs is $3.5 \times 10^{-8}\sqrt{\mathrm{m}}$ in the horizontal plane and $1.6 \times 10^{-8}\sqrt{\mathrm{m}}$ in the vertical plane. The resonance lines of the actual spectrum do not coincide perfectly with the $1/|n|$ approximation; however, this cannot be expected since $b_m = \mathrm{const.}$ is assumed and the coefficients $|a_{u,n}|$ of the Fourier series of $h_u(t)$ (see Eqs. 2.95 & 2.96) at low n do not drop monotonically with $1/|n|$. In addition, a $1/|n|$ approximation also requires $1/\beta_u(s) = \mathrm{const.}$ which does not hold in reality. An important observation is that two peaks at $Q_x = 0.272$ and $Q_x = 0.277$ have the lowest order in n and coincide with the predicted peaks of the $1/|n|$

plot; however, the $1/|n|$ plot predicts two additional peaks of virtually equal order in between these two tunes. These additional resonances do not occur because of the three-fold rotation symmetry of RHIC (see Sec. 2.2.1). This behaviour is therefore well understood and complies with the theory.

The tune oscillation in the centre left plot of Fig. 2.20 shows the evolution of the tune shift over $2T_m = 1272$ turns. The peak-to-peak tune oscillation has a range of 1.2×10^{-3} in both planes. The dynamics of the tune shift generated by long-range encounters (see Eq. 2.54) causes $\Delta Q_x \approx -\Delta Q_y$. The tune oscillation repeats itself with a period of roughly 212 turns. This number of turns corresponds to $T_m/3$ and mirrors the fact the encounter positions have shifted from one IR to the next. The effect of the abort gap is clearly visible as it masks the effect of two opposing IRs every 212 turns and the vertical and horizontal tunes oscillate with a smaller peak-to-peak range for a short time span (see also bottom left plot of Fig. 2.20). The tune oscillations follow distributions with $\sigma(\Delta Q_x) = \sigma(\Delta Q_x) = 4.1 \times 10^{-4}$ and constant tune shifts of $\langle \Delta Q_y \rangle = -\langle \Delta Q_x \rangle = 10^{-2}$.

The amplitude of the residual kick remaining after one turn $\delta_{t,u}$ (see Fig. 2.20 centre right) is at maximum $|\delta_{t,y}| = 14 \times 10^{-6} \sqrt{\mathrm{m}}$ vertically. In the horizontal plane, it is slightly smaller with approximately $|\delta_{t,x}| = 4 \times 10^{-6} \sqrt{\mathrm{m}}$. The constant components $|\langle \delta_{t,u} \rangle|$ are at $|\langle \delta_{t,x} \rangle| = 3.4 \times 10^{-7} \sqrt{\mathrm{m}}$ and $|\langle \delta_{t,y} \rangle| = 6.5 \times 10^{-6} \sqrt{\mathrm{m}}$, respectively. The constant components generate closed-orbit shifts smaller than $0.1\,\%$ of the Au beam size. The standard deviations of the coherent kicks are $\sigma(\delta_{t,x}) = 1.3 \times 10^{-6} \sqrt{\mathrm{m}}$ and $\sigma(\delta_{t,y}) = 5.7 \times 10^{-6} \sqrt{\mathrm{m}}$. Based on these numbers, the linear growth of the emittance in the vertical plane is expected to be significantly larger than in the horizontal plane; however, the exponential growth due to tune oscillations are presumably the same in both planes.

The bottom left plot of Fig. 2.20 gives the number of encounters in each IR. The plot is highly periodic with the previously mentioned period length of 212 turns; however, the abort gap distorts this periodicity slightly. Only single beam-beam encounters take place in the IRs because of the large bunch spacing. Hence, no cancellation of kicks can occur in the IRs $\mathcal{C}_{\mathrm{IR}i,u} = 0$ (bottom right plot of Fig. 2.20). The cancellation between the IRs, however, is still in the $\mathcal{C}_{\mathrm{glo},y} = 40\,\%$–$60\,\%$ range in the vertical plane and is strongly oscillating in the horizontal plane, i.e., the median and mean value in the horizontal plane are close to $\mathcal{C}_{\mathrm{glo},x} = 40\,\%$ (bottom right plot of Fig. 2.20; first two boxes from the right).

Comparison to the minimum-intensity (R1) and maximum-intensity (R3) filling patterns
Table 2.3 lists the key parameters for the R1 and R3 filling patterns, and the plots of the results are given in Appendix B.1 in Figs. B.1 & B.2. The maximum DFT amplitude is not the largest for 110 bunches. Because of the dense bunch spacing (two encounters per IR are possible), the frequency spectrum shifts towards smaller tunes. The maximum amplitudes for the single-bunch filling pattern R1 are smaller than for the other two filling patterns. In a strictly linear

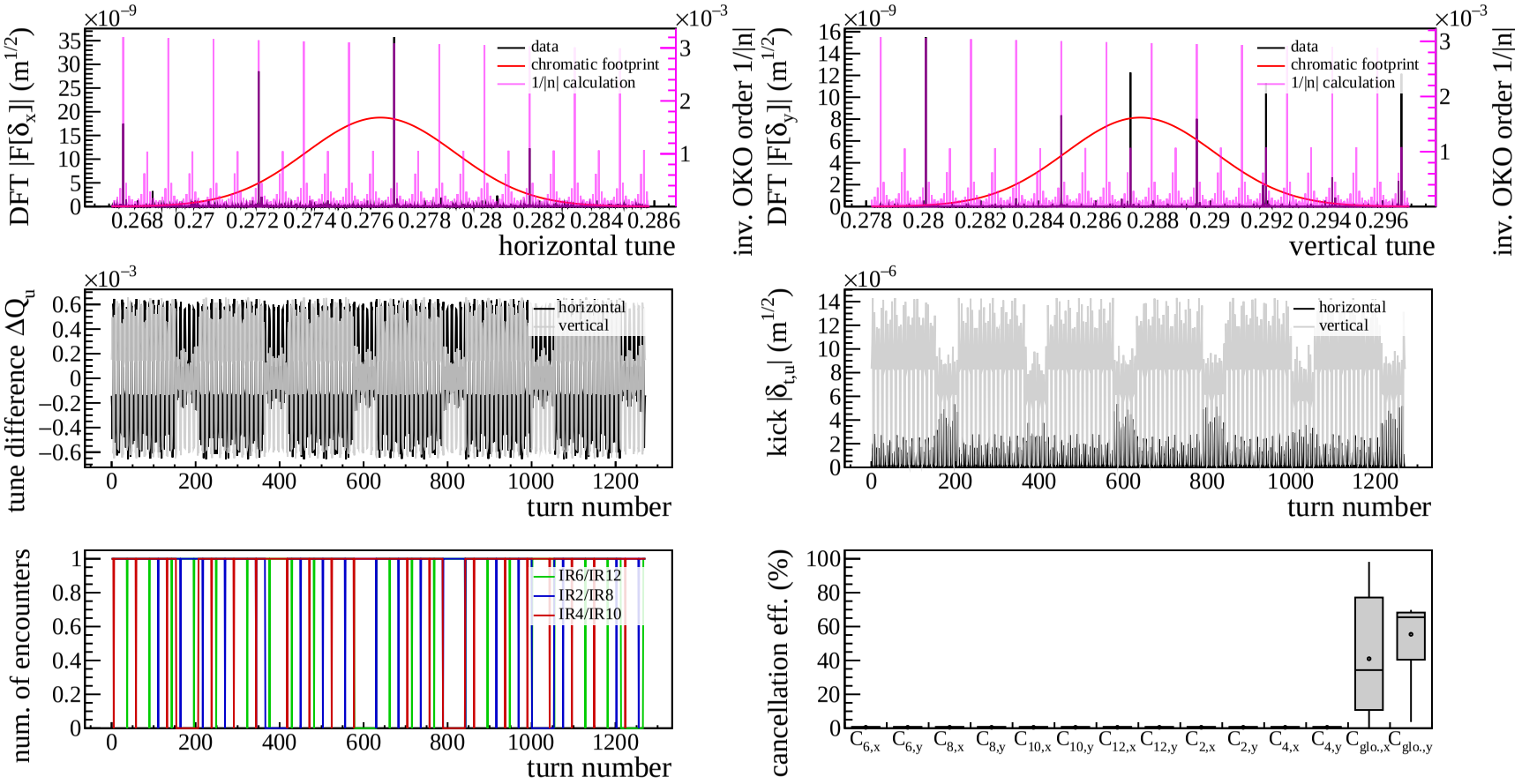

Figure 2.20: Top left: Plot of the absolute DFT amplitudes in the horizontal plane $|\mathcal{F}[\delta_x]|$ obtained from the IR matrices over 10^6 turns for RHIC with 55 deuteron bunches (R2). The magenta line indicates the $1/|n|$ approximation and the red line shows the chromatic tune footprint of the Au bunch. Top right: The absolute amplitudes of the DFT in the vertical plane $|\mathcal{F}[\delta_y]|$. Centre left: Plot of the tune shift ΔQ_u obtained from the one-turn matrix over the duration of $2T_m$ turns (constant tune offset subtracted). Centre right: Plot of the absolute kick strength $|\delta_{t,u}|$ in the vertical and horizontal plane obtained from the one-turn matrix. Bottom left: Number of beam-beam encounters in each IR. Bottom right: The cancellation efficiency of each IR in the horizontal $\mathcal{C}_{\mathrm{IR},x}$ and vertical plane $\mathcal{C}_{\mathrm{IR},y}$. The last two boxes show the global cancellation between the IRs $\mathcal{C}_{\mathrm{glo},u}$.

model and without tune modulation by the long-range beam-beam encounters, the horizontal growth rate would be the largest for R2 and the vertical growth rate would be the largest for R3 based on the maximum DFT amplitudes.

The constant tune shifts scale strictly with the number of bunches $\langle \Delta Q_u \rangle / n_b = \pm 0.01$ (negative in the horizontal plane and positive in the vertical plane). The standard deviations of the tune oscillation do not scale as linearly but increase by roughly $\sigma(\Delta Q_u)/n_b \approx 5.4 \times 10^{-4}$, i.e., the fastest emittance growth can be expected for 110 bunches (R3) and the smallest for one bunch (R1) based on the standard deviations of the tune oscillation.

The constant horizontal and vertical kicks remaining after one turn scale nearly linearly with $|\delta_{t,x}|/n_b = 6.1 \times 10^{-9}\,\sqrt{\mathrm{m}}$ in the horizontal and $|\delta_{t,y}|/n_b = 1.2 \times 10^{-7}\,\sqrt{\mathrm{m}}$ in the vertical plane. The values of $\sigma(\delta_{t,u})$ of the kicks do not follow a strict scaling with the number of bunches although $\sigma(\delta_{t,u})$ still increases monotonically with the number of bunches. While it is impossible to find cancellation in the IRs ($\mathcal{C}_{\mathrm{IR}i,u} = 0$) for a single bunch (R1) and 55 bunches (R2), the R3 filling pattern has a cancellation of roughly $\mathcal{C}_{\mathrm{IR}i,y} = 10\,\%$ in the vertical plane (crossing plane) in the IRs and no cancellation in the horizontal plane ($\mathcal{C}_{\mathrm{IR}i,x} = 0$). The vertical global cancellation efficiency between the IRs is larger than the horizontal one for all three filling patterns and varies in the $\mathcal{C}_{\mathrm{glo},y} = 40\,\%$–$60\,\%$ range. The horizontal global cancellation efficiency is strongly varying ($\mathcal{C}_{\mathrm{glo},x} = 10\,\%$ for R1, $\mathcal{C}_{\mathrm{glo},x} = 10\,\%$–$80\,\%$ for R2 and $\mathcal{C}_{\mathrm{glo},x} = 40\,\%$–$80\,\%$ for R3).

The emittance growth can be expected to increase with the number of counter-rotating deuteron bunches. Based on the values of $\sigma(\delta_u)$, one to two orders of magnitude faster growths for R3 compared to R1 is expected. In addition, the vertical emittance is expected to grow significantly faster than the horizontal emittance for all three filling patterns.

2.2.4.2 LHC – Pb-p operation

In the following, the Pb-p results for the nominal LHC are presented. The kick of the proton beam applied onto the Pb beam is slightly larger than in the other direction. Hence, the Pb beam is assumed to be the test beam while the proton beam is treated as rigid. Although the proton beam was stored more frequently in Beam 1 and the Pb beam in Beam 2 in the past p-Pb runs, the simulation is set up with the weak beam being in Beam 1. This configuration is not the most common configuration; however, the emittance evolution is expected to be the same in both configurations.

Three different filling patterns in terms of the number of bunches and bunch spacing are once again analysed. Figure 2.21 displays the three filing patterns. The filling pattern from the 2012 Pb-p pilot run comprising 15 proton bunches is used (L1) as the filling pattern with the lowest beam intensity. This filling pattern has a varying bunch spacing; therefore, no bunch harmonic k_b can easily be associated with L1. The maximum-intensity filling pattern from the

high-energy part of the 2016 p-Pb run with 684 proton bunches (19 SPS injections) and a bunch spacing of 100 ns is analysed as the second filling scheme (L2). To investigate the influence of the HL-LHC filling pattern on the LHC layout and optics (a potential 2023 p-Pb would be operated under these conditions), the nominal HL-LHC filling pattern is also considered with a bunch spacing of 50 ns and 1232 proton bunches (L3). In all considered scenarios, the proton bunch intensity is $N_b = 2.8 \times 10^{10}$ protons per bunch. Table 2.2 gives the optics settings in the IRs.

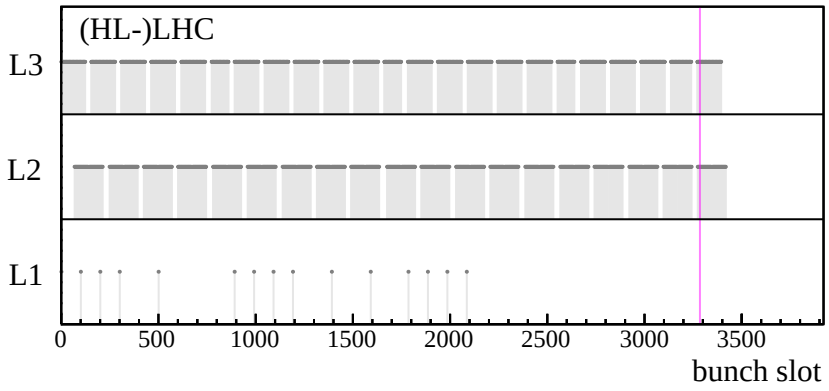

Figure 2.21: Filling patterns analysed for the LHC and HL-LHC. The magenta line indicates the abort-gap keeper, i.e., the last bunch slot the first bunch of the last SPS injection is still allowed to be injected in.

The 2016 main filling pattern – 684 proton bunches The L2 filling pattern is analysed in detail in the following. Here, the proton beam contains 684 proton bunches and features an abort gap with a length of roughly 3 μs. Table 2.4 presents the key results for the residual kicks and the tune oscillation. In good approximation, the bunch harmonic is $k_\mathrm{b} = 891$. The top left and top right plot of Fig. 2.22 show the DFT amplitudes $|\mathcal{F}[\delta_u]|$ that are calculated on the basis of 2×10^5 turns. The maximum DFT amplitude in the horizontal plane is $6.2 \times 10^{-10}\,\sqrt{\mathrm{m}}$ and in the vertical plane $5.4 \times 10^{-10}\,\sqrt{\mathrm{m}}$. These amplitudes are two orders of magnitudes smaller than in RHIC. The magenta $1/|n|$ approximation in the two top plots of Fig. 2.22 assumes $k_\mathrm{b} = 891$ (890 out of 891 consecutive Fourier coefficients b_m are zero). The strongest predicted resonant frequencies of the $1/|n|$ approximation coincide with the calculated frequency spectra. The frequency spectra are not reproduced in full detail since most coefficients b_m (see Eq. 2.106) are non-zero due to unevenness along the proton bunch train and the resulting excitation is rather constant in the vertical frequency space in particular.

The tune oscillation over $2T_m = 172\,378$ turns is presented in the centre left plot of Fig. 2.22. The bottom left plot of Fig. 2.22 shows that the abort gap shifts through the LHCb IR (no long-range beam-beam encounters taking place) at turn numbers close to 20 000. During that time,

Table 2.4: The top part of the table specifies the parameters of the counter-rotating deuteron beam of the filling patterns L1, L2 and L3 for the LHC in Pb-p operation. The bottom part shows the obtained key parameters.

Filling pattern		L1	L2	L3
Number of bunches n_b	1	15	684	1232
Bunch spacing d_b	ns	–	100	50
Bunch harmonic k_b	1	–	891	1782
Proton bunch intensity N_b	10^{10}	2.8	2.8	2.8
Constant horizontal tune shift $\langle \Delta Q_x \rangle$	10^{-6}	0.21	12	23
Constant vertical tune shift $\langle \Delta Q_y \rangle$	10^{-6}	-0.21	-12	-22
SD horizontal tune shift $\sigma(Q_x)$	10^{-5}	0.29	1.3	1.9
SD vertical tune shift $\sigma(Q_y)$	10^{-5}	0.29	1.3	2.0
Constant horizontal kick $\lvert\langle \delta_{t,x} \rangle\rvert$	$10^{-7}\sqrt{\mathrm{m}}$	0.24	9.3	17
Constant vertical kick $\lvert\langle \delta_{t,y} \rangle\rvert$	$10^{-7}\sqrt{\mathrm{m}}$	0.33	14	26
SD horizontal kick $\sigma(\delta_{t,x})$	$10^{-7}\sqrt{\mathrm{m}}$	0.81	5.0	7.9
SD vertical kick $\sigma(\delta_{t,y})$	$10^{-7}\sqrt{\mathrm{m}}$	0.82	5.6	9.9

the vertical tune increases while the horizontal tune drops by the same amount. This indicates that the LHCb IR was compensating the tune shift generated by the ALICE IR. LHCb or ALICE is not compensating the ATLAS and/or CMS tune shift since the tunes barely change at all when the abort gap covers the ATLAS and CMS IRs at turn numbers close to $85\,000$. When the ALICE IR is covered by the abort gap at turn numbers around $62\,000$, the horizontal tune increases while the vertical tune decreases. It can be concluded that ALICE and LHCb cancel each other's tune shift, and the same is valid for ATLAS and CMS. This proves that the concept of interchanging crossing and separation planes mitigates at least partially the effects on the tunes caused by long range beam-beam encounters. The tune oscillates in both planes with standard deviations of $\sigma(\Delta Q_x) = \sigma(\Delta Q_y) = 1.3 \times 10^{-5}$. This value is roughly an order of magnitude smaller than in RHIC.

The centre right plot of Fig. 2.22 shows the absolute (normalised) coherent kick remaining after each turn $|\delta_{t,u}|$. The kick in the horizontal plane increases the moment the LHCb IR is covered by the abort gap at turn numbers of roughly $20\,000$ and it drops when the ALICE IR is covered by the abort gap at turn numbers of approximately $62\,000$. ATLAS and CMS do not cancel each other's effects too well since the kicks in both planes drop significantly during the time span the ATLAS and CMS IRs do not have any long-range encounters at turn numbers near $85\,000$. The constant kick is $|\,\langle \delta_{t,x} \rangle\,| = 9.3 \times 10^{-7}\sqrt{\mathrm{m}}$ equivalent to $0.009\sigma_x$ in the horizontal plane. In the vertical plane, the constant kick is slightly larger with $|\,\langle \delta_y \rangle\,| = 14 \times 10^{-7}\sqrt{\mathrm{m}}$,

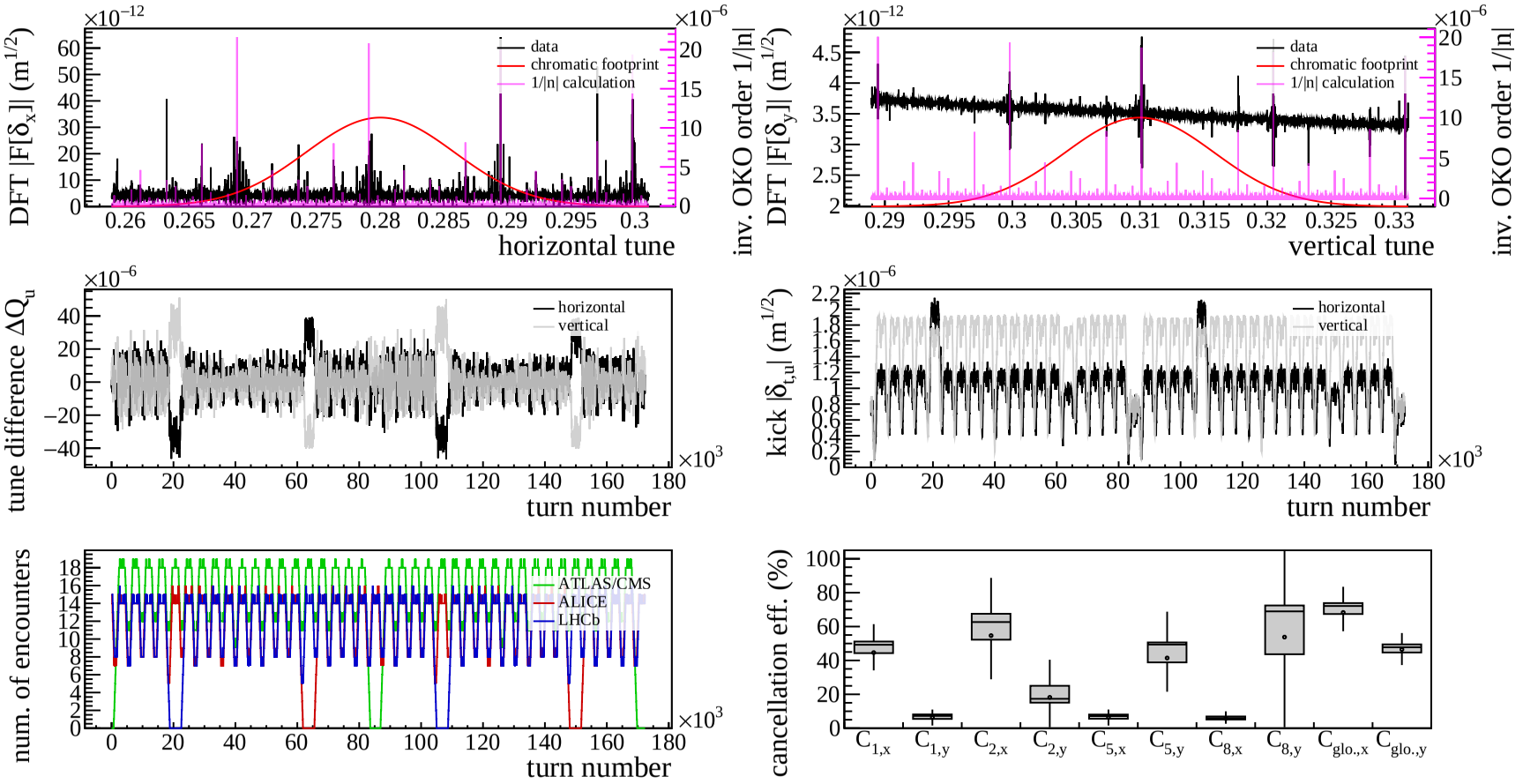

Figure 2.22: Top left: Plot of the absolute DFT amplitudes in the horizontal plane $|\mathcal{F}[\delta_x]|$ obtained from the IR matrices over 2×10^5 turns for the LHC for filling pattern L2 (2016 p-Pb run). The magenta line indicates the $1/|n|$ approximation and the red line shows the chromatic tune footprint of the Pb bunch. Top right: The absolute amplitudes of the DFT in the vertical plane $|\mathcal{F}[\delta_y]|$. Centre left: Plot of the tune shift ΔQ_u obtained from the one-turn matrix over the duration of $2T_m$ turns (constant tune offset subtracted). Centre right: Plot of the absolute kick strength $|\delta_{t,u}|$ in the vertical and horizontal plane obtained from the one-turn matrix. Bottom left: Number of beam-beam encounters in each IR. Bottom right: The cancellation efficiency of each IR in the horizontal $\mathcal{C}_{\mathrm{IR},x}$ and vertical plane $\mathcal{C}_{\mathrm{IR},y}$. The last two boxes show the global cancellation between the IRs $\mathcal{C}_{\mathrm{glo},u}$.

corresponding to $0.016\sigma_y$.[13] Hence, the closed orbit only shifts by values between 1–2 % of the beam size. The coherent kicks fluctuate with $\sigma(\delta_{t,x}) = 5.0 \times 10^{-7}\sqrt{\mathrm{m}}$ and $\sigma(\delta_{t,y}) = 5.6 \times 10^{-7}\sqrt{\mathrm{m}}$. Although the constant kicks $|\delta_{t,u}|$ are larger than the values in RHIC, the standard deviations $\sigma(\delta_{t,u})$ and the fluctuations are larger in RHIC than in the LHC. Since $|\delta_{t,u}|$ only shifts the closed orbit and fluctuations cause emittance growth, one can expect faster growth in RHIC; however, such a statement is based on the assumption of comparable auto-correlation functions of the kicks.

The bunch spacing is sufficiently dense that up to 19 (16) long-range beam-beam encounter may occur in the ATLAS and CMS (ALICE and LHCb) IRs. As expected, the cancellation in the IRs $\mathcal{C}_{\mathrm{IR}i,u}$ is large in the separation planes with $\mathcal{C}_{\mathrm{IR}i,u} = 40\,\%$–$60\,\%$. The global cancellation is very large in the horizontal plane with values around $\mathcal{C}_{\mathrm{glo},x} \approx 70\,\%$. In the vertical plane, it is slightly smaller with $\mathcal{C}_{\mathrm{glo},y} \approx 50\,\%$. This is also an explanation for smaller amplitudes of $|\delta_{t,x}|$ compared to $|\delta_{t,y}|$ in the centre right plot of Fig. 2.22. The cancellation is therefore much better in the LHC and less volatile than in RHIC. A bunch spacing that is small in comparison to the length of the common beam pipe in the IRs leads to a larger average kick but less fluctuations. Thus, smaller emittance growth is expected.

Comparison to the minimum-intensity (L1) and HL-LHC filling pattern (L3) Figures B.3 & B.4 in Appendix B.1 present the results for the other two filling patterns L1 and L3. Also, Tab. 2.4 lists the key findings and parameters.

The maximum amplitudes of $|\mathcal{F}[\delta_x]|$ and $|\mathcal{F}[\delta_x]|$ scale with the number of proton bunches n_b; however, the scaling is not linear in the small bunch-number regime (L1). The largest DFT amplitude is achieved for the HL-LHC filling pattern L3 with the horizontal plane facing more excitation than the vertical plane. The excitation is rather constant in tune space for the L1 filling pattern, i.e., no distinct resonance lines are visible. This is because of the poor periodicity of the filling pattern; therefore, all harmonics of ω_b/k_b are excited (see Eq. 2.102). As expected, the constant tune shifts $\langle \Delta Q_u \rangle$ increase with the number of bunches $\langle \Delta Q_u \rangle / n_b \approx 1.8 \times 10^{-8}$. For the filling pattern L3, smaller differences between the horizontal and vertical tune are visible because of betatron coupling introduced by the long-range encounters. The fluctuation of the tunes also increase with the number of bunches but not highly linearly. The standard deviations of the tune shifts are $\sigma(Q_x) \approx \sigma(Q_y) \approx 2 \times 10^{-5}$ for L3. This factor is 50 to 100 times smaller than in RHIC in the R2 or R3 configuration. If one assumes an exponential growth as suggested by Eq. 2.77, at least two orders of magnitude smaller growth rates are expected in the L3 setup than in the R3 case of RHIC. The constant kicks scale nicely with the number of bunches with $|\langle \delta_{t,x} \rangle|/n_b \approx 1.4 \times 10^{-9}$ and $|\langle \delta_{t,y} \rangle|/n_b \approx 2.1 \times 10^{-9}$. The standard deviations of the coherent kicks $\sigma(\delta_{t,u})$ increase with the number of bunches as well but not fully linearly.

[13] Elliptical beams are assumed (see Tab. 2.1).

The value is at $\sigma(\delta_{t,y}) \approx 10^{-6}\sqrt{\mathrm{m}}$ in the vertical plane for the pattern L3. This value is only 6.5 times smaller than for the high-intensity RHIC scenario R3. The kicks, however, are less volatile in the LHC compared to RHIC and the amplitudes $\mathcal{F}[\delta_{t,u}]$ of the kicks are two orders of magnitude smaller in the LHC.

2.2.4.3 HL-LHC – Pb-p operation

It is important to quantify the effects the IR redesign and optic changes have on the dynamics of moving long-range beam-beam encounters; however, the changes of the beam dynamics in the HL-LHC with respect to the nominal LHC are small. The considered filling patterns for the HL-LHC are the L2 and L3 patterns of the nominal LHC (see Fig. 2.21). The L2 pattern is analysed to compare the effect of the nominal 2016 pattern on the HL-LHC with the effect on the nominal LHC. The L3 pattern is analysed in two configurations L3a and L3b. The L3a configuration features the L3 filling pattern with the usual bunch intensity of $N_b = 2.8 \times 10^{10}$ protons per bunch. Since the simplest way to increase the luminosity is to inject higher proton-bunch intensities, the L3b filling pattern features the L3 filling pattern with nominal p-p bunch intensities of $N_b = 1.15 \times 10^{11}$ protons per bunch. Such intensities will most likely never be reached. Even if these proton intensities are manageable with respect to the Pb losses, the high proton intensities would drastically decrease the Pb beam lifetime, which is unfavourable for ALICE and LHCb. Nevertheless, it is important to identify a potential proton-intensity limit. Table 2.2 presents the optics parameters and IR crotch distances. The IR settings are chosen to match the parallel separations and the crossing angles of the 2016 p-Pb run.

The nominal HL-LHC filling pattern (L3a) The filling pattern that is analysed in detail in this section is the nominal HL-LHC filling pattern with a bunch spacing of $50\,\mathrm{ns}$ and 1232 bunches (L3a). The respective bunch harmonic is $k_\mathrm{b} = 1782$. Table 2.5 lists key parameters of the filling pattern and the results. The two top plots of Fig. 2.23 show the DFT amplitudes $|\mathcal{F}[\delta_{t,u}]|$. The peak amplitude that is reached in the horizontal plane is $|\mathcal{F}[\delta_{t,x}]| = 1.5 \times 10^{-10}\sqrt{\mathrm{m}}$. In the vertical plane, the peak amplitude is much smaller with $|\mathcal{F}[\delta_{t,y}]| = 8 \times 10^{-12}\sqrt{\mathrm{m}}$, and the excitation is rather constant in vertical tune space. These values are comparable to the values obtained for the L3 pattern in the nominal LHC.

The constant tune shifts are $\langle \Delta Q_x \rangle = 2.7 \times 10^{-5}$ and $\langle \Delta Q_y \rangle = -2.3 \times 10^{-5}$ in the respective planes. These values are equal to those of the nominal LHC in L3 configuration. The coupling, however, is slightly larger in the HL-LHC because the tunes behave slightly asymmetrically ($\Delta Q_x \neq -\Delta Q_y$). The standard deviations of the tunes are on average $\sigma(Q_u) \approx 1.9 \times 10^{-5}$. These values are virtually identical to the nominal LHC L3 case. The centre left plot of Fig. 2.23 confirms that the ALICE and LHCb IRs cancel each other's tune shift and the

Table 2.5: The top part of the table specifies the parameters of the counter-rotating proton beam of the filling patterns L2 and L3 for the HL-LHC in Pb-p operation. Two types of the L3 filling pattern are presented with the first version featuring proton intensities of $N_b = 2.8 \times 10^{10}$ protons per bunch (L2a) and the second version featuring $N_b = 1.15 \times 10^{11}$ protons per bunch (L3b).

Filling pattern		L2	L3a	L3b
Number of bunches n_b	1	684	1232	1232
Bunch spacing d_b	ns	100	50	50
Bunch harmonic k_b	1	891	1782	1782
Proton bunch intensity N_b	10^{10}	2.8	2.8	11.5
Constant horizontal tune shift $\langle \Delta Q_x \rangle$	10^{-5}	1.5	2.7	11
Constant vertical tune shift $\langle \Delta Q_y \rangle$	10^{-5}	-1.3	-2.3	-9.6
SD horizontal tune shift $\sigma(Q_x)$	10^{-5}	1.1	1.8	7.3
SD vertical tune shift $\sigma(Q_y)$	10^{-5}	1.2	1.9	7.7
Constant horizontal kick $\lvert\langle \delta_{t,x} \rangle\rvert$	$10^{-6}\sqrt{\mathrm{m}}$	1.9	3.4	14
Constant vertical kick $\lvert\langle \delta_{t,y} \rangle\rvert$	$10^{-6}\sqrt{\mathrm{m}}$	1.4	2.6	10
SD horizontal kick $\sigma(\delta_{t,x})$	$10^{-7}\sqrt{\mathrm{m}}$	6.0	11	44
SD vertical kick $\sigma(\delta_{t,y})$	$10^{-7}\sqrt{\mathrm{m}}$	5.0	8.9	36

same is true for ATLAS and CMS IRs. The turn numbers during which the abort gap is masking the respective IRs are same as for the nominal LHC (see Sec. 2.2.4.2).

The constant coherent kick component is $\lvert\langle \delta_{t,x} \rangle\rvert = 3.4 \times 10^{-6}\sqrt{\mathrm{m}}$ in the horizontal plane and it is $\lvert\langle \delta_{t,y} \rangle\rvert = 2.6 \times 10^{-6}\sqrt{\mathrm{m}}$ in the vertical plane. The orbit offset in units of the beam size is $0.01\sigma_u$ in both planes. The standard deviations are $\sigma(\delta_{t,x}) = 5 \times 10^{-7}$ and $\sigma(\delta_{t,x}) = 5.6 \times 10^{-7}$, respectively. These values are roughly equal to those of the LHC L3 case. The HL-LHC seems to have worse compensation of the kicks between the IRs since every time any IR is covered by the abort gap, the absolute value of the net kick drops. If the IRs were cancelling the effects of other IRs, the kicks would increase the moment long-range encounters are suppressed by the abort gap in one of the IRs.

With these large bunch numbers, the maximum number of long-range interaction per IR has increased to 31 (28) in ATLAS and CMS (ALICE and LHCb). The bottom left plot of Fig. 2.23 shows the corresponding data. The cancellation efficiency in the IRs $\mathcal{C}_{\mathrm{IR}i,u}$ is comparable to that of the nominal LHC; however, the global cancellation efficiency in the horizontal plane $\mathcal{C}_{\mathrm{glo},x} \approx 40\,\%$ has worsened substantially compared to $\mathcal{C}_{\mathrm{glo},x} \approx 70\,\%$ for the L2 filling pattern in the nominal LHC (see Fig. 2.22). This finding is in line with the observation regarding the net kicks: In the nominal LHC, the kicks increase in the horizontal plane when, e.g., ALICE

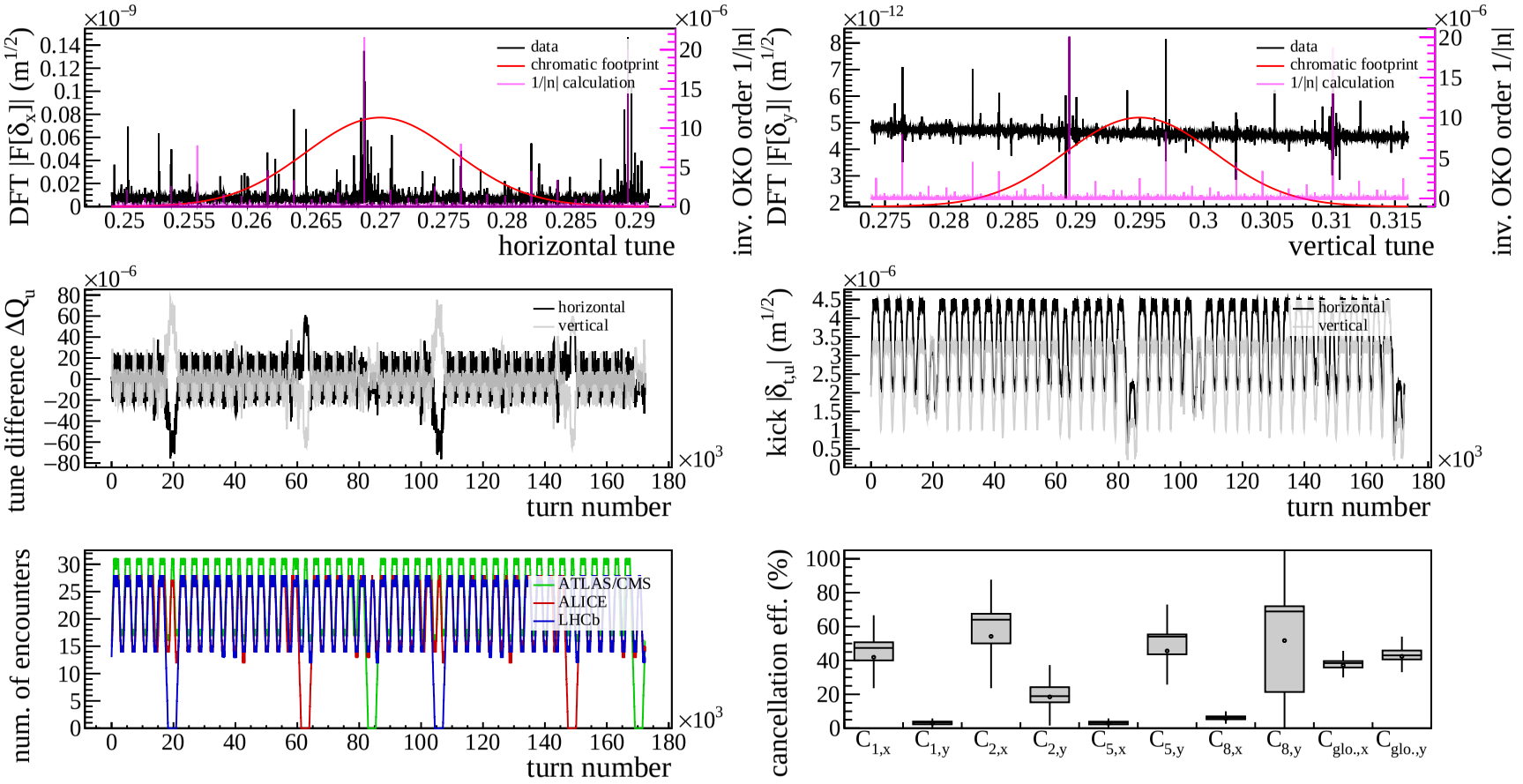

Figure 2.23: Top left: Plot of the absolute DFT amplitudes in the horizontal plane $|\mathcal{F}[\delta_x]|$ obtained from the IR matrices over 2×10^5 turns for the HL-LHC for filling pattern L3 with $N_p = 1.15 \times 10^{11}$. The magenta line indicates the $1/|n|$ approximation and the red line shows the chromatic tune footprint of the Pb bunch. Top right: The absolute amplitudes of the DFT in the vertical plane $|\mathcal{F}[\delta_y]|$. Centre left: Plot of the tune shift ΔQ_u obtained from the one-turn matrix over the duration of $2T_m$ turns (constant tune offset subtracted). Centre right: Plot of the absolute kick strength $|\delta_{t,u}|$ in the vertical and horizontal plane obtained from the one-turn matrix. Bottom left: Number of beam-beam encounters in each IR. Bottom right: The cancellation efficiency of each IR in the horizontal $\mathcal{C}_{\mathrm{IR},x}$ and vertical plane $\mathcal{C}_{\mathrm{IR},y}$. The last two boxes show the global cancellation between the IRs $\mathcal{C}_{\mathrm{glo},u}$.

is covered by the abort gap, whereas the kicks decrease in the HL-LHC since ALICE is not compensated by any other IR. Similar observations can be made for the other three IRs.

Comparison to the 2016 maximum-intensity filling pattern (L2) and the HL-LHC filling pattern with exaggerated proton bunch intensities (L3b) Figures B.5 & B.6 in Appendix B.1 present the results for the patterns L2 and L3b. In this high bunch-number regime, the parameters in Tab. 2.5 scale very linearly with the beam intensities. With L2 having roughly a factor $1/2$ less intensity and L3b having a factor 4 more intensity than the L3a proton beam, the effects on $\langle \Delta Q_u \rangle$, $\sigma(\Delta Q_u)$, $|\langle \delta_{t,u} \rangle|$ and $\sigma(\delta_{t,u})$ can simply be obtained by scaling the values with $1/2$ (4) to obtain the results for the L2 (L3b) filling pattern.

The HL-LHC is overall slightly more susceptible with respect to the effects of moving long-range beam-beam encounters than the nominal LHC in comparable scenarios. The emittances are expected to grow 4 times faster in the HL-LHC (L3a) than in the nominal LHC with the maximum intensity filling pattern from 2016 L2 based on the amplitudes of $\sigma(\delta_{t,u})$. A bunch intensity of $N_b = 1.15 \times 10^{11}$ protons per bunch is expected to create a growth rate that is 16 times larger than in the nominal HL-LHC based on the $\sigma(\delta_{t,u})$; however, this does not imply the growth rate is necessarily large in absolute terms.

2.3 Simplified non-linear multi-particle tracking

In the previous section, the effects of amplitude detuning were neglected. The effect of amplitude detuning on the emittance growth caused by moving long-range beam-beam encounters may change the emittance evolution substantially; therefore, it was not attempted until now to estimate the eventual growth rates. The analysis of the linear model in the previous section gave reason to believe that the emittance growth in the LHC is at least three orders of magnitude smaller than in RHIC. The HL-LHC should have similar or slightly larger growth rates than the nominal LHC. In addition to the lack of transverse amplitude detuning, the linear considerations were made on the basis of no transverse coupling. Coupling can lead to an exchange of emittances in the two transverse planes. In order to include amplitude detuning, coupling and the correct time structure and kick strength of the long-range encounters, a particle-tracking study is conducted in the following since an analytic description of the emittance evolution cannot be obtained without substantial simplifications.

Standard tracking codes like SixTrack [105], PTC [106] and elegant [107] are mostly not capable of implementing an effect like moving beam-beam encounters. Although the implementation of time-varying functions is possible, a shift of the location of an element is not easily realised. Furthermore, established concepts used in accelerator physics like tune footprints and analysis techniques like frequency-map analysis (FMA) [108] lose their effectiveness since

the one-turn map is no longer constant and is not necessarily periodic at all or at least for a long duration. The tracking of a large particle ensemble over large numbers of turns is required to model the emittance evolution of the beam appropriately. For this purpose, a fast pseudo six-dimensional non-linear tracking routine has been developed in the scope of this thesis.

This model neglects non-linearities of the magnetic lattice and the beam-beam force but considers the linear detuning parameters. The system has infinite dynamic aperture in this model; however, at injection, the dynamic aperture is well beyond the physical aperture which is defined by the primary collimators in the LHC. The physical aperture is around $5\sigma_u$ to $6\sigma_u$ (half gap) at the TCPs and is therefore much smaller than the dynamic aperture. By simply assuming that collimators intercept particles beyond this $5\sigma_u$ to $6\sigma_u$ threshold, the lack of the dynamic aperture is considered unimportant to the general outcome of the calculations. The model and the results of the tracking study have already been published partly in [9].

2.3.1 The simplified effective Hamiltonian

Amplitude detuning results from non-linear potentials and is created by the sextupoles and octupoles in a collider assuming the absence of head-on beam-beam encounters. Amplitude detuning is of utmost importance since the resulting tune spread enhances Landau damping and therefore makes the beam less susceptible to excitation. On the other hand, strong sextupole and octupole fields may cause shrinkage of the dynamic aperture. An important feature of amplitude detuning is that a particle close to a resonance in tune space may stabilise its transverse amplitude since a change of the action causes a tune shift (see Sec. 2.1.3.1). This tune shift drives the particle away from the resonance in tune space and thus leads to stability and a bounded action. Figure 2.4 demonstrates this effect.

Since the dynamic aperture is not a subject of this analysis and to avoid element-by-element tracking, a simplified Hamiltonian that contains the linear actions J_u up to second order is used. The Hamiltonian is constant in the arcs between the IRs and reads

$$H = \mu_x J_x + \mu_y J_y + 2\pi \left(\frac{1}{2}\alpha_{xx} J_x^2 + \frac{1}{2}\alpha_{yy} J_y^2 + \alpha_{xy} J_y J_x \right) + \mathcal{O}(J_u^3) \tag{2.114}$$

with the linear detuning parameters $\alpha_{ij} = \partial Q_i / \partial J_j |_{J_x = J_y = 0}$. In the LHC, the amplitude detuning at injection energy is mostly generated by the sextupoles and octupoles if these are switched on. During the 2016 p-Pb run of the LHC, the octupoles were switched off at injection and the octupole current was increased during the energy ramp. In RHIC, the octupoles are only switched on if the beam energy is close to the transition energy during the ramp. The Hamiltonian in Eq. 2.114 does not depend on ϕ_x and ϕ_y. Such a Hamiltonian is usually obtained by integration over the angle variables as the first step in classical perturbation theory. This approximation of the Hamiltonian is valid in particular if the non-linear elements are uniformly distributed along the linear phase advance rather than being concentrated at specific locations.

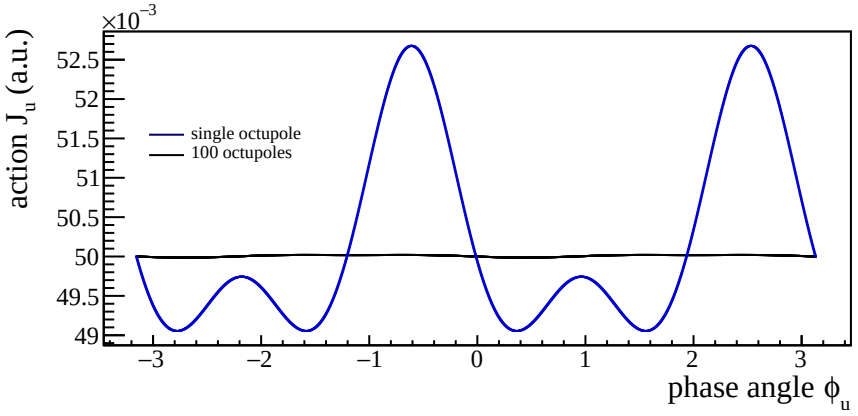

Figure 2.24: Dependence of the linear action J_u on the phase angle ϕ_u. If the integrated octupole strength is concentrated in a single octupole (blue), the linear action J_u oscillates. If the integrated octupole strength is distributed evenly on 100 octupoles equally distributed along the linear phase advance (black), the oscillatory behaviour reduces significantly. Appendix A gives the calculation of the effective Hamiltonian of a single and multiple octupoles in a linear lattice.

Figure 2.24 shows this effect: A single octupole of the integrated strength k_3 perturbs the linear action along the angle ϕ substantially while the same integrated octupole strength, although split up on 100 octupoles ($k_3/100$ per octupole), results in a roughly invariant linear action along the phase ϕ_u. This assumption is supported by a calculation using Lie algebra in Appendix A.3 for arbitrary octupole distributions.

The tune shift resulting from the Hamiltonian in Eq. 2.114 is

$$\Delta Q_u = \alpha_{ux} J_x + \alpha_{uy} J_y \,. \tag{2.115}$$

The synchrotron motion is another effect that has to be considered in a simulation. The synchrotron motion causes the relative momentum deviation δ_p of the particles to oscillate. Hence, the tunes oscillate because of the chromaticities ξ_u. This tune modulation introduces sidebands of optical and OKO resonances as derived in Sec. 2.1.6.2. Although the nominal tunes and chromaticities should be chosen in a way that strong sidebands of low-order optical resonances are not approaching the tune footprint, the same does not necessarily hold for OKO resonances and their sidebands. To omit six-dimensional tracking, the relative momentum deviation δ_p is artificially amplitude-modulated. Hence, the tune deviation from the nominal tune, comprising amplitude detuning and synchrotron motion, reads

$$\Delta Q_u(n) = \alpha_{ux} J_x + \alpha_{uy} J_y + \xi_u \delta_p \sin(2\pi Q_s n + \varphi_0) \tag{2.116}$$

with n being the turn number, Q_s is the synchrotron tune and φ_0 is an arbitrary initial phase of the synchrotron motion. Non-linearities of the RF wave are neglected, i.e., there is no de-

tuning of the synchrotron frequency with amplitude. The underlying effective Hamiltonian of Eq. 2.116 is

$$H = \mu_x J_x + \mu_y J_y + 2\pi\left(\frac{1}{2}\alpha_{xx}J_x^2 + \frac{1}{2}\alpha_{yy}J_y^2 + \alpha_{xy}J_yJ_x + (\xi_x J_x + \xi_y J_y)\delta_p \sin(2\pi Q_s n + \varphi_0)\right). \tag{2.117}$$

The linear detuning parameters α_{ij} are obtained for the LHC and RHIC using the PTC integration into MAD-X [109]. The simplified Hamiltonian in Eq. 2.117 applies in the arcs of the collider and transports the particles between the IRs while strictly linear motion is assumed in the actual IRs.

The effect of amplitude detuning can either reduce or enhance the emittance growth caused by the long-range beam-beam encounters. If the detuning is large, the de-coherence time is short and may help to stabilise the beam if the orbit drifts (filamentation damps the orbit offset), but it also can lead to faster emittance growth because beam offsets translate more quickly into an emittance increase (see Fig. 2.9).

The tracking process The code assumes no detuning within the IRs. Because of this assumption, the transfer through the IRs, in particular the matrices $\mathbf{M}_{\mathrm{IR}}$ in Eq. 2.110, is universal for all particles independently of their actions and energy deviations. The matrices $\mathbf{M}_{\mathrm{IR}}$ are consequently computed only once per turn and are applied to all particles regardless of their kinematics. The detuning in Eq. 2.116 refers to the full revolution in the accelerator. Since the detuning affects the particles only in the arcs, ΔQ_u is distributed uniformly over the remaining betatron phase advance, i.e., $\Delta Q(s)' = 1/\beta_u(s)$. The transfer in the arcs between IRj and IR$j+1$ modifies to

$$\mathbf{M}_{j,j+1} = \mathbf{V}^{-1}(s^{\mathrm{start}}_{\mathrm{IR},j+1})\mathbf{R}(\phi_{x,j+1}, \phi_{y,j+1})\mathbf{V}(s^{\mathrm{end}}_{\mathrm{IR},j}) \tag{2.118}$$

with (cf. Eqs. 2.9 & 2.10)[14]

$$\mathbf{R}(\phi_x, \phi_y) = \mathrm{diag}\left(\mathbf{R}(\phi_x), \mathbf{R}(\phi_y), 1\right), \tag{2.119}$$

$$\mathbf{V}(s) = \mathrm{diag}\left(\mathbf{V}_x(s), \mathbf{V}_y(s), 1\right), \tag{2.120}$$

$$\phi_{u,j+1} = \phi_u(s^{\mathrm{start}}_{\mathrm{IR}j+1}) - \phi_u(s^{\mathrm{end}}_{\mathrm{IR}j}) + \frac{\phi_u(s^{\mathrm{start}}_{\mathrm{IR}j+1}) - \phi_u(s^{\mathrm{start}}_{\mathrm{IR}j})}{\mu_u/(2\pi\Delta Q_u(n))}. \tag{2.121}$$

The approach of shifting the detuning into the rotation matrix $\mathbf{R}$ is also applied in the collective-effect computer code PyHEADTAIL [110, 111]. An actual one-turn matrix of turn n can only be given for a single particle because the one-turn map is particle-action dependent and therefore

[14] Equation 2.121 contains the phase advance at the start of IRj ($s^{\mathrm{start}}_{\mathrm{IR}j}$) in the nominator of the second term. If the end point of IRj would be used instead, the sum of all tune differences in the arcs is not equal to $\Delta Q_u(n)$.

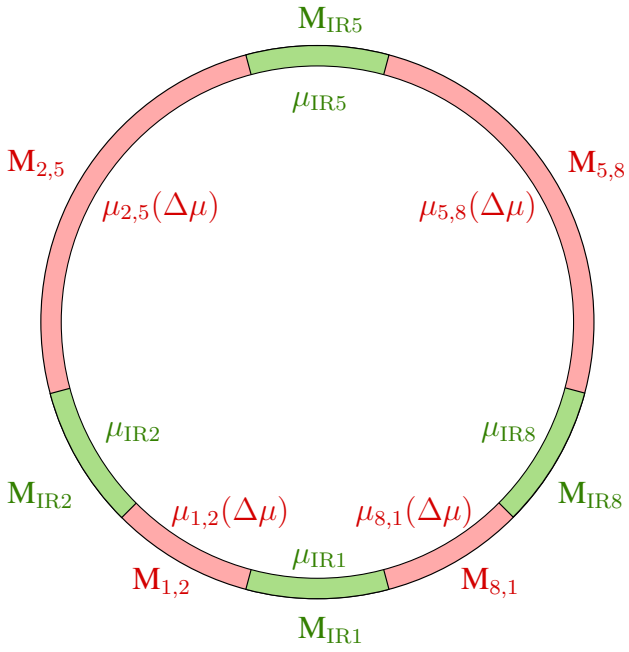

Figure 2.25: Sketch of how the LHC is split up into four IR matrices (green) of a fixed phase advance and four transfer matrices (red) with a varying phase advance depending on $\Delta\mu$. The sketch also applies for the HL-LHC despite slightly different tunes in the segments. The IR lengths are strongly exaggerated in this sketch.

varies among particles. The tracking of the phase space vector $\mathbf{r} = (x, x', y, y', 1)^{\mathrm{T}}$ obeys the iteration procedure in turn n at iteration step j

$$\mathbf{r}_{j+\frac{1}{2}} = \mathbf{M}_{\mathrm{IR}j}\mathbf{r}_j\,, \tag{2.122}$$

$$J_{u,j+1} = \frac{1}{2}(\tilde{u}^2_{j+\frac{1}{2}} + \tilde{u}'^2_{j+1/2})\,, \tag{2.123}$$

$$\Delta Q_{u,j+1} = \alpha_{ux}J_{x,j+1} + \alpha_{uy}J_{y,j+1} + \xi_u\frac{\Delta p}{p_0}\sin(2\pi Q_s n + \varphi_0)\,, \tag{2.124}$$

$$\phi_{u,j+1} = \phi_u(s^{\mathrm{start}}_{\mathrm{IR}j+1}) - \phi_u(s^{\mathrm{end}}_{\mathrm{IR}j}) + \frac{\phi_u(s^{\mathrm{start}}_{\mathrm{IR}j+1}) - \phi_u(s^{\mathrm{start}}_{\mathrm{IR}j})}{\mu_u/(2\pi\Delta Q_{u,j+1})}\,, \tag{2.125}$$

$$\mathbf{r}_{j+1} = \mathbf{V}^{-1}(s^{\mathrm{start}}_{\mathrm{IR},j+1})\mathbf{R}_{j,j+1}(\phi_{x,j+1}, \phi_{y,j+1})\mathbf{V}(s^{\mathrm{end}}_{\mathrm{IR},j})\mathbf{r}_{j+\frac{1}{2}}\,, \tag{2.126}$$

$$n = n + 1 \qquad \text{if turn is complete}\,. \tag{2.127}$$

The index n increases once per turn for the correct calculation of the synchrotron phase in Eq. 2.124. The model splits up the collider in IR matrices of fixed tunes between the beam-beam encounters and matrices of variable tunes in the arcs. Figures 2.25 & 2.26 show the split for the LHC and RHIC, respectively. The red-coloured arcs in the two sketches consider potential detuning, whereas the green-coloured IR sections cover a fixed phase advance. The LHC lattice is therefore approximated by four IR matrices and four arc matrices. These numbers

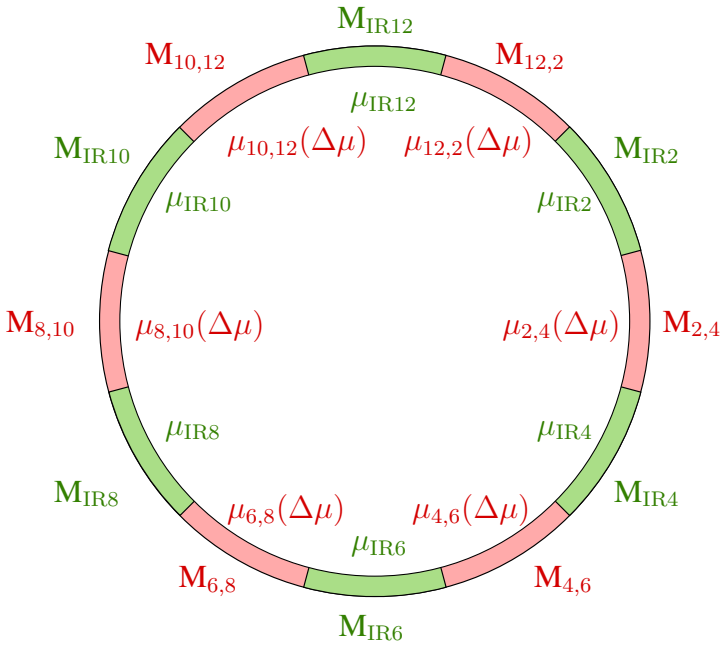

Figure 2.26: Sketch of how RHIC is split up into six IR matrices (green) with a fixed phase advance and six transfer matrices (red) with a varying phase advance. The IR lengths are strongly exaggerated.

increase to six IR matrices and six arc matrices in RHIC. The tracking process assumes once again a strong counter-rotating beam.

2.3.2 Simulation setup and tracking results at injection energy

A multi-particle tracking study is performed following the concepts of Sec. 2.3.1 and the iteration procedure given in Eqs. 2.122–2.127 in particular. For this purpose, a C++ simulation was set up that can be run parallelised on CERN's batch system HTCondor [112]. The simulation code uses as input the IR matrices M_{IR} calculated in Sec. 2.2.4. Hence, the code does not simulate the slippage between the two beams directly since the matrices M_{IR} cover this effect. The code only modifies the phase advance in the arcs depending on the transverse actions and the synchrotron phase. Otherwise, the code uses the IR matrices M_{IR} which are universal for all particles. The beam energy is equal to the injection energy at all times during the simulation since the growth rate is presumably the largest at injection energy.

Each simulation comprises the tracking of a bunch of the weak beam (Pb in LHC Pb-p operation; Au in RHIC Au-D operation) made of $N_b = 10^5$ particles over the duration of 10^6 turns. Initially, the particles are normally distributed in the transverse coordinates, transverse

momenta and energy deviation. To avoid collective energy oscillations, the code distributes the initial synchrotron phases φ_0 of the particles uniformly. The code calculates the emittances

$$\epsilon_u = \frac{1}{N_b} \sum_{i}^{N_b} J_{u,i} \tag{2.128}$$

each turn from the linear actions $J_{u,i}$ of the particle ensemble. This definition of the emittance assumes weak betatron coupling, which is the case throughout all simulations. Ten such simulations are performed for each filling pattern with different random seeds to avoid numerical artefacts. During a simulation, a few particles may get excited much more strongly than other particles and these strongly excited particles are possibly main contributors to the emittance growth. In reality, these particles impact the collimators and are therefore no longer part of the remaining particle ensemble from that time on. On the one hand, simulating the beam dynamics without aperture restrictions helps to understand the nature of the emittance growth, e.g., it is easily determined whether the emittance growth is exponential or linear; however, the emittance growth may follow a different evolution because of the physical aperture in the real accelerator. Hence, the emittance evolution is simulated with and without collimators set to $5\sigma_u$ half gap (typical width of the half gap of the LHC primary collimators).

2.3.2.1 RHIC – Au-D operation

In the following, the emittance evolution of an Au test bunch for the three different filling patterns of the deuteron beam presented in Sec. 2.2.4.1 is given. Comparison to data is not possible because RHIC does not feature a continuous emittance measurement. Although the emittance is known at injection, the emittance during the ramp and how it evolves is unknown. Even measurements before and after the energy ramp are not highly helpful since other effects during the ramp may influence the emittance evolution, e.g., the crossing of the transition energy.

Amplitude detuning During the attempts to accelerate Au-D in RHIC in 2002/2003, the octupoles were switched off except at transition energy [113]. Hence, the only contributors to the detuning were the sextupoles and non-zero chromaticities. The linear detuning parameters with the chromaticities matched to $\xi_u = -5$ for the Au beam are calculated via PTC and read

$$\alpha_{xx} = -216\,\mathrm{m}^{-1}\,, \qquad \alpha_{yy} = 422\,\mathrm{m}^{-1}\,, \qquad \alpha_{xy} = -84\,\mathrm{m}^{-1}\,. \tag{2.129}$$

The detuning resulting from the octupoles in RHIC is not known [114]. Assuming reasonable detuning parameters with octupoles switched on is maybe possible but remains speculative. The simulations are carried out without octupoles, i.e., the detuning parameters in Eq. 2.129 apply; however, the simulation with the filling pattern R3 is carried out with and without additional detuning from octupoles. This additional simulation scenario is supposed to indicate whether

larger detuning parameters lead to additional emittance growth due to a shorter decoherence time or whether the detuning reduces the emittance growth by stabilising the growth of the transverse actions via detuning. For the R3 simulation with additional detuning, the detuning parameters that are used are the LHC detuning parameters with octupole currents set to $I_{\mathrm{oct}} = 12\,\mathrm{A}$ normalised[15] to the RHIC emittance

$$\alpha_{xx} = 4.7 \times 10^3\,\mathrm{m}^{-1}\,, \qquad \alpha_{yy} = 4.8 \times 10^3\,\mathrm{m}^{-1}\,, \qquad \alpha_{xy} = -3.5 \times 10^3\,\mathrm{m}^{-1}\,. \quad (2.130)$$

For the filling patterns R1 and R2, only the scenario with octupoles switched off is simulated.

Emittance evolution Figure 2.27 presents the results of the tracking simulation for RHIC for the filling patterns R1, R2 and R3 (octupoles on and off). The simulations were performed over 10^6 turns equivalent to a time span of $12.8\,\mathrm{s}$ in the real machine. The error bars in Fig 2.27 and the plots for the LHC and HL-LHC (Figs. 2.28 & 2.29) are the statistical errors from applying a moving average to the data to reduce the data size and to improve the visibility of the plots. In these simulations, the maximum transverse amplitudes are limited to $5\sigma_u$ to include the influence of collimation on the emittance evolution. The tracking results with infinite physical aperture are given in Appendix B.2 in Fig. B.7 for completeness. Table 2.6 lists the relative linear growth rates $\dot{\epsilon}_u/\epsilon_{u0}$ obtained via linear fit. Here, ϵ_{u0} refers to the emittance of the Au test bunch at that start of the simulation. Table 2.6 also contains the fit results with an infinite physical aperture.

Over 10^6 turns, the horizontal emittance of the Au test bunch grows by $1.5\,\%$ ($\dot{\epsilon}_x/\epsilon_{x0} = (102 \pm 3) \times 10^{-5}\,\mathrm{Hz}$) if the counter-rotating deuteron beam has the filling pattern R1 (top left plot of Fig. 2.27). The emittance growth does not increase too linearly with the proton beam intensity. The emittance growth of the Au bunch is $7\,\%$ after the same time period ($\dot{\epsilon}_x/\epsilon_{x0} = (450 \pm 9) \times 10^{-5}\,\mathrm{Hz}$) for 55 deuteron bunches (R2). The growth is $11\,\%$ after 10^6 turns ($\dot{\epsilon}_x/\epsilon_{x0} = (758 \pm 14) \times 10^{-5}\,\mathrm{Hz}$) with 110 bunches (R3). The growth rates scale linearly with the number of bunches in the high-intensity regime. Active octupoles (large detuning) enhance the horizontal emittance growth strongly: The emittance growth in the horizontal plane has increased by $43\,\%$ over 10^6 turns. This growth is a factor 4 larger than with octupoles switched off.

In the vertical plane, the growth rates are even larger than seen in the top right plot of Fig. 2.27. The simulated growth for a single counter-rotating deuteron bunch is $3\,\%$ on 10^6 turns ($\dot{\epsilon}_y/\epsilon_{y0} = (169 \pm 3) \times 10^{-5}\,\mathrm{Hz}$). With 55 bunches, it is $11\,\%$ ($\dot{\epsilon}_y/\epsilon_{y0} = (901 \pm 26) \times 10^{-5}\,\mathrm{Hz}$) and with 110 bunches $20\,\%$ ($\dot{\epsilon}_y/\epsilon_{y0} = (1516 \pm 41) \times 10^{-5}\,\mathrm{Hz}$). The observation of stronger growth of the vertical plane compared to the horizontal plane can be explained with the findings of the linear calculations in Sec. 2.2.4.1. Although the tune oscillation is virtually the same

[15] Normalisation means α_{ij}/ϵ_i is equal among accelerators. In the normalisation process, round LHC beams are assumed $\epsilon_{\mathrm{n}x} = \epsilon_{\mathrm{n}y} = 2\,\mu\mathrm{m}$.

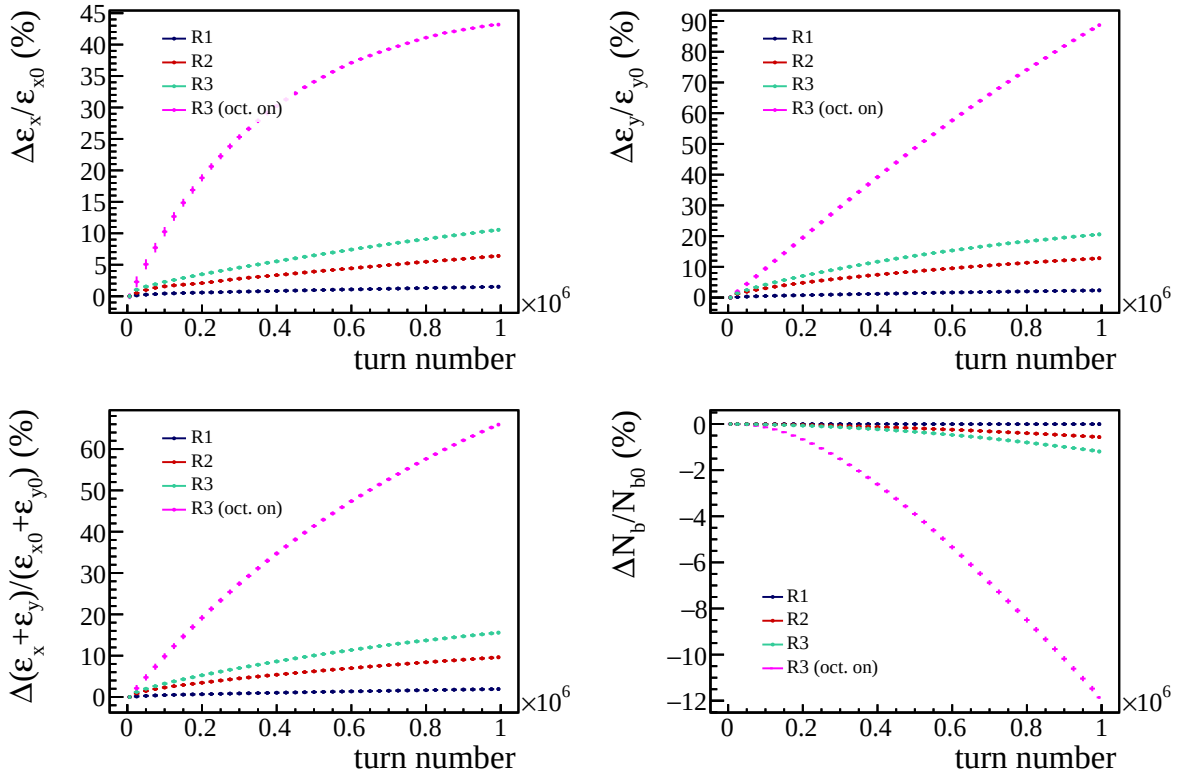

Figure 2.27: Top left: Relative horizontal emittance difference as a function of the turn number for the four previously described scenarios in RHIC over 10^6 turns with the physical aperture set to $5\sigma_u$ (half gap). Top right: Vertical relative emittance difference versus turn number. Bottom left: Relative change of the sum of the emittances. Bottom right: Relative intensity change as a function of the turn number.

in both planes, the variation of the dipole kicks in the vertical plane is much larger than in the horizontal plane. The setup with octupoles switched on causes nearly the doubling of the emittance on the time scale of 10^{10} turns (roughly $90\,\%$ total increase). Changing the signs of the detuning parameters (inverted the octupole polarity) leads to even stronger emittance growth rates. The plots with negative detuning parameters are omitted.

The sum of the emittances shown in the bottom left plot Fig. 2.27 displays the same behaviour as the emittance evolution in the two transverse planes. The growth of the sum of the emittances increases with the number of bunches of the deuteron beam, and additional amplitude detuning enhances the emittance growth even further.

Figure B.7 in Appendix B.2 shows that the emittance growth is larger with infinite aperture since strongly excited particles are considered in the emittance calculation even if the transverse amplitudes are large enough to impact the collimators/physical aperture in the real machine. The emittance growth for the filling patterns R2 and R3 in particular are much more enhanced. Table 2.6 lists the linear growth rates without collimation in grey. The growth rate of the sum

Table 2.6: List of filling patterns for the LHC, HL-LHC and RHIC. The number of proton/deuteron bunches, n_b, the bunch population, N_b, and the fitted linear emittance growth rates normalised to the initial emittance of the Pb/Au beam, $\dot{\epsilon}_u/\epsilon_{u0}$, are given. Simulation results without collimation for RHIC are given in grey.

	Filling pattern	n_b	N_b (10^{10})	$\dot{\epsilon}_x/\epsilon_{x0}$ (10^{-5} Hz) with (without) coll.	$\dot{\epsilon}_y/\epsilon_{y0}$ (10^{-5} Hz) with (without) coll.	$(\dot{\epsilon}_x+\dot{\epsilon}_y)/(\epsilon_{x0}+\epsilon_{y0})$ (10^{-5} Hz) with (without) coll.
RHIC	R1	1	12	102 ± 3 (103 ± 3)	169 ± 3 (170 ± 3)	135 ± 3 (137 ± 3)
	R2	55	12	450 ± 9 (489 ± 8)	901 ± 26 (1520 ± 10)	676 ± 17 (1006 ± 8)
	R3	110	12	758 ± 14 (934 ± 8)	1516 ± 41 (2720 ± 17)	1138 ± 28 (1829 ± 11)
	R3 (with oct.)	110	12	3127 ± 170 ($> 10^4$)	7079 ± 59 (9729 ± 89)	5102 ± 113 ($> 10^4$)
LHC	L1	15	2.8	0.01 ± 0.00	0.01 ± 0.00	0.01 ± 0.00
	L2	684	2.8	-0.04 ± 0.00	0.09 ± 0.01	0.01 ± 0.00
	L2 (with oct.)	684	2.8	0.01 ± 0.01	0.05 ± 0.02	0.03 ± 0.00
	L3	1232	2.8	-0.13 ± 0.01	0.25 ± 0.02	0.03 ± 0.00
HL-LHC	L2	684	2.8	0.05 ± 0.01	0.13 ± 0.01	0.09 ± 0.01
	L3a	1232	2.8	0.03 ± 0.01	0.10 ± 0.01	0.06 ± 0.01
	L3a (with oct.)	1232	2.8	0.01 ± 0.01	0.10 ± 0.01	0.05 ± 0.01
	L3b	1232	11.5	-1.42 ± 0.13	2.96 ± 0.10	0.45 ± 0.10

of the emittances $(\dot{\epsilon}_x + \dot{\epsilon}_y)/(\epsilon_{x0} + \epsilon_{y0})$ without collimation increases by $49\,\%$ for R2, $61\,\%$ for R3 and $136\,\%$ for R3 with octupoles switched on.

The bottom right plot of Fig. 2.27 shows the intensity losses. The deuteron beam with the three filling patterns R1, R2 and R3 causes the loss of 0–$1.3\,\%$ of the initial intensity of the Au test bunch during the initial $12.8\,\mathrm{s}$. These are large values considering that the loss rate increases over time due to the increasing emittance, i.e., the loss rate is small at the start of the simulations and increases once the bunch emittances become larger and particles approach the aperture limit. The Au beam in the simulation with octupoles switched on suffers intensity losses of $12\,\%$ in $12.8\,\mathrm{s}$. The total amount of losses is therefore a rough factor 9 larger compared to the same simulation with smaller detuning. This finding suggests that large detuning enhances emittance growth and the intensity loss rate while the detuning does not have any obvious stabilising effect or other beneficial side effects in this simulation.

The observation of the stronger growth with increasing numbers of bunches is understandable because the tune oscillation and the standard deviation of the dipole kicks increase. The effect of a larger DFT amplitude in the horizontal plane in case of R2 (see Tab. 2.3) seems to have little effect in this non-linear model. The growth rates seem to be predominantly linear in all cases. The emittance doubling time $\epsilon_{u0}/\dot{\epsilon}_u$ for 55 and 110 counter-rotating deuteron bunches ranges between $\epsilon_{y0}/\dot{\epsilon}_y = 0.6\,\mathrm{min}$ (R3 vertical) and $\epsilon_{x0}/\dot{\epsilon}_x = 3.4\,\mathrm{min}$ (R2 horizontal). An emittance doubling time in the range of $1\,\mathrm{min}$ was observed in RHIC [10]. The calculated values seem to more or less match the experimental finding. A reliable and continuous emittance measurement at injection energy is required to quantify exactly the agreement between the calculated values and reality. Although the exact comparison is not possible, the simulations gave important results since a correct model has to reproduce the beams in RHIC as unstable as was observed during the Au-D commissioning in 2002/2003.

Total emittance increase during the ramp The previous simulations only covered the effects of moving encounters at injection energy. During the energy ramp, the beam rigidity increases, the shift distance d_t of the encounter points shrinks and the order $|n|$ of the dipole OKO resonances close to the betatron tune increases. This translates into shrinking emittance growth rates during the ramp. A simulation of the emittance growth over the full duration of the ramp is difficult because of the simulation time, the adiabatic damping of the emittances and unknown effects occurring at transition energy that may have a strong influence on the beam dynamics in the real machine.

In a highly simplified model, the total emittance increase during the energy ramp can be estimated from the linear growth rate $\dot{\epsilon}_u/\epsilon_{u0}$ at injection energy given in Tab. 2.6. The linear relative emittance growth rates scale roughly like $\dot{\epsilon}_u/\epsilon_{u0} \propto (\sigma^2(\delta_u)+\epsilon_{u0}\sigma^2(\Delta Q_u))/|n|^2 \propto 1/\gamma^6$ (increase of the magnetic rigidity and $|n|$) if the exponential nature of the emittance growth due

to a varying focusing strength and the change of the time structure of the long-range encounters are neglected. The linear growth rate therefore reads

$$\dot{\epsilon}_u(t) = \dot{\epsilon}_u(0)\frac{\gamma_i^6}{(\gamma_i + \dot{\gamma}t)^6} - \epsilon_{u0}\frac{\gamma_i\dot{\gamma}}{(\gamma_i + \dot{\gamma}t)^2} \tag{2.131}$$

with the second term comprising the effect of adiabatic damping due to the energy increase. Here, a linear increase of the Lorentz factor from injection γ_i to the target $\gamma_f = \gamma_i + \dot{\gamma}T_{\mathrm{ramp}}$ is assumed with $\dot{\gamma} = \mathrm{const.}$ and T_{ramp} being the duration of the ramp. At the time the ramp ends, the normalised emittance has increased by the relative amount[16]

$$\frac{\Delta\epsilon_{\mathrm{n}u}}{\epsilon_{\mathrm{n}u}}(T_{\mathrm{ramp}}) = \left(\frac{\dot{\epsilon}_u}{\epsilon_{u0}}\right)\frac{1}{5\dot{\gamma}}\left(\gamma_f - \frac{\gamma_i^5}{\gamma_f^4}\right) . \tag{2.132}$$

Equation 2.132 can be used to estimate the total relative growth of the emittance just from the fit values of $\dot{\epsilon}_u/\epsilon_{u0}$ obtained in the previous paragraph. In RHIC, the duration of the ramp was $T_{\mathrm{ramp}} = 240\,\mathrm{s}$ and the Lorentz factor at target energy was $\gamma_f = 107.4$. Thus, the slope of the Lorentz factor is $\dot{\gamma} = 0.4\,\mathrm{Hz}$. Equation 2.132 reduces to

$$\frac{\Delta\epsilon_{\mathrm{n}u}}{\epsilon_{\mathrm{n}u}} = \frac{\dot{\epsilon}_u}{\epsilon_{u0}} \times 53.2\,\mathrm{s} \tag{2.133}$$

with these numbers. Applying the formula to the evolution of the sum of the normalised emittances $\epsilon_{\mathrm{n}x} + \epsilon_{\mathrm{n}y}$ estimates the total increase of $\epsilon_{\mathrm{n}x} + \epsilon_{\mathrm{n}y}$ at the end of the ramp to be in the range $7.2\,\%$ for the filling pattern R1, $36\,\%$ for the filling pattern R2 and $61\,\%$ ($271\,\%$) for the filling pattern R3 with small (large) detuning parameters. These numbers are only a rough estimate but confirm that RHIC is inoperable especially with large numbers of bunches.

2.3.2.2 LHC – Pb-p operation

Amplitude detuning The octupoles were not switched on at injection in 2016 p-Pb operation, i.e., the detuning was solely generated by the sextupoles. The respective linear detuning parameters

$$\alpha_{xx} = 1.1 \times 10^3\,\mathrm{m}^{-1}\,, \qquad \alpha_{yy} = 1.4 \times 10^3\,\mathrm{m}^{-1}\,, \qquad \alpha_{xy} = -3.7 \times 10^3\,\mathrm{m}^{-1} \tag{2.134}$$

are obtained once again via PTC. The filling patterns L1 and L3 are simulated with octupoles switched off; however, the L2 filling pattern (nominal 2016 filling pattern) is simulated with octupoles switched on and switched off to investigate whether additional detuning either suppresses or enhances the emittance growth that is induced by moving encounter positions. At

[16] The emittance growth that occurs at injection energy after both beams have already been injected but the ramp has not started yet contributes to the total growth additionally.

injection, an octupole current of $I_{\mathrm{oct}} = 12\,\mathrm{A}$ is assumed and the resulting detuning parameters are

$$\alpha_{xx} = 93.5 \times 10^3\,\mathrm{m}^{-1}\,, \qquad \alpha_{yy} = 95.8 \times 10^3\,\mathrm{m}^{-1}\,, \qquad \alpha_{xy} = -69.3 \times 10^3\,\mathrm{m}^{-1} - \quad (2.135)$$

These linear detuning parameters yield the same α_{ij}/ϵ_i as listed for RHIC in Eq. 2.130.

Emittance growth The simulated number of turns is again 10^6 equivalent to $88.9\,\mathrm{s}$ in the real machine. Figure 2.28 shows the emittance evolution for the filling patterns L1, L2 (octupoles switched on and switched off) and L3. Again, the error bars arise from applying a moving average on the data series to improve the visibility. The emittance growth rates in the LHC in Pb-p operation are three to four orders of magnitude smaller compared to those in RHIC. The emittances in the two transverse planes (top left and top right plots of Fig. 2.28) do not grow notably. The emittances are varying in an apparently random way in time, and trends are not easily identifiable. Changes of the horizontal emittances seem to have the exact opposite effect on the vertical emittance, i.e., $\epsilon_x + \epsilon_y = \mathrm{const.}$ holds in good approximation. While the horizontal emittance mostly shrinks in all four simulation scenarios, the vertical emittance increases by roughly the same amount. Since the simulated Pb test bunch has a slightly smaller vertical emittance ($\epsilon_{\mathrm{n}x} = 2\,\mu\mathrm{m}$, $\epsilon_{\mathrm{n}y} = 1.5\,\mu\mathrm{m}$), the relative effect of emittance transfer due to coupling between the two planes is different. The bottom plot of Fig. 2.28 shows the relative change of the sum of the emittances $\Delta(\epsilon_x+\epsilon_y)$, and Tab. 2.6 lists the linear growth rates obtained via fit for all filling patterns.

The L1 filling pattern with 15 counter-rotating proton bunches (filling pattern used during the 2012 p-Pb test [3]) causes a relative linear growth rate of $\dot{\epsilon}_u/\epsilon_{u0} = (1 \pm 0) \times 10^{-7}\,\mathrm{Hz}$ in both transverse planes of the Pb test bunch. This value is equivalent to an emittance doubling time of more than $2500\,\mathrm{h}$ and consequently fully negligible considering the presence of an IBS growth time of $\tau_{\mathrm{IBS},x} = 13\,\mathrm{h}$ in the horizontal plane for Pb ions at injection in the LHC. During the p-Pb pilot run in 2012, presumably unaccounted growth in the vertical plane of the Pb bunches was observed. It is highly cumbersome to determine whether the additional growth is due to uncertainties within the IBS model or due to moving beam-beam encounters. The simulation indicates that the likelihood of moving encounters influencing the emittances is small with only 15 counter-rotating proton bunches. This is particularly true since the proton-bunch intensity of $N_b = 2.8 \times 10^{10}$ protons per bunch in the simulation is much larger than during the p-Pb test in 2012 ($N_b = 1.2 \times 10^{10}$ protons per bunch).

The 2016 filling pattern L2 (684 bunches) was simulated with small and large detuning parameters. With octupoles switched off, the emittance shrinks with $\dot{\epsilon}_x/\epsilon_{x0} = (-4 \pm 0) \times 10^{-7}\,\mathrm{Hz}$ in the horizontal plane and the vertical emittance is growing with $\dot{\epsilon}_y/\epsilon_{y0} = (9 \pm 1) \times 10^{-7}\,\mathrm{Hz}$. The shrinkage in one plane and the growth in the other plane is most likely due to coupling. The sum of the emittances changes with $(\dot{\epsilon}_x + \dot{\epsilon}_y)/(\epsilon_{x0} + \epsilon_{y0}) = (1 \pm 0) \times 10^{-7}\,\mathrm{Hz}$,

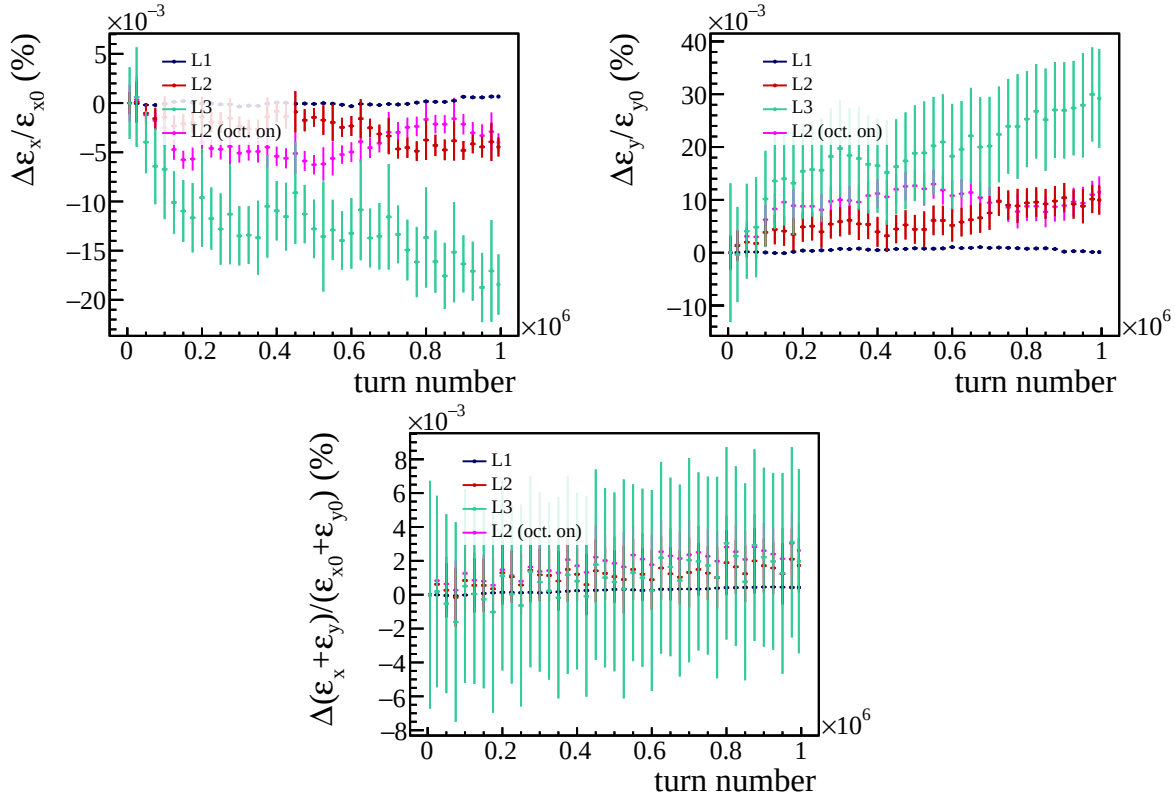

Figure 2.28: Top left: Relative emittance change in the horizontal plane normalised to the initial emittance as a function of the turn number for the four simulation scenarios in the nominal LHC. Top right: Vertical emittance change versus turn number. Bottom: Relative change of the sum of the emittances $\epsilon_x + \epsilon_y$. The changes in all three plots are very small and trends are identifiable only in the bottom plot.

i.e., the sum of the two emittances doubles in $2500\,\mathrm{h}$. Such a small growth rate can be fully neglected. With octupoles switched on, the growth rates change slightly. The horizontal and vertical emittance is growing with $\dot{\epsilon}_x/\epsilon_{x0} = (1 \pm 1) \times 10^{-7}\,\mathrm{Hz}$ and $\dot{\epsilon}_y/\epsilon_{y0} = (5 \pm 2) \times 10^{-7}\,\mathrm{Hz}$, respectively. With both individual growth rates being positive, the growth of the sum of the emittances is $(\dot{\epsilon}_x + \dot{\epsilon}_y)/(\epsilon_{x0} + \epsilon_{y0}) = (3 \pm 0) \times 10^{-7}\,\mathrm{Hz}$. This value is equivalent to an emittance doubling time of more than $900\,\mathrm{h}$. Hence, the additional amplitude detuning has increased the growth rate of the bunch volume rather than leading to the suppression of growth. This effect, however, is small and the potential beneficial side effects of a larger tune spread on collective effects and other effects not considered here may justify larger detuning. The results for the L2 filling pattern confirm the stable operation of the LHC with 684 proton bunches as observed during the 2016 p-Pb run.

Even with the high beam intensity of the HL-LHC filling pattern L3 (1232 proton bunches), the growth rates of the Pb test bunch are small. The horizontal growth rate is $\dot{\epsilon}_x/\epsilon_{x0} = (-13 \pm 1) \times 10^{-7}\,\mathrm{Hz}$, whereas the vertical growth rate is $\dot{\epsilon}_y/\epsilon_{y0} = (25 \pm 2) \times 10^{-7}\,\mathrm{Hz}$. The

emittance doubling time in the vertical plane is $110\,\mathrm{h}$, but the doubling time of the sum of the two transverse emittances is still longer than $900\,\mathrm{h}$. Thus, no significant emittance blow-up is likely to be observed in a potential p-Pb run in LHC Run 3 with 1232 proton bunches.

During all simulations of the different filling patterns and detuning scenarios, less than $10^{-4}\,\%$ of the total number of simulated particles were lost on the collimators at $5\sigma_u$ during any simulation. Because of this fully ignorable loss rate, no additional simulations with infinite physical aperture were conducted. Hence, Tab. 2.6 does not list values without collimation for the (HL-)LHC.

If the order of the calculated growth rates is more or less correct, the effect of moving encounter points is so small that only a very large number of bunches and high bunch intensities may lead to a visible effect. Over the duration of the energy ramp, the sum of the normalised emittances $\epsilon_{\mathrm{n}x} + \epsilon_{\mathrm{n}y}$ does not increase by more than $0.01\,\%$ for any filling pattern according to Eq. 2.132, assuming the target beam energy $E_b = 6.5Z\,\mathrm{TeV}$ is reached after $1200\,\mathrm{s}$ in the energy ramp. This effect is therefore fully masked by the effects of IBS. Measuring growth rates as small as those found in the simulations is close to impossible. The general idea of measuring such an effect is to observe the emittance growth of the test beam for different intensities of the counter-rotating proton beam. This way, the IBS growth rate can be disentangled from an additional growth rate resulting from moving encounter points.

2.3.2.3 HL-LHC – Pb-p operation

Amplitude detuning In the presence of sextupole fields as the only source of non-linearities, the linear detuning parameters are

$$\alpha_{xx} = -0.7 \times 10^3\,\mathrm{m}^{-1}\,, \qquad \alpha_{yy} = 0.5 \times 10^3\,\mathrm{m}^{-1}\,, \qquad \alpha_{xy} = -4.3 \times 10^3\,\mathrm{m}^{-1} \tag{2.136}$$

in the HL-LHC. The simulation for the filling patterns L2, L3a and L3b (p-p equivalent proton bunch intensities) are performed with these detuning parameters. Additionally, the L3a settings are also simulated with octupoles switched on, i.e., the detuning parameters equivalent to those in the nominal LHC with $I_{\mathrm{oct}} = 12\,\mathrm{A}$ are used. Equation 2.135 gives the values of the corresponding detuning parameters. These detuning values are not entirely equal to the detuning parameters if the octupoles in the HL-LHC are actually operated at $I_{\mathrm{oct}} = 12\,\mathrm{A}$; however, equal detuning parameters enable easier comparison and interpretation of the simulation results.

Emittance growth Figure 2.29 shows the emittance evolution in the HL-LHC for all four simulation scenarios. The two top plots show the horizontal (left) and vertical (right) emittance evolution while the bottom plot shows the evolution of the sum of the emittances. All simulations were again carried out over 10^6 turns and for 10^6 particles in the test bunch. Table 2.6 gives the linear growth rates obtained via fit for all four simulation scenarios.

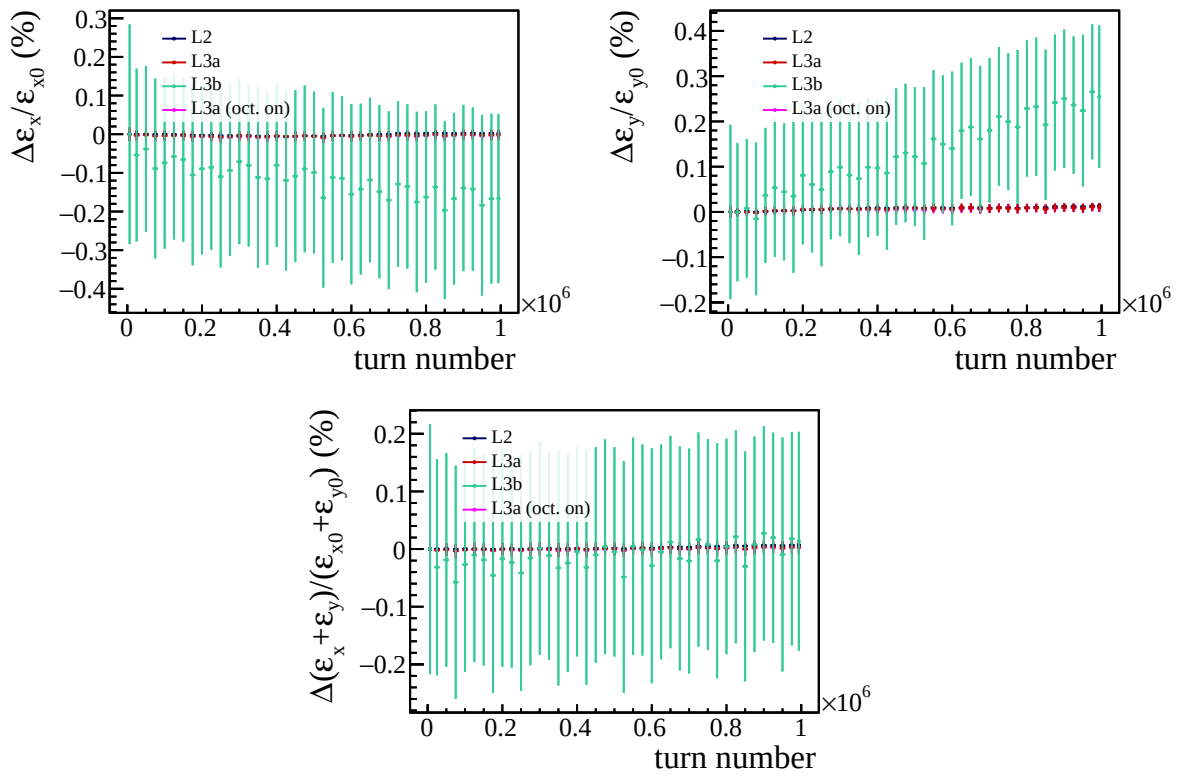

Figure 2.29: Left: Relative horizontal emittance growth normalised to the initial emittance for the HL-LHC over 10^6 turns. Only the HL-LHC filling pattern with $N_b = 1.15 \times 10^{11}$ protons per bunch leads to a small emittance growth. Right: Evolution of the relative vertical emittance growth. Bottom plot: Relative change of the sum of the emittances $\epsilon_x + \epsilon_y$. No obvious growth of the sum of the emittances $\epsilon_x + \epsilon_y$ is observed.

The L2 filling pattern with 684 proton bunches in the proton beam leads to positive growth rates in both transverse planes. The emittance grows in the horizontal plane with $\dot{\epsilon}_x/\epsilon_{x0} = (5 \pm 1) \times 10^{-7}\,\mathrm{Hz}$ and in the vertical plane with $\dot{\epsilon}_y/\epsilon_{y0} = (13 \pm 1) \times 10^{-7}\,\mathrm{Hz}$. The respective emittance doubling times are between 210–560 h. These durations are much larger than IBS growth rates of 13 h in the horizontal plane. These results show that the HL-LHC is slightly more susceptible to the effects of moving encounters than the nominal LHC. In the nominal LHC with the L2 filling pattern, the doubling of the combined emittances $\epsilon_x + \epsilon_y$ is larger than 2500 h, whereas it only takes roughly 310 h in the HL-LHC with the same number of proton bunches and proton bunch intensity to double $\epsilon_x + \epsilon_y$. This finding is coherent with the results from Sec. 2.2.4.3.

The nominal HL-LHC filling pattern with 1232 proton bunches L3a was simulated with octupoles switched on and switched off. Without octupoles, the growth rates in the horizontal plane $\dot{\epsilon}_x/\epsilon_{x0} = (3 \pm 1) \times 10^{-7}\,\mathrm{Hz}$ and in the vertical plane $\dot{\epsilon}_y/\epsilon_{y0} = (10 \pm 1) \times 10^{-7}\,\mathrm{Hz}$ are smaller than the growth rates with 684 bunches (L2), i.e., the growth remains negligible. The

opposite behaviour was observed in the nominal LHC, i.e., an increase of the growth rates was observed when the number of proton bunches was doubled. Active octupoles lead to a slightly smaller horizontal growth rate of $\dot{\epsilon}_x/\epsilon_{x0} = (1 \pm 1) \times 10^{-7}\,\mathrm{Hz}$ and the growth rate of the sum of the emittances reduces from $(\dot{\epsilon}_x + \dot{\epsilon}_y)/(\epsilon_{x0} + \epsilon_{y0}) = (6 \pm 1) \times 10^{-7}\,\mathrm{Hz}$ (octupoles switched off) to $(\dot{\epsilon}_x + \dot{\epsilon}_y)/(\epsilon_{x0} + \epsilon_{y0}) = (5 \pm 1) \times 10^{-7}\,\mathrm{Hz}$ (octupoles switched on). Thus, an increased amplitude detuning has a small mitigating effect in the HL-LHC. From the simulation of the L3a scenario, it can be concluded that no visible emittance growth is expected with 1232 proton bunches and proton bunch intensities of 2.8×10^{10} protons per bunch in future p-Pb runs of the HL-LHC. Stable operation of the HL-LHC in p-Pb configuration at injection energy can be inferred.

The HL-LHC filling pattern with p-p equivalent proton bunch intensities of $N_b = 1.15 \times 10^{11}$ protons per bunch, causes the strongest total emittance growth. While coupling causes the horizontal emittance to shrink with $\dot{\epsilon}_x/\epsilon_{x0} = (-1.42 \pm 0.13) \times 10^{-5}\,\mathrm{Hz}$, the vertical plane grows with $\dot{\epsilon}_y/\epsilon_{y0} = (2.96 \pm 0.10) \times 10^{-5}\,\mathrm{Hz}$. This growth rate corresponds to an emittance doubling time of only $9.4\,\mathrm{h}$. This effect should be visible since IBS effects are much smaller in the vertical plane compared to the horizontal plane. The sum of the emittances grows with $(\dot{\epsilon}_x + \dot{\epsilon}_y)/(\epsilon_{x0} + \epsilon_{y0}) = (45 \pm 10) \times 10^{-7}\,\mathrm{Hz}$ equivalent to a doubling time of $62\,\mathrm{h}$. A study of X. Buffat that is based on a fit of Eq. 2.71 has shown that the current transverse damper of the LHC (ADT) suppresses roughly $50\,\%$ of the growth created by noise [115]. A vertical emittance doubling time of $9.4\,\mathrm{h}$ is therefore possibly prolonged to values in the $20\,\mathrm{h}$ range with an active feedback system. The HL-LHC upgrade includes improved ADT pick-ups (less noise), i.e., this upgrade will possibly lead to a further prolongation of the emittance doubling time. It is therefore highly likely that even the operation with proton bunch intensities of 1.15×10^{11} particles per bunch is stable and still allows reliable operation. The total increase of the sum of the normalised emittances $\epsilon_{\mathrm{n}x} + \epsilon_{\mathrm{n}y}$ at the end of the energy ramp is only at $0.1\,\%$ with p-p equivalent proton bunch intensities. Such an increase would be fully acceptable. For the other filling patters, the total growth of $\epsilon_{\mathrm{n}x} + \epsilon_{\mathrm{n}y}$ at the end of the energy ramp does not exceed $0.02\,\%$ for any filling pattern. IBS remains a much more important effect.

Simulations with infinite physical aperture are once again omitted. During all simulations of the different scenarios, only a maximum of $1.4 \times 10^{-3}\,\%$ of the particles were lost during 10^6 turns. These loss rates are so small that differences between simulations with and without physical aperture are not noticeable. Hence, the growth rates in Tab. 5.2 apply for collimation switched on and switched off. The results for the HL-LHC show that the HL-LHC will face slightly larger growth rates compared to the nominal LHC. The linear analysis in Sec. 2.2.4.3 predicted this result.

2.4 Conclusion

The linear calculations in Sec. 2.2.4 indicated the key differences between the LHC and RHIC and why the effects of moving encounters may lead to potential operational restrictions in RHIC while the operation in the LHC is unproblematic. The lower injection energy of RHIC results in a larger shift d_t of the beam-beam encounter points. The larger shift allows lower orders of $|n|$ of the OKO dipole resonances that are created by the moving encounters to approach the betatron tune spread in RHIC. Besides a larger d_t, the beam-beam kicks applied onto the weak beam are much stronger compared to the LHC. Hence, tune shifts in RHIC tend to be larger compared to those in the LHC and faster emittance growth is expected in RHIC. The IR layout of RHIC enhances the negative influence of moving encounter locations on the beam. While the LHC has large numbers of long-range encounters in each IR (maximum of 19 beam-beam encounters in ATLAS/CMS with $100\,\mathrm{ns}$ bunch spacing), the common beam pipe in the IRs is short compared to the bunch spacing in RHIC (maximum of 2 long-range beam-beam encounters with 110 bunches). Hence, the integrated dipole kick generated by the long-range encounters fluctuates more strongly in relative terms than in the LHC once a long-range encounter moves in or out of the common beam pipe. The same observation can be made for the oscillation of the transverse tunes. In the LHC, the tunes and integrated dipole kicks fluctuate less because of more long-range encounters occurring in the IRs, and the emittance growth tends to be smaller. This is one of the main reasons the LHC is less susceptible to the effects of moving long-range encounters besides the much larger beam energy at injection.

The linear analysis neglects non-linear effects that may lead to either suppression or enhancement of the emittance growth caused by moving encounter points. A simplified pseudo non-linear tracking code was developed in Sec. 2.3 to include amplitude detuning and synchrotron motion into the simulation. The code confirmed RHIC as unstable for the three different deuteron filling patterns of different beam intensities. The growth rates are large enough that the emittance doubling time is in the range of $1\,\mathrm{min}$ or slightly larger as was reported in [10]. This is an important benchmark result, since a simulation code not reproducing the observed instabilities in RHIC is unlikely to model the effects of moving encounters accurately enough.

The different simulation scenarios for the nominal LHC have reproduced the LHC as stable. That was experimentally confirmed in 2011, 2012, 2013 and 2016. For three different filling patterns of different beam intensities, no significant emittance blow-up could be concluded. The smallest emittance doubling time of roughly $110\,\mathrm{h}$ is observed if the LHC is operated with 1232 bunches in LHC Run 3 (requires slip-stacking in the SPS). In all other cases, the emittance doubling time was much larger and easily multiple hundred hours long. The horizontal IBS growth time is expected to be $\tau_{\mathrm{IBS},x} \approx 13\,\mathrm{h}$ during the time the beams remain at injection energy (less than $1\,\mathrm{h}$) and IBS is therefore significantly more relevant than the growth rates that

were extracted from the simulations. Potential observations of unaccounted growth at injection due to moving encounter locations are not supported by these findings.

The emittance evolution in RHIC and the nominal LHC were reproduced qualitatively by the tracking routine. A quantitative comparison is hardly possible for the nominal LHC and a rough estimate of an emittance doubling time of $1\,\mathrm{min}$ was reproduced for RHIC. These are important results since they are consistent with the observations that were made in RHIC and the LHC. The agreement between the simulations and experimental observations strengthens the meaningfulness of predictions for p-Pb operation in the HL-LHC. The tracking study yielded emittance growth rates in the HL-LHC that are of the same magnitude as those in the nominal LHC. These results are highly encouraging and suggest that p-Pb operation in the HL-LHC will not face any issues resulting from the effects of moving beam-beam encounters. A study with p-p equivalent proton bunch intensities caused the sum of the emittances to double within $9.4\,\mathrm{h}$; however, the simulations did not include the transverse feedback system of the LHC, which is actively countering the emittance growth due to dipole noise. Hence, a vertical emittance doubling time of $9.4\,\mathrm{h}$ in the presence of nominal proton-proton intensities could improve to values close to $20\,\mathrm{h}$. The increase of the proton intensity is therefore a viable option to enhance the peak luminosity since no intensity limit for the proton beam was found up to bunch intensities of $N_b = 1.15 \times 10^{11}$ protons per bunch.

CHAPTER 3

Collisions with unequal beam sizes

The collision of beams with unequal beam sizes was of concern before the 2013 Pb-p run of the LHC took place. The Pb beam size is often $70\,\%$ larger than that of the proton beam and previous experiments at other accelerators have shown a reduced beam lifetime of the larger of the two beams during the collision of the beams in such conditions. The concern was that the strong non-linear part of the beam-beam force of the proton beam may cause diffusion close to the core of the Pb beam. In the Super Proton-Antiproton Synchrotron (Sp$\overline{\text{p}}$S), the beam lifetime of the proton beam reduced with an increasing ratio between the proton beam size and the smaller antiproton beam size [12]. The Hadron-Elektron-Ring-Anlage (HERA) faced difficulties to establish stable conditions when colliding protons and electrons of unequal sizes as well [11]. A much smaller beam size of the electron beam reduced the lifetime of the proton beam substantially from usually 50–$100\,\text{h}$ to $0.5\,\text{h}$ in very asymmetric conditions (electron beam size factor 4 smaller than that of the proton beam).

This chapter focuses on the tune footprint of the Pb beam colliding with a proton beam of a smaller geometric size. A first analysis is given in [3] and follows the arguments given in [116]. This analysis shows the shift of the particle distribution in tune space towards the non-linear part of the beam-beam force of the proton beam; however, the analysis does not quantify or prove whether actual tune diffusion in the bunch core is generated by the beam-beam interactions. In addition, differences between the two transverse planes are not made. This chapter assumes the 2016 Pb-p beam parameters and accelerator optics. Section 4.2 gives an in-depth description of the 2016 run.

3.1 Concepts

To study the tune diffusion close to the bunch core, a so-called frequency-map analysis (FMA) is used on a simplified model. The model is the same as in Chapter 2 in Sec. 2.3.1. This time, the approach of linearising the beam-beam force and calculating IR matrices is no longer sufficient and the actual non-linear beam-beam kick is used for the head-on and long-range encounters. If both beams have the same magnetic rigidity of the proton equivalent $B\rho = p_{\mathrm{p}}/e$ as in LHC collision, the tune shift does not depend on any parameter of the witness particle. Instead, it depends only on the bunch charge $N_{b2}Z_2$ and geometric emittance ϵ_2 of the source bunch (assuming a round beam)

$$\xi_u = \frac{N_{b2} r_p m_p Z_2^2}{4\pi m_2 \epsilon_{\mathrm{n2}}} = \frac{k}{8\pi\epsilon_2} \qquad \text{with} \qquad k = \frac{2N_{b2} r_p Z_2}{\gamma_p} \,. \tag{3.1}$$

The beam-beam tune shift is therefore the same for protons and Pb ions if the source bunch has the same geometric emittance and total charge. If the source bunch is not round and instead elliptical, as it often occurs in the LHC (slightly smaller vertical emittances), the beam-beam kick reads [95]

$$(\Delta x',\, \Delta y') = \frac{k}{2}(\mathrm{Im}\left[\Pi(x, y, \sigma_x, \sigma_y)\right],\, \mathrm{Re}\left[\Pi(x, y, \sigma_x, \sigma_y)\right]) \qquad \text{with} \tag{3.2}$$

$$\Pi(x, y, a, b) = \begin{cases} \sqrt{\frac{2\pi}{a^2-b^2}} \left[w\left(\frac{x+iy}{\sqrt{2(a^2-b^2)}}\right) \right. & \\ \qquad \left. - \exp\left(-\frac{x^2}{2a^2} - \frac{y^2}{2b^2}\right) w\left(\frac{xb/a+iya/b}{\sqrt{2(a^2-b^2)}}\right) \right] & (a > b,\ y \geq 0) \\ -\Pi^*(x, -y, a, b) & (a > b,\ y < 0) \\ 2\frac{ix+y}{x^2+y^2}\left[1 - \exp\left(-\frac{x^2+y^2}{a^2}\right)\right] & (a = b) \\ i\Pi^*(y, x, b, a) & (a < b)\,, \end{cases} \tag{3.3}$$

$$w(x) = (1 - \mathrm{erf}(-ix)) \exp\left(-x^2\right) \,. \tag{3.4}$$

The linear (head-on) tune shift is quite similar to the one given in Eq. 3.1, however, it depends now on both the vertical and horizontal emittances

$$\xi_{\mathrm{HO},u} = \frac{k}{4\pi(\epsilon_{u,2} + \sqrt{\epsilon_{x,2}\epsilon_{y,2}})} \,. \tag{3.5}$$

An important property of the beam-beam tune shift in Eqs. 3.1 & 3.5 is that it is constant with energy; therefore, important features of the tune footprint are maintained at different energies.

3.1.1 Simplified model

The simplified model which is used in this chapter is roughly the same as the model given in Sec. 2.3.1. The model therefore includes the pseudo non-linear transfer between the non-linear

beam-beam encounters. This approximation is assumed to be sufficient to investigate whether beam-beam interactions introduce tune diffusion close to the bunch core. The justification is that non-linearities from sextupoles and octupoles become stronger towards larger transverse amplitudes while this analysis is meant to investigate the behaviour close to the bunch core. With no head-on collisions, the LHC beams are stable with a lifetime of roughly $100\,\mathrm{h}$ for Pb beams at top energy. Hence, non-linearities of the lattice are expected to be considerably small; however, the effects of lattice non-linearities and beam-beam interactions do not behave linearly. This means the head-on beam-beam interaction does not limit the dynamic aperture by itself, but the dynamic aperture with switched on sextupoles and octupoles decreases when head-on beam-beam interactions are introduced, i.e., the combination of the beam-beam force with other non-linearities may reduce the dynamic aperture additionally.[1] If one considers this effect small in Pb-p collision because of the head-on beam-beam tune shift and the octupole current being much smaller than in p-p collisions, this model suffices. As in the previous chapter, the linear detuning by sextupoles and octupoles is still implemented via the modulation of the phase advance (see Eq. 2.121).

In contrast to the model in Sec 2.3.1, the IR matrices are replaced by the actual non-linear beam-beam kick given in Eq. 3.2 at the beam-beam encounter positions s_i in the IRs. The encounter points s_i are fixed since the RF cogging process equalises the revolution frequencies f_0 in Stable Beams. The model includes the head-on and all long-range encounters in the IRs, although the effect of the long-range encounters is small because of the large bunch spacing and crossing angles at the IPs. Between the different s_i, the linear phase advance ϕ_u is once again modified according to the linear detuning parameters α_{mn} generated by the sextupoles and octupoles. The iteration process for a phase space vector $\mathbf{r} = (x, x', y, y')^{\mathrm{T}}$ is (cf. Eqs. 2.122–2.127)

$$\mathbf{r}_{j+\frac{1}{2}} = \left(x_j, x'_j + \Delta x'(\mathbf{r}_j), y_j, y'_j + \Delta y'(\mathbf{r}_j)\right)^{\mathrm{T}} \tag{3.6}$$

$$J_{u,j+1} = \frac{1}{2}(\tilde{u}^2_{j+\frac{1}{2}} + \tilde{u}'^2_{j+1/2}) \tag{3.7}$$

$$\Delta Q_{u,j+1} = \alpha_{ux} J_{x,j+1} + \alpha_{uy} J_{y,j+1} \tag{3.8}$$

$$\phi_{u,j+1} = (\phi_u(s_{i+1}) - \phi_u(s_i)) \left(1 + \frac{2\pi \Delta Q_{u,j+1}}{\mu_u}\right) \tag{3.9}$$

$$\mathbf{r}_{j+1} = \mathbf{V}^{-1}(s_{i+1}) \mathbf{R}_{i,i+1}(\phi_{x,j+1}, \phi_{y,j+1}) \mathbf{V}(s_i) \mathbf{r}_{j+\frac{1}{2}} \tag{3.10}$$

$$i = i + 1\,. \tag{3.11}$$

The beam-beam kick in Eq. 3.6 uses the formula for elliptical beams from Eq. 3.2.

[1] The beam-beam force decreases towards large transverse amplitudes. It potentially introduces a chaotic layer at small transverse amplitudes if the beam-beam interaction is strong, but the motion stabilises towards larger transverse amplitudes as the beam-beam force gets weaker.

3.1.2 Frequency map and tune diffusion

An important tool to investigate non-linear dynamics in accelerator physics is FMA [108, 117]. In this study, the tracking process comprises the tracking of particles over 10^4 turns for different initial transverse coordinates and transverse momenta of the particles. After the tracking, the particle tunes are determined for the initial 500 turns $Q_{u,i}$ and for the last 500 of the 10^4 turns $Q_{u,f}$. The tune difference between the two results is $\Delta Q_u = |Q_{u,f} - Q_{u,i}|$. Particles close to a resonance will be display some sort of tune diffusion, i.e., the tune difference ΔQ_u is non-zero. By plotting the final tune state $(Q_{x,f}, Q_{x,f})$ (tune footprint) versus the diffusion coefficient

$$D = \frac{1}{2} \log \left(\Delta Q_x^2 + \Delta Q_y^2 \right) \tag{3.12}$$

in a three-dimensional plot or heat map (frequency map), the resonances interacting with the particles become visible in the tune diagram. This is because resonances create tune diffusion (increased coefficient D) along resonance lines and a *crack* may appear if a resonance is strong, i.e., particles are pushed away from the resonance line leaving an empty space in the tune footprint. A critical step during the generation of the frequency map is the reliable calculation of the tunes from the tracking data. The main difficulty arises from the limited number of turns. The resolution of a DFT performed on the tracking data of 500 turns is very limited (tune increment is only at 0.002). It is therefore advisable to obtain the tunes via the numerical analysis of fundamental frequencies (NAFF) [118]. A respective `python` implementation was developed at CERN [119].

3.2 Comparison between different collision systems

As a first step, the tune footprint for a single head-on beam-beam encounter is compared for the different collision systems p-p, Pb-Pb and p-Pb in the LHC. Table 3.1 lists the important beam parameters. The tune footprints for the different scenarios assuming a single beam-beam encounter and an otherwise linear lattice are calculated following the Hamiltonian given in Eq. 2.46 (elliptical beam-beam potential is considered). The tune footprints for the scenarios in Tab. 3.1 are shown in Fig. 3.1. A tune footprint embeds the tunes for different transverse amplitudes up to $6\sigma_u$. Along the transverse arcs of the tune footprint, the expression $\sqrt{(x/\sigma_x)^2 + (y/\sigma_y)^2} = j$ with $j \in \{0, 1, 2, 3, 4, 5, 6\}$ is fulfilled.

In p-p collisions, the bunch intensities are high with $N_b = 1.15 \times 10^{11}$ particles per bunch, generating a large beam-beam tune shift of $\xi_{\mathrm{HO}} = 0.007$. The tune shift is smaller in Pb-Pb collisions because of the smaller bunch charge of the counter-rotating Pb bunch and its larger geometric emittance. The tune shift with 2016 Pb bunch parameters is $\xi_{\mathrm{HO}} \approx 4.8 \times 10^{-4}$ and the particle tunes barely deviate from the nominal tune. Since the Pb bunch properties are the same in Pb-Pb and p-Pb collisions, the Pb footprint in Pb-Pb collisions and the proton footprint

Table 3.1: Listed are typical beam parameters in p-p, Pb-Pb and Pb-p collisions and the resulting linear tune shift from a single head-on collision. Values for Pb-p operation at $E_b = 4Z\,\mathrm{TeV}$ are given in grey.

Parameter		p-p	Pb-Pb	Pb - p	
Beam energy E_b	Z TeV	6.5	6.37	6.5 (4)	
Lorentz factor γ	1	6928	2697	2752 (1693)	6928 (4263)
Bunch intensity N_b	10^8	1150	2.1	2.1	280
Normalised emittance ϵ_n (x / y)	μm	1.9	2.0 / 1.5	2.0 / 1.5	1.4
Geometric beam-size ratio $\hat{r} = \frac{\sigma_{u1}}{\sigma_{u2}}$	1	1	1	1.6–1.9	0.5–0.6
Beam-beam constant k	pm	51.0	7.8	12.4 (20.2)	7.6 (12.4)
Beam-beam tune shift ξ_{HO} (x / y)	10^{-4}	73.9	4.5 / 5.2	24.4	4.5 / 5.2

in p-Pb collisions are roughly equal. In Pb-p collisions, the Pb tune footprint is of intermediate size. The beam-beam parameter is $\xi_{\mathrm{HO}} = 24.4 \times 10^{-4}$ here. The footprint is therefore well inside the p-p tune footprint. Even with four head-on collisions, the Pb-p footprint is just of the size of the p-p footprint of a single head-on collision. An argument for stable behaviour in asymmetric Pb-p configuration is therefore that the Pb-p tune footprint is well inside the p-p tune footprint and since no strong resonances by the magnetic lattice and beam-beam encounters lead to the deterioration of the proton beams in p-p configuration, stability in Pb-p operation can be expected. This argument is especially true since the dynamic aperture is larger than 6σ in p-p operation although small crossing angles and a small bunch spacing lead to strong long-range beam-beam encounters that excite destructive odd resonances. These strong long-range beam-beam encounters do not occur in Pb-p collisions.

The previous argument does not consider the possibility of diffusion close to the bunch core. This may occur if the ratio of the geometric beam sizes of the Pb and proton beam $\hat{r} = \sigma_{\mathrm{Pb}}/\sigma_{\mathrm{p}}$ is large. If a Pb bunch collides with a proton bunch which is, e.g., $40\,\%$ ($\hat{r} = 1.67$) smaller, the detuning and non-linear behaviour take place predominantly at small transverse actions. This means that the tune footprint stretches out at small amplitudes more and more with an increasing ratio $\hat{r}$ but remains unchanged in the 6σ area. The derivation of the particle density in the tune space is already discussed in [3, 116] and is not repeated here. The frequency maps for different ratios $\hat{r}$ are discussed in the next section.

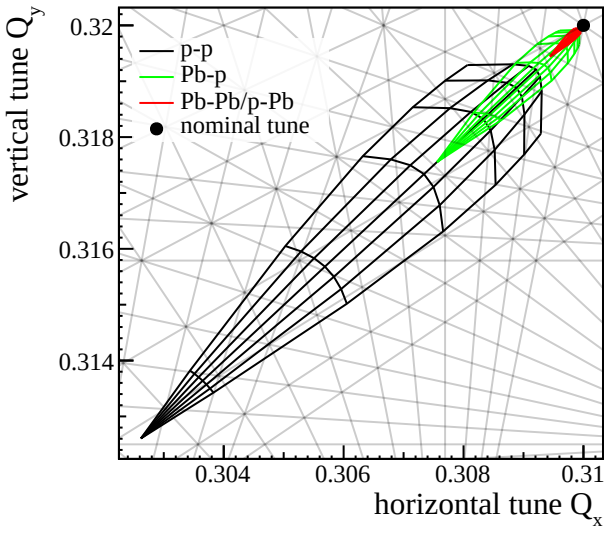

Figure 3.1: Displayed are the tune footprints for head-on collisions according to the system scenarios given in Tab 3.1 for the 2016 collision (fractional) tunes. Optical resonances up to 20th order are displayed (grey). The tune footprint refers to the first-mentioned particle type, i.e., it refers to particle A in a A-B collision system.

3.3 FMA of Pb-p collisions at $E_b = 6.5Z$ TeV for different beam-size ratios

The beam energy is assumed to be $E_b = 6.5Z\,\mathrm{TeV}$ in this analysis. The energy is not too important since the beam-beam tune shift remains unchanged. Linear detuning parameters of

$$\alpha_{xx} = 104.4 \times 10^3\,\mathrm{m}^{-1}\,, \qquad \alpha_{yy} = 106.4 \times 10^3\,\mathrm{m}^{-1}\,, \qquad \alpha_{xy} = -82.0 \times 10^3\,\mathrm{m}^{-1} \quad (3.13)$$

are assumed in the simulation. These values are accomplished at octupole currents of $I_{\mathrm{oct}} = 188\,\mathrm{A}$ at $E_b = 6.5Z\mathrm{TeV}$ ($\sqrt{s_{\mathrm{NN}}} = 8.16\,\mathrm{TeV}$) and were regularly used during the 2016 p-Pb run. Equal linear detuning parameters α_{uj} at $4Z\mathrm{TeV}$ are accomplished with an octupole current of $I_{\mathrm{oct}} = 116\,\mathrm{A}$.[2] The results at $E_b = 4Z\,\mathrm{TeV}$ ($\sqrt{s_{\mathrm{NN}}} = 5.02\,\mathrm{TeV}$) with an octupole current of $I_{\mathrm{oct}} = 116\,\mathrm{A}$ (the parameters in Eq. 3.13 apply) are given in Appendix B.3 in Figs. B.8–B.11 for completeness. The conclusions which are going to be drawn for $E_b = 6.5Z\,\mathrm{TeV}$ in this section are perfectly valid for the beam energy $E_b = 4Z\,\mathrm{TeV}$ as well. Each study for a different beam-size ratio $\hat{r}$ is performed with 5.8×10^4 particles that are randomly distributed in x, x', y and y' up to an equivalent of $6\sigma_u$. The sampling of the phase space is denser at small transverse actions since the bunch core is the region of interest in this study. The simulation assumes the head-on collision in all four IRs; however, this is not necessarily true since ALICE

[2]Because of adiabatic damping, the beam size is larger at $E_b = 4Z\,\mathrm{TeV}$ than at $E_b = 6.5Z\,\mathrm{TeV}$. The equivalent detuning per α_{uj}/ϵ_u is therefore achieved at the much smaller value $I_{\mathrm{oct}} = 71\,\mathrm{A}$ at $E_b = 4Z\,\mathrm{TeV}$.

is levelled via separation. Table 4.5 in Chapter 4 lists the IP parameters as used during the 2016 p-Pb run at $E_b = 6.5Z$ TeV. The parameters are not too important because the crossing angles are neglected in the calculation of the beam-beam kick and because the β^* is the same for the proton and Pb beam. The bunch intensities of the proton beam and the emittances of the test Pb bunch are taken from the Pb-p column of Tab. 3.1, i.e., the Pb bunch is slightly elliptical while the proton beam is assumed round in the following.

Roughly equal beam sizes – $\epsilon_{\mathrm{np}} = 3.5\,\mu\mathrm{m}$ The first considered case is the collision with a very large proton beam. The proton beam has a normalised emittance of $\epsilon_{\mathrm{np}} = 3.5\,\mu\mathrm{m}$; therefore, the beam-size ratio is roughly at $\hat{r} \approx 1.1$ (average between both planes). The proton beam is therefore well-matched to the Pb beam in terms of size. The left plot of Fig. 3.2 shows the full tune footprint.

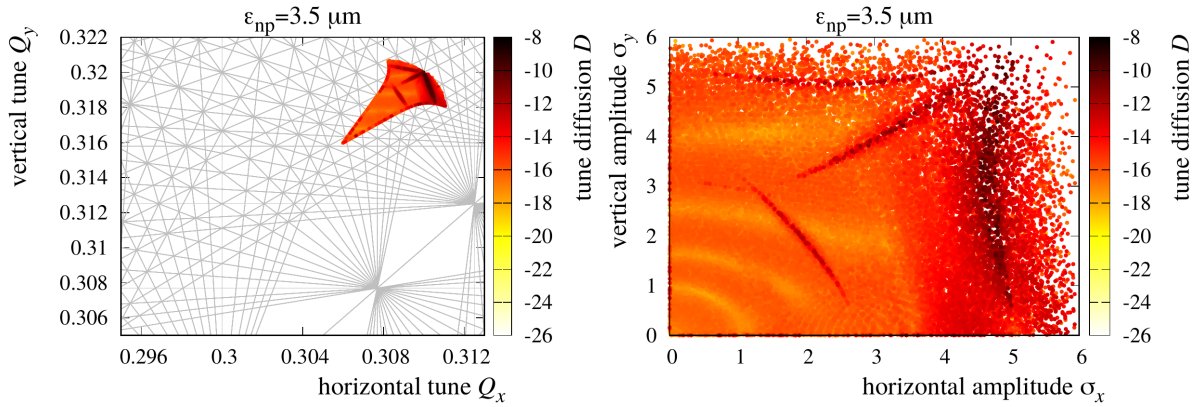

Figure 3.2: Left: Frequency map (explanation given in Sec. 3.1.2) of the Pb beam at $E_b = 6.5Z$ TeV with $\epsilon_{\mathrm{np}} = 3.5\,\mu\mathrm{m}$ ($\hat{r} \approx 1.1$). The optical resonances up to 20th order are drawn in grey. The footprint is small, and the diffusion reaches a maximum of $D = -8$. Right: The tune diffusion as a function of the initial absolute transverse amplitudes in units of the respective beam size. Particles close to the bunch core are virtually unaffected.

The head-on tune shift for the nominal particle ($J_x = J_y = 0$) is small with $\xi_u \approx -0.004$ considering the beams collide in all four IPs. The tune footprint is small and the maximum tune diffusion is $D = -8$. In FMA studies that include the lattice non-linearities, crossing angles and long-range beam-beam encounters, the tune diffusion close to the dynamic aperture is between $D = -5$ and $D = -2$ [117]. Hence, a tune diffusion of $D = -8$ is very small. The resonance lines appearing at large actions are mainly of 16th order. The right plot of Fig. 3.2 shows the tune diffusion as a function of the absolute transverse amplitude in units of the respective beam size. Most particles of the particle distribution are in the 0–$2\sigma_u$ region. No noteworthy tune diffusion is observed in this region.

Slightly different beam sizes – $\epsilon_{\mathrm{np}} = 2.5\,\mu\mathrm{m}$ The second case which is studied assumes a proton beam of a normalised emittance $\epsilon_{\mathrm{np}} = 2.5\,\mu\mathrm{m}$ equivalent to the beam-size ratio of roughly $\hat{r} \approx 1.3$. Figure 3.3 shows the frequency map on its left. With increasing ratio $\hat{r}$, the tune footprint stretches out at small actions. This results from the faster decrease of the detuning with increasing transverse amplitude than previously because of the smaller proton beam. The tune shift of the nominal particle is at $\xi_u \approx -5.5 \times 10^{-3}$. The maximum diffusion has not changed. The right plot of Fig. 3.3 shows that a weak resonance line moves towards the bunch core, but the diffusion is weak and only in the $D \approx -15$ range. It is unlikely that this weak diffusion enhances any resonance from the magnetic lattice in a way that it leads to a significant reduction of the dynamic aperture. The strongest diffusion is observed in the 5σ–6σ range of the tune footprint created by 16th order resonances.

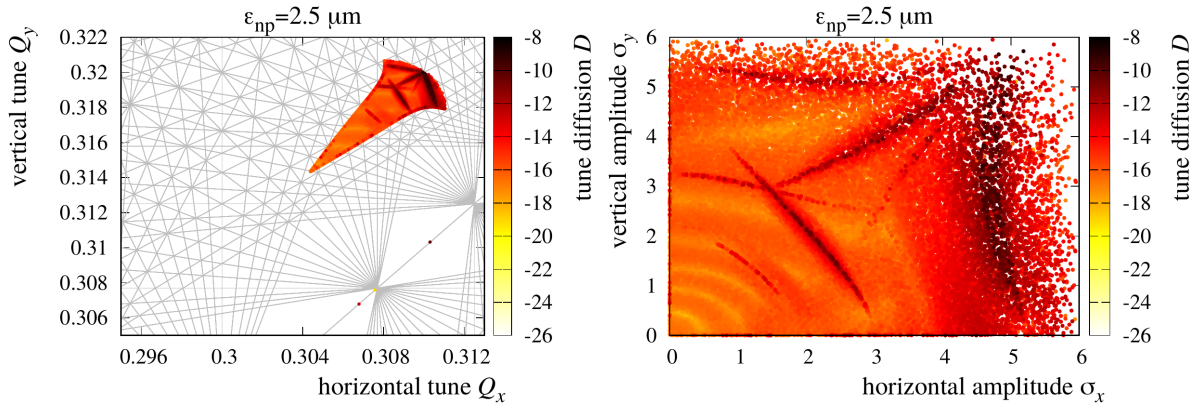

Figure 3.3: Left: Frequency map of the Pb beam at $E_b = 6.5Z\,\mathrm{TeV}$ with $\epsilon_{\mathrm{np}} = 2.5\,\mu\mathrm{m}$ ($\hat{r} \approx 1.3$). Optical resonances up to 20th order are drawn in grey. The footprint is slightly larger compared to Fig. 3.2 but remains small. The maximum diffusion has not changed. Right: The tune diffusion as a function of the initial absolute transverse amplitudes. A very weak resonance line is present at around 2σ.

Nominal beam sizes – $\epsilon_{\mathrm{np}} = 1.5\,\mu\mathrm{m}$ A proton emittance of $\epsilon_{\mathrm{np}} = 1.5\,\mu\mathrm{m}$ is the nominal case in Pb-p collisions and is equivalent to a beam-size ratio of roughly $\hat{r} \approx 1.7$. The left plot of Fig. 3.4 shows the frequency map. The tune footprint is stretched out in the small-action region while it remains unchanged at large actions. The maximum tune diffusion has not changed and is the strongest at large transverse amplitude. The width of the 16th order resonances has increased slightly. From the right plot of Fig. 3.4, it is easy to see that more resonances appear close to the bunch core mainly because the tune footprint moves toward the 10th order resonance at $Q_x = 0.3$ and crosses 12th and 14th order resonances. The simulation assumes head-on collisions in all four IRs; however, ALICE is mostly levelled and the maximum tune shift should therefore not reach the 10th order resonance during real operation.

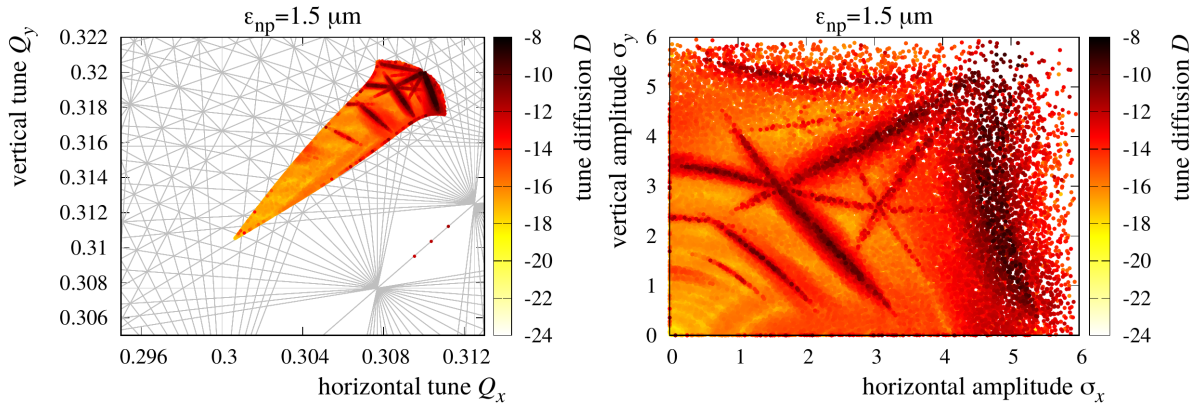

Figure 3.4: Left: Frequency map of the Pb beam at $E_b = 6.5Z\,\mathrm{TeV}$ with proton emittances of $\epsilon_{\mathrm{n,p}} = 1.5\,\mu\mathrm{m}$ ($\hat{r} \approx 1.7$). The beam-beam tune shift has increased and broader resonance lines appear towards larger transverse amplitudes. Right: The tune diffusion as a function of the initial absolute transverse amplitudes. Close to the bunch core, slightly more tune diffusion becomes noticeable. Since the proton beam is small, the tune shift becomes small quickly since the kick amplitude decreases fast with increasing Pb action.

Minimal proton beam size – $\epsilon_{\mathrm{np}} = 1\,\mu\mathrm{m}$ The last case that is analysed assumes very small proton emittances of $\epsilon_{\mathrm{np}} = 1\,\mu\mathrm{m}$. The ratio of the beam sizes is $\hat{r} \approx 2.1$, i.e., the proton bunch is less than half the size of the Pb bunch. The tune footprint in Fig. 3.5 is very large and the tune footprint extends beyond the 10th order resonance at $Q_x = 0.3$; however, the 10th order resonance is not strongly excited by the beam-beam force alone. One can conclude that the beam-beam force itself does not lead to strong diffusion in neither the bunch core nor the bunch tails in this model.

3.4 Conclusion

The presented FMA for beam-size ratios between $\hat{r} = 1.1$ and $\hat{r} = 2.1$ has shown that no noteworthy tune diffusion is generated in neither the bunch core nor at large amplitudes in the 5σ–6σ range. The model does not include the non-linear elements of the lattice and also does not consider off-energy particles; however, the results show that the additional diffusion generated by the beam-beam interactions in the IPs is unlikely to contribute in any significant way to the diffusion rates generated by non-linear elements of the lattice.

Much smaller proton beam sizes enhance the linear beam-beam tune shift and the tune footprint intersects consequently various resonance lines. Studies have shown that the 10th order resonance is slightly amplified when colliding with a non-zero crossing angle and not strictly head-on [120]; however, the extra diffusion generated by the collision with crossing

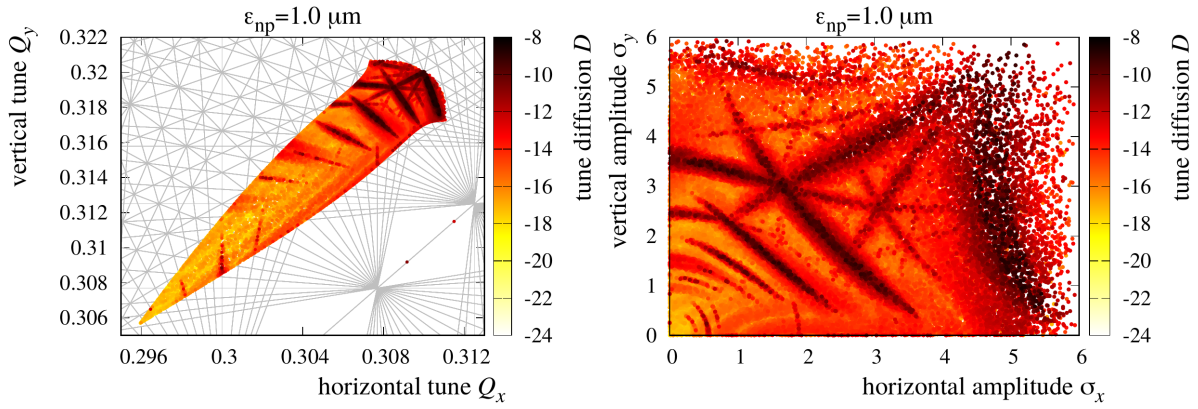

Figure 3.5: Left: Frequency map of the Pb beam at $E_b = 6.5Z$ TeV with proton emittances of $\epsilon_{\mathrm{n,p}} = 1.0\,\mu\mathrm{m}$ ($\hat{r} \approx 2.1$). The tune diffusion is still small. Right: The tune diffusion as a function of the initial absolute transverse amplitudes. Because of the small proton beam, the beam-beam tune shift is large, however, the detuning reduces quickly with increasing transverse action since the beam-beam force decreases rapidly. More resonance lines appear at small actions, but the tune diffusion is still very small.

angle is expected to be small and the 10th order resonance is only weakly driven by the non-linear lattice [121]. It can be inferred that the operation is stable even at large tune shifts.

This study and the experience of Pb-p operation with unequal beam sizes ($\hat{r} \approx 2.2$) do not give evidence of an effect similar to the observations made at HERA and the Sp$\bar{\mathrm{p}}$S. The LHC and the LHC working point is potentially less susceptible to diffusion from beam-beam encounters; however, there is also the possibility of other effects generating the poor beam lifetime in HERA and the Sp$\bar{\mathrm{p}}$S. In the case of HERA, multiple effects are mentioned in the respective paper which are potentially contributing to the poor beam lifetime of the proton beam. The HERA tune had to be adjusted carefully between $Q_{x,y} = 31.286$ and $Q_{x,y} = 31.3$ to avoid the 7th and 10th order resonances. The tune shift introduced by the beam-beam effect was in the $\xi_{\mathrm{HO}} \approx 0.001$ range for the proton beam. In combination with chromaticity and tune oscillations from power supply ripples [122, 123], additional sidebands to the optical resonances are introduced limiting the window in the tune diagram even further. The electron beam was not only smaller than the proton beam, but it was also highly elliptical. This generates different tune shifts in the two transverse planes. All the mentioned effects and misalignments of the electron beam in the IR may have led to the poor proton lifetime.

In the Sp$\bar{\mathrm{p}}$S, the strong 16th and 13th order resonances close to the working point are possibly the reason the poor proton lifetime was observed. Via scraping of the antiproton beam, the beam size was reduced; however, the linear beam-beam tune shift shrank by 40 % as the bunch intensity was reduced by the scraping. As a result, the tunes of more particles of the proton beam are possibly shifted into the vicinity of the two mentioned resonance lines.

CHAPTER 4

The 2016 proton-lead run of the Large Hadron Collider

The 2016 p-Pb run of the LHC [5] was the most recent and the most successful of the two full one-month p-Pb runs of the LHC. The 2016 p-Pb run was particularly challenging as the experiments requested two different beam energies and a beam direction reversal. Table 4.1 lists the requested and accomplished values of the experiments. A key parameter of heavy-ion collisions is the nucleon-nucleon (NN) centre-of-mass energy $\sqrt{s_{\mathrm{NN}}}$. In symmetric collisions (same ion species and momentum), the NN centre-of-mass energy reads $\sqrt{s_{\mathrm{NN}}} = 2cp_{\mathrm{p}}Z/A$ with Z being the atomic number and A being the number of nucleons of the ion type. If the two colliding ions are of a different type, the equation modifies to

$$\sqrt{s_{\mathrm{NN}}} = 2cp_{\mathrm{p}}\sqrt{\frac{Z_1 Z_2}{A_1 A_2}} \tag{4.1}$$

with the indices 1 and 2 referring to the two ion species. Equation 4.1 assumes equal magnetic rigidities for the two colliding ions as it is the case in p-Pb collisions in the LHC. The first part of the 2016 p-Pb run comprised operation at beam energies of $E_b = 4Z\,\mathrm{TeV}$ equivalent to the centre-of-mass energy $\sqrt{s_{\mathrm{NN}}} = 5.02\,\mathrm{TeV}$ (same $\sqrt{s_{\mathrm{NN}}}$ as during the 2013 p-Pb run, 2015 p-p reference run and 2015/2018 Pb-Pb runs). This part of the run was aimed for the ALICE experiment to accomplish 7×10^8 events with a minimum-bias event trigger and the luminosity production in the other three experiments was only of secondary interest. This part of the p-Pb run did not require a beam-direction reversal and was operated with protons in Beam 1 and Pb ions in Beam 2. The second and major part of the 2016 run was conducted with beam energies of $E_b = 6.5Z\,\mathrm{TeV}$ equivalent to a centre-of-mass energy of $\sqrt{s_{\mathrm{NN}}} = 8.16\,\mathrm{TeV}$. During this

part of operation, the priority was no longer primarily on ALICE and the design luminosity[1] $\mathcal{L} = 1.15 \times 10^{29}\,\mathrm{cm}^{-2}\mathrm{Hz}$ was exceeded regularly. The operation at $\sqrt{s_{\mathrm{NN}}} = 8.16\,\mathrm{TeV}$ included a beam-direction reversal as the asymmetric detectors ALICE and LHCb required interchanging the beams to cover a wider rapidity range. The rapidity $y = \frac{1}{2}\log\left((E+p_z)/(E-p_z)\right)$ is zero for particles emerging exactly transverse to the beam axis z while it is $\pm\infty$ for particles emerging parallel or antiparallel with respect to the beam direction. In collisions of unequal nuclei, particles emerge with a central rapidity shift

$$\Delta y \approx \frac{1}{2}\log\left(\frac{Z_1 A_2}{A_1 Z_2}\right) = \begin{cases} 0 & \text{in p-p, Pb-Pb collisions} \\ 0.47 & \text{in p-Pb collisions} \\ -0.47 & \text{in Pb-p collisions} \end{cases} \tag{4.2}$$

from the collisions since the NN centre-of-mass reference frame does not coincide with the laboratory frame of the detector.

Table 4.1: List of requested luminosities and beam time as well as the achieved values for the $\sqrt{s_{\mathrm{NN}}} = 5.02\,\mathrm{TeV}$ part (top) and $\sqrt{s_{\mathrm{NN}}} = 8.16\,\mathrm{TeV}$ part (bottom) of heavy-ion operation in 2016. Table adapted from [5].

	ATLAS/CMS	ALICE	LHCb	LHCf
	$\sqrt{s_{\mathrm{NN}}} = 5.02\,\mathrm{TeV}$; p-Pb			
Target	–	7×10^8 events	–	–
Achieved	0.48–$0.53\,\mathrm{nb}^{-1}$	7.8×10^8 events	–	–
	$\sqrt{s_{\mathrm{NN}}} = 8.16\,\mathrm{TeV}$; p-Pb / Pb-p			
Target	$50\,\mathrm{nb}^{-1}$ / $50\,\mathrm{nb}^{-1}$	$10\,\mathrm{nb}^{-1}$ / $10\,\mathrm{nb}^{-1}$	$10\,\mathrm{nb}^{-1}$ / $10\,\mathrm{nb}^{-1}$	9 h–12 h
Achieved	ATLAS: $66\,\mathrm{nb}^{-1}$ / $118\,\mathrm{nb}^{-1}$ CMS: $70\,\mathrm{nb}^{-1}$ / $124\,\mathrm{nb}^{-1}$	$14\,\mathrm{nb}^{-1}$ / $25\,\mathrm{nb}^{-1}$	$12\,\mathrm{nb}^{-1}$ / $19\,\mathrm{nb}^{-1}$	9.5 h

During the second part of the run with beam energies of $E_b = 6.5Z\,\mathrm{TeV}$, in particular, the evolution of the bunch properties (emittances, bunch length and intensity) during the fills varied strongly among bunches. The main reason for different lifetimes of the bunches was the collision schedule of head-on collisions in the IPs (see Sec. 4.1.5). Section 4.1 will provide the concepts of luminosity, cross sections and beam evolution in a heavy-ion collider. Section 4.2 will summarise the 2016 p-Pb run while Section 4.3 will analyse the phenomenon of different lifetimes and the evolution of the bunch properties of 2016 Pb-p fills at $E_b = 4Z\,\mathrm{TeV}$ and $E_b = 6.5Z\,\mathrm{TeV}$ [13]. This analysis will also give evidence on whether unaccounted losses occur in the LHC.

[1] The initial LHC design [1] did not foresee p-Pb operation. The first luminosity estimate of the LHC in p-Pb collisions is given in [36] as $\mathcal{L} = 1.15 \times 10^{29}\,\mathrm{cm}^{-2}\mathrm{Hz}$ and is referred to as the *design* p-Pb luminosity.

4.1 Concepts

Important concepts regarding radiation damping, intra-beam scattering and luminosity are explained in the following since these effects are predominantly influencing the performance of heavy-ion colliders and the evolution of the beam and bunch properties. One important concept in heavy-ion collider physics is the contribution of photonuclear processes and bound-free pair production to the total cross section. These processes have large contributions to the total cross section in symmetric collisions of heavy ions of high charge at high energies, e.g., Pb-Pb in the LHC [124] or Au-Au in RHIC [125], but the effects remain not entirely negligible in asymmetric collisions like p-Pb. The contributions of these processes to the total cross section in p-Pb collisions are also discussed in this section.

4.1.1 Radiation damping

It is well known that the deflection of charged particles in a magnetic field leads to the emission of electromagnetic radiation (synchrotron radiation) mostly tangential to the particle trajectory. The statistical fluctuations due to discrete photon emission cause quantum excitation, but the emission of radiation leads on average to the shrinkage of the transverse and longitudinal actions of the particles in a heavy-ion beam. In low-emittance electron storage rings, the statistical fluctuation of the radiation and the damping effect lead to an equilibrium emittance, i.e., quantum excitation and damping from synchrotron radiation cancel. In heavy-ion accelerators, however, the damping times are much longer and quantum excitation is negligible compared to intra-beam scattering (see Sec. 4.1.2). An equilibrium between intra-beam scattering and radiation damping eventually sets in. This equilibrium, however, depends on the respective bunch properties and may therefore vary between bunches. The damping rates $\alpha_{\mathrm{rad},u} = 1/\tau_{\mathrm{rad},u}$ resulting from the emission of synchrotron radiation read

$$\alpha_{\mathrm{rad,u}} = \frac{W_0}{2E_b T_0}\mathcal{J}_u \tag{4.3}$$

with u being x, y or z, the revolution time T_0 and the energy loss per turn

$$W_0 = \frac{e^2 Z^2}{3\epsilon_0 (mc^2)^4}\frac{E_b^4}{\rho}\,. \tag{4.4}$$

Here, Z is the atomic number of the ion, ϵ_0 is the vacuum permittivity, m is the ion mass and ρ is the curvature of the orbit. The different $\mathcal{J}_u$ are the so-called partition numbers obeying Robinson's sum rule $J_x + J_y + J_z = 4$. Here and in the following, the damping and growth rates refer to the respective amplitude and not to the underlying emittance. The expression of the partition numbers via five radiation integrals [126, 127] is omitted at this point. Without vertical dispersion and neglecting skew-quadrupole effects, the partition numbers simplify to

$$\mathcal{J}_x = 1 - \mathcal{D}\,, \qquad \mathcal{J}_y = 1\,, \qquad \mathcal{J}_z = 2 + \mathcal{D} \tag{4.5}$$

Table 4.2: Values of radiation damping times and IBS growth times in the LHC as given in [1] for protons and Pb ions at injection energy $E_b = 450Z\,\mathrm{GeV}$ and LHC design energy $E_b = 7Z\,\mathrm{TeV}$.

Particle species		p		Pb	
Beam energy E_b	$Z\,\mathrm{GeV}$	450	7000	450	7000
Longitudinal damping time $\tau_{\mathrm{rad},z}$	h	$> 10^4$	26	$> 10^4$	12.6
Transverse damping time $\tau_{\mathrm{rad},x/y}$	h	$> 10^4$	52	$> 10^4$	25.2
Longitudinal IBS growth time $\tau_{\mathrm{IBS},z}$	h	60	122	6	15.4
Horizontal IBS growth time $\tau_{\mathrm{IBS},x}$	h	76	160	13	26

with

$$\mathcal{D} = \oint \left(\frac{D_x(s)}{\rho(s)} \left[2k_1(s) - \rho^{-2}(s) \right] \right) \mathrm{d}s \Big/ \oint \rho^{-2}(s) \mathrm{d}s \approx 0\,, \tag{4.6}$$

D_x being the dispersion function in the horizontal plane and k_1 being the quadrupole strength. The approximation $\mathcal{D} \ll 1$ is perfectly valid for most synchrotrons including the LHC. As can be seen from Eqs. 4.3–4.4, radiation damping depends strongly on Z, m and E_b. Under the assumption of the same magnetic rigidity among different particle species at the energy $E_b = ZE_{b,\mathrm{p}}$ ($E_{b,\mathrm{p}}$ is the proton energy at equal rigidity $B\rho$), the damping rates scale according to $\alpha_{\mathrm{rad},u} \propto Z^5/A^4$. This dependence causes Pb ions to damp approximately twice as fast as protons, whereas oxygen ions damp roughly half as fast as protons at equal $B\rho$ (see Chapter 7). While the damping time in electron light sources is in the ms range, the damping times of protons and ions in the LHC are multiple hours long. Table 4.2 lists damping times of protons and Pb ions at LHC injection and design energy. The values of $\tau_{\mathrm{rad},u}$ and $\tau_{\mathrm{IBS},u}$ in the reference [1] refer to the respective emittance and are therefore a factor 2 smaller compared to those in Tab. 4.2.

4.1.2 Intra-beam scattering

Intra-beam scattering (IBS) is an effect occurring between particles of the same bunch. While the Touschek effect [128] is a single scattering process in the transverse plane leading to the longitudinal loss of both participating particles, particles under the influence of IBS undergo multiple scattering processes of small angles in all three dimensions. This process leads to transverse emittance and bunch length growth on a macroscopic level. On a microscopic (single particle) level, the transverse amplitudes of single particles may grow and exceed the physical or dynamic aperture leading to particle losses (de-bunching). Multiple IBS theories have been developed over time, and multiple approximations to these have been found. The first theory was developed by Piwinski for weakly focusing lattices [129]. The theory was extended to

strong-focussing lattices by Bjorken-Mtingwa using the formalism of quantum scattering theory [130]. The Bjorken-Mtingwa model was developed further by a high-energy approximation suggested by Bane [131]. The Piwinski model was extended by including parameter variations along the lattice (modified Piwinski model) and a fully integrated form, the so-called completely integrated modified Piwinski (CIMP) model [132, 133], was developed. All analytical models, however, assume normally distributed coordinates and momenta of the particles within the bunch the IBS growth rates are calculated for.

The CIMP model is used in this chapter and throughout the beam-evolution studies in the Chapters 6–7 and is therefore described in the following. The CIMP model yields good agreement with the Bjorken-Mtingwa model at high energies [133]. According to the CIMP model, the three amplitude growth rates $\alpha_{\mathrm{IBS},u} = 1/\tau_{\mathrm{IBS},u}$ read

$$\alpha_{\mathrm{IBS},z} = 2\pi^{3/2} A_{\mathrm{IBS}} \frac{1}{C} \int C_{\log} \left[\frac{\sigma_H^2}{\sigma_p^2} \left(\frac{g(b/a)}{a} + \frac{g(a/b)}{b} \right) \right] \mathrm{d}s \,, \tag{4.7}$$

$$\alpha_{\mathrm{IBS},x} = 2\pi^{3/2} A_{\mathrm{IBS}} \frac{1}{C} \int C_{\log} \left[-ag(b/a) + \frac{\mathcal{H}_x \sigma_H^2}{\epsilon_x} \left(\frac{g(b/a)}{a} + \frac{g(a/b)}{b} \right) \right] \mathrm{d}s \,, \tag{4.8}$$

$$\alpha_{\mathrm{IBS},y} = 2\pi^{3/2} A_{\mathrm{IBS}} \frac{1}{C} \int C_{\log} \left[-bg(a/b) + \frac{\mathcal{H}_v \sigma_H^2}{\epsilon_v} \left(\frac{g(b/a)}{a} + \frac{g(a/b)}{b} \right) \right] \mathrm{d}s \,. \tag{4.9}$$

Equations 4.7–4.9 depend on a variety of parameters which are mostly position dependent. The common factor A_{IBS} reads

$$A_{\mathrm{IBS}} = \frac{r_0^2 c N_b}{64\pi^2 \beta^3 \gamma^4 \epsilon_x \epsilon_y \sigma_z \sigma_p} \tag{4.10}$$

with the particle radius $r_0 = (Ze)^2/(4\pi\varepsilon_0 mc^2)$, the number of particles in the bunch N_b, the relativistic β and relativistic Lorentz factor γ, emittances ϵ_u, bunch length σ_z and momentum spread σ_p. The integrals in Eqs. 4.7–4.9 make use of the position dependent dispersion invariant

$$\mathcal{H}_u(s) = \frac{D_u^2(s) + \left(\beta_u(s) D_u'(s) - \beta_u'(s) D_u(s)/2\right)^2}{\beta_u(s)} \tag{4.11}$$

with u being x or y. Further position dependent quantities are

$$\sigma_H(s) = \left(\frac{1}{\sigma_p^2(s)} + \frac{\mathcal{H}_x(s)}{\epsilon_x(s)} + \frac{\mathcal{H}_y(s)}{\epsilon_y(s)} \right)^{-1/2} \tag{4.12}$$

and the parameters

$$a(s) = \frac{\sigma_H(s)}{\gamma} \sqrt{\frac{\beta_x(s)}{\epsilon_x(s)}} \,, \quad b(s) = \frac{\sigma_H(s)}{\gamma} \sqrt{\frac{\beta_y(s)}{\epsilon_y(s)}} \,, \quad q(s) = \sigma_H(s) \beta \sqrt{2\sigma_y(s)/r_0} \,. \tag{4.13}$$

The parameter q is used to evaluate the Coulomb logarithm factor

$$C_{\log} = \log(q^2/a^2) \,. \tag{4.14}$$

The function $g(\omega)$ is used multiple times in Eqs. 4.7–4.9 and reads

$$g(\omega) = \sqrt{\frac{\pi}{\omega}} \left(P^{0}_{-1/2}\left(\frac{\omega^2+1}{2\omega}\right) \pm \frac{3}{2} P^{-1}_{-1/2}\left(\frac{\omega^2+1}{2\omega}\right)\right) \tag{4.15}$$

with $P^a_b(x)$ being the Type 3 Associated Legendre functions (the minus sign applies if $\omega < 1$). Table 4.2 gives values of the IBS growth rates for protons and Pb ions at LHC injection and design energy. Pb bunches at energies in the energy range $E_b = 6.5Z\,\mathrm{TeV}$ to $E_b = 7Z\,\mathrm{TeV}$ experience roughly equally strong radiation damping and growth from IBS. Hence, small parameter changes can either lead to the overall shrinkage or growth of the bunch volume.

4.1.3 Luminosity

The luminosity is the proportionality factor connecting the event rate $\mathrm{d}N/\mathrm{d}t$ with the cross section σ

$$\frac{\mathrm{d}N}{\mathrm{d}t} = \sigma\mathcal{L}\,. \tag{4.16}$$

The luminosity is a key parameter with respect to the collider performance since the main purpose of the collider is to provide as many collisions as possible to the experiments. The general definition of the luminosity per bunch crossing is

$$\mathcal{L}_{\mathrm{bb}} = K N_{b1} N_{b2} \iiiint_{-\infty}^{\infty} \rho_1(x,y,s,t)\rho_2(x,y,s,t)\mathrm{d}x\,\mathrm{d}y\,\mathrm{d}s\,\mathrm{d}t \tag{4.17}$$

with the number of particles N_b in the colliding two bunches (indices 1 and 2) and the kinematic factor

$$K = \frac{1}{c}\sqrt{(\mathbf{v}_1-\mathbf{v}_2)^2 - (\mathbf{v}_1\times\mathbf{v}_2)^2/c^2} \approx 2\,. \tag{4.18}$$

The last approximation assumes high energy $v_i \approx c$ and head-on collision, i.e., $|\mathbf{v}_1| = |\mathbf{v}_2| = c$ and $\mathbf{v}_1 = -\mathbf{v}_2$. The quantity $\mu = \sigma\mathcal{L}_{\mathrm{bb}}$ is the number of events per bunch crossing and is often called pile-up. With the Gaussian-shaped density functions

$$\rho_i(x,y,s,t) = \frac{1}{(2\pi)^{3/2}\sigma_{x,i}\sigma_{y,i}\sigma_{s,i}} \exp\left(-\frac{x^2}{2\sigma_{x,i}^2} - \frac{y^2}{2\sigma_{y,i}^2} - \frac{(s\pm|\mathbf{v}_i|\,t)^2}{2\sigma_{s,i}^2}\right) \tag{4.19}$$

for both colliding bunches, the evaluation of Eq. 4.17 for an ultra-relativistic head-on collision yields the analytic expression

$$\mathcal{L}_{\mathrm{bb}} = \frac{N_{b1}N_{b2}}{2\pi\Sigma_x\Sigma_y} \qquad \text{with} \qquad \Sigma_u = \sqrt{\sigma_{u,1}^2+\sigma_{u,2}^2}\,, \qquad \sigma_{u,i} = \sqrt{\beta^*\varepsilon_{u,i}}\,. \tag{4.20}$$

The quantity β^* is the β-function at the IP. Throughout this chapter $\beta^*_x = \beta^*_y = \beta^*$ is assumed (round optics) and the β^* is equal for both colliding bunches. The luminosity for n_c colliding bunch pairs and revolution frequency f_0 is then

$$\mathcal{L} = n_c f_0 \mathcal{L}_{\mathrm{bb}}\,. \tag{4.21}$$

In heavy-ion collisions, nuclei comprising large numbers of nucleons collide with each other. While in p-p collisions only the two participating nucleons (protons) collide, much more nucleons collide in a Pb-Pb or Pb-p collision event. To compare the luminosity among collision systems like p-p, p-Pb and Pb-Pb collisions, the nucleon-nucleon (NN) luminosity is introduced as

$$\mathcal{L}_{\mathrm{NN}} = A_1 A_2 \mathcal{L} \tag{4.22}$$

with the two nucleon numbers A_1 and A_2 of the collision partners. Over the duration of a fill, the experiments accumulate more and more luminosity. A measure of the accumulated luminosity is therefore the integrated luminosity

$$\mathcal{L}_{\mathrm{int}}(t) = \int_0^t \mathcal{L}(\tau)\mathrm{d}\tau \,. \tag{4.23}$$

The integrated luminosity is a key parameter to measure the performance of a collider over a longer time period and experiments request specific integrated luminosity targets for a certain time span. Analogously to Eq. 4.22, the integrated NN luminosity is

$$\mathcal{L}_{\mathrm{NN,int}}(t) = A_1 A_2 \int_0^t \mathcal{L}(\tau)\mathrm{d}\tau \,. \tag{4.24}$$

In the previous calculations, the analytic expressions are only valid for straight head-on collisions; however, in a collider like the LHC, the beams collide at a crossing angle θ. A crossing angle is necessary to avoid parasitic collisions near the actual IPs since the bunch spacing is small in a collider like the LHC. The crossing angle has to be large enough that potential long-range beam-beam encounters do not occur at a too small separation since this would excite strong odd resonances and may reduce the dynamic aperture. The downside of a large θ is that the overlap between the colliding bunches becomes inefficient. Besides a non-zero θ, the β-function is not constant on the scale of the bunch length at the IPs. This also causes luminosity deterioration. These effects reduce the luminosity below the value given in Eq. 4.21.

4.1.3.1 Luminosity reduction

Analytic formulas for the reduction of the luminosity are mostly valid for the case of Gaussian bunch shapes. In more complicated cases, the numerical evaluation of Eq. 4.17 cannot be avoided. Assuming the two Gaussian bunches collide with a crossing angle θ in the u plane, the luminosity reduces by the factor[2] [134]

$$\mathcal{S}_g = \frac{\Sigma_u \cos^2\frac{\theta}{2}}{\sqrt{\Sigma_u^2 \cos^2\frac{\theta}{2} + \Sigma_s^2 \sin^2\frac{\theta}{2}}} \approx \left(1 + \frac{\theta^2}{4}\frac{\Sigma_s^2}{\Sigma_u^2}\right)^{-1/2} \tag{4.25}$$

[2]Equation 4.25 contains the second power of $\cos(\theta/2)$ in the nominator because of the contribution of the kinematic factor K given in Eq. 4.18.

with $\Sigma_s^2 = \sigma_{s,1}^2 + \sigma_{s,2}^2$. The approximation is valid if $\sigma_u \ll \sigma_s$ and the crossing angle are small, i.e., $\cos\theta/2 \approx 1$ and $\sin\theta/2 \approx \theta/2$. Often, the factor $\mathcal{S}_g$ is referred to as the geometry factor. Further deterioration of the luminosity is introduced if the bunches collide with a small transverse separation of the central orbits. Here, the separation is expected to be exclusively in the separation plane, i.e., the plane perpendicular to the crossing plane. The reduction factor then reads [91]

$$\mathcal{S}_d = \exp\left(-\frac{d_u^2}{2\Sigma_u^2}\right) \tag{4.26}$$

with d_u being the separation of the orbits of the two beams in the separation plane u. An additional reduction factor results from a non-constant β-function at the IP. The beam envelopes follow an hourglass like shape and the reduction because of this so-called hourglass effect is [135]

$$\mathcal{S}_h = \int_{-\infty}^{\infty} \frac{\exp(-t^2)}{\sqrt{\pi\left(1 + t^2/t_x^2\right)\left(1 + t^2/t_y^2\right)}}\mathrm{d}t \qquad \text{with} \qquad t_u^2 = \frac{2\beta^{*2}}{\Sigma_s^2}\,. \tag{4.27}$$

The numerical integration in Eq. 4.27 is easily performed by transforming into a proper integral. In a collider with a small bunch spacing like the LHC, all reduction factors apply simultaneously if the luminosity levelling (see Sec. 4.1.3.2) is achieved via separation. The reduction of the luminosity due to a large θ is an important topic in the scope of the HL-LHC. High bunch intensities will require increased angles θ. This will lead to a larger luminosity reduction than in the nominal LHC. As a countermeasure, the installation of crab cavities, cavities applying transverse kicks of different amplitude to the bunch head and bunch tail, is envisaged for the HL-LHC [59]. These crab cavities will optimise the overlap of the two colliding beams; therefore, they will improve the luminosity substantially.

4.1.3.2 Luminosity levelling

Luminosity levelling is applied if the pile-up $\mu = \mathcal{L}_{\mathrm{bb}}\sigma$ exceeds the read-out rate of detector components and/or to reduce background in the detector. In the LHC, the levelling of the luminosity was usually achieved by separating the beam central orbits on the scale of the beam size (multiple μm) in LHC Run 1 and Run 2. Levelling by separation is the only levelling technique which has been applied during heavy-ion operation until this point. The LHCb and the ALICE experiments are limited in maximum luminosity in contrast to ATLAS and CMS. ALICE requires constant levelling at $\mathcal{L} = 10^{27}\,\mathrm{cm}^{-2}\mathrm{Hz}$ during Pb-Pb operation and $\mathcal{L} = 10^{29}\,\mathrm{cm}^{-2}\mathrm{Hz}$ during p-Pb operation because of the maximum read-out rate of the TPC. Levelling the luminosity in ATLAS and CMS to extend the fill lengths has been performed regularly in heavy-ion operation of the LHC in the past. Although the two detectors are not restricted in terms of pile-up during heavy-ion operation, levelling is sometimes desirable to extend the fill duration for

ALICE and LHCb. The downside of levelling by separation (in p-p operation especially) is the reduction of dynamic aperture because of the excitation of odd resonances and the reduction of the stabilising tune spread (Landau damping) caused by the head-on collisions [134, 136–138].

Besides levelling via separation, two other levelling schemes are possible. Crossing-angle levelling is one possibility; however, it is more conveniently used in so-called anti-levelling scenarios, i.e., once the beam intensities start to decay, the crossing angles at the IPs are gradually reduced to increase the luminosity while keeping the dynamic aperture constant. Anti-levelling has been successfully applied since 2017 regularly during p-p fills [134, 139]. Levelling by manipulating the β^* at the IPs over time has been applied in multiple machine development studies (MDs) in 2012, 2015 and 2017 [134, 140–142]. This levelling technique is the hardest to implement since a constant change of the optics is required. The advantage of this levelling technique is that the maximum tune spread resulting from the head-on beam-beam effect remains. Levelling via β^* is envisaged as the primary levelling tool in p-p collisions in LHC Run 3 and beyond.

4.1.4 Cross section and secondary effects

The inelastic hadronic cross section σ_{had} in heavy-ion collisions is responsible for the number of events generating the QGP, the high-density state that is predominantly analysed in heavy-ion physics. If the impact parameter $\hat{b}$ in a collision fulfils $\hat{b} > 2R$ with R being the nuclear electric radius, the collision is categorised as ultra peripheral. During such a collision, the strongly contracted electromagnetic fields of the colliding ions interact with each other and the respective other ion's nucleus. This collision type leads to secondary processes contributing to the total cross section. The first important process is lepton-pair production and especially the production of electron-positron pairs in bound-free states. The other process is nuclear dissociation of colliding nuclei in the beams. Both processes lead to a shift of the magnetic rigidity of the particles and consequently cause particle losses. The cross sections of these processes are not necessarily small and are even the main contributors to the total cross section of symmetric heavy-ion collisions like Pb-Pb in the LHC.

The hadronic cross section σ_{had} scales weakly with $\sqrt{s_{\mathrm{NN}}}$. This behaviour is shown for the Pb-p and Pb-Pb cross sections in Fig. 4.1. These values for the hadronic cross sections are obtained via theoretical calculations. The ALICE experiment performed a measurement of the visible p-Pb cross section at $\sqrt{s_{\mathrm{NN}}} = 5.02\,\mathrm{TeV}$ based on 2013 data [143]. Also, the CMS experiment conducted a measurement of the total p-Pb cross section at $\sqrt{s_{\mathrm{NN}}} = 5.02\,\mathrm{TeV}$ based on 2013 p-Pb data [144] and obtained a hadronic p-Pb cross section of $\sigma_{\mathrm{had}} = (2.061 + \pm 0.082)\,\mathrm{b}$. This value is in good agreement with the value $\sigma_{\mathrm{had}} = (2.08 + \pm 0.01)\,\mathrm{b}$ obtained from a Monte-Carlo Glauber calculation [16]. For the collision energy of $\sqrt{s_{\mathrm{NN}}} = 8.16\,\mathrm{TeV}$,

the hadronic cross section estimate is $\sigma_{\mathrm{had}} = (2.12 \pm 0.01)\,\mathrm{b}$, but no experimental measurement has been published (see Chapter 5).

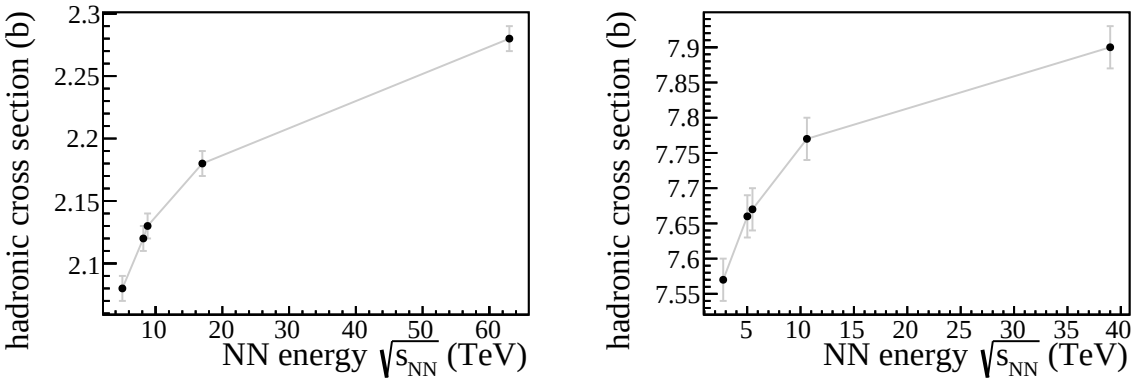

Figure 4.1: Left: Hadronic cross section of p-Pb collisions at different $\sqrt{s_{\mathrm{NN}}}$. The cross section is only weakly scaling with energy. Right: Hadronic cross section of Pb-Pb collisions in dependence of $\sqrt{s_{\mathrm{NN}}}$. The cross-section values of both graphs result from Monte-Carlo Glauber calculations presented in [16].

4.1.4.1 Lepton-pair production

The strongly Lorentz contracted electromagnetic fields of ultra-relativistic ions generate a (virtual) photon flux. This behaviour is described by the Weizsäcker-Williams approximation [145–147]. The flux of virtual quanta $N(\omega)$ in the laboratory frame at the photon energy $E = \hbar\omega \gg \hbar\gamma v/\hat{b}$ can be expressed as [148, 149]

$$N(\omega) \propto Z^2 e^{-2\omega\hat{b}/(\gamma v)} \tag{4.28}$$

with ω being the photon angular frequency, $h = 2\pi\hbar$ being Planck's constant, Z being the atomic number of the ion, $\hat{b}$ being the minimum impact parameter and v being the particle velocity. The photon flux $N(\omega)$ gives rise to the possibility of lepton-pair production in ultra-peripheral collisions. This effect is negligible in standard p-p operation of the LHC; however, it gains importance once a collision partner is an ion with an atomic number $Z \gg 1$. A likely event that leads to particle losses is the production of positron-electron pairs. A small fraction of the produced electrons are possibly *caught* by one of the collision partners and end up in a bound state. This process is called bound-free pair production (BFPP) [149, 150] and leads to the loss of the ion binding the electron since the magnetic rigidity of the ion shifts because of the change of the ion charge (outside the LHC momentum acceptance). This process may even occur at photon energies slightly smaller than $\hbar\omega = 2m_e$ as the bound state reduces the

required energy by the amount of the binding energy. For the symmetric Pb-Pb case, the first order BFPP1 process reads

$$^{208}\mathrm{Pb}^{82+} + {}^{208}\mathrm{Pb}^{82+} \rightarrow {}^{208}\mathrm{Pb}^{82+} + {}^{208}\mathrm{Pb}^{81+} + e^{+} \qquad (\mathrm{BFPP1}). \tag{4.29}$$

and the rigidity shift of the Pb ion is equal to an effective relative momentum deviation of $\delta_p = 1.2\,\%$. However, more important in the context of this thesis is the asymmetric Pb-p collision type

$$^{208}\mathrm{Pb}^{82+} + \mathrm{p} \rightarrow {}^{208}\mathrm{Pb}^{81+} + \mathrm{p} + e^{+}\,. \tag{4.30}$$

The BFPP1 cross section is orders of magnitudes smaller in Pb-p collisions (see Eq. 4.30) compared to symmetric Pb-Pb collisions since the proton generates a roughly $1/82^2$ times smaller photon flux compared to that of a Pb ion (see Eq. 4.28). The creation of a hydrogen atom ($p + e^- \rightarrow \mathrm{H}$) is strongly suppressed compared to the process given in Eq. 4.30 and is not considered. The pair production is not restricted to a single electron-positron pair; however, the cross section of multiple pairs being produced

$$^{208}\mathrm{Pb}^{82+} + \mathrm{p} \rightarrow {}^{208}\mathrm{Pb}^{(82-m)+} + \mathrm{p} + me^{+} \qquad (\mathrm{BFPP}m) \tag{4.31}$$

decreases rapidly with increasing number m of produced electron-positron pairs. The cross section of BFPP processes in general and that of BFPP into the $1s$ bound state behave approximately [149, 151, 152]

$$\sigma_{1s} = Z_1^5 Z_2^2 a \log(\gamma_c/\gamma_0) \tag{4.32}$$

with the index 1 referring to the ion binding the electron and the index 2 referring to the projectile ion. The constants a and γ_0 can be found in, e.g., [151]. The γ_c (fixed-target Lorentz factor) refers to Lorentz factor of the projectile in the rest frame of the target particle. The fixed-target Lorentz factor γ_c can be obtained via consecutive Lorentz transformations, which is equal to the product of the four-velocities of the colliding particles, i.e.,

$$\gamma_c = \left(\frac{^1p_\mu}{m_1}\right)\left(\frac{^2p^\mu}{m_2}\right) = \gamma_1\gamma_2 + \gamma_1\gamma_2\sqrt{1 - \frac{\gamma_1^2 + \gamma_2^2 - 1}{\gamma_1^2\gamma_2^2}} \approx 2\gamma_1\gamma_2\,. \tag{4.33}$$

The last step in Eq. 4.33 assumes high energies ($\gamma_{1/2} \gg 1$). The Greek indices indicate whether the vectors are co- or contra-variant and the Minkowski metric applies. The BFPP1 cross section of Pb-Pb collisions at $\sqrt{s_{\mathrm{NN}}} = 5.52\,\mathrm{TeV}$ ($E_b = 7\,\mathrm{TeV}$) is $\sigma_{\mathrm{BFPP1}} \approx 281\,\mathrm{b}$. This estimate is calculated by the finding that the cross-section contribution of the s states are $\sigma_{ns} = \sigma_{1s}/n^3$ and the sum of all s states is therefore $\sum_n \sigma_{ns} = \zeta(3)\sigma_{1s} = 270.5\,\mathrm{b}$ [152] with ζ being Riemann's zeta function [153]. Potential p states $\sum_n \sigma_{np} \approx 10.3\,\mathrm{b}$ [152] also contribute to the total cross section. The BFPP2 cross section in Pb-Pb collisions at $\sqrt{s_{\mathrm{NN}}} = 5.52\,\mathrm{TeV}$ of $\sigma_{\mathrm{BFPP2}} = 6\,\mathrm{mb}$ [150] is small compared to the BFPP1 cross section. Section 4.1.4.3 presents the calculation of the BFPP cross sections in p-Pb collisions at the desired beam energy. Table 4.3 lists the cross sections of the BFPP processes in Pb-Pb and Pb-p collisions in the LHC.

4.1.4.2 Electromagnetic dissociation

A second process coming into effect in high-energy heavy-ion collisions is the so-called electromagnetic dissociation (EMD) [124, 154, 155]. The photon flux from the charged projectile particle excites the nucleus of the target ion. The dominant excitation occurs at a photon energy of roughly $E_{\mathrm{GDR}} \approx 80/A^{1/3}\,\mathrm{MeV}$ [155]. This resonance is the so-called giant dipole resonance (GDR). Here, the protons oscillate coherently against the neutrons of the nucleus. The relaxation eventually takes place by emitting one or more neutrons from the nucleus. The reaction formulas for the first order EMD process (EMD1) for Pb-Pb and Pb-p collision systems are

$$^{208}\mathrm{Pb}^{82+} + {}^{208}\mathrm{Pb}^{82+} \rightarrow {}^{207}\mathrm{Pb}^{82+} + {}^{208}\mathrm{Pb}^{82+} + \mathrm{n}\,, \tag{4.34}$$

$$^{208}\mathrm{Pb}^{82+} + \mathrm{p} \rightarrow {}^{207}\mathrm{Pb}^{82+} + \mathrm{p} + \mathrm{n} \qquad (\mathrm{EMD1})\,. \tag{4.35}$$

The magnetic rigidity shift leads to particle losses; however, the $^{207}\mathrm{Pb}^{82+}$ ions may survive for multiple turns since the rigidity shift is small. The effective relative momentum shift for $^{207}\mathrm{Pb}^{82+}$ ions is only $\delta_p = -0.5\,\%$.[3] Higher order EMDm processes

$$^{208}\mathrm{Pb}^{82+} + {}^{208}\mathrm{Pb}^{82+} \rightarrow {}^{208}\mathrm{Pb}^{82+} + {}^{208-m}\mathrm{Pb}^{82+} + m\mathrm{n} \qquad (\mathrm{EMD}m) \tag{4.36}$$

cause losses during the same turn because of the larger change of the rigidity ($\delta_p = -m0.5\,\%$). The cross section of higher order EMD processes does not decrease as rapidly as for BFPP. The total EMD1 cross section is at $\sigma_{\mathrm{EMD1}} = 96\,\mathrm{b}$ in Pb-Pb collisions at $E_b = 7Z\,\mathrm{TeV}$ and represents $1/3$ of the total EMD cross section $\sigma_{\mathrm{EMD}} = 226\,\mathrm{b}$ [124] (see Tab. 4.3). A general expression for the EMDm processes in Pb-p collisions is

$$^{208}\mathrm{Pb}^{82+} + \mathrm{p} = {}^{208-m}\mathrm{Pb}^{82+} + \mathrm{p} + m\mathrm{n} \qquad (\mathrm{EMD}m)\,. \tag{4.37}$$

The EMDm cross section is expected to scale roughly like the BFPP cross section [156, 157]

$$\sigma_{\mathrm{EMD}m} \propto Z_2^2 \log(\gamma_c)\,. \tag{4.38}$$

The scattering of ions on collimator jaws may also cause EMD[4]

$$^{208}\mathrm{Pb}^{82+} + {}^{12}\mathrm{C} = {}^{208-m}\mathrm{Pb}^{82+} + {}^{12}\mathrm{C} + m\mathrm{n} \qquad (\mathrm{EMDm})\,. \tag{4.39}$$

These EMD processes occur at the primary collimators (TCPs) in particular; however, these processes may take place at collimators in general and at the collimators of the collimation section in IR7 (important in Chapter 5). The modified $^{208-m}\mathrm{Pb}^{82+}$ ions coming out of the

[3] This calculation assumes no recoil on the ion momentum.

[4] The equation assumes a carbon collimator. Although the primary collimators are made of carbon, this does not apply to all LHC collimators.

collimation section of IR7 generate specific loss patterns in the dispersion suppressors and arcs downstream of IR7 [158, 159].

The EMD and BFPP cross sections may contribute significantly to the total cross section

$$\sigma = \sigma_{\text{had}} + \sigma_{\text{BFPP}} + \sigma_{\text{EMD}} \tag{4.40}$$

as was explained previously. The total Pb-Pb cross section at $\sqrt{s_{\text{NN}}} = 5.52\,\text{TeV}$ is $\sigma = 515\,\text{b}$ with $507\,\text{b}$ being the contributions from EMD and BFPP effects. Cross sections of BFPP and EMD in p-Pb collisions at energies of $\sqrt{s_{\text{NN}}} = 5.02\,\text{TeV}$ and $\sqrt{s_{\text{NN}}} = 8.16\,\text{TeV}$ are not published. Hence, a simple scaling is applied to retrieve these cross sections in the next section.

4.1.4.3 BFPP and EMD cross-section scaling

Most calculations of the BFPP and EMD cross sections focus on either Pb-Pb or Pb-e collisions. To get the respective cross section values in Pb-p collisions at $\sqrt{s_{\text{NN}}} = 5.02\,\text{TeV}$ ($E_b = 4Z\,\text{TeV}$) and $\sqrt{s_{\text{NN}}} = 8.16\,\text{TeV}$ ($E_b = 6.5Z\,\text{TeV}$), a simple scaling is used to scale the BFPP and EMD cross sections in Pb-Pb collisions at LHC design energy to the desired p-Pb system configuration and energy. Based on the overall scaling behaviour of $\sigma_{\text{BFPP/EMD}} \propto Z_2^2 \log(\gamma_c)$ (see Eqs. 4.32 & 4.38), the scaling factors read

$$\kappa_{\text{Pb-p}}^{6.5Z\,\text{TeV}} = \frac{1}{Q_{\text{Pb}}^2} \frac{\log(\gamma_{c,\text{Pb-p}}^{6.5Z\,\text{TeV}})}{\log(\gamma_{c,\text{Pb-Pb}}^{7Z\,\text{TeV}})} = 1.56 \times 10^{-4}\,, \tag{4.41}$$

$$\kappa_{\text{Pb-p}}^{4Z\,\text{TeV}} = \frac{1}{Q_{\text{Pb}}^2} \frac{\log(\gamma_{c,\text{Pb-p}}^{4Z\,\text{TeV}})}{\log(\gamma_{c,\text{Pb-Pb}}^{7Z\,\text{TeV}})} = 1.47 \times 10^{-4} \tag{4.42}$$

with the fixed target Lorentz factors

$$\gamma_{c,\text{Pb-p}}^{6.5Z\,\text{TeV}} = 3.81 \times 10^7\,, \qquad \gamma_{c,\text{Pb-p}}^{4Z\,\text{TeV}} = 1.44 \times 10^7\,, \qquad \gamma_{c,\text{Pb-Pb}}^{7Z\,\text{TeV}} = 1.76 \times 10^7\,. \tag{4.43}$$

This scaling is applied to the different BFPPm and EMDm cross sections in Pb-Pb collisions. Table 4.3 gives the scaled values for p-Pb at $\sqrt{s_{\text{NN}}} = 5.02\,\text{TeV}$ and $\sqrt{s_{\text{NN}}} = 8.16\,\text{TeV}$. The total cross section at $\sqrt{s_{\text{NN}}} = 5.02\,\text{TeV}$ is then $\sigma = 2.15\,\text{b}$ and the cross section at $\sqrt{s_{\text{NN}}} = 8.16\,\text{TeV}$ is $\sigma = 2.20\,\text{b}$.

4.1.5 Beam-beam equivalence classes

The beam dynamics of bunches in the LHC often depends on the bunch slot they are occupying. Reason for this is unevenness along the bunch trains caused by the LHC abort gap and the different injection-kicker rise times of the LHC and those of the accelerators in the injector chain. Because of this unevenness, not all bunches collide in all IPs. In proton operation with a bunch spacing of $25\,\text{ns}$ and more than 2500 bunches per beam, all four experiments get close

Table 4.3: Cross sections of the different electromagnetic interactions for Pb-Pb collisions at $\sqrt{s_{\mathrm{NN}}} = 5.52\,\mathrm{TeV}$. The values for Pb-p collisions at $\sqrt{s_{\mathrm{NN}}} = 5.02\,\mathrm{TeV}$ and $\sqrt{s_{\mathrm{NN}}} = 8.16\,\mathrm{TeV}$ are obtained via scaling (see Eqs. 4.41–4.42).

	Collision system	Pb-Pb	Pb-p	
	NN energy $\sqrt{s_{\mathrm{NN}}}$	5.52 TeV	5.02 TeV	8.16 TeV
Cross section σ	BFPP1	281 b	41.3	43.7 mb
	BFFP2	6 mb	1 μb	1 μb
	EMD1	96 b	14.1 mb	14.9 mb
	EMD2	29 b	4.3 mb	4.5 mb
	EMDn>2	101 b	14.8 mb	15.8 mb
	Hadronic σ_{had}	8 b	2.08 b	2.12 b
	Total σ	515 b	2.15 b	2.20 b

to the same number of colliding bunch pairs. This, however, does not apply during heavy-ion operation. During the 2016 p-Pb run, the bunch spacing was 100 ns and it was further reduced to 75 ns in 2018. While a dense 25 ns bunch spacing in p-p operation results in roughly the same number of colliding bunch pairs in the different IPs, the number of colliding bunch pairs varies between the IPs in heavy-ion operation, especially since the IPs are not positioned symmetrically along the circumference.

ATLAS and CMS are at diametrically opposite positions (see Fig. 1.1). Hence, a bunch pair colliding in ATLAS therefore also collides in CMS and vice versa. The position of the ALICE IP is shifted by $C/8$ clockwise with respect to the ATLAS IP and the LHCb IP is shifted $C\left(\frac{1}{8} + \frac{1.5}{3564}\right)$ counterclockwise with respect to the ATLAS IP. The additional shift of $\frac{1.5}{3564}C$ of the LHCb IP with respect to an eight-fold rotation symmetry breaks the symmetry sufficiently enough that a quarter-wise bunch filling does not create collisions in LHCb at all with a 100 ns filling pattern.[5] In contrast, a 75 ns filling pattern as was used in the 2018 Pb-Pb run gives many collisions to LHCb. Throughout this thesis, the expression *beam-beam equivalence class* [160] is used to categorise bunches according to their collision schedules in the IPs. In the LHC, there are $2^3 = 8$ equivalence classes. Table 4.4 lists these classes and indicates the IPs the bunches of each class are colliding in. The class numbering in the table is obtained via the pseudo formula

$$\text{class number} = 4 \times (\mathrm{IP1/5?}) + 2 \times (\mathrm{IP2?}) + (\mathrm{IP8?})\ . \tag{4.44}$$

with the operator $(\mathrm{IP}n?)$ being 1 if the bunch collides in IPn or 0 if it does not. The properties of bunches in one equivalence class may evolve differently over time compared to bunches of other classes. The bunch evolution of two bunches belonging to the same class is mostly the same,

[5] A quarter-wise filling refers to both beams being filled according to the same filling pattern that remains invariant under a shift of 891 bunch slots, which corresponds to a quarter of the 3564 available bunch slots.

Table 4.4: The crosses in the top part of the table indicate the IPs the bunches of the equivalence classes are colliding in. Bunches colliding in IP1 also collide in IP5 by design. The class numbering is expressed by the pseudo formula given in Eq. 4.44. The bottom part of the table lists the number of bunches in the different equivalence classes of both beams in the fills 5510 and 5549. These fills are analysed in the context of simulating the beam evolution of different 2016 fills (see Sec. 4.3).

		Equivalence class							
		0	1	2	3	4	5	6	7
	IP1/5					✗	✗	✗	✗
	IP2			✗	✗			✗	✗
	IP8		✗		✗		✗		✗
		Number of bunches in equivalence class							
Fill 5510	Beam 1 (p)	269	17	298	37	27	0	54	0
	Beam 2 (Pb)	24	54	389	0	81	0	0	0
Fill 5549	Beam 1 (Pb)	8	17	6	104	34	130	241	0
	Beam 2 (p)	130	8	26	115	149	46	128	82

however, the starting parameters of the two bunches and the parameters of the bunches they are colliding with are not entirely equal. Hence, small differences in the parameter evolution among bunches of the same class are observed. Another reason for the different evolution of bunches of the same class is the collision partners in the IPs have different collision schedules themselves. As an example, one may want to consider two bunches only colliding in IP2 (class 2). Further, we assume the bunch of the counter-rotating beam the first bunch is colliding with is also exclusively colliding in IP2; however, we now assume the collision partner in the counter-rotating beam of the second bunch is not only colliding in IP2 but also in IP8 (class 3). Hence, the luminosity burn-off of the first bunch will be faster since the intensity of the collision partner decreases more slowly in time than the collision partner of the second bunch (also collides in LHCb).

4.2 2016 heavy-ion run overview

The 2016 p-Pb run of the LHC took place from 5 November 2016 until 5 December 2016. In contrast to previous runs with Pb beams, the LHC injectors were able to provide Pb bunch trains with a $100\,\mathrm{ns}$ bunch spacing to the LHC and the decision was made to have the same bunch spacing for the proton beam. The SPS injection-kicker rise time could have been $200\,\mathrm{ns}$

Table 4.5: IP settings during the 2016 heavy-ion run at the two different $\sqrt{s_{\mathrm{NN}}}$. The positive (negative) crossing angle applies for CMS (ATLAS).

IP		IP1/5	IP2	IP8
		$\sqrt{s_{\mathrm{NN}}} = 5.02\,\mathrm{TeV}$		
β-function at IP β^*	m	11	2	10
External half crossing angle $\theta_{\mathrm{ext}}/2$	μrad	± 140	185	-230
Half crossing angle $\theta/2$	μrad	± 140	63	-466
Extra loss rate at the IP α_{IP}	1/h	1/77	1/290	1/95
		$\sqrt{s_{\mathrm{NN}}} = 8.16\,\mathrm{TeV}$		
β-function at IP β^*	m	0.6	2	1.5
External half crossing angle $\theta_{\mathrm{ext}}/2$	μrad	± 140	138	-180
Half crossing angle $\theta/2$	μrad	± 140	63	-325
Extra loss rate at the IP α_{IP}	1/h	1/74	1/34	1/420

or 150 ns. Using a 150 ns gap between the PS batches had the downside of poor alignment of Pb and proton trains in the LHC and 200 ns was used instead [161].

The LHC optics was significantly different at the IPs during the two parts of operation at $\sqrt{s_{\mathrm{NN}}} = 5.02\,\mathrm{TeV}$ and $\sqrt{s_{\mathrm{NN}}} = 8.16\,\mathrm{TeV}$. Table 4.5 gives the full list of optics parameters at the IPs. Only during the $\sqrt{s_{\mathrm{NN}}} = 8.16\,\mathrm{TeV}$ part, a squeeze of the β^* took place after the ramp. During the $\sqrt{s_{\mathrm{NN}}} = 5.02\,\mathrm{TeV}$ part of operation, the squeeze in ALICE was performed during the energy ramp while the other experiments remained unsqueezed.

The LHC injection kicker (MKI) had a limit of 3.6 μs long SPS bunch trains equivalent to 144 slots in 25 ns operation. The 200 ns SPS batch spacing enabled the injection of two batches with 18 proton bunches per batch and seven batches with four Pb bunches per batch from the SPS into the LHC with SPS train lengths of 3.6 μs and 3.4 μs, respectively. The LHC injection-kicker rise time was at 800 ns during the 2016 heavy-ion run and the abort-gap keeper bucket, i.e., the last bucket the *head* of the last SPS train is allowed to be injected in while giving the LHC extraction kicker sufficient time to rise without disturbing any bunches, was at 32851. This value was slightly larger than in previous operation and enabled the injection of 20 proton and Pb trains from the SPS into the LHC throughout the run.

4.2.1 Commissioning

The commissioning started with a setup phase comprising measurements of the optics and corrections of the beta beating. After that, loss maps at injection as well as at top energy were taken to ensure sufficient protection of the machine. Also, loss maps to cover the possibility of

an asynchronous beam dump[6] were taken. One important aspect of the initial commissioning was the test of the RF cogging procedure and the alignment of the proton and the Pb bunch train to ATLAS, i.e., the bunch occupying the first bunch slot of Beam 1 collides in the ATLAS IP with the bunch occupying the first bunch slot of Beam 2. At the target energy of $E_b = 4Z\,\mathrm{TeV}$, the intrinsic relative momentum shift of the proton and Pb beam was at $\delta = \pm 2.3 \times 10^{-4}$. This leads to a maximum beta beating according to Eq. 2.3 of $1.5\,\%$ [161]. Although the momentum shift is equal to the one in 2013, no special corrections of the beta beating were required in 2016 because of weaker chromatic effects. Hence, special corrections using quadrupoles while leaving the natural tunes $(Q_x, Q_y) = (64.31, 59.32)$ and the dispersion function D_x unchanged [85] were unnecessary. The same corrections were also omitted during the $E_b = 6.5Z\,\mathrm{TeV}$ part of the run (smaller relative momentum shift of $\delta = \pm 8.8 \times 10^{-5}$).

During the initial part of the run, the interlock BPMs in IR6 that are common to both beams, were imposing intensity limits on the bunch intensities. The proton bunch intensities were not allowed to exceed 5×10^{10} protons per bunch since otherwise the simultaneous measurement of the Pb bunches with roughly 1.5×10^{10} charges per bunch was no longer ensured if proton and Pb bunches passed a common stripline BPM in short succession. Besides that, if Pb bunches had dropped below 2×10^{9} charges, these bunches would have been outside the dynamic range and therefore the visibility of the BPMs. This would have caused an immediate beam dump. The first of the two restrictions was removed later on by gating the interlock BPMs during times when proton and Pb bunches were passing a common stripline BPM in short succession. This operational mode is called synchronous orbit measurement and was implemented during the Pb-p part of the operation at $\sqrt{s_{\mathrm{NN}}} = 8.16\,\mathrm{TeV}$.

Figure 4.2 shows the intensity and luminosity evolution of the one-month long heavy-ion operation. In the following, short summaries of the operation at $\sqrt{s_{\mathrm{NN}}} = 5.02\,\mathrm{TeV}$ and $\sqrt{s_{\mathrm{NN}}} = 8.16\,\mathrm{TeV}$ are given. Also, the overall performance of the injector chain and the LHC is summarised similarly to [5, 13].

4.2.2 $\sqrt{s_{\mathrm{NN}}} = 5.02$ TeV p-Pb operation

The optics during the $\sqrt{s_{\mathrm{NN}}} = 5.02\,\mathrm{TeV}$ ($E_b = 4Z\,\mathrm{TeV}$) part of heavy-ion operation comprised a squeeze to $\beta^* = 2\,\mathrm{m}$ (performed during the energy ramp) in the ALICE experiment. The priority was given to ALICE and the luminosity production in the other experiments was of secondary importance during this part of the run with the respective β^* being *unsqueezed* at

[6] An asynchronous beam dump [1, 162] occurs if the extraction kicker modules (MKD) misfire or are falsely triggered. If this happens, the magnetic field of the kickers influence bunches outside the dedicated abort gap while the magnetic field is not yet at full strength. Bunches are kicked with an insufficient amplitude and are consequently *swept* along the LHC aperture potentially damaging magnets and equipment and causing magnet quenches.

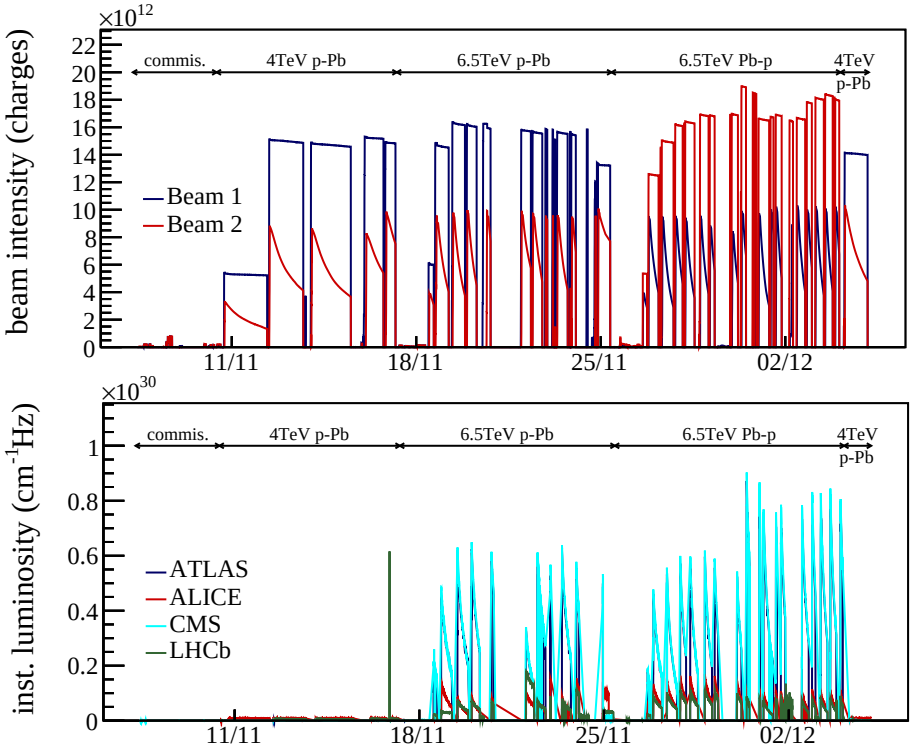

Figure 4.2: Overview of the 2016 p-Pb run of the LHC. The top plot shows the evolution of the beam intensities over the duration of the one month of heavy-ion operation in 2016. The bottom plot displays the evolution of the luminosities. Fill 5506 with the energy $E_b = 4Z\,\mathrm{TeV}$ is the longest fill in LHC history with roughly $38\,\mathrm{h}$ in Stable Beams, starting on 10 November and ending on 12 November. The peak luminosity $\mathcal{L} = 8.9 \times 10^{29}\,\mathrm{cm}^{-1}\mathrm{Hz}$ was achieved with beam energies of $E_b = 6.5Z\,\mathrm{TeV}$ in Fill 5559 that also had the highest proton bunch intensities of the whole run with roughly $N_b = 2.8 \times 10^{10}$ protons per bunch. Plots are based on corrected luminosity data ("Massi files") downloaded in May 2019.

either $\beta^* = 10\,\mathrm{m}$ or $\beta^* = 11\,\mathrm{m}$ in the IPs 1, 5 and 8. The half crossing angle at ALICE was $\theta/2 = 63\,\mu\mathrm{rad}$. This angle is small enough for spectator nucleons to reach the ZDCs at the beam-pipe crotches at the end of the ALICE IR without being intercepted by the physical aperture. The IP settings of ALICE and the three other experiments during the $\sqrt{s_{\mathrm{NN}}} = 5.02\,\mathrm{TeV}$ part of the run are listed in Tab. 4.5.

The first Stable Beams was achieved in Fill 5505 on 10 November with only 20 bunches in each beam to avoid extensive beam commissioning. The fill remained in Stable Beams for $2\,\mathrm{h}$. This fill was followed by the longest fill in LHC history. Fill 5506 remained for $38\,\mathrm{h}$ in Stable Beams and functioned as the operational guideline for the remaining part of operation at $E_b = 4Z\,\mathrm{TeV}$. The main goal was to keep ALICE levelled at $\mathcal{L} = 0.5 \times 10^{28}\,\mathrm{cm}^{-2}\mathrm{Hz}$ for as long as possible to achieve the requested event number of 7×10^8 events as fast as possible. Whenever required, the high burn-off experiments ATLAS and CMS were separated to prolong

the fill duration and to prevent bunches to approach the visibility threshold of the BPMs at 2×10^9 charger per bunch.[7]

The filling patterns used during this part of the run provided large numbers of colliding bunch pairs to ALICE, while only a few pairs collided in the other three experiments. Fill 5506 had beams of only 196 Pb bunches and 252 proton bunches, giving 196 collisions (per turn) to ALICE and no collisions to the other experiments. In the following five fills, the beams had 548 Pb bunches and 702 proton bunches, giving 389 collisions to ALICE, 81 collisions to ATLAS/CMS and 54 collisions to LHCb.

The operation with $\sqrt{s_{\mathrm{NN}}} = 5.02\,\mathrm{TeV}$ lasted for roughly eight days and comprised five high-intensity fills. The time span was not sufficient to reach the goal of 7×10^8 minimum bias events for ALICE. After the successful operation at $E_b = 6.5Z\,\mathrm{TeV}$ for two weeks, one additional p-Pb fill at $E_b = 4Z\,\mathrm{TeV}$ (the fifth high-intensity fill) was incorporated on the last day of operation to reach 7.8×10^8 events in ALICE and the requested target. It is worth mentioning that LHCb could take data in fixed-target collisions via the SMOG experiment [163, 164]. This experiment injects helium gas into the beam pipe at the LHCb IP providing p-He collisions at $\sqrt{s_{\mathrm{NN}}} = 87\,\mathrm{GeV}$.

4.2.3 $\sqrt{s_{\mathrm{NN}}} = 8.16$ TeV p-Pb/Pb-p operation

Operation at $\sqrt{s_{\mathrm{NN}}} = 8.16\,\mathrm{TeV}$ started on 17 November with the setup of the new optics. The optics included squeezed β^* in all four IPs $\beta^* = (0.6, 2.0, 0.6, 1.5)\mathrm{m}$ (see Tab. 4.5). Special corrections of the beta beating were omitted again. The total setup time was only on the scale of a single day.

p-Pb operation The operation started with protons remaining in Beam 1 and Pb in Beam 2 (p-Pb). The strategy was to perform the beam reversal to provide a wider rapidity range for the asymmetric experiments ALICE and LHCb only once $50\,\mathrm{nb}^{-1}$ was reached in ATLAS/CMS. The p-Pb operation included two intensity ramp-up fills. The first of the two fills featured 20 proton and Pb bunches, and the second fill featured 288 proton and 224 Pb bunches. After these fills, ten high-intensity fills took place with the peak luminosity exceeding the design value $\mathcal{L} = 1.15 \times 10^{29}\,\mathrm{cm}^{-1}\mathrm{Hz}$ by a rough factor 5 regularly (see Fig. 4.2). During these ten fills, four different filling patterns were applied giving different numbers of colliding bunch pairs to the different experiments depending on which experiment had fallen behind in terms of luminosity production. The fills were only kept for a few hours in the LHC with the longest fill being in Stable Beams for 9.6 h (Fill 5521). The intensity lifetime was highly reduced by the rapid luminosity burn-off in the ATLAS and CMS experiments (see Sec. 4.3). Thus, the optimum fill

[7] In 2013, bunches regularly dropped in intensity below this threshold and caused multiple premature beam dumps [4, 5].

duration was rather short. Bunches never dropped below the BPM visibility threshold and no premature beam dumps occurred.

The target of $50\,\mathrm{nb}^{-1}$ in ATLAS and CMS was achieved at the end of Fill 5534 in the evening of 23 November. A last fill in p-Pb operation was performed to give the LHCf experiment the requested 9–12 h beam time with ATLAS levelled to $\mathcal{L} = 10^{28}\,\mathrm{cm}^{-2}\mathrm{Hz}$. The other experiments took data with a minimum-bias trigger during that time.

Pb-p operation – beam-direction reversal The setup after the beam-direction reversal took once again a time slot of roughly a single day. Two intensity ramp-up fills were required by Machine Protection before the first full-intensity fill (Fill 4447) was stored. The Pb-p operation at $\sqrt{s_{\mathrm{NN}}} = 8.16\,\mathrm{TeV}$ comprised 17 high-intensity fills starting on 26 November. Only two different filling patterns were applied during this part of operation. Figure 4.3 shows an example filling pattern. Throughout the run, the proton intensity was continuously increased

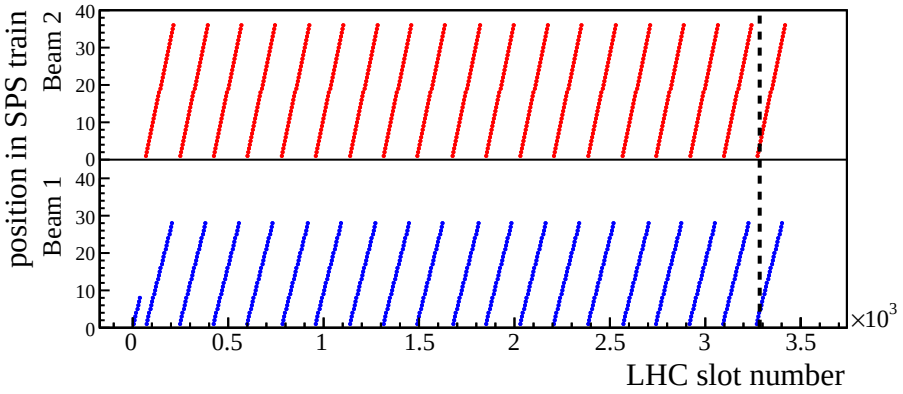

Figure 4.3: Filling pattern of Fill 5554 with Pb ions in Beam 1 and protons in Beam 2. The dashed line indicates the abort-gap keeper. The filling pattern comprises 684 proton (red) and 540 Pb bunches (blue) resulting from 19 proton and 20 Pb injections from the SPS. The filling pattern provides 405 collisions to IP1/5, 352 collisions to IP2 and 251 collisions to IP8.

as the synchronous orbit configuration for the interlock BPMs had successfully been implemented. Peak performance was achieved in Fill 5559. With proton bunch intensities of roughly 2.8×10^{10} particles per bunch and the Pb bunch intensity at 2.1×10^{8} ions per bunch, the peak luminosity reached $\mathcal{L} = 8.9 \times 10^{29}\,\mathrm{cm}^{-2}\mathrm{Hz}$ in ATLAS and CMS, which is equivalent to 7.8 times the design value. During the high-luminosity fills, the BLMs that are located in the dispersion suppressors downstream of the ATLAS IP and CMS IP detected loss signals close to the dump threshold, i.e., there was a high likelihood of beam dumps or magnet quenches at that time. Thus, the proton intensity was slightly decreased thereafter. The particles detected in the dispersion suppressors were most likely collision debris from the Pb-p collisions at the IPs. The analysis of the losses ending up in the dispersion suppressors is performed in Chapter 6. The

last fill (Fill 5575) of the 2016 heavy-ion run was operated once again at $E_b = 4Z\,\mathrm{TeV}$ in p-Pb configuration to complete the ALICE minimum bias data set. The run ended on 5 December 2016 at 06:00 in the morning.

4.2.4 Performance

Injectors The injector performance during the 2016 run is described in [13]. The performance was outstanding with a high transmission efficiency throughout the whole run. The two locations at which most of the intensity was lost are LEIR, with a transmission between $70\,\%$ and $80\,\%$, and the SPS, with a transmission between $60\,\%$ and $70\,\%$ (see Fig. 4.4). The LEIR losses are mostly because of space charge and IBS (short bunch length after RF capture). In the SPS, the bottleneck in terms of transmission efficiency, seven PS shots were accumulated before the start of the energy ramp. During the accumulation at the injection plateau, IBS and space charge led to rapid deterioration of the bunches. The stripping efficiency was high with $96\,\%$ efficiency of the aluminium foil between PS and SPS changing the charge state from Pb^{54+} to Pb^{82+}.

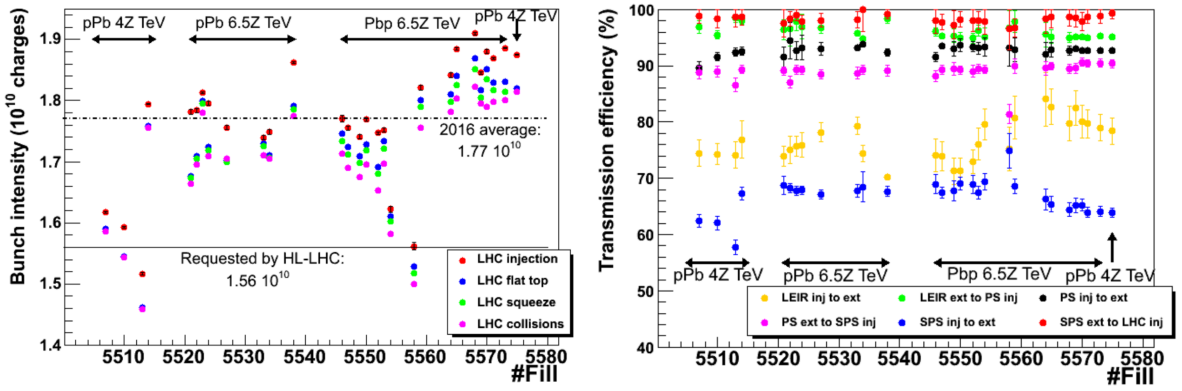

Figure 4.4: Left: Pb bunch intensity over the course of the p-Pb run. The bunch intensity average was at 1.77×10^{10} charges per bunch, while the HL-LHC request is 1.56×10^{10} charges per bunch. The achieved peak intensity was 1.9×10^{10} charges per bunch, equivalent to $N_b = 2.3 \times 10^8$ ions per bunch. Right: The plot shows the transmission efficiencies of the injector chain from the injection into LEIR until the injection into the LHC. Courtesy of R. Alemany-Fernández. Plots taken from [13].

The injectors provided on average Pb bunch intensity of 1.77×10^{10} charges per bunch to the LHC (see Fig. 4.4), which is even larger than the HL-LHC request of 1.56×10^{10} charges per bunch. The emittances were outstandingly small throughout the run with normalised emittances of reproducible $\epsilon_n = 1.5\,\mu\mathrm{m}$ at LHC injection. Figure 4.5 shows the emittance transmission throughout the injectors; however, measurements were rarely performed in the injectors; therefore, the statistical fluctuations are presumably large.

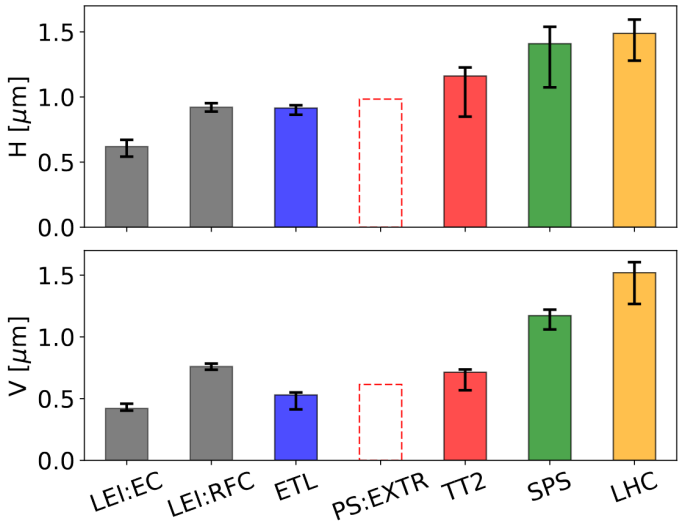

Figure 4.5: Evolution of the normalised emittance along the injector chain. Courtesy of R. Alemany-Fernández. Plot taken from [13].

LHC The LHC transmission efficiency between injection and start of collisions was $95\,\%$ [13]. The previously achieved and assumed transmission for the HL-LHC throughout the cycle was $90\,\%$ before the run. The integrated luminosity during operation at $\sqrt{s_{\mathrm{NN}}} = 5.02\,\mathrm{TeV}$

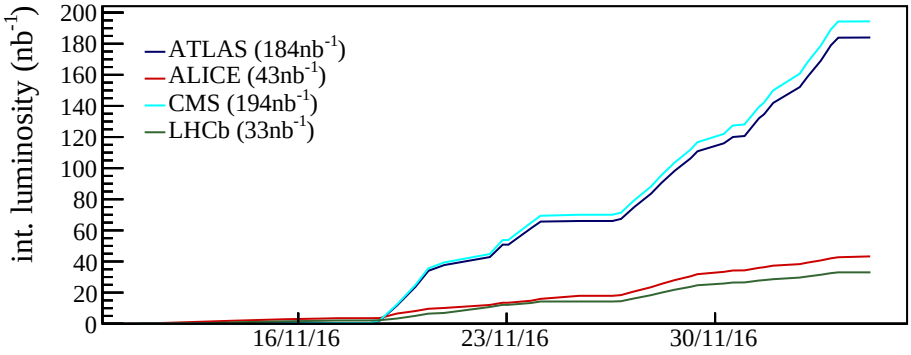

Figure 4.6: Integrated luminosity of the four LHC experiments throughout the one month of proton-nucleus operation in 2016. The ATLAS and CMS luminosities start to increase rapidly with the start of the $E_b = 6.5Z\,\mathrm{TeV}$ operation. Unequal horizontal and vertical emittances of the Pb bunches in combination with different crossing planes in ATLAS (vertical) and CMS (horizontal) explain partly the difference in integrated luminosity between the two detectors.

was low with the priority being on ALICE. ALICE accumulated 7.8×10^8 events during that time while the integrated luminosity in ATLAS and CMS was roughly $0.5\,\mathrm{nb}^{-1}$. Table 4.1 lists the achieved parameters. It is highly likely that LHCb published too optimistic luminosities

Table 4.6: The table compares the 2016 p-Pb run with the previous run from 2013. The integrated luminosity refers to the high-luminosity experiments ATLAS and CMS. Adapted from [17].

Year		2013	2016
Beam energy E_b	$Z\,\mathrm{TeV}$	4	4.0, 6.5
NN energy $\sqrt{s_{\mathrm{NN}}}$	TeV	5.02	5.02, 8.16
Run duration	weeks	3	3
Peak Pb bunch intensity N_b	10^8	1.2	2.1
Peak stored beam energy W_{stored}	MJ	2.3	9.7
Pb normalised emittance ϵ_n	μm	2	1.5
Pb bunch Length σ_z	m	0.07–0.1	
Peak luminosity $\mathcal{L}$	$10^{29}\,\mathrm{cm}^{-2}\mathrm{Hz}$	1.16	8.9
Integrated luminosity $\int \mathcal{L}\mathrm{d}t$	nb^{-1}	32	190

during the $\sqrt{s_{\mathrm{NN}}} = 5.02\,\mathrm{TeV}$ operation.[8] Therefore, a total luminosity close to $31\,\mathrm{nb}^{-1}$ seems more likely than $33\,\mathrm{nb}^{-1}$ throughout the whole run for LHCb. The luminosity production was outstanding as displayed in Fig. 4.6. During operation at $\sqrt{s_{\mathrm{NN}}} = 8.16\,\mathrm{TeV}$, ATLAS and CMS achieved values close to $200\,\mathrm{nb}^{-1}$, which is a factor 6 larger than in 2013 in an even shorter time. ALICE and LHCb were able to achieve integrated luminosities between $30\,\mathrm{nb}^{-1}$ and $45\,\mathrm{nb}^{-1}$. The peak luminosity exceeded $\mathcal{L} = 8.9 \times 10^{29}\,\mathrm{cm}^{-2}\mathrm{Hz}$ in Fill 5559 and was more than a factor 7.8 larger than in 2013 [4]. The difference between ATLAS and CMS in terms of instantaneous and integrated luminosity is at least partly caused by a different crossing plane and different transverse emittances (elliptical Pb beams).

Record-breaking Pb intensities were injected into the LHC with bunch intensities exceeding $N_b = 2.1 \times 10^8$ ions per bunch and outstandingly small (normalised) emittances of approximately $\epsilon_n = 1.5\,\mu\mathrm{m}$ were achieved.[9] The emittance in the LHC as measured by the wire scanners is also shown in Fig. 4.5 but in restricted conditions (low beam intensity). Measurements of the emittance in the LHC was performed regularly with wire scanners. The synchrotron radiation telescopes (BSRTs) that are responsible for measuring the beam emittances were not calibrated during the first half of the operation at $\sqrt{s_{\mathrm{NN}}} = 8.16\,\mathrm{TeV}$.

[8] Comparison of bunch numbers and optics parameters between the experiments indicates a too large luminosity published by LHCb during fills at $\sqrt{s_{\mathrm{NN}}} = 5.02\,\mathrm{TeV}$.

[9] Equally small emittances were not achieved during the 2018 Pb-Pb run [46]; however, the bunch intensities were slightly higher compared to 2016 towards the end of the 2018 run.

4.3 Beam evolution

Understanding the observed beam evolution in the collider is important since trying to reproduce the beam evolution may give insight on whether the beams behave differently from theoretical predictions. If the beams do not behave as predicted, potential reasons can be identified. In this section, the beam evolution at the two beam energies $E_b = 4Z\,\mathrm{TeV}$ and $E_b = 6.5Z\,\mathrm{TeV}$ are reproduced using differential equations. Part of the results at $E_b = 6.5Z\,\mathrm{TeV}$ have already been published in [13]. Under specific restriction, i.e., the particles within the bunches are normally distributed in all coordinates and momenta, four ordinary differential equations (ODEs) per bunch

$$\dot{N}_b(t) = -\sigma \sum_{i \in \mathrm{IPs}} L_i(\sigma_x, \sigma_y, \sigma_z, N_b, \tilde{\sigma}_{x,i}, \tilde{\sigma}_{y,i}, \tilde{\sigma}_{z,i}, \tilde{N}_{b,i}, t) - \alpha_{\mathrm{ex}} N_b(t) \tag{4.45}$$

$$\dot{\sigma}_u(t) = \alpha_{\mathrm{IBS},u}(\sigma_x, \sigma_y, \sigma_z, N_b, \sigma_p, \ ..., t)\sigma_u(t) - \alpha_{\mathrm{rad},u}\sigma_u(t) \tag{4.46}$$

describe the parameter evolution of the respective bunch. The luminosity is calculated from the bunch properties of the bunch and of the bunches it is colliding with (indicated by a tilde symbol). The collision process couples the ODEs and consequently the evolution of the different bunches. The total number of coupled ODEs is $4n_b$ with n_b being the number of bunches within the two beams. The different bunches do not suffer losses solely from luminosity, but other effects come into play, e.g., residual gas scattering, de-bunching (losses due to IBS in the lateral parts of the bunch), the Touschek effect and excitation by resonances. Therefore, the additional loss rate α_{ex} is introduced to cover these effects. The loss rates of most of the effects contributing to α_{ex} scale linearly with the particle number. Hence, N_b is factorised out of α_{ex}. Further dependencies of α_{ex} are not listed, but it can depend on a variety of parameters, e.g., emittances ε_u, the bunch length σ_z but also time t. In this simulation code, however, these losses are assumed to be a constant $\alpha_{\mathrm{ex}} = \mathrm{const}$.

Under the assumption of a constant bunch size, a constant α_{ex} (exponential decay) and all bunches of both beams being of the same bunch equivalence class (see Sec. 4.1.5), the intensity evolution of the beams $N_{\mathrm{Pb}}(t)$ is calculable analytically. In the symmetric Pb-Pb scenario, the beam intensities are then described by the differential equation

$$\frac{\mathrm{d}N_{\mathrm{Pb}}(t)}{\mathrm{d}t} = -\alpha N_{\mathrm{Pb}}^2(t) - \alpha_{\mathrm{ex}} N_{\mathrm{Pb}}(t) \tag{4.47}$$

and its solution

$$N_{\mathrm{Pb}}(t) = \frac{N_{\mathrm{Pb}}(0)\alpha_{\mathrm{ex}}}{N_{\mathrm{Pb}}(0)\alpha(e^{\alpha_{\mathrm{ex}}t} - 1) + \alpha_{\mathrm{ex}}e^{\alpha_{\mathrm{ex}}t}} \tag{4.48}$$

with $\alpha = \sigma\mathcal{L}_{\mathrm{tot}}(t)/N_{\mathrm{Pb}}^2(t) = \mathrm{const.}$ and $\mathcal{L}_{\mathrm{tot}}$ being the combined luminosity in all IPs. If both beams are subject to different α_{ex}, e.g., asymmetric p-Pb operation, the solution becomes

highly complicated. The proton intensity, however, can be assumed as constant $N_\mathrm{p}(t) = \mathrm{const.}$ throughout the duration of a fill. This dynamic occurs since a collision between a proton and Pb ion removes both participants from their respective beam. At a certain moment in time, the loss rate for both beams reads $\dot{N}_\mathrm{p} = \dot{N}_\mathrm{Pb} = -\alpha N_\mathrm{p} N_\mathrm{Pb}$ if only luminosity burn-off is considered. The ratio of the intensity lifetimes is[10]

$$\frac{\tau_\mathrm{p}}{\tau_\mathrm{Pb}} = \frac{-\dot{N}_\mathrm{Pb}/N_\mathrm{Pb}}{-\dot{N}_\mathrm{p}/N_\mathrm{p}} \approx \frac{N_{b,\mathrm{p}}}{N_{b,\mathrm{Pb}}} = \frac{2.15 \times 10^{10}}{1.85 \times 10^{8}} = 116\,. \tag{4.49}$$

Thus, the intensity lifetime of the protons bunches is expected to be two orders of magnitude longer. In typical p-Pb fills in 2016, Pb bunches that collide in most IPs (equivalence classes 5 and 6) have intensity lifetimes between $\tau_\mathrm{Pb} \approx 5\,\mathrm{h}$–$7\,\mathrm{h}$ (see Sec. 4.3.2). Proton bunches of the same equivalence class easily have intensity lifetimes of $\tau_\mathrm{p} \approx 600\,\mathrm{h}$. Hence, the approximation of a constant proton-beam intensity on the time scale of a fill duration of roughly $10\,\mathrm{h}$ is fully valid. The intensity evolution of the Pb beam is given by the differential equation (including non-luminous losses)

$$\frac{\mathrm{d}N_\mathrm{Pb}(t)}{\mathrm{d}t} = -\alpha N_\mathrm{p} N_\mathrm{Pb}(t) - \alpha_\mathrm{ex} N_\mathrm{Pb}(t)\,. \tag{4.50}$$

Thus, the Pb intensity decays exponentially

$$N_\mathrm{Pb}(t) = N_\mathrm{Pb}(0) e^{-(\alpha N_\mathrm{p} + \alpha_\mathrm{ex})t} \qquad \text{and} \qquad N_\mathrm{p}(t) = \mathrm{const.} \tag{4.51}$$

The approximation of a constant bunch volume is inaccurate for the evolution of Pb bunches in the LHC. Also, assuming all bunches being part of the same equivalence class is unrealistic because of the large bunch spacing in heavy-ion operation and filling patterns optimised for the special needs of the different experiments. Thus, the bunch-by-bunch numerical integration of the ODEs in Eqs. 4.45–4.46 is required.

Calculating the evolution of the properties of the different bunches via ODEs, however, is restricted to Gaussian-shaped particle distributions, i.e., analytic descriptions of radiation damping and IBS are bound to normal distributions. Deviations of the transverse amplitudes or longitudinal bunch shape from a Gaussian shape lead to inaccuracy of the analytic descriptions. In lepton synchrotrons, this feature is insignificant since radiation damping and quantum excitation results in an equilibrium Gaussian-shaped particle distribution. In hadron synchrotrons, this is no longer the case. The damping is slow and deviations from a Gaussian bunch shape may persist for many hours. Also, the luminosity burn-off is not proportional to the transverse coordinate distributions, i.e., the distribution of the burn-off has a smaller variance (see Chapter 6). The smaller variance enhances the luminosity burn-off in the bunch core and is weaker in lateral parts of the transverse particle distribution.

[10] Values for proton and Pb bunch intensities in Eq. 4.49 are taken from start of Fill 5549. Same bunch numbers n_b are assumed for both beams.

There are major advantages of the ODE approach over a single-particle treatment. First, solving ODEs is fast. IBS is only a slowly varying property (radiation damping is constant); therefore, the integration time steps can easily be in the $\Delta t = 100\,\mathrm{s}$ range or larger. Furthermore, the number of simulated bunches can easily be multiple thousands without pushing the simulation time to more than a few minutes.

Collider Time Evolution (CTE) [56, 82, 165] is a code for simulating the beam evolution of a collider using macro particles to model a bunch instead of assuming Gaussian-shaped particle distributions in coordinates and momenta. CTE was programmed by M. Blaskiewicz (Brookhaven National Laboratory), R. Bruce (CERN) and Tom Mertens (CERN, now affiliated with Helmholtz-Zentrum Berlin). Recently, T. Mertens has developed a `python` version of CTE called CTEPY. CTE/CTEPY considers betatron and synchrotron motion. Furthermore, IBS and radiation damping are modelled as random processes acting on each particle separately; however, these processes are still based on analytical formulas. In the past, CTE/CTEPY was used to simulate single bunches of specific equivalence classes and the results were scaled to the actual bunch and collision numbers to obtain the total collider performance. A simulation of all bunches of both beams using CTE would be too time intensive. The approach of simulating single bunches and scaling the results to correct bunch numbers has multiple disadvantages:

- Bunches are coupled with bunches of both beams because of the collisions in the IPs. This leads to bunches forming clusters in which the bunches depend on each other. Truncating these dependencies by simulating only a single bunch and its respective collision partners leads to errors if there is high luminosity burn-off.
- Bunches may have different starting conditions. By simulating only a small sample of bunches, the simulation is possibly not entirely representative for the fill.
- Luminosity levelling becomes inaccurate when it is based on a few bunches because bunches that collide in the respective IP are possibly members of different bunch equivalence classes. This effect becomes more significant when simulating long fills.

A code capable of simulating all bunches of both colliding beams based on the ODEs in Eqs. 4.45–4.46 was developed in the scope of this work and is presented in the next section.

4.3.1 Beam-evolution code

For the purpose of analysing LHC fills, a `C++` code was developed to simulate the evolution of all bunches of both beams using the ODEs in Eqs. 4.45–4.46. Hence, the mechanisms which are included in the code are radiation damping (see Eq. 4.3), IBS (see Eqs. 4.7–4.9), luminosity burn-off (see Eq. 4.21), non-luminous losses (α_{ex} in Eq. 4.45) and luminosity levelling (see Sec. 4.1.3.2). To simplify the bookkeeping of multiple thousand bunches, an object-orientated

approach is used to reduce the effective code length and to improve the legibility. The integration is a simple explicit Euler algorithm

$$\mathbf{x}(t_{n+1}) = \mathbf{x}(t_n) + \dot{\mathbf{x}}(t_n)\Delta t \qquad \text{with} \qquad \mathbf{x} = (N_b, \sigma_x, \sigma_y, \sigma_z)\,, \qquad \Delta t = t_{n+1} - t_n \tag{4.52}$$

that yields acceptable results because of slowly varying growth and particle loss rates.

luminosity levelling The code provides the option of luminosity levelling via a simple scaling factor. This form of levelling neglects the dependence of the luminosity reduction $\mathcal{S}_d$ on the bunch emittance if the levelling is achieved via separation of the central orbits (see Eq. 4.26). In fact, the luminosity reduction $\mathcal{S}_d$ varies between bunches of different emittance in reality. Although the code provides much better levelling compared to simulating single bunch pairs and then scale the luminosity to the real number of bunches, an implementation of the real feedback loop via separation levelling is omitted. Instead, the potential luminosity

$$\mathcal{L}_{\text{pot}} = \sum_{j \in \text{bunches}} \mathcal{L}_j \tag{4.53}$$

is calculated by adding up the luminosities $\mathcal{L}_j$ of the bunches j in the IP if no luminosity levelling would be applied. If the potential luminosity $\mathcal{L}_{\text{pot},i}$ exceeds the targeted luminosity levelling value $\mathcal{L}_{\text{t}}$, the levelling value is backwards applied to the respective bunches. This means the luminosity in the experiment is then

$$\mathcal{L} = \min(\mathcal{L}_{\text{t}}, \mathcal{L}_{\text{pot}}) \tag{4.54}$$

and the reduction factor

$$\mathcal{S}_d = \min\left(1, \mathcal{L}_{\text{t}}/\mathcal{L}_{\text{pot}}\right) \qquad \text{with} \qquad \mathcal{S}_d \in [0, 1] \tag{4.55}$$

is applied to the luminosity of the bunches colliding in the IP $\mathcal{L} = \sum_j \mathcal{S}_d \mathcal{L}_j = \mathcal{L}_{\text{t}}$. This procedure is an approximation since $\mathcal{S}_d$ is a function of the bunch emittances. Assuming the same reduction for all bunches therefore implies same emittances among all bunches. The required separation d_u in the separation plane u to achieve the reduction of the luminosity by $\mathcal{S}_d$ is approximated via

$$d_u \approx \langle \Sigma_u \rangle \sqrt{-2\log(\mathcal{S}_d)}\,. \tag{4.56}$$

with the average convoluted beam size $\langle \Sigma_u \rangle$. Reconstructing the separation can help to give insight on the beam emittances when comparing the simulated beam evolution with reality. The reconstruction of the separation was used to estimate the separations in the IPs at the start of the fills for the 2018 Pb-Pb run [166].

Corrections A code based on ODEs cannot be expected to yield correct IBS results if the measured bunch lengths and emittances are incorrect because of systematic uncertainties or they are non-Gaussian and instead follow, e.g., q-Gaussian distributions. In addition, coupling between the planes leads to the mixing of the transverse IBS growth rates. Therefore, potential IBS correction factors can be given as input to the code. One correction factor is for the scaling of all IBS growth rates $\kappa_{\mathrm{glo}} \in \mathbb{R}$ and another factor $\kappa_{\mathrm{coup}} \in [0, 1]$ controls the coupling of the transverse IBS growth rates into the other transverse plane. The modified IBS growth rates $\alpha^*_{\mathrm{IBS},u}$ read

$$\alpha^*_{\mathrm{IBS},x}(\kappa_{\mathrm{coup}}, \kappa_{\mathrm{glo}}) = \kappa_{\mathrm{glo}} \left[\left(1 - \frac{\kappa_{\mathrm{coup}}}{2}\right) \alpha_{\mathrm{IBS},x} + \frac{\kappa_{\mathrm{coup}}}{2} \alpha_{\mathrm{IBS},y} \right] , \tag{4.57}$$

$$\alpha^*_{\mathrm{IBS},y}(\kappa_{\mathrm{coup}}, \kappa_{\mathrm{glo}}) = \kappa_{\mathrm{glo}} \left[\left(1 - \frac{\kappa_{\mathrm{coup}}}{2}\right) \alpha_{\mathrm{IBS},y} + \frac{\kappa_{\mathrm{coup}}}{2} \alpha_{\mathrm{IBS},x} \right] , \tag{4.58}$$

$$\alpha^*_{\mathrm{IBS},z}(\kappa_{\mathrm{glo}}) = \kappa_{\mathrm{glo}} \alpha_{\mathrm{IBS},z} . \tag{4.59}$$

An important observation that was made during the analysis of the 2016 heavy-ion run was that the intensity decay of all bunches could not be reproduced when only luminosity burn-off and non-luminous losses were considered. In Sec. 4.3.2, the necessity to include additional losses at the IPs, i.e., bunches colliding in certain IPs suffer intensity losses which cannot be explained by luminosity burn-off, into the simulation code is described. Including these losses allows the reproduction of the bunch-intensity evolution to a high degree. The code provides the possibility to give additional loss rates α_{IP} which depend on the IPs the bunch is colliding in, i.e., only bunches colliding in the respective IP are subject to these extra losses. This modifies Eq. 4.45 to

$$\dot{N}_b(t) = -\sum_{i \in \mathrm{IPs}} \left(\sigma \mathcal{L}_i + \alpha_{\mathrm{IP}i} N_b(t)\right) - \alpha_{\mathrm{ex}} N_b(t) . \tag{4.60}$$

The non-colliding lifetime $\tau_{\mathrm{ex}} = 1/\alpha_{\mathrm{ex}}$ is assumed to be constant and is estimated by calculating the mean lifetime of the bunch class 0 (non-colliding bunches).

The code is used in the next section to reproduce the evolution of fills of the 2016 p-Pb run at $E_b = 4Z\,\mathrm{TeV}$ and $E_b = 6.5Z\,\mathrm{TeV}$. The code is also used in Chapters 6 & 7 to estimate the performance of future p-Pb runs of the LHC and HL-LHC as well as the operation with ion species other than Pb in p-A collisions.

4.3.2 Beam evolution at $E_b = 6.5Z$ TeV

In this part, Fill 5549 at $E_b = 6.5Z\,\mathrm{TeV}$ is analysed with 540 Pb bunches in Beam 1 and 684 proton bunches in Beam 2 (Pb-p). The beam-evolution code is used to reproduce the luminosity, intensity, emittance and bunch-length evolution as observed during the fill as well as possible. The focus is on the evolution of the Pb bunches since luminosity burn-off is only weak for the

proton beam because of the much larger proton intensity compared to that of the Pb bunches. The filling pattern provides bunches of all equivalence classes except no Pb bunch is colliding in all four IPs (class 7; see Tab. 4.4). The C++ code is used to simulate the first $8\,\mathrm{h}$ of the fill in 160 times steps, i.e., the time increment is $\Delta t = 180\,\mathrm{s}$. A non-luminous lifetime of $1/\alpha_{\mathrm{ex}} = 100\,\mathrm{h}$ for the Pb bunches and $1/\alpha_{\mathrm{ex}} = 5.8 \times 10^3\,\mathrm{h}$ for the proton bunches is estimated by calculating the intensity lifetimes of the bunches colliding in no IP.

Bunch-by-bunch intensities Figure 4.7 displays the evolution of the bunch intensities of bunch 5 (class 1; single collision in IP8) and bunch 73 (class 5; collides in IPs 1, 5 and 8) of the Pb beam.[11] Simulation results obtained from CTEPY are also shown for comparison. The intensity evolution obtained from the ODE model does not match the data of the intensity, the intensity evolution of bunch 73 in particular. In reality, the intensity decreases faster than expected. Also, when considering bunches of other equivalence classes (not presented here), a common pattern seems that the intensity decays are underestimated. CTEPY faces the same issue, i.e., the simulated intensity does not decay fast enough to match with the measurements.

To achieve better agreement between simulations and data, the CTEPY model and the ODE model are modified to find potential reasons for the discrepancies. Using fully coupled IBS growth rates does not improve the predicted intensity evolution of CTEPY. Since the evolution cannot be perfectly reproduced based on ODEs, extra loss rates $\alpha_{\mathrm{IP}i}$ (see Eq. 4.60) that vary for the different IPs are introduced to find the amount of losses the ODE model and CTEPY cannot reproduce. These extra loss rates are between $\alpha_{\mathrm{IP}} = 1/420$–$1/34\,\mathrm{h}^{-1}$, and Tab. 4.5 gives the full list of all α_{IP}. Bunches colliding in IP1 and IP5 are subject to the extra loss rate given in Tab. 4.5 for IP1/5 twice.[12] The loss rates follow a rough scaling with crossing angle $\alpha_{\mathrm{IP}i} \propto 1/\theta_i$. These extra loss rates were estimated by calculating the measured average and simulated average of the intensity evolution of all bunches of the respective equivalence class first. In a second step, the extra loss rates are adjusted to maximise the agreement of the simulated average intensity evolution and the measured average intensity evolution of the class. Hence, the extra loss rates are optimised on the average of the equivalence class and not for a single specific bunch of that class. For ALICE, the experiment with the smallest crossing angle, the most extra losses are required $1/\alpha_{\mathrm{IP}} = 34\,\mathrm{h}$ to achieve an acceptable agreement between simulation and data while the respective loss rate in LHCb (largest crossing angle) is the smallest with $1/\alpha_{\mathrm{IP}} = 420\,\mathrm{h}$.

[11] The simulation results in Figs. 4.7–4.9 were produced assuming a total cross section of $\sigma = 2.06\,\mathrm{b}$ and a Piwinski IBS model using averaged optical functions only [165]; however, the extra loss rates at the IPs described here assume a total cross section of $\sigma = 2.20\,\mathrm{b}$ (more accurate than $\sigma = 2.06\,\mathrm{b}$) and the model uses the CIMP IBS formalism. These changes barely influence the simulation results, and the conclusions in reference [165] are fully valid. Table 4.5 gives the extra losses estimated with a cross section of $\sigma = 2.20\,\mathrm{b}$. The resulting evolution of the bunch properties barely deviate from the evolutions given in [165] and in Figs. 4.7–4.9.

[12] The extra loss rates for IP1 and IP5 cannot be disentangled and are assumed to be equal.

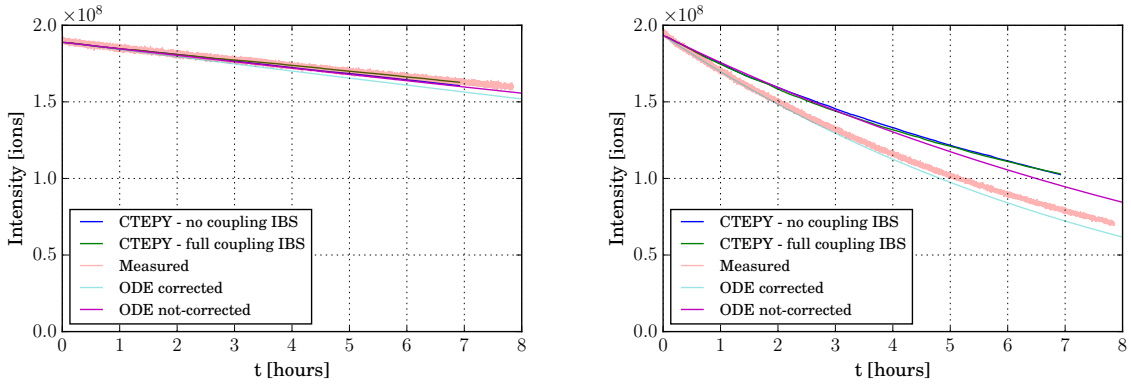

Figure 4.7: The intensity evolution of bunch 5 (left) and bunch 73 (right). Besides the measured data (light red), the curves of the ODE model (purple) and CTEPY (blue) are also displayed. The agreement between simulation and data is not perfect. There is a 20 % difference between all simulated and the observed intensity at around $t = 7\,\mathrm{h}$ for bunch 73. Using CTE with coupled IBS growth rates (green) does not improve the agreement in terms of intensity; however, by applying extra loss rates, the ODE model (cyan) accomplishes good agreement. Plots taken from [165].

Similar extra losses were estimated for the proton beam; however, these loss rates are very small with $1/\alpha_{\mathrm{IP}} > 2.6 \times 10^3\,\mathrm{h}$. Although the beam evolution at $E_b = 6.5Z\,\mathrm{TeV}$ is only presented for Fill 5549, these extra losses also occurred in other fills that were analysed, e.g., Fill 5565.

Regarding the two bunches shown in Fig. 4.7, the agreement between this modified ODE model and the actual data of bunch 73 improves substantially. The existence of these extra losses is hard to interpret. It is unlikely that the extra losses result from parasitic long-range beam-beam encounters since bunches not colliding in the respective IP would also be subject to these losses if there are long-range beam-beam encounters close to that IP. This behaviour, however, is not observed. Additionally, the scaling of α_{IP} with the crossing angle θ makes losses due to odd resonances excited by the beam-beam interaction under a crossing angle unlikely because the losses should become smaller with decreasing crossing angle and Chapter 3 did not provide any evidence on diffusion close to the bunch core. Uncertainties in terms of the total p-Pb cross section are a potential explanation; however, an additional scaling of α_{IP} with $1/\beta^*$ is then expected. One explanation could also be the increase of the head-on tune shift with decreasing crossing angle. This could shift the beam core of the particles in the bunches towards destructive resonances in tune space and may cause these extra losses; however, these explanations are highly speculative and hard to verify.

Bunch-by-bunch emittances and bunch lengths Simulating the evolution of the bunch emittances and bunch lengths using the ODE model and CTEPY does not reproduce the experimen-

tal data to a high degree. Figure 4.8 shows this behaviour for two bunches. A common issue

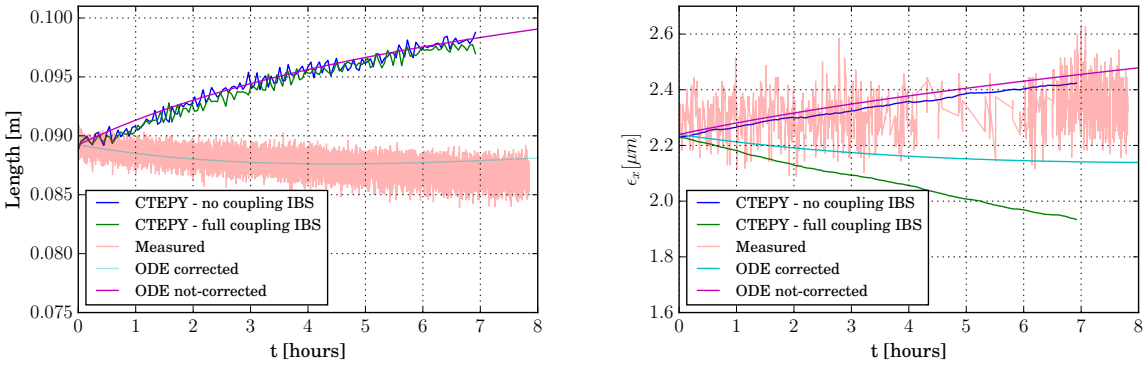

Figure 4.8: Left: Bunch-length evolution of bunch 5 (class 1; single collision in IP8). Only the corrected ODE simulation with extra losses and global scaling of the IBS growth rates yields acceptable agreement. In all other cases, a $10\,\%$ discrepancy between data and simulation is observed at $t = 7\,\mathrm{h}$. Right: Evolution of the horizontal emittance of bunch 73 (class 5; collisions in IPs 1, 5 and 8). Since the starting emittance of the simulations is probably too small, the simulated evolutions are slightly misleading. If the initial offset of roughly $-0.08\,\mu\mathrm{m}$ is subtracted, the corrected ODE model would yield an acceptable result. Plots taken from [165].

of the ODE simulation and CTEPY simulation is that the IBS growth rates are overestimated. The bunch length of bunch 5 of the Pb beam shrinks throughout the first $8\,\mathrm{h}$ of the fill (left plot of Fig. 4.8); however, the simulations (ODE and CTEPY) predict a $10\,\%$ growth. To correct for this discrepancy, the IBS growth rates of Pb are scaled down by $50\,\%$ in the corrected ODE model, i.e., $\kappa_{\mathrm{glo}} = 0.5$ in Eqs. 4.57–4.59. This is a very large factor that shows the bunch length evolution is not fully understood when considering only radiation damping and IBS. Uncertainties in terms of bunch shape and initial condition may contribute to the discrepancies. With this correction to the IBS model, the bunch length is reproduced on an acceptable level as shown by the magenta line in the left plot of Fig. 4.8. The simulation of the horizontal emittance of bunch 73 (see Fig. 4.8) faces the same issues; however, the starting emittance was not perfectly chosen for the different simulations. With no corrections, CTEPY and the ODE model overestimate the emittance growth. By coupling the transverse IBS growth rates ($\kappa_{\mathrm{coup}} = 1$), CTEPY produces shrinkage of the emittance; however, it does not improve overlap between simulation and data.[13] With significantly reduced IBS growth rates, the corrected ODE model yields the best agreement if the initial offset of $-0.08\,\mu\mathrm{m}$ between the starting emittance and actual emittance is removed.

[13] Since full coupling is applied, a smaller coupling value would have improved the agreement between data and CTEPY.

Bunch-by-bunch luminosity Reproducing the luminosity turns out to be a challenging task. As an example, Fig. 4.9 shows the bunch luminosity at IP5 of bunch 73. All simulations overestimate the luminosity. This is not surprising considering the intensity decay was too small in most simulations. The corrected ODE model reproduces more or less the intensity decay of bunch 73; however, it still cannot match the luminosity decay. Since the initial luminosities coincide, the starting parameters seem acceptable. It is likely that the transverse and longitudinal distributions of the particles within the bunch are deviating from normal distributions; however, Gaussian shapes are required for the correct analytic calculations. This could be an explanation but remains speculative.

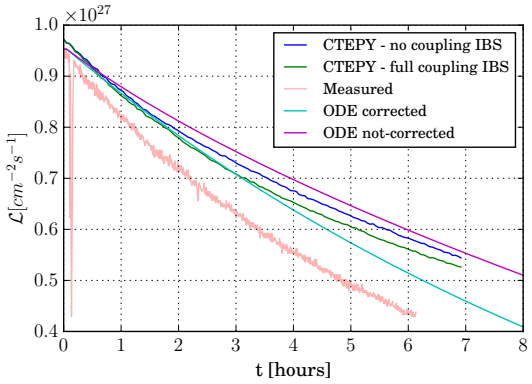

Figure 4.9: Luminosity evolution of bunch 73 (class 5; collisions in IPs 1, 5, and 8) in IP5. All simulations overestimate the bunch luminosity. This appears to happen even if the intensity evolution is well matched (modified ODE model; magenta). Plot taken from [165].

Beam intensity and luminosity Figure 4.10 shows the beam-intensity evolution and also the total luminosity in all detectors obtained from the ODE model including extra loss rates α_{IP} (no IBS corrections). With the corrections, the total intensities are reproduced to a very high degree. The luminosities, however, are in general overestimated. Even at the start of the fill, the initial luminosities do not coincide. This pattern gives evidence on either non-Gaussian distributions and/or systematic uncertainties of the measurements of the bunch parameters. One possibility is also inaccuracy in terms of the luminosity measurements of the experiments. These can easily have systematic uncertainties of $5\,\%$ to $10\,\%$ (see Chapter 5). In particular, the simulation of the ALICE luminosity yields differences to the measurement, whereas good agreement is achieved for ATLAS. Although the same bunch pairs provide the luminosities in ATLAS and CMS, the simulation of the CMS luminosity evolution is less accurate compared to that of ATLAS. This indicates that the horizontal emittance is not reproduced as well as the vertical emittance since the crossing plane is horizontal in CMS and vertical in ATLAS.

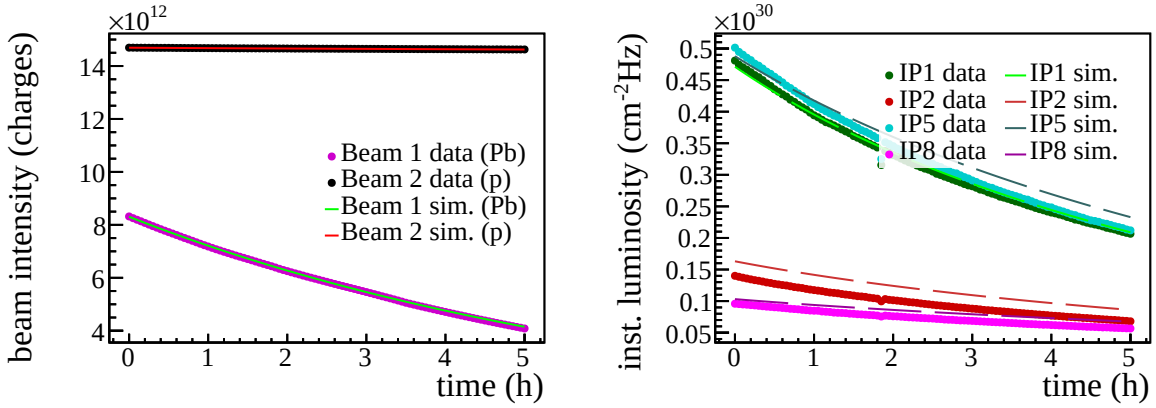

Figure 4.10: Left: Intensity evolution over $5\,\mathrm{h}$ of Fill 5549. The beam intensities simulated via the corrected ODE model (solid lines) and the measured intensities (dots) are displayed. Good accuracy is achieved as data and simulation coincide well. Right: Luminosity evolution over the same time period of the same fill. The simulated luminosities (dashed lines) and the measured luminosities (dots) do not coincide perfectly throughout the full fill duration.

From the bunch intensities, the individual intensity lifetimes τ of the bunches can be estimated via exponential fit (see Eq. 4.51). Figure 4.11 presents the bunch lifetimes versus bunch number for the Pb beam and proton beam. The agreement between the simulation and the measurement is excellent for the Pb beam. Variations and oscillations along the bunch train are reproduced by the corrected ODE model. Only if the luminosity burn-off is small (non-luminous losses are dominant), the agreement worsens. Similar behaviour is observed for the proton beam. Since the luminosity burn-off is weak for the proton beam, the overall agreement is understandably poor since the parameterisation of α_{ex} becomes crucial and assuming it as a constant independently of the bunch properties becomes an unsatisfactory approximation.

4.3.3 Beam evolution at $E_b = 4Z$ TeV

An equivalent simulation of Fill 5510 at $E_b = 4Z\,\mathrm{TeV}$ was performed. Extremely low luminosity burn-off effects the bunches during the fills since the levelling in ALICE was at $\mathcal{L} = 5 \times 10^{27}\,\mathrm{cm}^{-2}\mathrm{Hz}$ and ATLAS, CMS and LHCb had low numbers of colliding bunch pairs as is listed in Tab. 4.4, i.e., there were only 81 collisions in ATLAS/CMS and 54 collisions in LHCb while ALICE had 389 colliding bunch pairs. At $E_b = 4Z\,\mathrm{TeV}$, the non-colliding lifetimes of both beams are roughly halved compared to the values at $E_b = 6.5Z\,\mathrm{TeV}$, i.e., the non-colliding lifetime of the Pb bunches is only at $\tau_{\mathrm{ex}} = 41\,\mathrm{h}$. Similar corrections as in the $E_b = 6.5Z\,\mathrm{TeV}$ case are necessary. Table 4.5 lists the required extra loss rates α_{IP}. The extra losses show the same characteristics as before, in the sense that a smaller crossing angle requires a larger extra loss rate. The ATLAS/CMS extra loss rate changes by only $3\,\mathrm{h}$. This

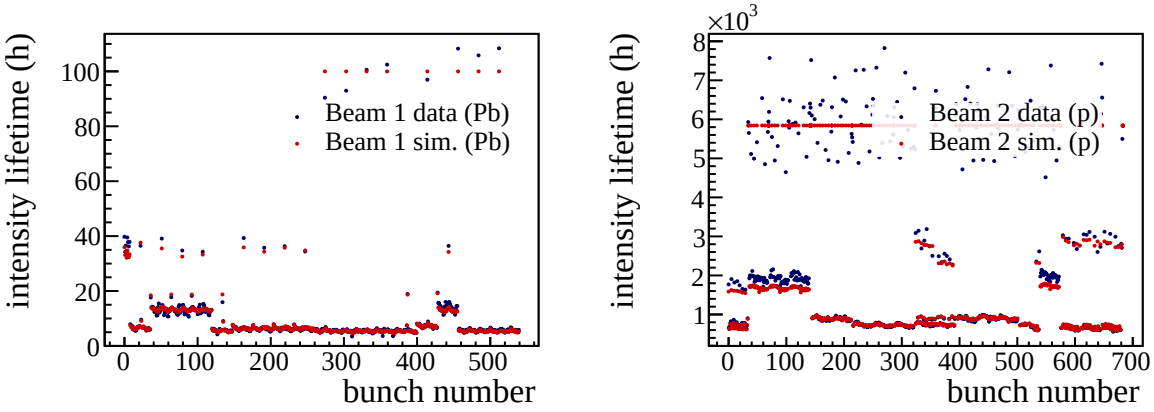

Figure 4.11: Left: Intensity lifetimes τ of the Pb bunches in Fill 5549. The clusters of bunches of the same bunch equivalence class form plateaus of roughly the same lifetime. Right: Intensity lifetimes of the proton bunches of the same fill. The proton lifetimes are clearly larger compared to these of the Pb beam.

suggests that this effect seems to be energy independent. The ALICE extra loss rate decreases substantially due to the luminosity levelling by separation. The LHCb loss rate increases to $\alpha_{\mathrm{IP}} = 1/95\,\mathrm{h}^{-1}$. This behaviour is hard to interpret since the crossing angle is larger compared to the $E_b = 6.5Z\,\mathrm{TeV}$ scenario; however, this loss rate is still small and underlies strong statistical uncertainties due to the small number of colliding bunch pairs in LHCb.

A detailed bunch-by-bunch analysis is omitted in the following. Figure 4.12 shows the beam lifetime of the measured data and the simulated data from the corrected ODE model. The model, however, does not include any modifications of the IBS growth rates. The nature of the non-luminous losses α_{ex} becomes highly significant in this low burn-off case. Previously, the approximation of a constant non-luminous loss rate yielded poor results only for the proton beam at $E_b = 6.5Z\,\mathrm{TeV}$. At $E_b = 4Z\,\mathrm{TeV}$, the simulation of both beams face this issue, i.e., the lifetimes of the proton and the Pb beam cannot be reproduced on a bunch-by-bunch basis. While the lifetimes for the Pb bunches can be reproduced on average, more complicated oscillations of the lifetimes along the bunch train are not reproduced. The head of each SPS train has a larger lifetime compared to its tail. This behaviour cannot be reproduced since this requires a correct parameterisation of α_{ex}. The simulated proton lifetimes are on average too small. Additional loss rates α_{IP} are switched off for the proton beam. The only explanation is that the luminosity and the resulting burn-off is overestimated in the simulation. This is hard to verify since the experiments were not able to provide adequate luminosity values at the start of the heavy-ion run.

A common feature of the proton beam among all fills was that two bunches per SPS injection were degraded. These bunches are clearly visible as they have significantly smaller lifetimes between $\tau = 1000$–$1500\,\mathrm{h}$ (see Fig. 4.12). The SPS injection kicker was not able to perfectly

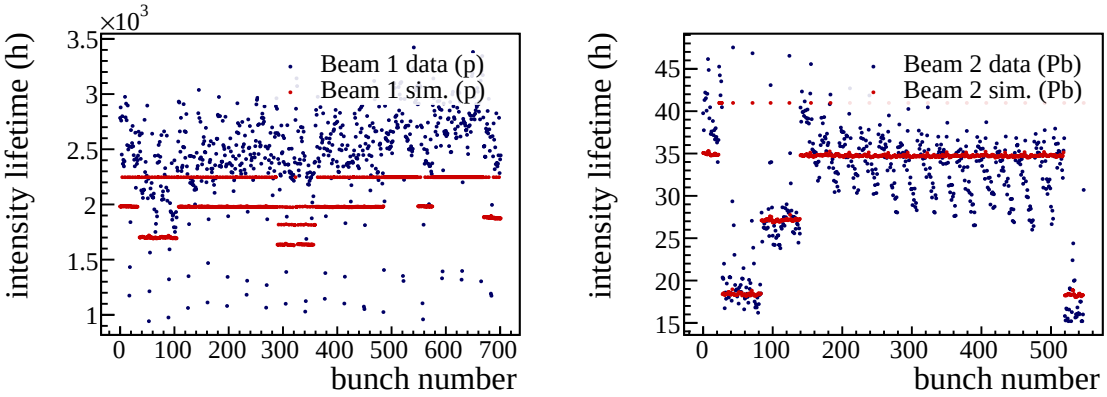

Figure 4.12: Left: Intensity lifetimes τ of the proton bunches in Fill 5510. Right: The intensity lifetimes of the Pb bunches. The fluctuations of the lifetime along the Pb bunch train are not reproduced by the corrected ODE model.

inject the second PS batch of 18 bunches without partially kicking the last bunch of the already injected batch and the first bunch of the newly injected batch. *Degenerated* refers to reduced bunch intensities and blown up emittances in this context. As a result, the non-luminous lifetime of these bunches is much shorter than those of the other bunches. The degenerated bunches influence the fitting process of the extra losses; therefore, the bunch-by-bunch lifetimes of the proton beam are shifted with respect to the bunches with normal lifetimes. Figure 4.13 shows that the total beam intensities are reproduced to a very high degree, but this is not achieved on a bunch-by-bunch basis.

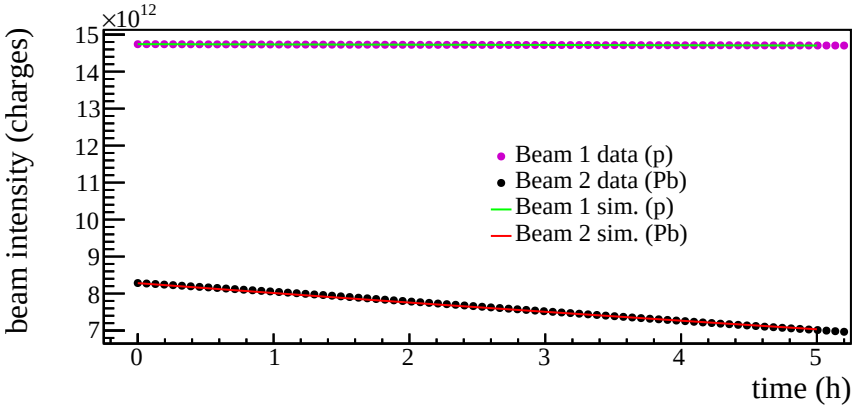

Figure 4.13: Intensity evolution of both beams in Fill 5510. The simulated evolution (solid lines) coincide very well with the measured evolution (dots). Although the total bunch intensities are reproduced to a very high degree, the bunch-by-bunch intensities are not perfectly matched.

4.4 Conclusion

This chapter presented a beam-evolution code based on ODEs. The code can simulate all bunches of both beams and includes the most important effects in a heavy-ion collider like the LHC, i.e., IBS, radiation damping, luminosity burn-off, luminosity levelling and non-luminous losses. The code was used to find evidence of unaccounted losses, i.e., losses that are neither generated by luminosity burn-off nor the loss mechanisms that contribute to the decay of non-colliding bunches. The beam-evolution study at $E_b = 6.5Z\,\mathrm{TeV}$ showed that the Pb beams in the LHC are subject to extra loss rates caused by head-on collisions in the IPs. The presence of the effect was unknown until this study was conducted. These extra loss rates at the IPs seem to depend on the crossing angles the beams are colliding with in the IPs. Estimating these loss rates was only possible by simulating the evolution of all bunches of both beams since the loss rates are not too large; however, they have an obvious effect on the beam evolution. Since bunches colliding in IP1 also collide in IP5 by design, the loss rates for IP1 and IP5 could not be disentangled and were considered as equal. Based on the fact that only head-on collisions cause the extra decay and the loss rates scale with the respective crossing angles, the loss rates are unlikely to be caused by parasitic beam-beam encounters or odd resonances excited by the collision with a crossing angle. As already mentioned in Sec. 4.3.2, a potential explanation could be the larger head-on tune shift which potentially shifts particles closer to destructive resonances in tune space. The presence of these extra losses is not supported by the FMA conducted in Chapter 3, i.e., no tune diffusion due to the non-linear part of the beam-beam force close to the bunch core of the Pb beam is observed. The FMA did not consider the crossing angles in the IPs; however, the loss rates increase with decreasing crossing angles. Hence, the FMA considered the *worst case* if one extrapolates the loss rates to zero crossing angles. The potential sources of the additional loss rates remain speculative. The analysis of Pb-Pb fills of, e.g., the 2018 heavy-ion run would be an important step to get a better understanding of these losses. In Pb-Pb collisions, both colliding beams are equal (no effects from colliding beams of different size). This will either verify or falsify whether the extra losses are caused from the collision of Pb bunches with smaller-sized proton bunches. Another important finding of the beam-evolution study is that the IBS growth rates are overestimated for the Pb bunches. The reduction of the IBS growth rate by $50\,\%$ led to acceptable results. This is a large factor and demonstrates some lack of understanding of the respective Pb IBS growth rates. The modified model (extra loss rates at the IPs) is capable of reproducing the beam evolution and oscillations of the intensity lifetime along the Pb bunch train to a very high degree; however, small discrepancies in terms of the detector luminosities and bunch length evolution remain.

The reproduction of a fill at $E_b = 4Z\,\mathrm{TeV}$ was much less successful compared to the fill at $E_b = 6.5Z\,\mathrm{TeV}$. The reason for the poor agreement at the smaller energy is that the modelling of the non-colliding lifetime becomes important since the luminosity burn-off was small during

this part of the 2016 heavy-ion run. During the early stages of the run, the luminosities published by the experiments were not highly accurate. Although the BSRT monitors were calibrated during this part of the heavy-ion run, even the initial luminosities in the simulation do not match with the measurements. Additional loss rates α_{IP} are also required at $E_b = 4Z\,\mathrm{TeV}$; however, it is more difficult to identify a scaling with the crossing angle since the ALICE luminosity is levelled and LHCb has only a few colliding bunch pairs. Much larger fluctuations in terms of lifetime of the bunches and bunch properties are observed in this low burn-off regime. The non-colliding lifetime of $1/\alpha_{\mathrm{ex}} \approx 41\,\mathrm{h}$ at $E_b = 4Z\,\mathrm{TeV}$ is significantly smaller compared to $1/\alpha_{\mathrm{ex}} \approx 100\,\mathrm{h}$ at $E_b = 6.5Z\,\mathrm{TeV}$.

CHAPTER 5

Proton-lead cross-section study at $\sqrt{s_{\mathrm{NN}}} = 8.16\,\mathrm{TeV}$

The total cross section in heavy-ion collisions is an important quantity useful for understanding the underlying particle physics and to benchmark existing models, e.g., Monte-Carlo Glauber calculations; however, it is also important for accelerator physicist to understand the observed beam intensity losses and loss patterns around the circumference of the accelerator. Even the four large experiments at the LHC have to make some effort to estimate these cross section quantities for, e.g., p-p, Pb-Pb and p-Pb collisions at the different beam energies and the experiments are partly limited by the rapidity range the respective detector is covering (extrapolation is required). In the scope of asymmetric p-Pb collision in the LHC, the ALICE and CMS collaborations have released measurements of the p-Pb cross section at the NN centre-of-mass energy of $\sqrt{s_{\mathrm{NN}}} = 5.02\,\mathrm{TeV}$ [143, 167] based on data taken during the 2013 p-Pb run of the LHC [4]. In 2016, the LHC was operated in p-Pb collisions at the two centre-of-mass energies $\sqrt{s_{\mathrm{NN}}} = 5.02\,\mathrm{TeV}$ and $\sqrt{s_{\mathrm{NN}}} = 8.16\,\mathrm{TeV}$ [5, 13, 165]. Although the cross section is only weakly dependent on the NN centre-of-mass energy at these high energies (see Fig. 4.1), the p-Pb cross section at $\sqrt{s_{\mathrm{NN}}} = 8.16\,\mathrm{TeV}$ has not been experimentally determined yet. The goal of this chapter is to obtain the total p-Pb cross section at $\sqrt{s_{\mathrm{NN}}} = 8.16\,\mathrm{TeV}$ using only the luminosity data provided by the experiments in combination with beam-intensity data and BLM signals. Such an analysis is challenging in the case of the LHC because of substantial non-luminous losses. Moreover, it is not possible to disentangle the contribution of ultra-peripheral collisions (BFPP and EMD) from the inelastic hadronic cross section. RHIC features stochastic cooling and therefore does not face this issue since non-luminous losses are virtually non-existent. This allowed the successful determination of the uranium-uranium (U-U) cross section at $\sqrt{s_{\mathrm{NN}}} = 192.8\,\mathrm{GeV}$ and the Au-Au cross section at $\sqrt{s_{\mathrm{NN}}} = 200\,\mathrm{GeV}$ by directly compar-

ing the total luminosity to the beam intensity decay [14, 15]. To overcome the disadvantage of substantial non-luminous losses in the LHC, a technique that uses the signals of selected BLMs to still determine the total cross section effectively is proposed.

5.1 Effective cross section

The main source of the beam intensity decay observed in a circular hadron collider like the LHC or RHIC is the luminosity burn-off. Although the luminous losses dominate the decay of the two colliding beams, other effects like the transport of particles to large betatron amplitudes by non-linearities, residual gas scattering and de-bunching also contribute to the total beam losses

$$\dot{N}_i = -\sigma \mathcal{L}_{\mathrm{tot}} - \alpha_{\mathrm{ex},i}(t, N, ...)\,. \tag{5.1}$$

Here, the index i refers to either the Pb or proton beam, N is the number of particles in the beam, σ is the total cross section and $\mathcal{L}_{\mathrm{tot}}$ is the total luminosity obtained by summing over all IPs

$$\mathcal{L}_{\mathrm{tot}}(t) = \sum_{i \in \mathrm{IPs}} \mathcal{L}_i(t)\,. \tag{5.2}$$

As previously mentioned in Sec. 4.3, the parameter α_{ex} comprises all non-luminous losses and depends on a variety of parameters, e.g., time t, intensity N but also bunch properties like the bunch length σ_z and emittances ϵ_u. An exact expression for α_{ex}, however, cannot be given generally. Because of unequal particle and bunch properties, the loss rate α_{ex} differs for the Pb and proton beam. At RHIC, stochastic cooling in all three planes [68–70] minimises the non-luminous losses. The losses become insignificant $\alpha_{\mathrm{ex}} \approx 0$ and the total cross section σ is easily obtained via linear fit of Eq. 5.1 as was successfully demonstrated for U-U and Au-Au collisions in RHIC [14, 15]. The LHC does not feature stochastic cooling. This makes a total cross-section estimate more challenging since the non-luminous losses α_{ex} are substantial. An important property indicating the magnitude of additional unwanted non-luminous losses is the so-called effective cross section (index i dropped)

$$\sigma_{\mathrm{eff}}(t) = -\frac{\dot{N}(t)}{\mathcal{L}_{\mathrm{tot}}(t)} = \sigma + \frac{\alpha_{\mathrm{ex}}(t)}{\mathcal{L}_{\mathrm{tot}}(t)}\,. \tag{5.3}$$

Besides being time dependent, this quantity has the property of being equal to the total cross section $\sigma_{\mathrm{eff}} = \sigma$ in the absence of other losses ($\alpha_{\mathrm{ex}} = 0$) and therefore gives a limit of the total cross section, i.e., the total cross section obeys $\sigma \leq \sigma_{\mathrm{eff}}$. Figure 5.1 shows an example of the evolution of the effective cross section over time of Fill 5571 of the 2016 Pb-p run of the LHC. The loss rate α_{ex} is potentially decreasing over time; however, the fill length is limited and whether σ_{eff} converges and, if so, to which value is unknown because of the lack of parameterisation of α_{ex}.

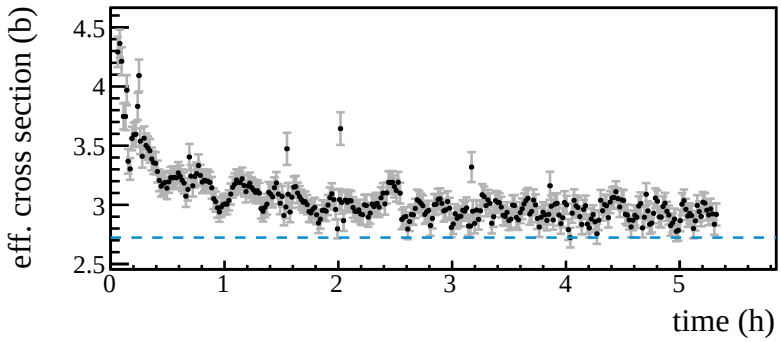

Figure 5.1: Evolution of σ_{eff} during Fill 5571 of the 2016 p-Pb run at $\sqrt{s_{\text{NN}}} = 8.16\,\text{TeV}$. The effective cross section and therefore the non-luminous losses decrease over time. The dashed line indicates the smallest value of σ_{eff} achieved during the fill. It is not clear whether σ_{eff} converges. The error bars are the statistical errors resulting from aligning the luminosity and intensity data to the same timestamps via moving average.

5.1.1 Beam-loss monitor signals

As previously mentioned, it is difficult to determine the cross section if non-luminous losses are masking the total cross section σ ($\sigma_{\text{eff}} > \sigma$). The proposed solution is to use the signals of BLMs to resolve this dilemma. The BLMs are mostly ionisation chambers distributed along the collider circumference. By selecting BLMs that measure signals exclusively generated by non-luminous losses α_{ex}, the total cross section can still effectively be determined. If a BLM measures only non-luminous losses, the BLM signal is

$$\Omega(t) = \Omega_0 + \Omega_1 \alpha_{\text{ex}}(t, N, ...)\,. \tag{5.4}$$

Here, Ω_0 is the BLM specific noise floor and Ω_1 is a scaling factor unknown at this point in time. Equation 5.4 assumes that the BLM behaves strictly linearly and that there is no cross-talk between the beams, i.e., the losses of the counter-rotating beam do not influence the BLMs of the other beam. Substituting Eq. 5.4 into Eq. 5.3 yields

$$\sigma_{\text{eff}}(t) = \sigma + \frac{1}{\Omega_1}\frac{\Omega(t) - \Omega_0}{\mathcal{L}_{\text{tot}}(t)}\,. \tag{5.5}$$

A linear fit of the data pairs $(\sigma_{\text{eff}}(t), (\Omega(t) - \Omega_0)/L_{\text{tot}}(t))$ with σ and Ω_1 as the two degrees of freedom yields the cross section. This procedure requires determining the noise level Ω_0 beforehand. The statistical errors are correlated when evaluating the cross section using multiple BLMs of the same fill; however, considering larger numbers of BLMs reduces the standard error of the mean significantly. The total cross section σ in Eq. 5.5 is the combination of the inelastic hadronic cross section σ_{had} and the contributions of the ultra-peripheral effects BFPP and

EMD $\sigma = \sigma_{\mathrm{had}} + \sigma_{\mathrm{EMD}} + \sigma_{\mathrm{BFPP}}$. Contributions of elastic scattering processes leading to particle losses are negligible. The inelastic hadronic cross section based on Monte-Carlo Glauber calculations at $\sqrt{s_{\mathrm{NN}}} = 8.16\,\mathrm{TeV}$ is given in [16] as

$$\sigma_{\mathrm{had}} = (2.12 \pm 0.01)\,\mathrm{b}\,. \tag{5.6}$$

The hadronic cross section represents therefore close to $96\,\%$ of the total cross section if one assumes the contribution of BFPP and EMD to the total cross section to be $0.079\,\mathrm{b}$ (see Sec. 4.1.4.3 and Tab. 4.3). This is in stark contrast to Pb-Pb operation. There, the hadronic cross section of roughly $\sigma_{\mathrm{had}} \approx 8\,\mathrm{b}$ is even less than $1.5\,\%$ of the total cross section. The predicted total p-Pb cross section then reads

$$\sigma = (2.20 \pm 0.03)\,\mathrm{b} \tag{5.7}$$

assuming the scaled BFPP and EMD cross sections having a systematic uncertainty of $20\,\%$.

5.2 Data acquisition

The beam intensity data obtained from the DC beam current transformer (DCBCT) are stored with a sampling rate of roughly $1\,\mathrm{Hz}$ in the LHC database. This analysis is based on the post-fill corrected offline luminosity data ("Massi files") which have a sampling rate of $1/60\,\mathrm{Hz}$. Depending on the BLM, the sampling rate is different but also roughly at $1/60\,\mathrm{Hz}$. In the following, the alignment of data series is always performed on the timestamps of the slower devices' sampling rate (mostly that of the luminosity data rather than those of the BLMs). The data series with the higher sampling rate is aligned to these time stamps using a moving average. An integration time of $1.31\,\mathrm{s}$ is used for the BLMs ("running sum 9").

The technique to obtain σ via fit of Eq. 5.5, can be performed for the Pb beam and the p beam separately; however, since the proton intensity is large compared to the luminous loss rate in nominal Pb-p operation, the loss rate calculation $\mathrm{d}N/\mathrm{d}t$ (required for the calculation of σ_{eff}) displays extremely large statistical fluctuations making an analysis of the proton beam close to impossible (see discussion in Sec. 4.3). Hence, the analysis is restricted to the Pb beam.

5.3 Beam-loss monitor selection

Considering any BLM to estimate the total cross section makes little sense as the BLM is required to measure mostly non-luminous losses. The selection process of the BLMs is explained in the following.

Two collimation sections are installed in the LHC as was already explained in Sec. 1.2.3. The first collimation section is located at IR3 at the 9 o'clock position of the LHC (see Fig. 1.1)

and applies momentum cleaning to the beam, i.e., particles with a large longitudinal momentum deviation are intercepted by collimators. A second collimation section at IR7 at the 3 o'clock position of the LHC provides amplitude cleaning, i.e., particles that have too large transverse actions are scraped by the collimators and are removed from the beam. The BLMs in these two sections are expected to detect most of the beam intensity losses occurring during operation. Nevertheless, the IR3 BLMs are excluded from this analysis. Reason for this is that $^{207}\mathrm{Pb}^{82+}$ ions generated by EMD processes at the IPs (see Eq. 4.35) propagate large distances in the machine before they are intercepted at the position of the smallest energy acceptance, the IR3 TCP collimators. Hence, the BLMs in IR3 are presumably measuring partly luminous losses, and a reliable calculation of the total cross section becomes impossible.

To ensure the selection of BLMs only measuring non-luminous losses in IR7, the linear correlation coefficient $l = \mathrm{cov}(x, y)/(\sigma_x \sigma_y)$ is calculated for the data pairs $(\sigma_{\mathrm{eff}}(t), (\Omega(t) - \Omega_0))/\mathcal{L}_{\mathrm{tot}})$ of each BLM located there. Only BLMs measuring non-luminous losses should display a large linear correlation coefficient l, i.e., their behaviour is expressed by Eq. 5.4. To exclude potential non-linearities at high BLM signals, a cut is applied to the data of large $(\Omega(t) - \Omega_0)/\mathcal{L}_{\mathrm{tot}}(t)$ in order to maximise the correlation coefficient l. The top plot of Fig. 5.2 shows the correlation coefficients of the BLMs in IR7 for Fill 5571. Visible are the large correlation coefficients at the TCP collimators and TCSG collimators as well in two regions at $s = 20\,330\,\mathrm{m}$ and $s = 20\,420\,\mathrm{m}$ which are in the dispersion suppressor, a matching section necessary to reduce the dispersion function in the IR. This loss pattern is consistent with simulated loss patterns using a combination of tracking and fragmentation software displayed in [158, 159]. The losses in the dispersion suppressors are mostly due to $^{207}\mathrm{Pb}^{82+}$ ions from EMD1 interactions and of unmodified but scattered Pb ions with the collimators in IR7 (see Eq. 4.39). The bottom plot of Figure 5.2 displays the fitted cross section versus the correlation coefficients. Clearly, BLMs featuring a large correlation coefficient yield a cross section closer to the calculated value of $\sigma = 2.20\,\mathrm{b}$. As an example, Fig. 5.3 shows such a fit of a BLM located at a TCSG collimator.

A phenomenon observed during this study was the behaviour of the BLMs at the TCPs. The BLMs at the TCPs displayed a range of correlation coefficients l from moderate to high correlation. Although one expects a cross section close to the theoretical value if l is large, the TCP BLMs yield a minimal cross section (50 % deviation from the theoretical value). One potential explanation is again the measurement of luminous losses. In the following, the selection is restricted to BLMs in regions the loss mechanisms are well understood and of non-luminous nature:

- The BLMs located at the loss clusters in the dispersion suppressors of IR7 at $s = 20\,330\,\mathrm{m}$ and $s = 20\,420\,\mathrm{m}$ in Pb-p operation and $s = 19\,580\,\mathrm{m}$ and $s = 19\,660\,\mathrm{m}$ in p-Pb operation are selected. The losses in the dispersion suppressor are mostly due to EMD1 particles of unmodified Pb generated at the different collimator stages in IR7.

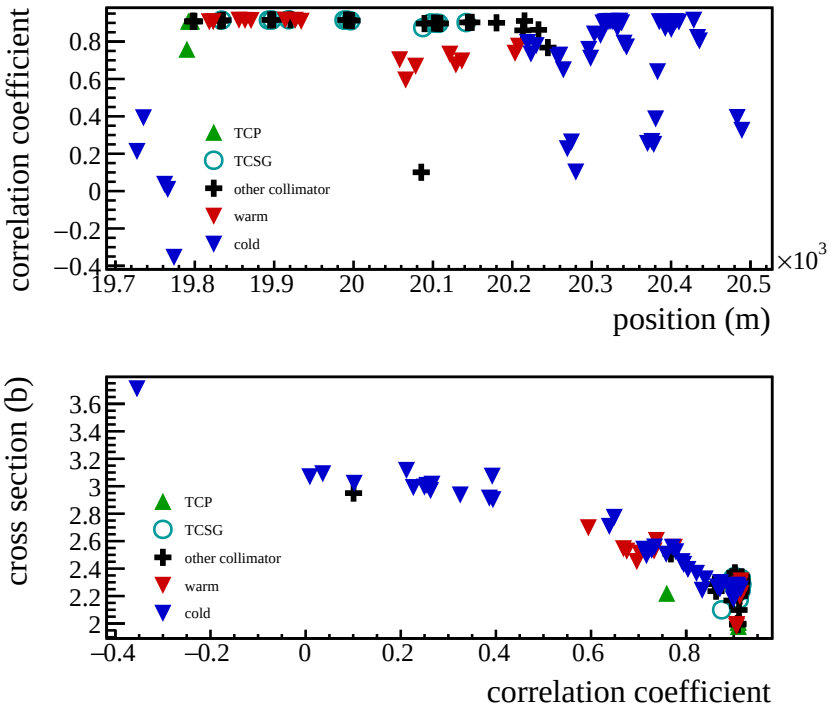

Figure 5.2: Top: The correlation coefficients of the BLMs along IR7 for Fill 5571. The plot indicates whether the BLMs are positioned close to collimators and if the aperture at the BLMs is superconducting (cold) or warm. The Pb direction of flight is left to right. Bottom: The cross sections versus the correlation coefficients of all BLMs in IR7 of Fill 5571. For reasons that are not known, the results for the cross section at the TCPs (green triangles) are much lower than the expected value of $\sigma = 2.20\,\mathrm{b}$, although the correlation coefficients l are above 0.9. The error bars are omitted for visibility in this plot.

- The second group of BLMs that are considered are the BLMs at the TCSG collimators in IR7. The correlation coefficients of these BLMs are the largest throughout all fills. The TCSG losses are mostly due to unmodified Pb ions that scatter on the TCPs. The scattered Pb ions are then colliding with the TCSGs and break up.

The possibility of the BLMs being influenced by the losses of the counter-rotating proton beam is not considered in this analysis.

Although the selected BLMs have generally large correlation coefficients l, there are particular fills during which the loss patterns are disturbed and specific BLMs do not behave as expected. To disqualify BLMs that measure not only non-luminous losses, a threshold of $l \geq 0.8$ is applied. Hence, only BLMs at TCSGs and in the dispersion suppressors with a correlation coefficient above this threshold are considered.

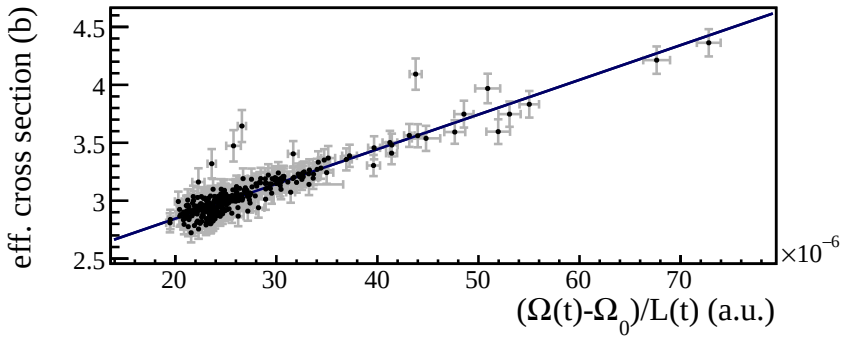

Figure 5.3: The effective cross section $\sigma_{\text{eff}}(t)$ as a function of $(\Omega(t) - \Omega_0)/\mathcal{L}_{\text{tot}}(t)$ for the BLM at TCSG collimator of IR7 ("TCSG.A4L7.B1") during Fill 5571 (black dots). The cross section is obtained via a weighted linear fit (blue line). The error bars of the data are the statistical error arising from aligning the data via moving average (systematic errors not shown here). The fitted total cross section σ, i.e., the intersection of the linear fit with the ordinate, is $\sigma = 2.25 \pm 0.02\,\text{b}$. The correlation coefficient is $l = 0.92$. No data points at high BLM signals were truncated to maximise l for this BLM (all data points considered).

5.4 Fill selection

Figure 5.4 shows all fills of the 2016 heavy-ion run of the LHC at the centre-of-mass energy $\sqrt{s_{\text{NN}}} = 8.16\,\text{TeV}$ that reached Stable Beams status. The Stable Beams duration was strongly varying and also the quality of the data. Nine of the 31 fills were rejected beforehand since these fills were either meant for Van-der-Meer scans or the luminosity data were faulty. Because of the correlation coefficient threshold of $l \geq 0.8$, additional four fills were excluded from the analysis. In these fills, not a single BLM displayed a sufficiently large l as shown in Figure 5.5. This leaves five fills in p-Pb and 13 in Pb-p configuration. The first-mentioned ion species occupies the first LHC beam (clockwise rotating) and the latter species the second beam (counterclockwise rotating).

5.5 Systematic uncertainties

The total cross section, if obtained via fit of Eq. 5.5, is susceptible to systematic and statistic uncertainties of multiple measuring devices. The relative systematic error of the cross section σ is

$$\frac{\delta\sigma^{\text{sys.}}}{\sigma} = \frac{\delta N^{\text{sys.}}}{N} + \frac{\delta\mathcal{L}_{\text{tot}}^{\text{sys.}}}{\mathcal{L}_{\text{tot}}} + \frac{\delta\Omega_0^{\text{sys.}}}{|\Omega_1\mathcal{L}_{\text{tot}}\sigma|}\,. \tag{5.8}$$

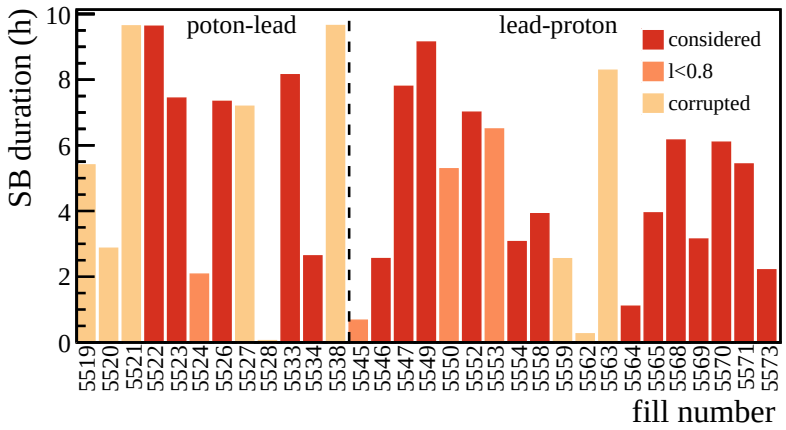

Figure 5.4: All fills with their duration in Stable Beams (SB). The fills in dark red are considered in the analysis. The other fills have either corrupted luminosity data, are fills of Van-der-Meer scans or have displayed poor correlation coefficients, i.e., no BLM signal was sufficiently measuring the non-luminous losses. At Fill 5545, the beam directions were switched, i.e., protons (Pb) switched from Beam 1 (Beam 2) to Beam 2 (Beam 1).

The relative error of $\dot{N}$ is equal to that of N, i.e., the DCBCT measurement [168]. A potential error of the time t leads to a negligible systematic error compared to the other systematic errors. The relative error of the total luminosity $\mathcal{L}_{\mathrm{tot}}$ is fill dependent and reads

$$\frac{\delta\mathcal{L}^{\mathrm{sys.}}}{\mathcal{L}_{\mathrm{tot}}} = \frac{\sum_i \delta\mathcal{L}_i{}^{\mathrm{sys.}}}{\sum_i \mathcal{L}_i}\,. \tag{5.9}$$

The contribution of each experiment to the total luminosity influences the total relative error since the errors are unequal among the experiments and depend on the beam direction (Pb-p or p-Pb). The systematic error of the luminosity has multiple sources. An overview can be found in [169]. At the time of this analysis, the systematic uncertainties of the ALICE and LHCb luminosity measurements are not known. Since these uncertainties are crucial for the analysis, the systematic uncertainties are estimated from the ATLAS and CMS relative uncertainties in Sec. 5.5.1.

The extrapolation of BLM data is not sensitive to a systematic relative error of the real BLM signal $(\Omega(t) - \Omega_0)$ because of the free parameter Ω_1 during the fitting process. Therefore, a discussion of the BLM systematic error is not of interest. A systematic error of the noise floor Ω_0, on the other hand, influences the cross section σ although only weakly since the BLM signals of the selected BLMs at the TCSGs and the dispersion suppressors are large compared to the respective noise floor $(\Omega(t) \gg \Omega_0)$. The systematic uncertainty of the noise floor Ω_0 is estimated as the standard deviation of the BLM signal between the fills (no circulating beams). Potential non-linear behaviour of the BLMs would also influence the result. Hence, large BLM

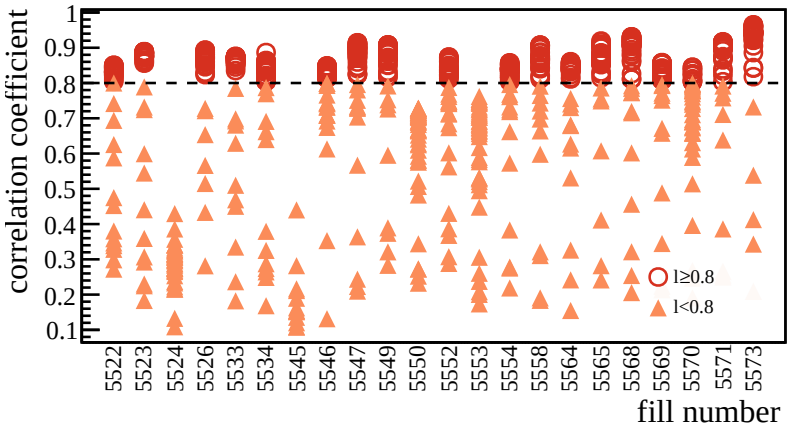

Figure 5.5: Linear correlations coefficients of the selected BLMs for all fills. Circles indicate the BLMs with a correlation coefficient larger than the threshold $l \geq 0.8$, while the triangles show the BLMs with $l < 0.8$. Five fills do not have a single BLM in the required $l \geq 0.8$ range and are therefore disqualified from the analysis.

signals that lead to a smaller correlation coefficient l are disregarded from the analysis, i.e., a correlation coefficient l maximising cut is applied to the data sets and only BLMs that feature data sets $(\sigma_{\text{eff}}(t), (\Omega(t) - \Omega_0))/\mathcal{L}_{\text{tot}}(t))$ with a correlation coefficient $l \geq 0.8$ are considered. This way, the effects of potential non-linear behaviour are minimised. Since $\mathcal{L}_{\text{tot}}$ in the third summand of Eq. 5.8 changes over the duration of the fill, $\mathcal{L}_{\text{tot}}$ is chosen to be the minimum luminosity of the fill at this instant to obtain a pessimistic but constant relative systematic error $\delta\sigma^{\text{sys.}}/\sigma$ for the entire duration of the fill. Table 5.1 gives a list of the systematic uncertainties.

Table 5.1: List of the systematic uncertainties influencing the result for σ. Pairs of two values separated by comma refer to the different beam configurations (Pb-p, p-Pb). In case of ALICE and LHCb, the averages of the systematic uncertainties of the luminosities among all fills are given.

Measured quantity	Rel. systematic uncertainty	Reference
Beam current (DCBCT)	0.2 %	[168]
Luminosities		
ATLAS	(6.4 %, 6.2 %)	[170]
ALICE	28 %	
CMS	(3.2 %, 3.7 %)	[169]
LHCb	14 %	
BLM noise floor	various	

5.5.1 Systematic uncertainties of the ALICE and LHCb luminosities

The systematic uncertainty of the IP1 (IP5) luminosity is used to estimate the systematic uncertainty of IP2 (IP8) since the collisions take place in the same vertical (horizontal) crossing plane in each of these pairs of detectors. From the luminosity values of IP1 and IP5, the expected luminosity for either IP2 or IP8 can be obtained via $\mathcal{L}^{\mathrm{exp}}_{\mathrm{IP1/2}} = \mathcal{S}\mathcal{L}_{\mathrm{IP1/5}}$. The scaling factor $\mathcal{S}$ takes the ratio between the number of colliding bunch pairs n_c in IP1/5 and IP2/8 into account as well as the ratio of the β^* and the luminosity reduction factors (see Eqs. 4.25–4.27). Because of different beam parameters at the IPs, $\mathcal{S}$ is different for IP2 and IP8. The relative systematic uncertainty of $\mathcal{S}$ is not expected to exceed $5\,\%$ (uncertainties of the crossing angles and β^*) and statistical fluctuations of the bunch properties are assumed to vanish on average based on the large numbers of colliding bunch pairs. The difference between the expected and measured luminosity is $\left|\mathcal{L}_{\mathrm{IP2/8}} - \mathcal{S}\mathcal{L}_{\mathrm{IP1/5}}\right|$. With these definitions, the relative systematic uncertainty is then estimated as

$$\frac{\delta\mathcal{L}^{\mathrm{sys}}_{\mathrm{IP2/8}}}{\mathcal{L}_{\mathrm{IP2/8}}} = \left|\frac{\mathcal{L}_{\mathrm{IP2/8}} - \mathcal{S}\mathcal{L}_{\mathrm{IP1/5}}}{\mathcal{L}_{\mathrm{IP2/8}}}\right| + \frac{\delta\mathcal{L}^{\mathrm{sys}}_{\mathrm{IP1/5}}}{\mathcal{L}_{\mathrm{IP1/5}}} + \frac{\delta\mathcal{S}^{\mathrm{sys}}}{\mathcal{S}}\,. \tag{5.10}$$

Table 5.1 gives the average relative systematic uncertainties of the ALICE and LHCb luminosities.

5.6 Results

Fills in the p-Pb configuration are analysed separately from fills in Pb-p configuration. This is necessary since different BLMs are used for the two beams and the loss patterns along the LHC are different for the two beam directions.

5.6.1 p-Pb operation

Five fills are considered in p-Pb configuration, i.e., protons are stored in Beam 1 (rotating clockwise) and Pb ions are stored in Beam 2 (rotating counterclockwise). Six other fills have either corrupted luminosity data or do not display any BLMs with sufficiently large correlation coefficients. The results for the cross section of each of the five fills are listed in the top part of Tab. 5.2 and are shown in Fig. 5.6. The result for each fill is obtained by calculating the average of σ between the considered BLMs while assuming correlated statistical and systematic errors since the fitted cross section for each BLM of that fill is based on the same intensity and luminosity data. Thus, the statistical and systematic uncertainty of each cross section in Tab. 5.2 is the mean of the uncertainties between the considered BLMs of a fill. The number of considered

Table 5.2: List of the considered LHC fills and results for the total cross section σ that were obtained via the linear fit of Eq. 5.5. For each fill, the listed cross section is the combined result of all considered BLMs in that fill.

Fills		Considered BLMs	Total cross section σ (b)
p-Pb fills	5522	30	$2.36 \pm 0.01\,(\text{stat.}) \pm 0.18\,(\text{sys.})$
	5523	32	$2.38 \pm 0.01\,(\text{stat.}) \pm 0.18\,(\text{sys.})$
	5526	33	$2.56 \pm 0.01\,(\text{stat.}) \pm 0.26\,(\text{sys.})$
	5533	31	$2.36 \pm 0.01\,(\text{stat.}) \pm 0.24\,(\text{sys.})$
	5534	32	$2.44 \pm 0.03\,(\text{stat.}) \pm 0.22\,(\text{sys.})$
Pb-p fills	5546	24	$2.27 \pm 0.05\,(\text{stat.}) \pm 0.28\,(\text{sys.})$
	5547	32	$2.23 \pm 0.03\,(\text{stat.}) \pm 0.17\,(\text{sys.})$
	5549	35	$2.24 \pm 0.03\,(\text{stat.}) \pm 0.21\,(\text{sys.})$
	5552	26	$2.27 \pm 0.03\,(\text{stat.}) \pm 0.22\,(\text{sys.})$
	5554	32	$2.35 \pm 0.04\,(\text{stat.}) \pm 0.20\,(\text{sys.})$
	5558	33	$2.33 \pm 0.04\,(\text{stat.}) \pm 0.24\,(\text{sys.})$
	5564	33	$2.26 \pm 0.07\,(\text{stat.}) \pm 0.17\,(\text{sys.})$
	5565	37	$2.26 \pm 0.05\,(\text{stat.}) \pm 0.16\,(\text{sys.})$
	5568	33	$2.25 \pm 0.02\,(\text{stat.}) \pm 0.17\,(\text{sys.})$
	5569	33	$2.31 \pm 0.04\,(\text{stat.}) \pm 0.16\,(\text{sys.})$
	5570	11	$2.29 \pm 0.03\,(\text{stat.}) \pm 0.16\,(\text{sys.})$
	5571	35	$2.27 \pm 0.02\,(\text{stat.}) \pm 0.17\,(\text{sys.})$
	5573	39	$2.32 \pm 0.04\,(\text{stat.}) \pm 0.17\,(\text{sys.})$
p-Pb fills		–	$2.42 \pm 0.01\,(\text{stat.}) \pm 0.22\,(\text{sys.})$
Pb-p fills		–	$2.28 \pm 0.01\,(\text{stat.}) \pm 0.19\,(\text{sys.})$
All fills		–	$2.32 \pm 0.01\,(\text{stat.}) \pm 0.20\,(\text{sys.})$

BLMs per fill is at least 30 in all five fills. The combined total cross section in p-Pb operation is

$$\sigma_{\text{p-Pb}} = (2.42 \pm 0.01\,(\text{stat.}) \pm 0.22\,(\text{sys.}))\,\text{b}\,. \tag{5.11}$$

Here, the statistical (systematic) uncertainties are assumed to be uncorrelated (correlated) between the fills. The value for $\sigma_{\text{p-Pb}}$ is $10\,\%$ larger than the expected value of $\sigma = (2.20 \pm 0.03)\,\text{b}$. The combined statistical and systematic relative error of $\sigma_{\text{p-Pb}}$ is $9.0\,\%$. By subtracting the BFPP and EMD contributions from the total cross section, the hadronic cross section is obtained

$$\sigma_{\text{had,p-Pb}} = (2.34 \pm 0.01\,(\text{stat.}) \pm 0.23\,(\text{sys.}))\,\text{b}\,. \tag{5.12}$$

The calculated value $\sigma_{\text{had}} = (2.12 \pm 0.01)\,\text{b}$ in Eq. 5.6 is just inside the uncertainty range.

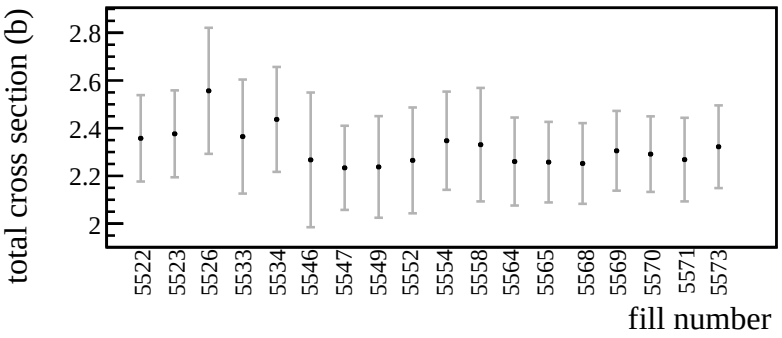

Figure 5.6: The total estimated cross section for each of the 18 considered fills. Slightly larger values are obtained for the first five fills, all being in p-Pb configuration. The errors are the combined statistical and systematic errors.

5.6.2 Pb-p operation

Thirteen fills are considered in Pb-p operation. Seven fills featured either faulty luminosity data or not a single BLM with a correlation coefficient larger than $l \geq 0.8$. Except for three out of the 13 fills, over 30 BLMs are considered for estimating the cross section. The bottom part of Tab. 5.2 gives the number of the considered BLMs and the results for the total cross section for each fill in Pb-p operation. Combining the results of all fills in Pb-p configuration yields the total cross section

$$\sigma_{\text{Pb-p}} = (2.28 \pm 0.01\,(\text{stat.}) \pm 0.19\,(\text{sys.}))\,\text{b}\,. \tag{5.13}$$

The combined relative error of $8.3\,\%$ is slightly smaller than in p-Pb operation. The value of $\sigma_{\text{Pb-p}}$ is only $3.6\,\%$ larger than the predicted value of $\sigma = (2.20 \pm 0.03)\,\text{b}$. Based on Eq. 5.13, the hadronic cross section is expected to be

$$\sigma_{\text{had,Pb-p}} = (2.20 \pm 0.01\,(\text{stat.}) \pm 0.21\,(\text{sys.}))\,\text{b}\,. \tag{5.14}$$

The value $\sigma_{\text{had}} = (2.12 \pm 0.01)\,\text{b}$ given in Eq. 5.6 is well within the uncertainty range, i.e., the estimate of the total cross section in p-Pb configuration deviates only by $3.8\,\%$ from that value. Thus, the result for the hadronic cross section in Pb-p configuration seems to be closer to the predicted value than with inverted beam directions.

5.7 Conclusion

The analysis has shown slightly different estimates for the total cross section depending on the beam directions. The p-Pb configuration yields a slightly larger value for σ than that obtained

in Pb-p configuration. The overall result for the total cross section considering all fills in p-Pb and Pb-p configuration is

$$\sigma = (2.32 \pm 0.01\,(\text{stat.}) \pm 0.20\,(\text{sys.}))\,\text{b}\,. \tag{5.15}$$

This value deviates by only $5.4\,\%$ from the predicted total cross section given in Eq. 5.7. After the subtraction of the EMD and BFPP contributions, the hadronic cross section then is

$$\sigma_{\text{had}} = (2.24 \pm 0.01\,(\text{stat.}) \pm 0.21\,(\text{sys.}))\,\text{b}\,. \tag{5.16}$$

The theoretical value $\sigma_{\text{had}} = (2.12 \pm 0.01)\,\text{b}$ given in Eq. 5.6 is well within the uncertainty range. The overall result for σ_{had} deviates by only $5.7\,\%$ from that value. This is a good result considering the presence of substantial non-luminous losses. Using BLM signals to estimate the cross section is therefore a viable method to estimate the total cross section even without active stochastic cooling. Because of the low luminosity burn-off in the proton beam and consequently small relative beam intensity changes $\dot{N}/N$, the analysis had to be restricted to the Pb beam. In a symmetric case with the same particle species in both beams and equal luminosity burn-off, the extrapolation of BLM data to determine the total cross section σ is applicable to both beams simultaneously. This would improve the overall statistics of the final result.

The result for the total and hadronic cross section features large systematic uncertainties ($8.6\,\%$ combined relative uncertainty). The largest contributors are the uncertainties of the luminosity measurement of the experiments. ATLAS and CMS are the high-luminosity experiments; therefore; the uncertainties of $3.2\,\%$ (CMS in Pb-p configuration) to $6.4\,\%$ (ATLAS in p-Pb configuration) are limiting the systematic uncertainty of the final result. The ALICE and LHCb systematic uncertainties on the measured luminosity had to be estimated from the ATLAS and CMS systematic uncertainties. Hence, a pessimistic approach for the estimate of the ALICE and LHCb systematic uncertainties had to be chosen to ensure a sufficient systematic uncertainty. Although the contributions from ALICE and LHCb to the total luminosity are much smaller than those of ATLAS and CMS, large systematic uncertainties of $28\,\%$ (average among all fills) on the ALICE luminosity and $14\,\%$ on the LHCb luminosity increase the systematic uncertainty of the result for σ significantly. The first step to improve the accuracy of σ is the analysis of the ALICE and LHCb Van-der-Meer scans to get exact values for the systematic uncertainty of the ALICE and LHCb luminosities. That way, the pessimistic estimate for the ALICE/LHCb systematic uncertainties can be avoided.

The presented analysis lacks explanation regarding the behaviour of the BLMs at the TCP collimators. The smaller values for σ in the presence of large correlation coefficients are not understood. Possible explanations are luminous losses or contributions from the proton beam to the Pb BLM signals. As a potential next step, the contribution of the proton beam to the BLM signals of the Pb beam should be analysed. This would identify BLMs that are not (or at least

weakly) influenced by the counter-rotating beam and consequently a better BLM selection can be performed.

The result for the total cross section of $\sigma = (2.32 \pm 0.01\,(\mathrm{stat.}) \pm 0.20\,(\mathrm{sys.}))\,\mathrm{b}$ gives evidence of the extra loss rates that were determined in Chapter 4; however, an underestimated total cross section σ in the beam-evolution study would also cause a scaling of the extra loss rates with $\alpha_{\mathrm{IP}} \propto 1/\beta^*$. This is because the dependence of the luminosity reduction on θ is weaker than its dependence on β^*. Nevertheless, a larger total cross section would decrease the required extra loss rates α_{IP} to match the measured intensity decay during the beam-evolution study slightly.

CHAPTER 6

Performance of future proton-lead runs of the LHC

The LHC will continue to collide p-Pb in future runs. The next p-Pb run of the LHC is scheduled for 2028. In the context of CERN's working group 5 (WG5) of the workshop on the physics of the CERN HL-LHC and perspectives at the HE-LHC, the experiments agreed to request the next p-Pb run for 2023. This run, however, has not been confirmed yet. Table 6.1 contains the proposed heavy-ion run schedule for the upcoming years. The report [17] of WG5 was part of the submission to the European Strategy Particle Physics Update (ESPPU) [79, 171].

In this chapter, the study that was carried out in the context of the WG5 to estimate the potential performance of such a future p-Pb run is presented. The HL-LHC [59] will officially operate from LHC Run 4 on and beyond. The third long shutdown of the LHC (LS3) from 2024 until the 2027 will include major upgrades of the LHC, enhancing mainly the p-p performance. These upgrades, however, will only have minor effects on the heavy-ion performance of the LHC. The upgrade effecting the heavy-ion performance of the (HL-)LHC the most is longitudinal slip-stacking in the SPS (see Chapter 1). This upgrade will reduce the bunch spacing in the LHC to $50\,\mathrm{ns}$ and is expected to be operational already at the end of LS2, i.e., at the start of LHC Run 3. Hence, the Run 3 p-Pb performance should mostly be equal to the Run 4 performance besides potentially improved β^* and crossing angles θ once the HL-LHC starts operation. The ALICE detector upgrade foresees the upgrade of the ALICE TPC [172], the system with the slowest read-out rate of the ALICE detector. The TPC read-out rate was limiting the instantaneous luminosity to $\mathcal{L} = 10^{29}\,\mathrm{cm}^{-2}\mathrm{Hz}$ in p-Pb operation at $\sqrt{s_{\mathrm{NN}}} = 8.16\,\mathrm{TeV}$ in 2016. The TPC upgrade will unlock a five times larger levelling value $\mathcal{L} = 5 \times 10^{29}\,\mathrm{cm}^{-2}\mathrm{Hz}$ in ALICE in upcoming p-Pb runs after LS2.

Compared to the 2016 p-Pb run, larger luminosities are expected in upcoming p-Pb runs mainly due to increased bunch numbers. In 2016, the performance limit was set by the losses in the dispersion suppressors at IP1 and IP5 due to collision debris [21], i.e., particles resulting from fragmentation of Pb ions due to the collision with counter-rotating protons. Since the collimation-debris collimators (TCLs) were not inserted into the beams in 2016, this chapter also contains a study on whether adequately aligned TCLs would intercept these fragments. This study is critical since otherwise uncertainties on whether peak performance can be achieved in the future remain. If the losses in the dispersion suppressors cannot be mitigated in the future, the peak luminosity is limited to the 2016 value in IP1 and IP5.

Besides a potential p-Pb run in LHC Run 3, a potential proton-oxygen (p-O) pilot run is also requested for Run 3 (see Tab. 6.1). This would be the second asymmetric beam configuration the LHC has accelerated and collided. A potential p-O pilot run comparable to the p-Pb pilot run in 2012 [3] and the Xe-Xe pilot study in 2017 [47] will take place in 2023. Such a pilot run, however, has not been confirmed yet. Symmetric A-A collisions of intermediately sized ions are planned to take place in LHC Run 5 and beyond. As reference for symmetric A-A data, it is highly likely respective p-A collisions will be requested for LHC Run 6 and beyond. The potential performance of the LHC in a short p-O pilot run and in p-A collisions with ion species lighter than Pb is analysed in Chapter 7. This chapter focuses exclusively on the future p-Pb performance of the LHC.

6.1 Future performance in p-Pb collisions

In this section, the one-month performance of a p-Pb run taking place either in 2023 or 2028 is estimated. This estimate is based on a beam-evolution code presented in Chapter 4, i.e., the evolution of each bunch is calculated via the coupled ordinary differential Eqs. 4.45–4.46. At first, the simulation setup and the collider parameters are explained. After that, the performance results are presented. As previously mentioned, this study was carried out in the context of CERN's WG5. Parts of the results that are going to be presented have already been published [17, 18].

6.1.1 Simulation setup

Filling pattern If slip-stacking is available in the SPS, future filling patterns will feature a $50\,\mathrm{ns}$ bunch spacing, i.e., the number of bunches per beam is roughly doubled compared to 2016. As a potential filling pattern, the HL-LHC Pb-Pb filling pattern presented in [58] is used. Each bunch train comprises 23 injections from the SPS with a maximum of 56 bunches per SPS injection leading to a total of 1232 bunches per beam. The filling patterns for both beams are displayed in Fig. 6.1 and provide 1136 collisions to ATLAS/CMS, 1120 collisions to ALICE and

Table 6.1: Proposed run schedule for heavy-ion operation as presented by the WG5. In contrast to the present schedule, Run 3 may comprise short oxygen-oxygen (O-O) and proton-oxygen (p-O) pilot runs as well as a three-week to four-week long p-Pb run. For Run 5, an intermediately sized ion species will most likely be requested. Table adapted from [173].

Run	Year	Collision system	Centre-of-mass energy $\sqrt{s_{\mathrm{NN}}}$	Run duration
Run 3	2021	Pb-Pb	5.5 TeV	3 weeks
		p-p	5.5 TeV	1 week
	2022	p-O, O-O	5.5 TeV	1 week
		Pb-Pb	5.5 TeV	5 weeks
	2023	p-p	8.8 TeV	few days
		p-Pb	8.8 TeV	3–4 weeks
	Long Shutdown 3			
Run 4	2027	Pb-Pb	5.5 TeV	3 weeks
		p-p	5.5 TeV	1 week
	2028	Pb-Pb	5.5 TeV	2 weeks
		p-Pb	8.8 TeV	3–4 weeks
		p-p	8.8 TeV	few days
	2029	Pb-Pb	5.5 TeV	4 weeks
	Long Shutdown 4			
Run 5		intermediate A-A	–	11 weeks
		p-p	–	1 week

81 collisions to LHCb. The filling pattern is not final and the numbers of colliding bunch pairs in the IPs are most likely going to be redistributed (more collisions in LHCb). The proton injection is expected to be flexible enough to reproduce the Pb bunch train.[1] In the simulation, Beam 1 is assumed to contain the Pb bunches and Beam 2 the proton beam; however, interchanging the beams does not influence the simulation outcomes and conclusions.

Optics at the IPs The smallest β^* values in heavy-ion operation were achieved during the 2018 Pb-Pb run with $\beta^* = (0.5, 0.5, 0.5, 1.5)$ m in IP1, IP2, IP5 and IP8. The same parameters are expected for the future Pb-Pb runs in 2021 and 2022. A potential p-Pb run will most likely make use of the same optics cycle; therefore, the same β^* can be assumed for p-Pb operation in either 2023 or 2028. The β^* values of $0.5\,\mathrm{m}$ do not require the telescopic part of the squeeze of the ATS optics [174, 175]. Comparable to the 2018 Pb-Pb run [46], a new optics independent

[1] Since the filling pattern presented in [58] is a dedicated Pb-Pb filling pattern, both beams are identically filled and feature Pb bunch train characteristics. Whether the injection of protons is flexible enough to reproduce such a Pb bunch train is beyond the scope of this thesis.

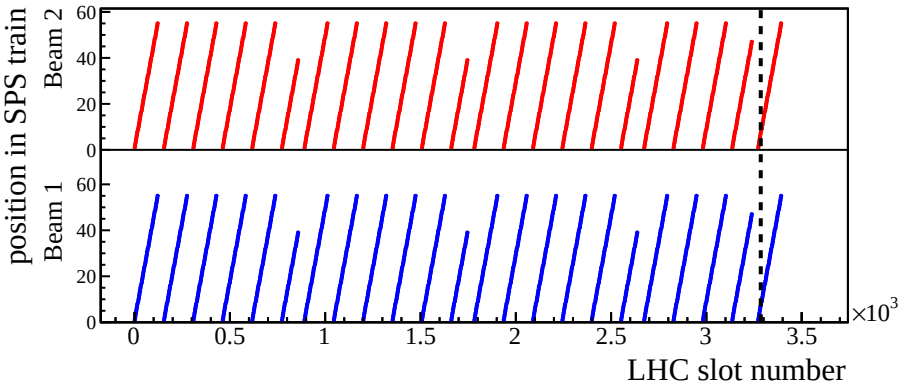

Figure 6.1: Displayed is the filling pattern of the Pb beam in Beam 1 (blue) and the proton filling pattern in Beam 2 (red). The dashed line indicates the abort-gap keeper (AGK).

of the p-p optics will be used with a combined ramp and squeeze, i.e., the reduction of the β^* values starts already during the energy ramp and the final β^* values are achieved via a short squeeze after the ramp at top energy. The crossing angles at the IPs are different according to the requirements of the respective detector. The half crossing angles at the four IPs are expected to be $\theta/2 = (170, 100, 170, 318)\,\mu\text{rad}$.[2] Table 6.2 lists the full set of IP parameters. The vertical aperture at ALICE was restricted because of injection hardware until LS2. The limited physical aperture required the crossing angle in ALICE to fulfil $|\theta/2| \leq 60\,\mu\text{rad}$. The small crossing angle was necessary since otherwise large fractions of the spectator-nucleon cone would have been intercepted by the physical aperture and only nucleons emitted under larger angles would have reached the zero-degree calorimeters (ZDCs) in $115\,\text{m}$ distance from the IP. The ZDCs are located at the beam-pipe crotches at which both beams exit the common beam pipe of the IR. A wider aperture is going to be installed during LS2. Hence, much more flexibility to adjust the ZDCs vertically is given during LHC Run 3 and a crossing angle of $|\theta/2| \leq 100\,\mu\text{rad}$ in ALICE will still be acceptable [176].

Extra losses at the IPs In Chapter 4, the intensity decay of the Pb beam could not be reproduced with the intensity losses solely caused by luminosity burn-off and a base lifetime that was obtained from the bunches not colliding in any IP. Therefore, extra losses were implemented into the simulation. These losses are of exponential nature, i.e., $\dot{N}_b(t) = -\alpha_{\text{IP}} N_b(t)$, and affect only the bunches colliding in the respective IP. This means that bunches not colliding in any IP are not subjected to extra losses, whereas a bunch colliding in all four IPs is subjected to four extra loss rates. These extra losses are most likely caused by beam-beam interactions.

[2]The signs of the crossing angles are not all necessarily positive in terms of the Beam 1 coordinate frame. The signs of the crossing angles do not make a difference in this study. It can be expected that the half crossing angles in ATLAS and ALICE will be of opposite sign as well as those in CMS and LHCb.

Table 6.2: List of IP specific parameters. The extra losses are applied to each bunch colliding in the respective IP and are obtained by scaling the values found in 2016 [165].

IP		IP1/5	IP2	IP8
Number of colliding bunch pairs n_c	1	1136	1120	81
β-function at IP β^*	m	0.5	0.5	1.5
Half crossing angle $\theta/2$	μrad	170	100	318
Extra loss rate at the IP α_{IP}	1/h	1/76.8	1/47.8	1/317

This assumption is based on the fact that the loss rates scale with the crossing angles $\alpha_{\mathrm{IP}} \propto 1/\theta$. The 2016 extra losses were estimated at a beam energy of $E_b = 6.5Z\,\mathrm{TeV}$ in Chapter 4. Since this study assumes that the beam energy will be the LHC design energy of $E_b = 7Z\,\mathrm{TeV}$, the extra losses may change slightly (the crossing angles also change). The losses should become smaller with larger energy because of a weaker beam-beam interaction. A scaling of the extra loss rates at the IPs $\alpha^*_{\mathrm{IP}} = \alpha_{\mathrm{IP}}\theta E_b N^*_b/(\theta^* E^*_b N_b)$ is applied to the loss rates α_{IP} obtained for the 2016 fills. Here, N_b refers to the proton bunch intensity, and the star refers to the Run 3 parameters (2016 parameters without star). Table 4.5 gives the extra loss rates that were obtained for the 2016 run, and Tab. 6.2 lists the scaled values for a future p-Pb run. For all detectors, the loss rates have increased except for ALICE because of an increased crossing angle.

The non-colliding lifetime was found to be $100\,\mathrm{h}$ for Pb bunches and $5.8 \times 10^3\,\mathrm{h}$ for proton bunches in 2016 (see Chapter 4).[3] The same non-colliding lifetimes are assumed for future p-Pb runs. The higher top energy of $E_b = 7Z\,\mathrm{TeV}$ will presumably lead to slightly improved non-colliding lifetimes if the losses are mostly generated by residual gas scattering [23]. Nevertheless, uncertainties regarding these losses remain; therefore, a scaling of the non-colliding lifetime with the beam energy is omitted.

Beam parameters The Pb bunches are expected to have normalised emittances of $\epsilon_{\mathrm{n}} = 1.65\,\mu\mathrm{m}$ and intensities of $N_b = 1.8 \times 10^8$ ions per bunch. At injection, emittances of $\epsilon_{\mathrm{n}} = 1.5\,\mu\mathrm{m}$ and intensities of $N_b = 1.9 \times 10^8$ ions per bunch are expected; however, some degradation of the beams will take place during the ramp and until collisions [58, 178]. The proton bunches should have normalised emittances in the $\epsilon_{\mathrm{n}} = 2.5\,\mu\mathrm{m}$ range. The bunch intensities are chosen to be at $N_b = 3 \times 10^{10}$ protons per bunch in this study. This value is slightly larger than the maximum proton intensity achieved in 2016; however, Sec. 6.2 is going to show that adequately aligned TCLs will eventually intercept the critical losses in the dispersion suppressors of IP1 and IP5 enabling proton intensities of that magnitude in future p-Pb operation. Proton intensities larger than $N_b = 3 \times 10^{10}$ protons per bunch make little sense with ALICE being levelled to $\mathcal{L} = 5 \times 10^{29}\,\mathrm{cm}^{-2}\mathrm{Hz}$. Larger proton intensities accelerate the degradation of the

[3] During the LHC design phase, a non-colliding lifetime of $100\,\mathrm{h}$ was envisaged [177].

Pb beam as a result of the fast luminosity burn-off in ATLAS and CMS. The resulting short beam lifetime and fill duration is unfavourable for ALICE/LHCb. Table 6.3 gives the list of the beam parameters.

Table 6.3: Beam parameters of the proton and Pb beam used to estimate the potential performance of a p-Pb run either in LHC Run 3 or Run 4.

Particle species		p	Pb
Beam energy E_b	Z TeV	7	
Collision energy $\sqrt{s_{\mathrm{NN}}}$	TeV	8.78	
Bunch intensity N_b	10^8	300	1.8
Transverse normalised emittance ϵ_{n}	μm	2.5	1.65
Bunch length σ_z	m	0.09	0.08

6.1.2 Simulation results

Simulation of a single fill The simulation is performed with a time increment of $\Delta t = 360\,\mathrm{s}$. The top left plot of Fig. 6.2 shows the evolution of the instantaneous luminosity. While the ATLAS/CMS luminosity is quickly decaying, the luminosity levelling in ALICE can be maintained for slightly more than 7 h. The peak luminosity achieved in ATLAS and CMS is at $\mathcal{L} = 17.4 \times 10^{29}\,\mathrm{cm}^{-2}\mathrm{Hz}$, i.e., the peak luminosity is a rough factor 2 larger than in 2016. The top right plot of Fig. 6.2 shows the intensity decay for the two beams. The intensity of the proton beam remains more or less unchanged as the losses caused by the luminosity are small compared to the total proton intensity. The Pb beam loses one order of magnitude in terms of intensity during the time span of 10 h. During Run 1 and Run 2 of the LHC, an interlock BPM threshold of 2×10^9 charges per bunch led to the dumping of the beams if one of the Pb bunches eventually dropped below that threshold. This threshold is likely to be non-existent from Run 3 on [179].

The bottom left plot of Fig. 6.2 presents the integrated luminosities $\mathcal{L}_{\mathrm{int}}(t)$ of the detectors. The integrated luminosity in ATLAS and CMS is much larger compared to those in the other two detectors. At around $t = 8\,\mathrm{h}$, roughly $26\,\mathrm{nb}^{-1}$ is achieved in ATLAS/CMS while it is approximately half of that in ALICE. With a turnaround time of $T_r = 2.5\,\mathrm{h}$, i.e., the time it takes from the beam dump until achieving collisions in back-to-back fills, the average luminosity reads

$$\langle \mathcal{L}(t) \rangle = \frac{1}{T_r + t} \int_0^t \mathcal{L}(\tau) \mathrm{d}\tau \,. \tag{6.1}$$

The bottom right plot of Fig. 6.2 presents the average luminosities of the detectors. The optimum fill duration τ_{opt} is a detector-dependent quantity and is defined as the point in time the

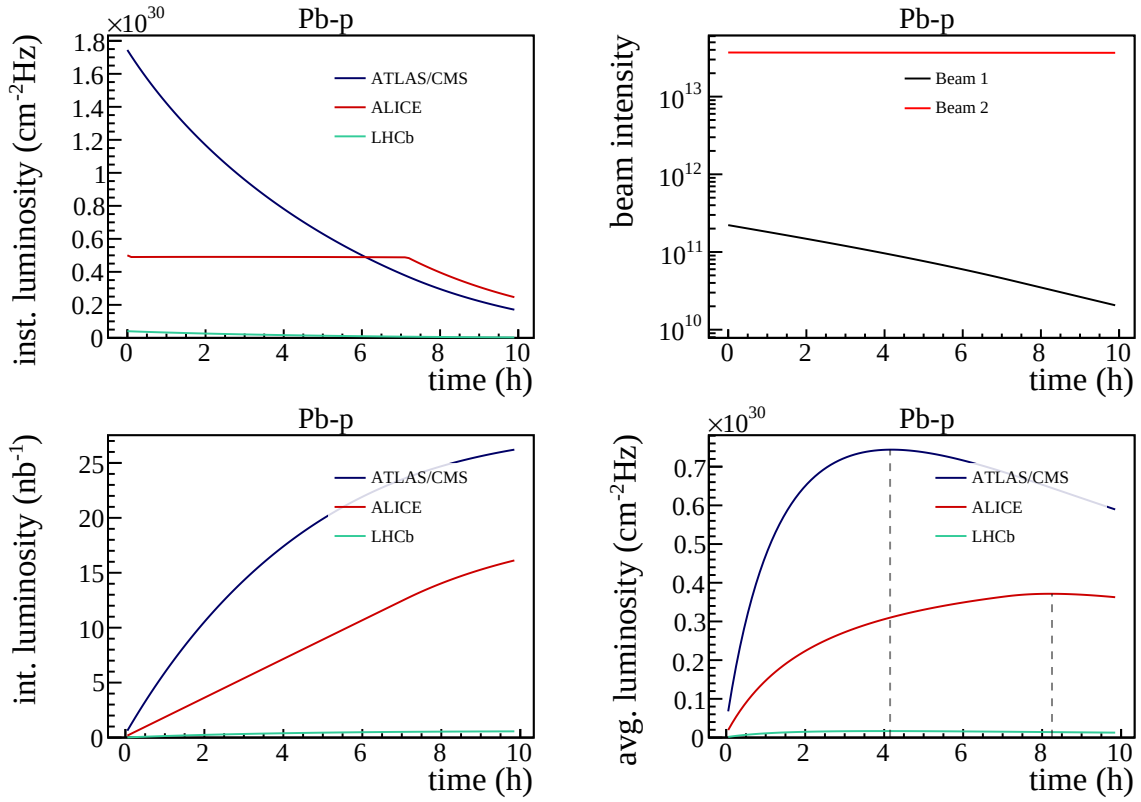

Figure 6.2: Top left: Instantaneous luminosities versus time. The levelling in ALICE is maintained for slightly more than 7 h. Top right: Evolution of the beam intensities versus time. The proton beam barely faces any losses as the loss rate is small compared to the total proton intensity. Bottom left: Integrated luminosities versus time. Bottom right: Average luminosities versus time. The optimum fill length is found to be $\tau_{\text{opt}} = 4.2\,\text{h}$ in ATLAS and CMS, whereas it is roughly $\tau_{\text{opt}} = 8.2\,\text{h}$ in ALICE.

average luminosity is at its maximum. The optimum fill length for ATLAS and CMS is approximately $\tau_{\text{opt}} = 4.2\,\text{h}$ and the ALICE optimum is at $\tau_{\text{opt}} = 8.2\,\text{h}$ (vertical dashed lines in bottom right plot of Fig. 6.2). Table 6.4 lists values of the peak luminosities and the optimum fill durations.

Extrapolation to one-month p-Pb operation The one-month performance is calculated by estimating the LHC fill duration first. With the optima of IP1/5 and IP2 being a factor 2 apart, the fill time is estimated as the geometric mean of the two optima. Thus, the resulting fill duration is assumed to be $\tau_{\text{fill}} = 5.2\,\text{h}$. A full month of heavy-ion operation is expected to have $24\,\text{d}$ of operation following the initial commissioning. To take operational issues, machine faults and delays into account, an operational efficiency of $50\,\%$ is assumed, i.e., the final integrated luminosity is scaled by a factor $1/2$. It is unclear whether the proton injection is flexible enough

to reproduce the Pb filling pattern in Fig. 6.1. To cover the possibility that the filling pattern cannot be reproduced, additional $5\,\%$ of the total integrated luminosity is subtracted.

Table 6.4 gives the final predictions for the integrated luminosities of the detectors as well as other key parameters. An integrated luminosity of $712\,\mathrm{nb}^{-1}$ ($30\,\mathrm{nb}^{-1}/\mathrm{d}$) is expected in ATLAS and CMS. Thus, the integrated luminosity per day is roughly a factor 3 larger compared to 2016 with approximately 14–$15\,\mathrm{nb}^{-1}/\mathrm{d}$. The projection also shows that ALICE will accumulate more than $340\,\mathrm{nb}^{-1}$ in a single future p-Pb run. This value is significantly larger than $43\,\mathrm{nb}^{-1}$ accumulated in ALICE in 2016. The LHC experiments propose to have two p-Pb runs in LHC Run 3 and Run 4 setting the total goal in terms of integrated luminosity to $1.2\,\mathrm{pb}^{-1}$ for ATLAS and CMS and $0.6\,\mathrm{pb}^{-1}$ for ALICE and LHCb [180]. Two p-Pb runs should suffice to reach this goal; however, filling patterns providing larger numbers of colliding bunch pairs to LHCb are required to meet the request. Table 1.2 in Chapter 1, puts the HL-LHC p-Pb performance parameters in perspective with the previous p-Pb runs in 2013 and 2016 and the design values [36]. The operation with p-Pb beams in the LHC faces a bright future.

Table 6.4: The top part of the table gives the optimum fill duration τ_{opt} for each detector and the assumed fill duration τ_{fill} to estimate the one-month performance. The fill duration is the geometric mean of the ATLAS/CMS and ALICE optimum fill length $\tau_{\mathrm{fill}} = \sqrt{\tau_{\mathrm{opt,IP1/5}} \cdot \tau_{\mathrm{opt,IP2}}}$. The bottom part gives the peak luminosities of the detectors. The ALICE value is underlined since the luminosity is initially levelled and the achievable peak luminosity would be close to that of ATLAS and CMS. Also, the one-month (NN) integrated luminosities are listed.

		IP1/5	IP2	IP8
Turnaround time T_r	h		2.5	
Optimum fill duration τ_{opt}	h	4.2	8.2	4.0
Assumed fill duration τ_{fill}	h		5.75	
Peak luminosity $\mathcal{L}$	$10^{29}\,\mathrm{cm}^{-2}\mathrm{Hz}$	17.4	<u>5</u>	0.4
Integrated luminosity $\int_{\mathrm{month}} L\mathrm{d}t$	nb^{-1}	712	340	16
Integrated NN luminosity $\int_{\mathrm{month}} L_{\mathrm{NN}}\mathrm{d}t$	pb^{-1}	148.0	70.6	3.3

6.2 Dispersion-suppressor losses

In this section, the dispersion-suppressor losses as observed during the 2016 p-Pb run are analysed and the potential mitigation using the TCL collimators is discussed.

During the 2016 heavy-ion run, the luminosity limit was given by the losses detected roughly $300\,\mathrm{m}$ downstream of the IPs of the two high luminosity experiments ATLAS and CMS in the propagation direction of the Pb beam. These losses were most likely Pb fragments from the

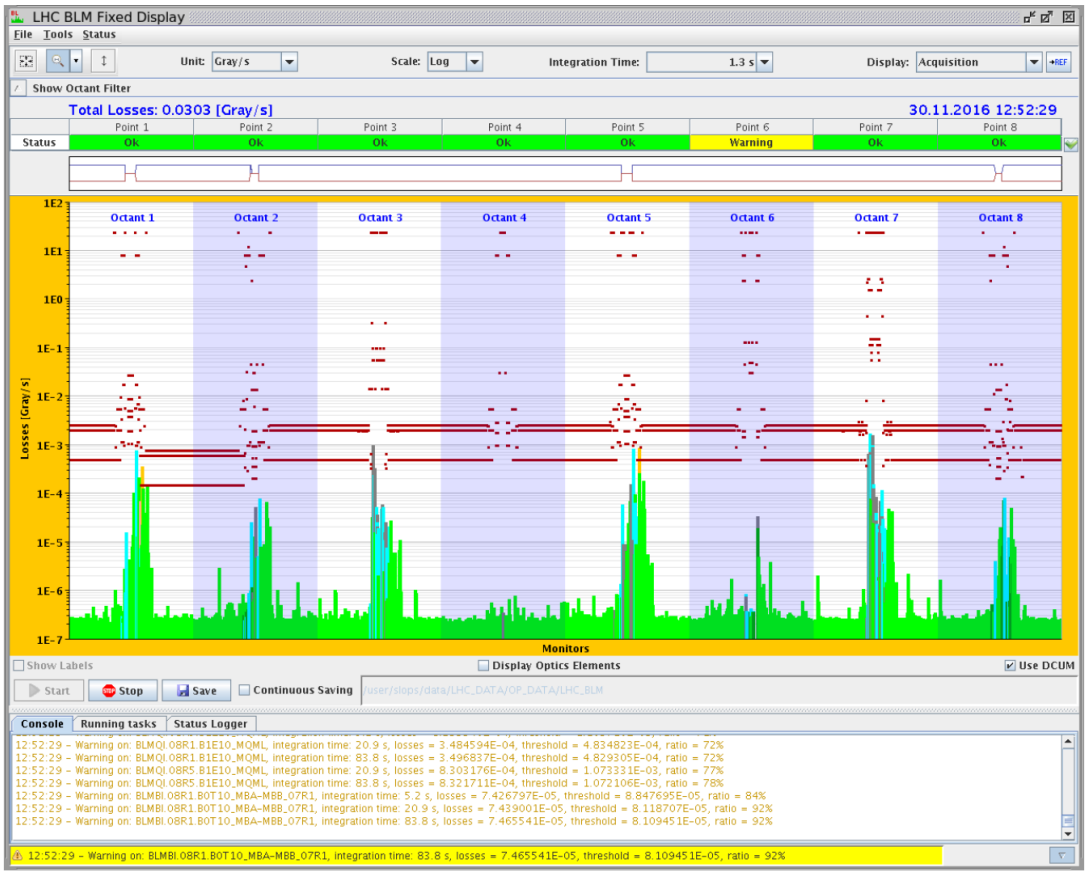

Figure 6.3: Loss pattern around the LHC circumference during Fill 5559 as displayed in the LHC control room at 12:52:29 local time on 30 November 2016. In the centre plot, the green bars indicate the measured losses by the BLMs and the dark red dots indicate the dump thresholds. The smaller thresholds in the arc between IP1 and IP2 were set because of a magnet-circuit issue. In the bottom panel, warning messages are displayed because the losses in the dispersion suppressors on the right side of IP1 and IP5 are close to the dump threshold.

p-Pb collisions in the IPs. The fragments continue to propagate in the direction of the Pb beam and impact the vacuum pipe at the position the dispersion functions increases rapidly in the dispersion suppressors. Figure 6.3 shows the BLM monitor as displayed in the LHC control room. The loss pattern was measured during Fill 5559, the fill with the highest luminosity and proton intensity during the 2016 p-Pb run. Warnings indicate that 92 % (78 %) of the BLM threshold is reached on the right side of IP1 (IP5). The BLM thresholds were slightly smaller in the arc between IP1 and IP2 due to a dipole-circuit issue. The proton intensity was decreased in the following fills to avoid premature beam dumps if BLM thresholds are temporarily breached. Figure 6.4 contains plots of the critical regions on the left and right side of the four IPs. On the left side of the IPs (the propagation direction of the protons), no significant signal is detected by the BLMs. On the right side (the propagation direction of the Pb ions), however, large spikes are

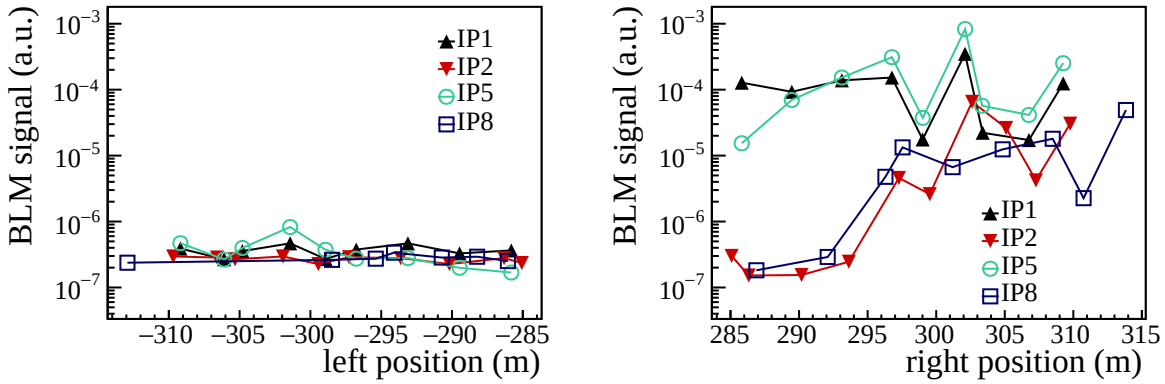

Figure 6.4: Left: BLM signals versus position in Cell 8 left of the four IPs (285 m to 315 m downstream of the IPs) in Fill 5559 in Pb-p beam configuration. Small but insignificant loss peaks are visible at $s \approx -302\,\mathrm{m}$. Right: Equivalent plot on the right side of the IPs. Loss peaks at $s \approx 303\,\mathrm{m}$ are visible except for IP8. Also, secondary peaks at around $s \approx 296\,\mathrm{m}$ are visible.

measured downstream of ATLAS/CMS at around 296 m and 303 m. Also, a spike downstream of ALICE at 303 m is detected.

During the 2016 p-Pb run, the TCL collimators of IP1 and IP5 located at roughly 151 m (TCL4), 185 m (TCL5) and 220 m (TCL6) from the respective IP were not closed. These collimators could have provided nearly perfect protection of the IP1 and IP5 dispersion suppressors as will be shown. During the run, the TCL could not be closed to mitigate the losses in the dispersion suppressors since the TCLs were not included in the initial commissioning and closing the half gaps of the TCL collimators without validation would have risked potential damage to the collimators and other hardware. The feasibility of the TCLs to protect the ATLAS/CMS dispersion suppressors against fragments coming out of the IPs in future p-Pb runs is studied in the next section.

6.2.1 TCL collimators at ATLAS and CMS

The magnetic rigidity is expressible as

$$B\rho = \frac{p}{q} = \frac{\sqrt{\gamma^2 - 1}mc}{q}\,. \tag{6.2}$$

In the presence of a momentum shift Δp, the rigidity changes to

$$B\rho = (B\rho)_0 + \frac{\Delta p}{q} \tag{6.3}$$

with the rigidity of the nominal beam $(B\rho)_0 = p_0/q$. Expressing Eq. 6.3 in terms of the relative momentum change $\delta_p = \Delta p/p_0$ results in

$$B\rho = (B\rho)_0(1 + \delta_p)\,. \tag{6.4}$$

Hence, any rigidity shift due to a change of either the charge q, mass m or Lorentz factor γ can be expressed by an effective relative momentum error

$$\delta_{\text{eff}} = \frac{B\rho}{(B\rho)_0} - 1 = \left(\frac{m_f q}{m q_f}\right)\left(\frac{\sqrt{\gamma_f^2 - 1}}{\sqrt{\gamma^2 - 1}}\right) - 1 \tag{6.5}$$

with the index f indicating the final state. This expression can be further simplified to

$$\delta_{\text{eff}} = \frac{1 + \frac{\Delta m}{m_0}}{1 + \frac{\Delta q}{q_0}}(1 + \delta_p) - 1 \qquad \text{with} \qquad \Delta m = m_f - m\,, \qquad \Delta q = q_f - q \tag{6.6}$$

and δ_p being the relative momentum error to cover the case of recoil on the momentum. Equation 6.6 can be used to translate charge-state changes, mass changes or any form of momentum change caused by the collision of Pb ions with protons into an effective momentum error.

Open TCL collimators with $J_x = J_y = 0$ At the critical locations $300\,\text{m}$ downstream of the IPs, the dispersion function starts to increase rapidly towards its first peak at $s \approx 340\,\text{m}$ (see Fig. 6.5). Since the derivative of the dispersion function is large towards that first dispersion peak, particles of a wide rigidity range are deposited at roughly the same longitudinal position, making the identification of a single trajectory difficult. Thus, the identification of a potential particle or isotope type that is mainly responsible for the respective loss peak is cumbersome and non-trivial. Assuming the 2016 Pb-p condition, i.e., the TCLs are retracted from the beams with a half gap of $2.5\,\text{cm}$, the trajectories of particles with zero transfers actions $J_x = J_y = 0$ and relative momentum (rigidity) deviations δ_{eff} running from $\delta_{\text{eff}} = -25\,\%$ to $\delta_{\text{eff}} = 25\,\%$ are displayed in Fig. 6.6. Figure 6.7 shows the position of impact versus the effective momentum error. The dependence of the impact position on the momentum error is rather weak since most particles with momentum errors in the range $3\% < |\delta_{\text{eff}}| < 22\%$ end up in the critical region at $s = 300\,\text{m}$ independently of the sign of momentum error.

Closed TCL collimators with $J_x = J_y = 0$ In future runs, it is desirable to remove the dispersion-suppressor losses to reach higher peak luminosities in ATLAS and CMS and consequently to remove proton-intensity constraints. The horizontal TCLs may remove particles and fragments in the rapidity range that leads to the losses in the dispersion suppressors downstream of IP1 and IP5. During p-p operation, the half gaps of the TCL4 and TCL5 collimators are usually set to $15\sigma_x$ of the horizontal beam size, whereas the TCL6 half gap is set to $20\sigma_x$ [181]. Setting the TCL4 and TCL5 half gaps to $15\sigma_{x,\text{Pb}}$ and the TCL6 half gap to $20\sigma_{x,\text{Pb}}$ with the Pb emittance $\epsilon_{\text{n}x} = 1.65\,\mu\text{m}$ in p-Pb operation is analysed in the following. The top plots of Fig. 6.8 display the beam envelopes with closed TCLs for IP1 and IP5. The bottom plots of Fig. 6.8 show the trajectories with closed TCLs for the momentum error range

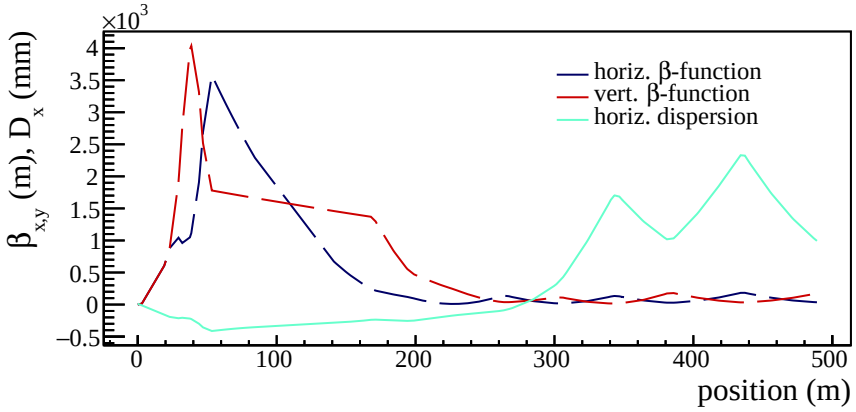

Figure 6.5: Displayed are the β-functions (red and blue) as well as the horizontal dispersion function (teal) as functions of the position on the right side of IP1 (2016 Pb-p collision optics).

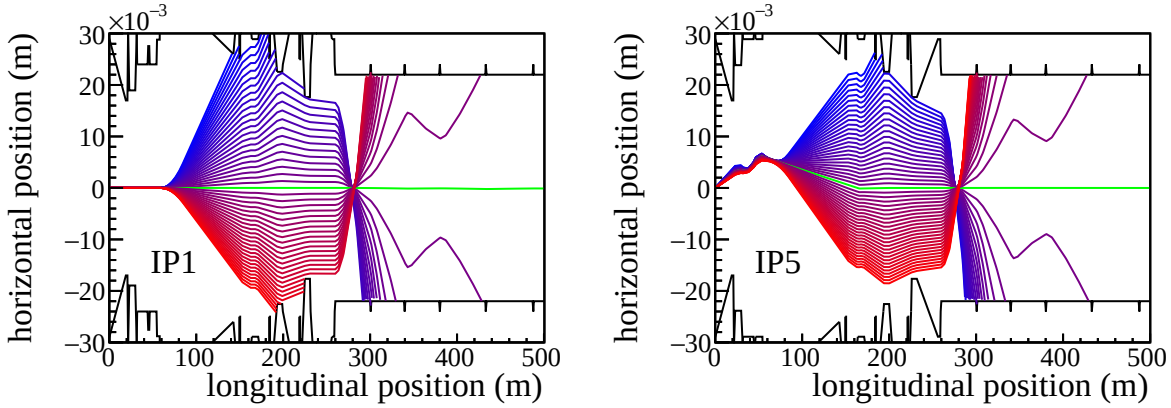

Figure 6.6: Trajectories for particles with effective momentum errors starting at $\delta_{\text{eff}} = -25\,\%$ (blue) to $\delta_{\text{eff}} = -25\,\%$ (red) with open TCLs for IP1 (left) and IP5 (right). The transverse actions are set to zero $J_x = J_y = 0$. The design orbit ($\delta_{\text{eff}} = 0$) is indicated in green.

$-25\% \leq \delta_{\text{eff}} \leq 25\%$ and no transverse excursion in neither coordinate nor momentum, i.e., $J_x = J_y = 0$. Only the particles with $|\delta_{\text{eff}}| \leq 2\,\%$ can pass through all three TCL pairs but impact the vacuum pipe more than $330\,\text{m}$ downstream of the respective IP. Figure 6.7 also shows the position of impact versus the effective momentum error with closed TCLs, underlining the effectiveness of the TCLs in protecting the dispersion suppressors. The analysis makes the simplification of fragments interacting with the TCLs do not produce any additional particle showers. The question arises whether particles with non-zero transverse actions can reach the dispersion suppressors even with closed TCLs. For this analysis, it is important to understand the spot size the fragments are emerging from first.

Spot size The beam size at the IP is given by the emittance and the β-function. However, when two beams collide, the actual luminous region, i.e., the transverse distribution of events,

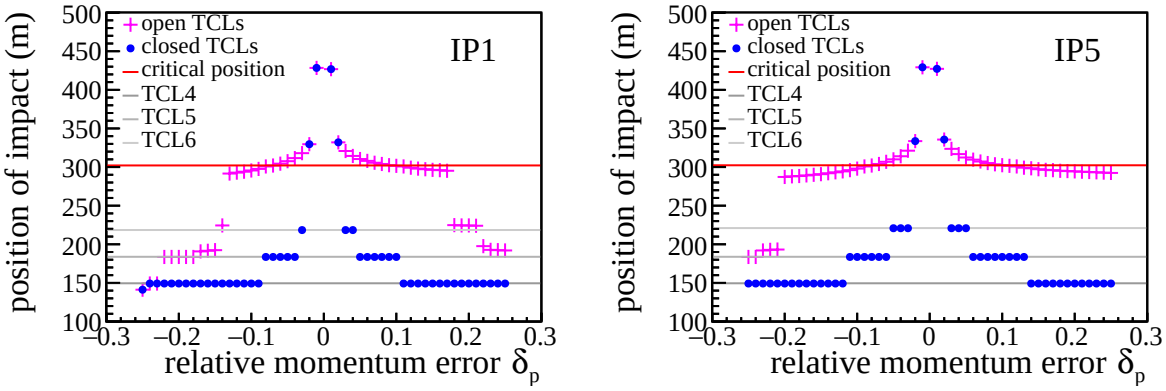

Figure 6.7: The position of impact of particles emerging from IP1 (left) and IP5 (right) for different effective momentum errors. The magenta crosses indicate the impact positions with open TCLs. Most particles end up at the critical positions at roughly $s \approx 300\,\mathrm{m}$. The blue dots indicate the positions with closed TCLs. Only particles with $|\delta_{\mathrm{eff}}| \leq 2\,\%$ do not impact the TCLs (grey lines).

is the product of the two transverse distributions of the beams. The transverse distribution of the beams at the IP is

$$\rho(x,y) = \frac{1}{2\pi\sigma_x\sigma_y}\exp\left(-\frac{x^2}{2\sigma_x^2} - \frac{y^2}{2\sigma_y^2}\right) \qquad \text{with} \qquad \sigma_u = \sqrt{\beta^*\epsilon_u}\,. \tag{6.7}$$

The product of the two beam distributions ρ_p and ρ_{Pb} reads (re-normalised)

$$\rho_{\mathrm{p}}(x,y)\rho_{\mathrm{Pb}}(x,y) = \frac{1}{2\pi\tilde{\Sigma}_x\tilde{\Sigma}_y}\exp\left(-\frac{x^2}{2\tilde{\Sigma}_x^2} - \frac{y^2}{2\tilde{\Sigma}_y^2}\right) \qquad \text{with} \qquad \tilde{\Sigma}_u = \frac{\sigma_{u,\mathrm{Pb}}\sigma_{u,\mathrm{p}}}{\sqrt{\sigma_{u,\mathrm{Pb}}^2 + \sigma_{u,\mathrm{p}}^2}}. \tag{6.8}$$

Therefore, the density function in the coordinates has a smaller standard deviation $\tilde{\Sigma}_u$ compared to the actual beam sizes σ_u. When both beams are of the same size, the standard deviation reduces by $1/\sqrt{2}$. The density of the fragments emerging from the collision point is given by Eq. 6.8. The changed standard deviation only effects the x and y coordinates but not the respective momenta x' and y'.

Closed TCL collimators with $J_x \neq J_y \neq 0$ A tracking study is performed using PTC to investigate if particles with a non-zero horizontal action $J_x \neq 0$ can impact the dispersion suppressors even with closed TCL collimators. The vertical direction is not of interested because of a vanishing vertical dispersion function. The tracking study was performed in the boundaries $|x| \leq 23\tilde{\Sigma}_x$ in the horizontal coordinate and $|x'| \leq 12\sigma_{x',\mathrm{Pb}}$ in the horizontal angle. The study is performed with the beam energy $E_b = 6.5Z\,\mathrm{TeV}$, the Pb emittance $\epsilon_{nx} = 1.65\,\mu\mathrm{m}$, the proton emittance $\epsilon_{nx} = 1.5\,\mu\mathrm{m}$ and $\beta^* = 0.6\,\mathrm{m}$.

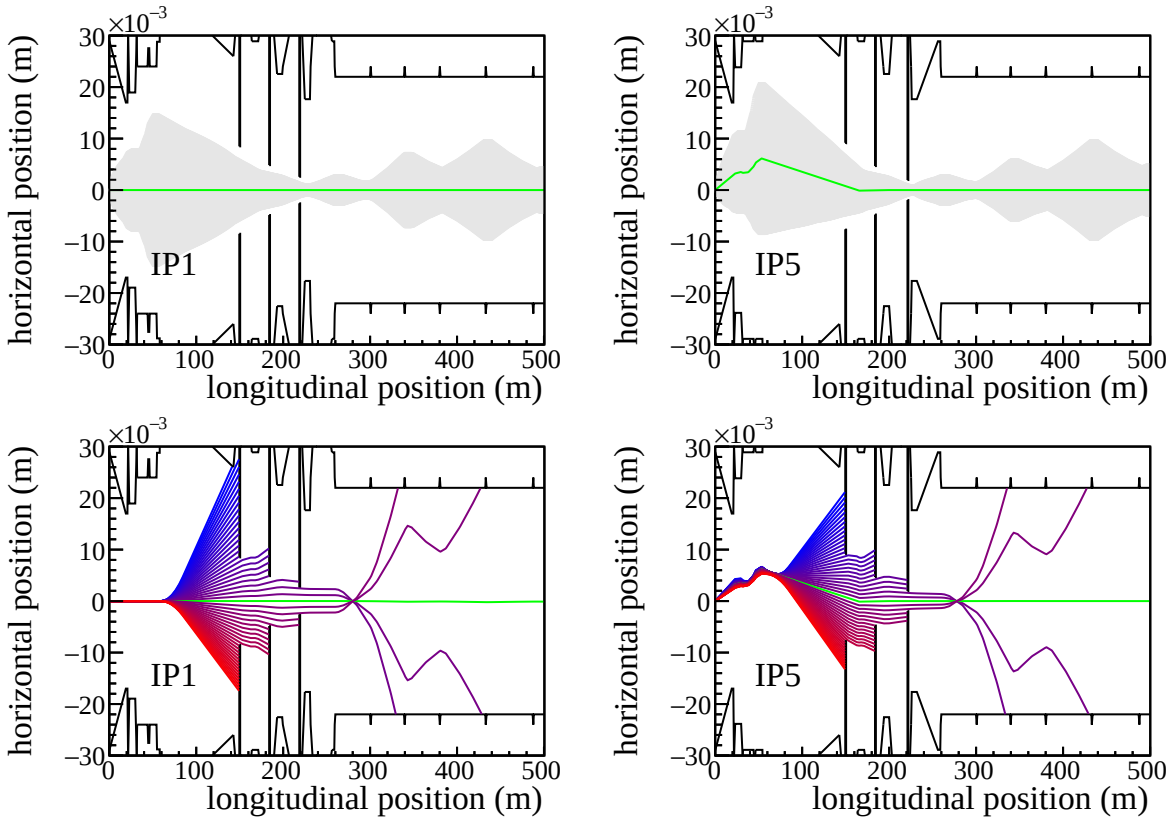

Figure 6.8: Top: Horizontal beam envelope ($|x| \leq 10\sigma_{x,\mathrm{Pb}}$) downstream of IP1 (left) and IP5 (right) with closed TCL collimators. Bottom: Trajectories for particles with momentum errors starting at -25% (blue) to 25% (red) with closed TCLs for IP1 (left) and IP5 (right). The transverse actions are vanishing $J_x = J_y = 0$ in the simulated scenarios. Only particles with small momentum deviations make it through the three stages of TCL collimators.

Figure 6.9 presents the results of the tracking study for IP1. The top four plots of Fig. 6.9 (open TCL collimators) show particles freely impacting the critical region in the Cell 8 close to IP1 independently of the momentum error δ_{eff}, horizontal position x and mostly also independently of the transverse angle x' if the TCL collimators are open. Closing the TCL collimator jaws down to $15\sigma_{x,\mathrm{Pb}}$ (TCL4/5) and $20\sigma_{x,\mathrm{Pb}}$ (TCL6) protects the critical region at around 300 m (red) well against all kinds of δ_{eff}, x and x' offsets (bottom four plots of Fig. 6.9). Particles with very specific transverse momenta in the $x' \geq 7\sigma_{x',\mathrm{Pb}}$ range can reach the dispersion suppressors; however, the number of particles with these properties is negligible.

Figure 6.10 shows the analogous results for IP5. Again, particles can freely interact with the dispersion suppressor downstream of IP5 if the TCL collimators are retracted from the beam (top four plots of Fig. 6.10). By closing the TCLs, the dispersion suppressor is well protected (bottom four plots of Fig. 6.10); however, because of the horizontal crossing angle in IP5, particles with transverse momenta in the range $5\sigma_{x',\mathrm{Pb}} \leq x' \leq 11\sigma_{x',\mathrm{Pb}}$ may reach the critical

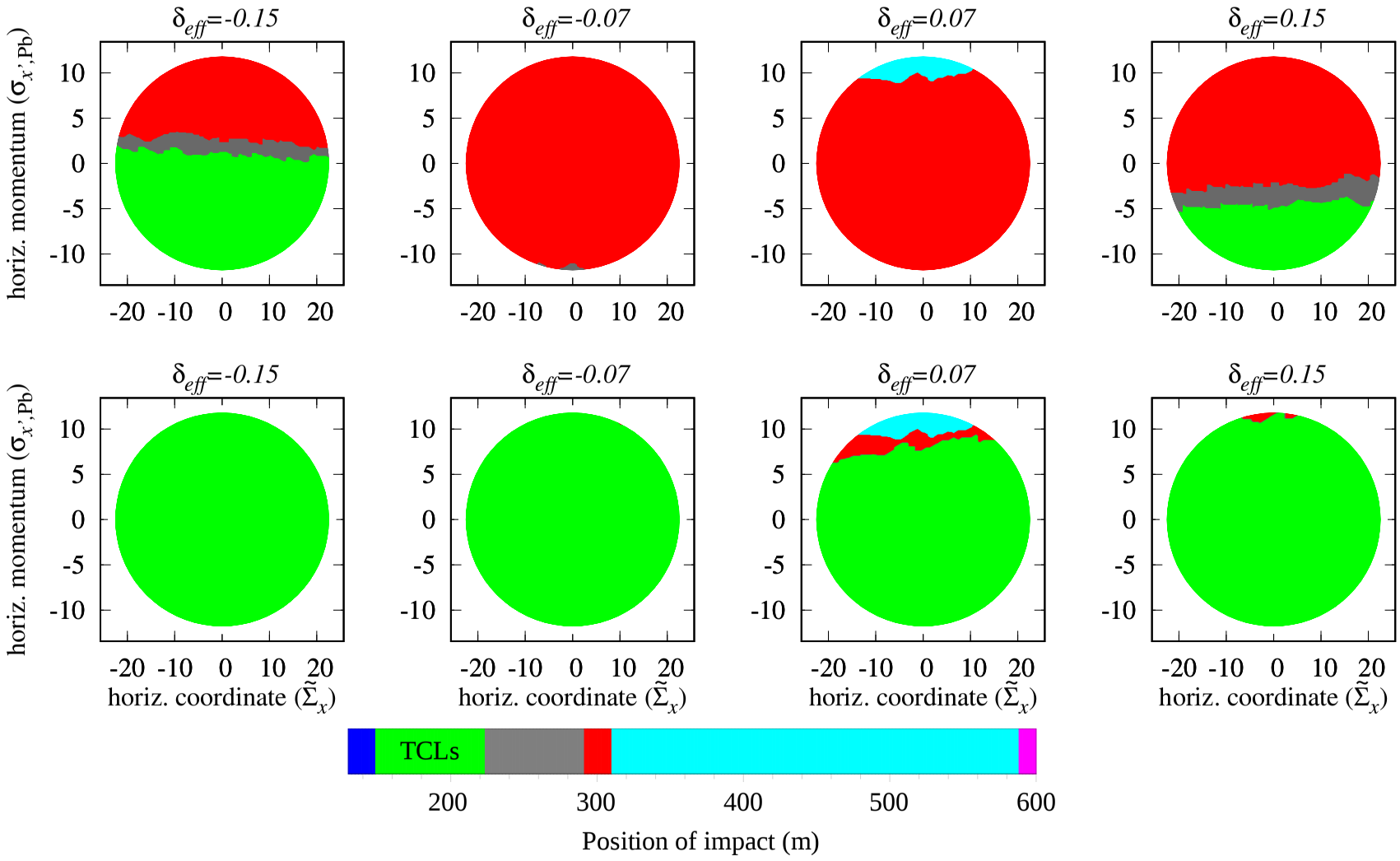

Figure 6.9: The plots show the positions of impact for fragments emerging from IP1 with different initial conditions for open TCLs (top plots) and closed TCLs (bottom plots) and also for different effective momentum errors $\delta_{\text{eff}} = -15\,\%$ (left), $\delta_{\text{eff}} = -7\,\%$ (centre left), $\delta_{\text{eff}} = 7\,\%$ (centre right) and $\delta_{\text{eff}} = 15\,\%$ (right).

region at $300\,\mathrm{m}$ (red) even with closed TCL collimators. The required angles x', however, are large and the IR5 dispersion suppressor should be well shielded and barely influenced by any fragments.

Closing the TCL collimator half gaps down to $15\sigma_{x,\mathrm{Pb}}$ (TCL4/5) and $20\sigma_{x,\mathrm{Pb}}$ (TCL6) will be an adequate and necessary step to further improve the peak luminosities in ATLAS and CMS in upcoming p-Pb runs of the LHC. Even though particles may still reach the dispersion suppressors downstream of the respective IP, the required horizontal angles are large and a low quantity of particles should feature such initial conditions at the respective IP. It was attempted to reproduce the distribution of fragments emerging out of the IPs due to p-Pb collisions; however, the current FLUKA [182] version (FLUKA uses the DPMJET-III [183] event generator) features a bug that does not allow to produce the distribution of particles emerging out of p-Pb collisions at $\sqrt{s_{\mathrm{NN}}} = 8.16\,\mathrm{TeV}$.[4] Even without the respective simulation of fragments, the tracking study has shown that the dispersion suppressors are highly likely to be well shielded with closed TCL collimators.

HL-LHC The HL-LHC will operate with slightly changed layouts of IP1 and IP5 and also the TCL4 will be replaced by the TCLX collimators located at $136\,\mathrm{m}$ from the IPs. The TCL5 collimators are moved by $14\,\mathrm{m}$ closer to the IPs, while the TCL6 locations remain unchanged. Secondary simulations using the modified HL-LHC optics and aperture are omitted at this point because the dispersion functions at IP1 and IP5 will change insignificantly and the TCL collimator efficiency should remain the same even with slightly changed positions.

6.3 Potential ALICE and LHCb luminosity limits

The two experiments ALICE and LHCb do not have dedicated TCL collimators to protect their respective dispersion suppressors. This imposes a luminosity limit on both detectors as fragments impacting the dispersion suppressors can either lead to a BLM threshold breach or magnet quenches. The losses in the ALICE dispersion suppressor were a factor 16.5 beneath the BLM threshold in 2016 during Fill 5559 at the instantaneous luminosity of $\mathcal{L} = 1.1 \times 10^{29}\,\mathrm{cm}^{-2}\mathrm{Hz}$. A potential increase of the ALICE levelling value to $\mathcal{L} = 5 \times 10^{29}\,\mathrm{cm}^{-2}\mathrm{Hz}$ during Run 3 would lead to losses in the range of 0.3 times the 2016 BLM thresholds. Thus, no operational restrictions from the side of ALICE are expected. The proton bunch intensity is irrelevant to this discussion since the luminosity is strictly levelled to the target value of $\mathcal{L} = 5 \times 10^{29}\,\mathrm{cm}^{-2}\mathrm{Hz}$. Without a detailed analysis, it should be possible to achieve the target luminosity in ALICE

[4] An attempt was made to reproduce the distribution of fragments using `crmc` (Cosmic Ray Monte Carlo) [184, 185] and its built-in event generators EPOS LHC, QGSJETII-04 and SIBYLL2.3; however, no satisfying transverse distribution was produced and a lack of EMD products was observed.

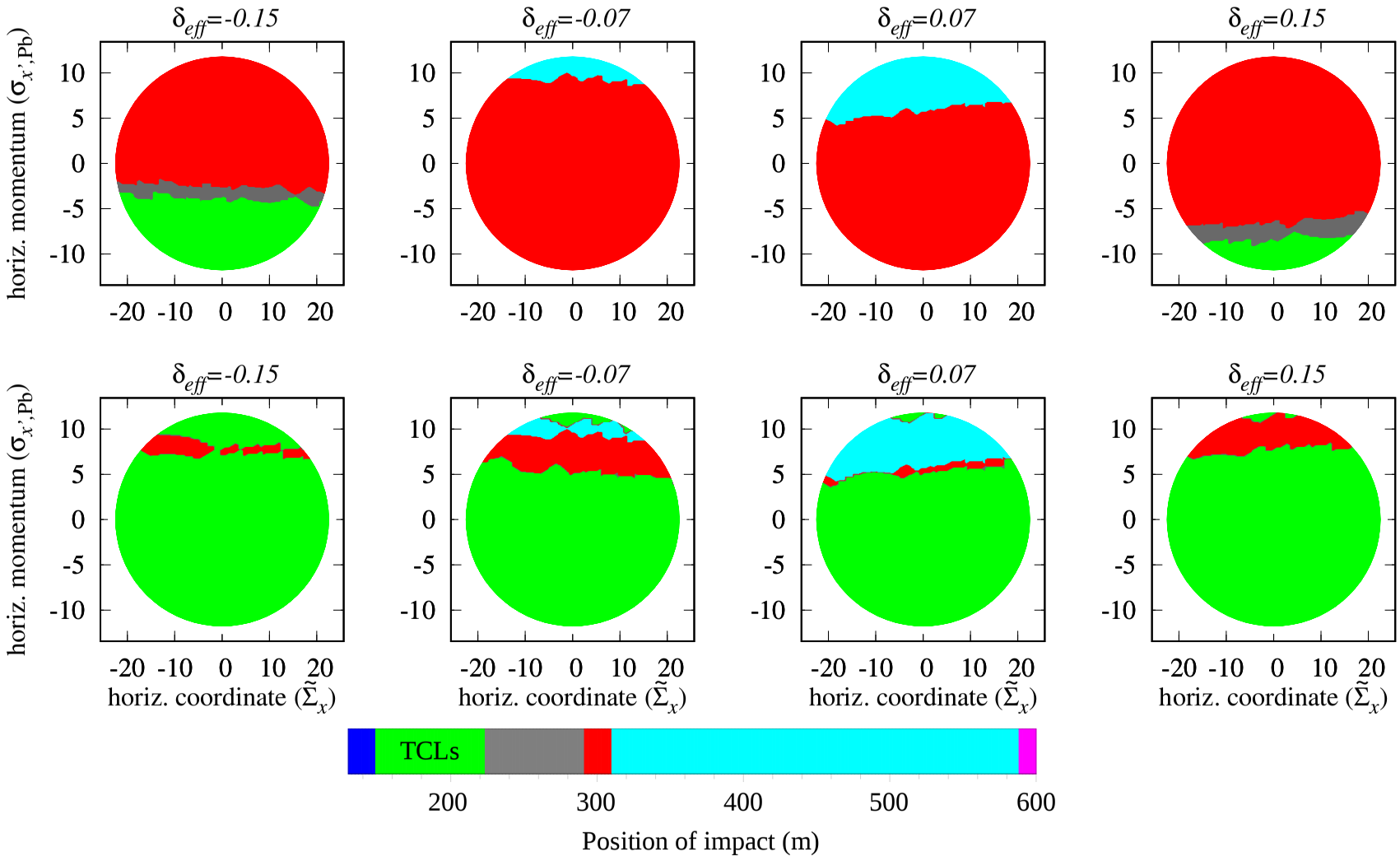

Figure 6.10: The plots show the positions of impact for fragments emerging from IP5 with different initial conditions for open TCLs (top plots) and closed TCLs (bottom plots) and also for different effective momentum errors $\delta_{\text{eff}} = -15\,\%$ (left), $\delta_{\text{eff}} = -7\,\%$ (centre left), $\delta_{\text{eff}} = 7\,\%$ (centre right) and $\delta_{\text{eff}} = 15\,\%$ (right).

without collimation between the IP and dispersion suppressors and also orbit bumps to guide fragments to the TCLD collimators $s = 430\,\mathrm{m}$ downstream of the ALICE IP should be unnecessary.[5] The losses in the LHCb dispersion suppressor were a factor 21 smaller than the dump threshold at the LHCb luminosity of $\mathcal{L} = 0.97 \times 10^{29}\,\mathrm{cm}^{-2}\mathrm{Hz}$ in Fill 5559. LHCb will not necessarily be levelled to any specific luminosity value in upcoming runs; however, it seems unlikely that LHCb will ever feature a 21 times higher luminosity in a future run.

6.4 Conclusion

The p-Pb operation of the LHC in future runs will be significantly enhanced mostly because of the longitudinal slip-stacking in the SPS. Increased bunch numbers will lead to integrated luminosities of roughly $30\,\mathrm{nb}^{-1}/\mathrm{d}$ in ATLAS and CMS and $14.2\,\mathrm{nb}^{-1}/\mathrm{d}$ in ALICE. These values are a rough factor 3 larger than in 2016. The ATLAS/CMS peak luminosity is expected to be roughly $\mathcal{L} = 1.7 \times 10^{30}\,\mathrm{cm}^{-2}\mathrm{Hz}$ at the start of a fill, and ALICE is expected to be levelled at $\mathcal{L} = 5 \times 10^{29}\,\mathrm{cm}^{-2}\mathrm{Hz}$ for roughly $7\,\mathrm{h}$. Because of the large proton bunch intensities, a fast luminosity burn-off will be observed and fills are expected to not last much longer than 5–6 h. The target integrated luminosities of $1.2\,\mathrm{pb}^{-1}$ in ATLAS/CMS and $0.6\,\mathrm{pb}^{-1}$ in ALICE/LHCb are expected to be achievable within two p-Pb runs in Run 3 and Run 4 of the LHC; however, filling schemes that give more colliding bunch pairs to LHCb are most likely going to be required.

The analysis of the TCL collimators has shown that half-gap widths of $15\sigma_{x,\mathrm{Pb}}$ (TCL4/5) and $20\sigma_{x,\mathrm{Pb}}$ (TCL6) suffice to protect the dispersion suppressors of IP1 and IP5 well enough that no obvious luminosity limit is expected in future p-Pb runs. The identification of a particle trajectory that might have caused the dispersion-suppressor losses as observed in 2016 was not possible since particles of a wide rigidity range end up impacting the beam pipe at virtually the same longitudinal position because of the rapid increase of the horizontal dispersion at that location. Tracking studies of the fragments with non-zero transverse actions have shown that only particles with a large initial angle ($x' \geq 7\sigma_{x',\mathrm{Pb}}$ at IP1 and $x' \geq 5\sigma_{x',\mathrm{Pb}}$ at IP5) can make it past the TCL collimators if these are closed; however, only very small numbers of particles feature these initial conditions. Because of this, the dispersion suppressors are expected to be well shielded in upcoming runs by adequately aligned TCL collimators. Although ALICE and LHCb do not feature TCL collimators between the IP and dispersion suppressor, virtually no luminosity limits will exist at these two experiments in future runs. Only if the luminosity increases by a factor 17 (21) in ALICE (LHCb) in a future p-Pb run, the dump thresholds in the

[5] Guiding the fragments into the TCLD collimators is unlikely to be successful since large orbit bumps are required to guide fragments with large rigidity deviations into the TCLDs.

dispersion suppressors would be breached; however, these factors are unrealistically large, i.e., no luminosity limits are expected.

CHAPTER 7

Prospects of future asymmetric collisions in the LHC

In the scope of the heavy-ion programme of the LHC, ion species lighter than Pb are also considered for symmetric collisions (A-A) and asymmetric collisions with protons (A-p). Although the initial p-Pb runs were expected to be solely used as reference for Pb-Pb data at the same NN centre-of-mass energy, $\sqrt{s_{\mathrm{NN}}}$, the p-Pb runs yielded numerous important new results in high-density QCD.

Within CERN's working group 5 (WG5) of the workshop on the physics of the CERN HL-LHC and perspectives at the HE-LHC, predictions for the HL-LHC and beyond have been made for potential A-A collisions [17]. The advantage of colliding light ion species is that the EMD and BFPP cross sections as described in Chapter 4 scale strongly with the particle charge. Intermediately sized ion species with smaller charge than Pb therefore face fewer losses from unwanted BFPP and EMD interactions, and the hadronic cross section takes a larger share of the total cross section compared to Pb-Pb collisions. Short low-luminosity oxygen-oxygen (O-O) and proton-oxygen (p-O) pilot runs are possibly going to be requested in LHC Run 3. Such a p-O run would operate at low luminosity and has the purpose of improving the understanding of cosmic rays interacting with Earth's atmosphere [186–188]. Also, oxygen collisions would allow to compare and interpolate phenomena like jet quenching between ion species. A benefit of using oxygen in p-A collisions is that oxygen is already present as a buffer gas in the electron-cyclotron resonance (ECR) ion source. The ECR ion source is responsible for the ionisation of Pb in standard ion operation and the setup phase of oxygen is expected to be considerably shorter compared to preparing the ECR source, RFQ and linac for a new ion species.

Accelerating and colliding different ion species in p-A collisions raises the question of potential operational restrictions resulting from moving beam-beam encounters as explained and

analysed for p-Pb in Chapter 2. Besides the potential performance of the LHC when colliding light ion species in Run 5 and beyond, key parameters in the scope of moving encounters are calculated to predict qualitatively whether the influence of moving encounters on the beams is weaker or stronger compared to p-Pb operation.

Besides O-O collisions, the A-A study in [17] also considers other ion species like the noble gases argon (Ar), krypton (Kr) and xenon (Xe). Using noble gases avoids the potential difficulty of evaporating the respective material. Evaporating the material for the ECR source is possibly a limiting factor for a wide range of elements. Besides the noble gases and oxygen, calcium (Ca) is also considered in [17] and in the following study. The temperature and vapour pressure of the oven used for Pb should be sufficient for Ca operation [189]. Table 7.1 lists the isotopes of the respective elements.

The aspects of moving beam-beam encounter points and the effects of the energy ramp with unequal revolution frequencies on the different ion species are analysed in the next section. After that, the one-month performance of the LHC in p-A operation and the performance of a potential p-O pilot run is evaluated.

7.1 Moving long-range beam-beam locations

As in the case of p-Pb operation, the injection and acceleration of the proton beam and the ion beam in p-A operation are going to be performed with equal magnetic rigidities $(B\rho)_{\mathrm{p}} = (B\rho)_{\mathrm{A}}$ and unequal revolution frequencies $f_{0,\mathrm{p}} \neq f_{0,\mathrm{A}}$. As a consequence, the beam-beam encounter locations in the IRs shift turn-by-turn. The dynamics and consequences of accelerating ions with different f_0 are explained in detail in Chapter 2 and are not recalled in the following. To avoid tracking simulations for each p-A system, only the key parameters characterising the dynamics of moving encounters are given. One of these parameters is the positional shift d_t of the interaction points (see Eq. 2.4)

$$d_t \approx C\frac{c^2}{4p_{\mathrm{p}}^2}\left(\frac{m_A^2}{Z_A^2} - m_{\mathrm{p}}^2\right) . \tag{7.1}$$

The parameter d_t is a good measure of the order $|n|$ of the dipole OKO resonances close to the betatron tune, i.e., the rough relation $|\mathcal{F}[d_u]| \propto d_t$ (see Eq. 2.106) holds. Chapter 2 clarified that there is no noteworthy influence on the beam in p-Pb operation in the LHC. By comparison of d_t between p-Pb and the different p-A scenarios, qualitative statements can be made and potential stable or unstable operation is inferred. Another key parameter is the momentum shift caused by the RF lock at the target energy of $E_b = 7Z\,\mathrm{TeV}$ (see Eq. 2.2)

$$\delta_p \approx \pm\frac{1}{\eta}\frac{c^2}{4p_{\mathrm{p}}^2}\left(\frac{m_A^2}{Z_A^2} - m_{\mathrm{p}}^2\right) \approx \pm\frac{d_t}{C\eta} . \tag{7.2}$$

A large momentum shift may cause too large excursions of the beam orbits in the arcs because of the dispersion D_x generated by the arc dipoles. If the orbit excursions in p-A operation are larger than those in p-Pb operation, it is necessary to verify that they are still acceptable.

The two key parameters d_t and $\delta_{\mathrm{p/A}}$ are both functions of the charge-density difference $m_A^2/Z_A^2 - m_{\mathrm{p}}^2$. Among the considered ion species, the charge-to-mass ratio difference is the largest for p-Pb operation and the smallest for p-O and p-Ca operation. It follows that the shift per turn d_t and fractional tune Q_v (see Eq. 2.101) are the largest in p-Pb configuration and the smallest in p-O/p-Ca configuration. The same also holds for the absolute value of the momentum shift $|\delta_p|$ from the RF lock at injection energy and throughout the whole energy ramp. The top part of Tab. 7.1 gives a full list of the parameters for all ion species, and Fig. 7.1 shows the dependence of the shift d_t on the beam energy. The initial shift of the encounter positions for p-Pb is roughly $d_t = 15.47\,\mathrm{cm}$ and the shift becomes smaller towards the smallest collision system p-O with $d_t = 8.51\,\mathrm{cm}$ shift per turn. The same behaviour is observed for the momentum shift δ_p. The shifts of p-O and p-Ca are identical with O and Ca having the same charge-to-mass ratio.

It can be concluded without detailed analysis that the excitation from moving beam-beam encounters is the strongest in p-Pb operation compared to the other p-A collision systems. Since the p-Pb configuration has already been analysed in Chapter 2 and no noteworthy excitation has been observed, it can be inferred that all other p-A systems are even less influenced by moving encounter points and OKO resonances. A similar conclusion regarding the momentum shift from the RF lock can be made. The relative momentum shift for p-Pb is $\delta_p = \pm 7.4 \times 10^{-3}\,\%$, whereas it is significantly smaller for the other species, e.g., the beams have relative momentum shifts of $\delta_p = \pm 4.1 \times 10^{-3}\,\%$ in p-O operation at top energy. The beta beating resulting from the momentum shifts has not caused any issues in past p-Pb operation. Based on the even smaller momentum shifts for the other p-A systems, the beta beating is expected to be manageable for those systems with smaller momentum shifts.

7.2 One-month performance

The one-month performance is estimated in the exact the way the LHC p-Pb performance was estimated in Chapter 6. The bunch properties, radiation damping, IBS and also the cross section vary among the ion species. The difference in terms of beam and bunch parameters are described in the following. After that, the performance for one month of p-A operation is estimated. ALICE will be luminosity levelled in all p-A scenarios. The ALICE levelling value is simply matched to the same NN luminosity value as in p-Pb operation $\mathcal{L}_{\mathrm{NN}} = A_{\mathrm{Pb}} 5 \times 10^{29}\,\mathrm{cm}^{-2}\mathrm{Hz} = 1.04 \times 10^{32}\,\mathrm{cm}^{-2}\mathrm{Hz}$ in all p-A scenarios (see Tab.7.1).

Table 7.1: Parameter list for the different ion species in proton-nucleus collisions in the LHC at beam energies of $E_b = 7\,Z\,\mathrm{TeV}$. The bottom part of the tables gives performance estimates of a one-month long p-A LHC run. Table adapted from [18].

	Isotope			$^{16}O^{8+}$	$^{40}Ar^{18+}$	$^{40}Ca^{20+}$	$^{78}Kr^{36+}$	$^{129}Xe^{54+}$	$^{208}Pb^{82+}$
Injection	Ion Lorentz factor γ	1		242	218	242	223	202	191
	Encounter shift per turn d_t	cm		8.51	11.17	8.50	10.47	13.37	15.47
	Rel. momentum shift (RF) δ_p	10^{-5}		± 4.1	± 5.4	± 4.1	± 5.0	± 6.4	± 7.4
Collision	Ion Lorentz factor γ	1		3760	3386	3762	3473	3149	2964
	Collision energy $\sqrt{s_{\mathrm{NN}}}$	TeV		9.90	9.31	9.90	9.51	9.06	8.80
	Normalised emittance ϵ_n	µm		2.09	1.89	2.09	1.93	1.75	1.65
	Ions per bunch N_{b}	10^8		19.5	18.5	15.8	6.5	3.6	1.9
	EMD cross section σ_{EMD}	mb		1.20	4.01	4.08	9.84	18.68	35.47
	BFPP cross section σ_{BFPP}	mb		< 0.01	0.02	0.04	0.71	5.41	44.10
	Hadronic cross section σ_{had}	b		0.45	0.83	0.83	1.14	1.60	2.13
	Long. rad. damping time τ_z	h		50.3	34.0	20.1	15.4	15.1	12.7
	IBS factor f_{IBS}	1		0.06	0.36	0.31	0.48	0.73	1
Performance	Fill duration τ_{fill}	h		9.7	9.8	9.7	8.0	6.4	5.2
	ALICE levelling $\mathcal{L}$	$10^{29}\,\mathrm{Hz/cm^2}$		65.0	26.0	26.0	13.3	8.1	5.0
	Peak luminosity $\mathcal{L}$	$10^{29}\,\mathrm{Hz/cm^2}$		228.5	216.6	185.0	76.6	41.7	22.3
	Peak NN luminosity $\mathcal{L}_{\mathrm{NN}}$	$10^{32}\,\mathrm{Hz/cm^2}$		3.66	8.66	7.40	5.97	5.38	4.63
	$\int_{\mathrm{month}} \mathcal{L}$	IP1/5	nb^{-1}	11763	9583	8507	3376	1695	835
		IP2		5065	2024	2021	991	564	327
		IP8		221	179	159	63	31	15
	$\int_{\mathrm{month}} \mathcal{L}_{\mathrm{NN}}$	IP1/5	pb^{-1}	188.2	383.3	340.3	263.3	218.7	173.7
		IP2		81.0	81.0	80.8	77.3	72.7	68.0
		IP8		3.5	7.2	6.4	4.9	4.0	3.2

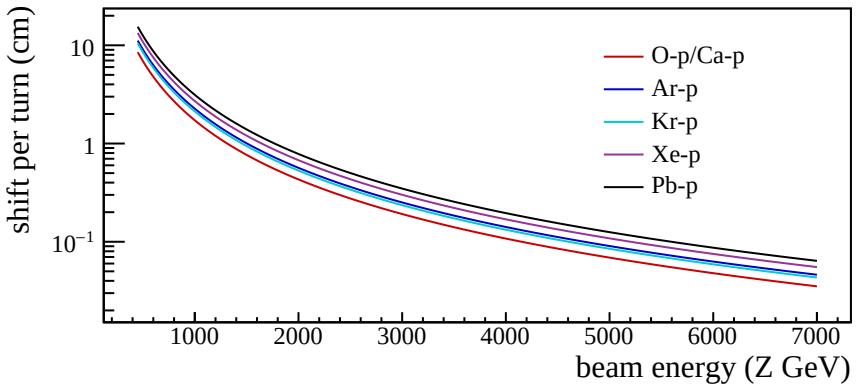

Figure 7.1: The turn-wise shift of beam-beam encounters during the energy ramp versus the beam energy in the LHC for different p-A systems.

7.2.1 Beam parameters

The bunch intensities delivered by the LHC injector chain depend strongly on the ion charge. During the passage of the ions through the injector chain (ECR source, RFQ, Linac3, LEIR, PS and SPS), the ions are additionally subject to multiple stripping stages that increase the charge state, electron cooling in LEIR as well as IBS and space charge effects. The intensities provided by the injectors can therefore only be estimated approximately. Even during a full one-month run, the intensities of the ion beam increase over time with operators being able to optimise parameters at the different positions along the injector chain. Hence, a fully reliable prediction is not possible. The SPS has already provided Pb and Xe ions [47] to the LHC in the past; however, the list of ions that have been accelerated in the SPS is extended by argon, which has been accelerated and sent to CERN's North Area in the past (besides Pb and Xe) [190]. In the scope of the HL- and HE-LHC yellow report [17], the highly simplified formalism

$$N_b(Z) = 1.9 \times 10^8 \left(\frac{82}{Z}\right)^p \tag{7.3}$$

for the bunch intensities of different ion species has been proposed by J. Jowett. Here, Z is the atomic number of the respective ion and p is a scaling parameter. The parameter p was found to be $p \approx 1.5$ for the ion species in [190], but only $p = 1$ was achieved during the Xe-Xe test in 2017; however, only a short amount of time was spent on the optimisation of the Xe bunch intensities. The parameter p is expected to be in the range between $p = 1$ (pessimistic) and $p = 1.9$ (highly optimistic) for the different ion species. To give moderate predictions for the one-month performance, $p = 1.5$ is assumed for all ion species except oxygen. For oxygen, $p = 1$ is assumed to not obtain too optimistic bunch intensities. Table 7.1 also lists the bunch intensities for the different ion species. Equation 7.3 yields for Pb an improved bunch intensity

of $N_b = 1.9 \times 10^8$ ions per bunch at the start of collisions compared to $N_b = 1.8 \times 10^8$ Pb ions per bunch in Run 3 and 4 (see Chapter 6).

The proton intensity in p-A operation is expected to be at 3×10^{10} protons per bunch compared to only 2.8×10^{10} protons per bunch in 2016. This, however, requires the successful mitigation of the luminosity-driven losses in the dispersion suppressors downstream of IP1 and IP5 (explained in detail in Chapter 6). The characteristics of the losses and the mitigation using the TCL collimators are not recalled at this point.

The beam emittance for the different ion species can only be guessed. Besides Pb, only Xe has been accelerated in the LHC; however, reliable emittance information is only available for Pb. The HL-LHC baseline foresees a (normalised) Pb emittance of $\epsilon_n = 1.65\,\mu\mathrm{m}$ in both transverse planes (see Chapter 6). For simplicity, the geometric emittance equal to that of Pb bunches $\epsilon_{n,\mathrm{A}}/\gamma_\mathrm{A} = \epsilon_{n,\mathrm{Pb}}/\gamma_\mathrm{Pb}$ is assumed among all ion species. The centre part of Tab. 7.1 gives the normalised emittance for each particle species. The normalised proton emittance is expected to be $\epsilon_n = 2.5\,\mu\mathrm{m}$. This means that the proton geometric emittance is slightly smaller than the ion emittance. Based on the study carried out in Chapter 3, this fact should not lead to an unacceptable dynamic aperture as the tune footprint and driving terms are equal to those of p-Pb; a direct consequence of the same rigidity among all particle types.

The collimation efficiency cannot easily be extrapolated for all different ion species. The 2017 Xe-Xe pilot run of the LHC [47] showed an acceptable collimation efficiency for the extremely low intensities of the Xe beams. Full-intensity beams would have caused issues mainly in the dispersion suppressors of downstream of IR7 (betatron cleaning) [191]. Assuming TCLD collimators will be installed in the IR7 dispersion suppressors until a potential p-A run, these kinds of losses are not of concern in upcoming runs. Full intensity beams of the mentioned ion species should be achievable in a future p-A run without having intensity-limiting effects resulting from an insufficient collimation efficiency.

7.2.2 Total cross section

Important parameters in p-A collisions are the cross section σ and the contributions of BFPP and EMD processes to σ. As already explained in Chapter 4, the total cross section reads

$$\sigma = \sigma_\mathrm{had} + \sigma_\mathrm{BFPP} + \sigma_\mathrm{EMD}\,. \tag{7.4}$$

The hadronic cross sections σ_had for the different p-A systems at $E_b = 7Z\,\mathrm{TeV}$ have been calculated by David d'Enterria [192] using a Monte-Carlo Glauber calculation as described in [16]. The hadronic cross sections scale roughly with $\sigma_\mathrm{had} \propto A^{2/3}$ [177] between the different

p-A systems. The centre part of Tab.7.1 gives a full list of hadronic cross sections at the different centre-of-mass energies (see Eq. 4.1)

$$\sqrt{s_{\mathrm{NN}}} \approx 2cp_{\mathrm{p}}\sqrt{\frac{Z}{A}} \tag{7.5}$$

with $p_{\mathrm{p}} = 7\,\mathrm{TeV/c}$. The BFPP and EMD cross sections are not published for the different p-A systems at $E_b = 7Z\,\mathrm{TeV}$. The cross-section values for the different A-A systems at $E_b = 7Z\,\mathrm{TeV}$ beam energy can be found in [17]. The same scaling as described in Sec. 4.1.4.3 with the scaling factor

$$\kappa = \frac{1}{Z^2}\frac{\log(\gamma_{\mathrm{c,pA}})}{\log(\gamma_{\mathrm{c,AA}})} \qquad \text{with} \qquad \gamma_{\mathrm{c,AB}} \approx 2\gamma_A\gamma_B \tag{7.6}$$

is performed on the A-A values in [17] to obtain the p-A values for σ_{BFPP} and σ_{EMD}. Table 7.1 gives a list of all BFPP and EMD cross sections. In p-Pb collisions, roughly $3.6\,\%$ of the total cross section is due to ultra-peripheral processes while for p-O the contribution is less than $0.3\,\%$. Therefore, the hadronic cross section σ_{had} is responsible for close to $100\,\%$ of the total cross section for the smaller p-A systems like p-O, p-Ar and p-Ca.

7.2.3 Radiation damping and intra-beam scattering

The radiation damping rates of different ion species at the same magnetic rigidity scale like $\alpha_{\mathrm{rad},u} \propto Z^5/m^4$ (see Eqs. 4.3–4.4). It can be observed that for heavier ion types the damping rate is larger than for light ions because of the stronger scaling with the charge than the mass. As an example, the damping rates of Pb ions are a factor 4 larger than those of oxygen ions, i.e., protons damp twice as fast as oxygen. Table 7.1 lists the longitudinal damping times $\tau_{\mathrm{rad},z} = 1/\alpha_{\mathrm{rad},z}$ of all considered ion species. The transverse damping times are usually obtained by multiplying the longitudinal damping times by a factor 2 (cf. Eqs. 4.3–4.5).

A simplified comparison between the IBS growth rates of the different ion species is performed in the following (cf. reference [17]). A simplification is made by assuming equal integrals in Eqs. 4.7–4.9. Hence, the key parameter for different IBS growth rates is the factor A_{IBS} in Eq. 4.10. By substituting $\gamma \approx Z\gamma_p/A$ and $\beta \approx 1$, the factor A_{IBS} scales between ion species according to $A_{\mathrm{IBS}} \propto N_b A^2$ (common factors are dropped). The parameter $f_{\mathrm{IBS}} = A_{\mathrm{IBS,A}}/A_{\mathrm{IBS,Pb}}$ is used as a scaling factor to obtain the IBS growth rates of the different ion species from the IBS growth rate of Pb.[1] The values of f_{IBS} are given in the centre part of Tab. 7.1. Listing the growth rate itself is cumbersome in the sense that beam size and intensity are constantly changing. Longitudinal IBS growth rates of roughly $\tau_{\mathrm{IBS},z} \approx 7\,\mathrm{h}$ can be expected

[1] A different definition of f_{IBS} is used in [17]. The two definitions are not comparable.

for Pb ions.[2] The horizontal growth time can be expected to be roughly twice as long. As an example, the longitudinal growth time of oxygen is obtained via $\tau_{\mathrm{IBS},z} \approx 7\,\mathrm{h}/f_{\mathrm{IBS}} \approx 115\,\mathrm{h}$. Hence, radiation damping is dominant compared to IBS for most light ion species; however, this does not imply that the bunch volume shrinks significantly during the fill since the damping effect is small for most ion species. The IBS growth rate depends on the parameter p used to estimate the bunch intensities N_b. A more optimistic p therefore shortens the IBS growth time.

7.2.4 Performance results

The HL-LHC filling pattern shown in Chapter 6 in Fig. 6.1 for Pb-Pb is used throughout all p-A systems. Also, the IP settings as listed in Chapter 6 in Tab. 6.2 are used in all cases except the half-crossing angles are set to $\theta/2 = (100,\, 100,\, 100,\, 318)\mu\mathrm{rad}$. The smaller crossing angles in ATLAS and CMS compared to the Run 3/4 values are expected to be operational in Run 5 and beyond. The non-colliding lifetimes are those also used in Chapter 6 and the extra losses at the detectors are $1/\alpha_{\mathrm{IP}} = (45.2,\, 47.8,\, 45.2,\, 317)\mathrm{h}$. Analogously to Chapter 6, the one-month performance is estimated by first simulating the beam evolution for a single fill via the beam-evolution code presented in Chapter 4. The turnaround time is once again assumed to be $T_r = 2.5\,\mathrm{h}$. The optimum fill times τ_{opt} of ATLAS/CMS and ALICE are estimated by calculating the maximum of the average luminosity. As a compromise between the two optima of ATLAS/CMS and ALICE, the geometric mean of the two fill times is assumed as the fill duration τ_{fill}. With the fill duration τ_{fill}, the average luminosities $\langle L(\tau_{\mathrm{fill}})\rangle$ for each detector are calculated and the performance in $24\,\mathrm{d}$ of operation is extrapolated. To cover for operational issues, an operational efficiency of $50\,\%$ is once again assumed, and a $5\,\%$ reduction is applied to cover the possibility the proton injection is incapable of reproducing the ion filling pattern.

The evolution of the instantaneous luminosities and average luminosities are given in Fig. 7.2 for p-O, p-Ar and p-Ca operation. Figure 7.3 shows the analogous plots for p-Kr, p-Xe and p-Pb operation. The peak luminosity achievable in ATLAS and CMS at start of collisions decreases with ion size mostly because of the reduced bunch intensity with larger Z. The peak NN luminosity in p-Ar operation is at $\mathcal{L}_{\mathrm{NN}} = 8.66 \times 10^{32}\,\mathrm{cm}^{-2}\mathrm{Hz}$ while it is $\mathcal{L}_{\mathrm{NN}} = 4.63 \times 10^{32}\,\mathrm{cm}^{-2}\mathrm{Hz}$ in p-Pb collisions. Hence, the NN luminosity is enhanced by roughly a factor 2. Because $p = 1$ was used for oxygen and $p = 1.5$ for all other ion species to estimate the bunch intensity, there is a discontinuity when comparing the NN luminosity of p-O with these of the other p-A systems.

The optimum fill durations change dramatically between p-A systems. While in the case of p-Pb, the ATLAS/CMS optimum is at $\tau_{\mathrm{opt}} = 3.6\,\mathrm{h}$ and the ALICE optimum is at $\tau_{\mathrm{opt}} = 7.3\,\mathrm{h}$

[2]The longitudinal IBS growth time $\tau_{\mathrm{IBS},z} \approx 15.4\,\mathrm{h}$ is given in [1] for the nominal LHC; however, the bunch intensity and emittances are different compared to the p-Pb HL-LHC scenario. Hence, the resulting growth time in the HL-LHC should be roughly $\tau_{\mathrm{IBS},z} \approx 7\,\mathrm{h}$ in the here discussed case with correct emittances and intensities.

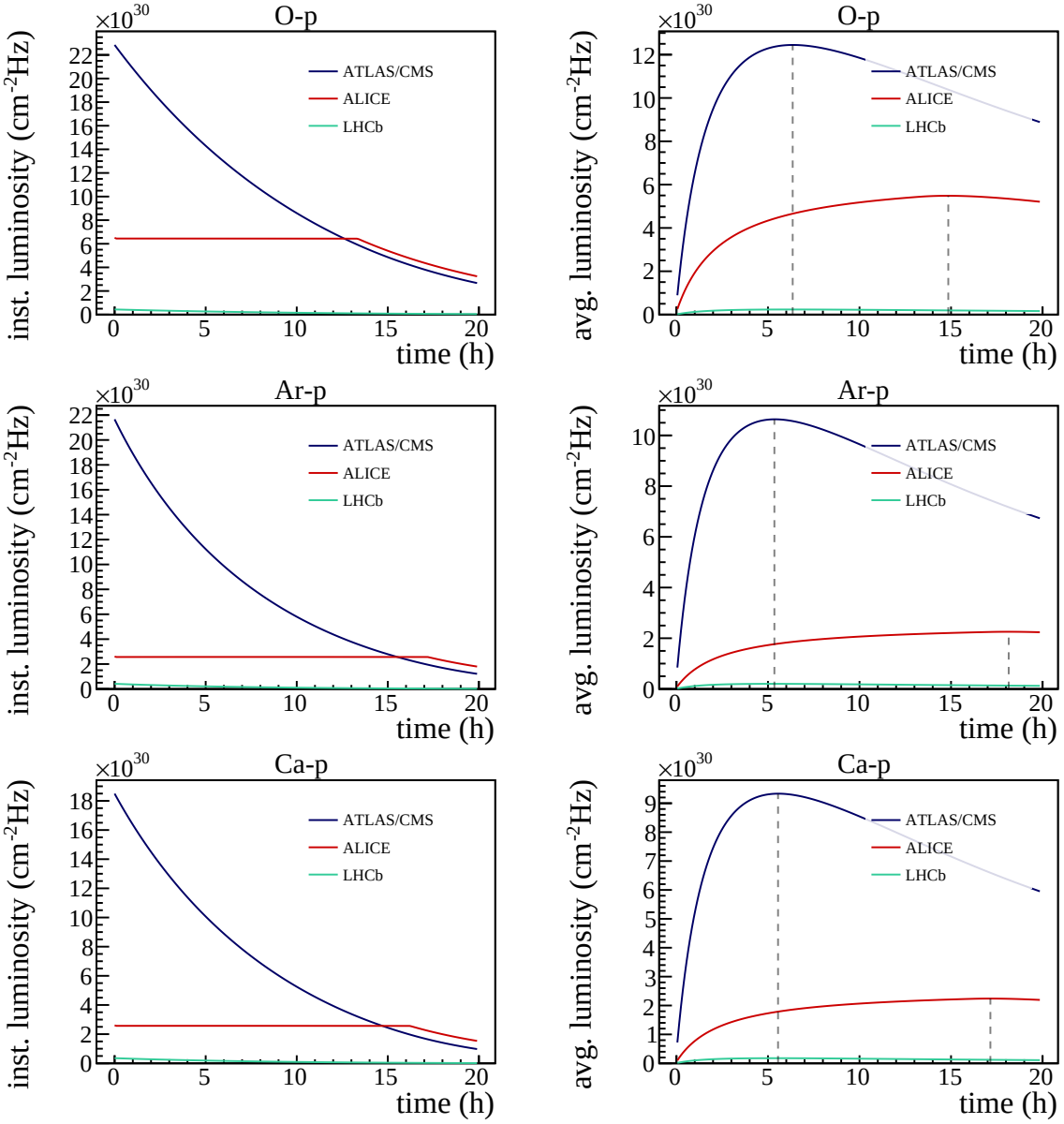

Figure 7.2: Left: The three plots on the left show the evolution of the instantaneous luminosities in O-p (top), Ar-p (centre) and Ca-p (bottom) operation. Right: The three plots show the average luminosities versus time for the same collision systems. The grey dashed lines indicate the optimum fill duration τ_{opt} for ATLAS/CMS and ALICE.

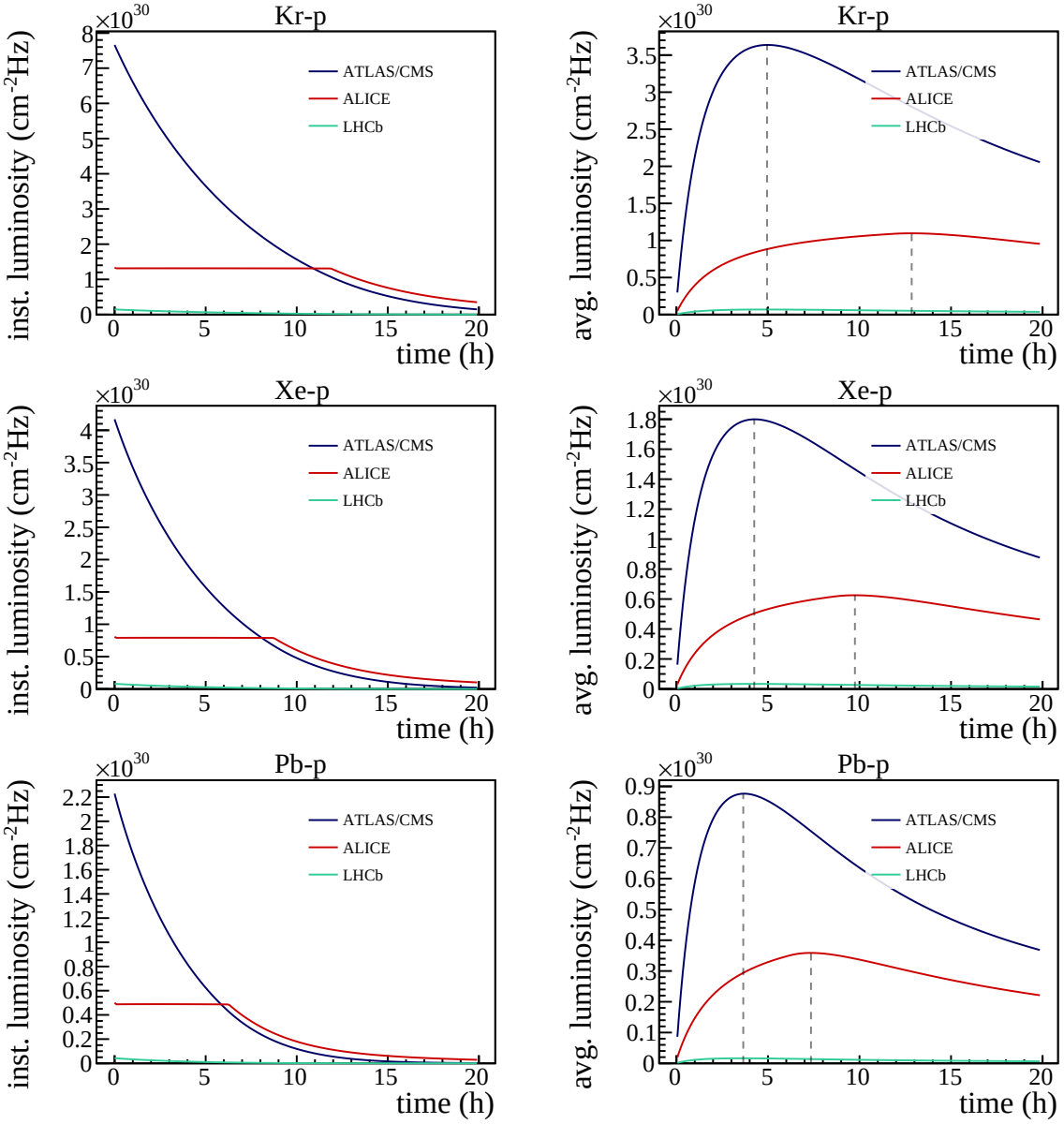

Figure 7.3: Left: The three plots on the left show the evolution of the instantaneous luminosities in Kr-p (top), Xe-p (centre) and Pb-p (bottom) operation. Right: The three plots show the average luminosities versus time for the same collision systems. The grey dashed lines indicate the optimum fill duration τ_{opt} for ATLAS/CMS and ALICE.

($\tau_{\text{fill}} = 5.2\,\text{h}$), the optimum has shifted for ATLAS/CMS to $\tau_{\text{opt}} = 5.3\,\text{h}$ and to $\tau_{\text{opt}} = 18.1\,\text{h}$ ($\tau_{\text{fill}} = 9.8\,\text{h}$) for ALICE in p-Ar operation. Hence, the fill duration becomes significantly longer for the smaller sized p-A collisions. One reason for extended fill durations is that the time span ALICE is levelled becomes longer the lighter the ion species. This is because the ALICE levelling value depends on the nucleon number A, whereas the bunch intensity scales like $N_b \propto Z^{-1.5}$ with the atomic number. Because of these dependencies, the luminosity burn-off is slower in ALICE and the luminosity available to ATLAS/CMS increases, resulting in the prolongation of the optimum fill duration τ_{opt} of ATLAS, ALICE and CMS.

The performance of an one-month p-A run is given in the bottom part of Tab. 7.1 for the four LHC experiments. The integrated NN luminosity in ATLAS/CMS in p-Ar collisions with $383\,\text{pb}^{-1}$ is a rough factor 2.2 larger than that in p-Pb collisions with $174\,\text{pb}^{-1}$. This increase is quite substantial. The gain in terms of integrated NN luminosity for ALICE is less significant since ALICE is levelled to the same instantaneous NN luminosity among all p-A scenarios. The increase in integrated NN luminosity is therefore only the result of an improved (longer) fill duration because of the longer achievable levelling in ALICE. The integrated NN luminosity in ALICE in p-Pb collisions is at $68\,\text{pb}^{-1}$ and it increases by $20\,\%$ in p-Ar operation to a total integrated NN luminosity of $81\,\text{pb}^{-1}$. This increase is because of the increased fill duration of $\tau_{\text{fill}} = 9.8\,\text{h}$ compared to only $\tau_{\text{fill}} = 5.2\,\text{h}$ in p-Pb operation. The LHCb performance is much smaller compared to the other detectors since the number of colliding bunch pairs is only 81. A redistribution of colliding bunch pairs favouring LHCb would obviously enhance the LHCb integrated luminosity.

7.3 Prospects of a potential p-O pilot run

A potential p-O pilot run in combination with an O-O pilot run is envisaged for LHC Run 3 potentially taking place in 2023 [17, 180, 193, 194]. The goal is to get a better understanding of the interaction of cosmic particles with the atmosphere of Earth. LHCb and LHCf [195] are the two LHC experiments mainly interested in p-O collisions. LHCb aims for an integrated luminosity of $2\,\text{nb}^{-1}$ or more in such in a pilot run to accumulate roughly 10^4 J/Ψ particles. LHCf would like to accumulate the data of roughly 4×10^5 π^0 particles. This requires roughly an accumulated luminosity of $1.5\,\text{nb}^{-1}$. LHCf is located downstream of the ATLAS IP and detects particles in the high-rapidity range. The data taking of LHCf requires a maximum pile-up in the ATLAS IP of $\mu \approx 0.01$ and a $2\,\mu$s spacing between the colliding bunches. With 36 bunches per beam and 24 colliding bunch pairs in each IP, the ATLAS pile-up requirement of $\mu = 0.01$ is fulfilled if ATLAS is levelled to an instantaneous luminosity of $\mathcal{L} = 6 \times 10^{27}\,\text{Hz/cm}^2$. The requested time period for accommodating multiple low intensity O-O and p-O fills is only one week. This requires the setup time to be short to achieve sufficient luminosity production in this

time span. Comparably to the Xe-Xe pilot run in 2017 [47], the beam intensities are limited to 3×10^{11} charges per beam to avoid the otherwise extensive beam commissioning required by Machine Protection. Prior to the p-O test run, the O-O run would take place. The operation in O-O collisions would take between two and three days of commissioning and the following p-O run would only require a maximum of one day of commissioning. During the p-O setup, mainly the ramp with unequal revolution frequencies and the cogging process have to be commissioned. The run would be operated with protons in Beam 1 and oxygen in Beam 2. No beam-direction reversal is requested. In the next sections, the potential beam parameters and the potential performance of such a short p-O pilot run are discussed.

7.3.1 Beam parameters

The bunch intensity of the oxygen bunches defines the number of bunches that can be injected into the LHC while remaining under the threshold of 3×10^{11} charges per beam. The proton bunch intensities are going to match these of the oxygen bunches in order to store the same number of bunches to provide as many colliding bunch pairs to the detectors as possible. As in Sec. 7.2.1, the oxygen bunch intensity is estimated via Eq 7.3 with the parameter $p = 1$ yielding a bunch intensity of $N_b = 1.95 \times 10^9$ oxygen ions per bunch. Such a bunch intensity would allow the storage of roughly 19 bunches per beam. Such a high bunch intensity, however, is relatively large considering the requested small pile-up in ATLAS. It is therefore envisaged to store roughly 36 bunches per beam with 8.33×10^9 charges per bunch. The total beam intensity is then exactly at 3×10^{11} charges per beam and within the previously mentioned limit. The number of colliding bunch pairs would be 24 in all four IPs and the time intervals between collisions are larger than $2\,\mu$s in ATLAS. The filling pattern is preliminary and more than 24 colliding bunch pairs are possible with 36 bunches per beam. The bunches would be of the bunch equivalence classes 3, 5 and 6 (see Tab. 4.4 and Eq. 4.44). Each of these three classes comprises 12 bunches per beam. The bunch classes 5 and 6 collide in three experiments. Hence, the bunches of these classes are expected to drop slightly faster in intensity than the bunches of equivalence class 3.

The IP settings would be comparable to these used in the 2021 Pb-Pb run which should be roughly equal to the Pb-p values listed in Tab. 6.2. The half-crossing angles in the experiments may change in the future, especially since the bunch spacing is large enough to have collisions without crossing angles ($\theta/2 = 0$). The extra losses are different compared to the previous analysis for p-A because of the significantly smaller proton intensity. The extra loss rates at the detectors are $1/\alpha_{\mathrm{IP}} = (\infty, 277, 172, 1142)\mathrm{h}$. These values are considerably large due to the small proton bunch intensity. The ATLAS losses are set to zero (infinity lifetime), since ATLAS is levelled to an extremely small luminosity value and potential extra losses are impossible to predict. The non-colliding lifetime is expected to be $\tau_{\mathrm{ex}} = 100\,\mathrm{h}$ once again.

7.3.2 Beam evolution

The beam evolution is again simulated by integrating the ODEs from Eqs. 4.45–4.46 with time steps of 180 s. Figure 7.4 presents the resulting beam evolution.

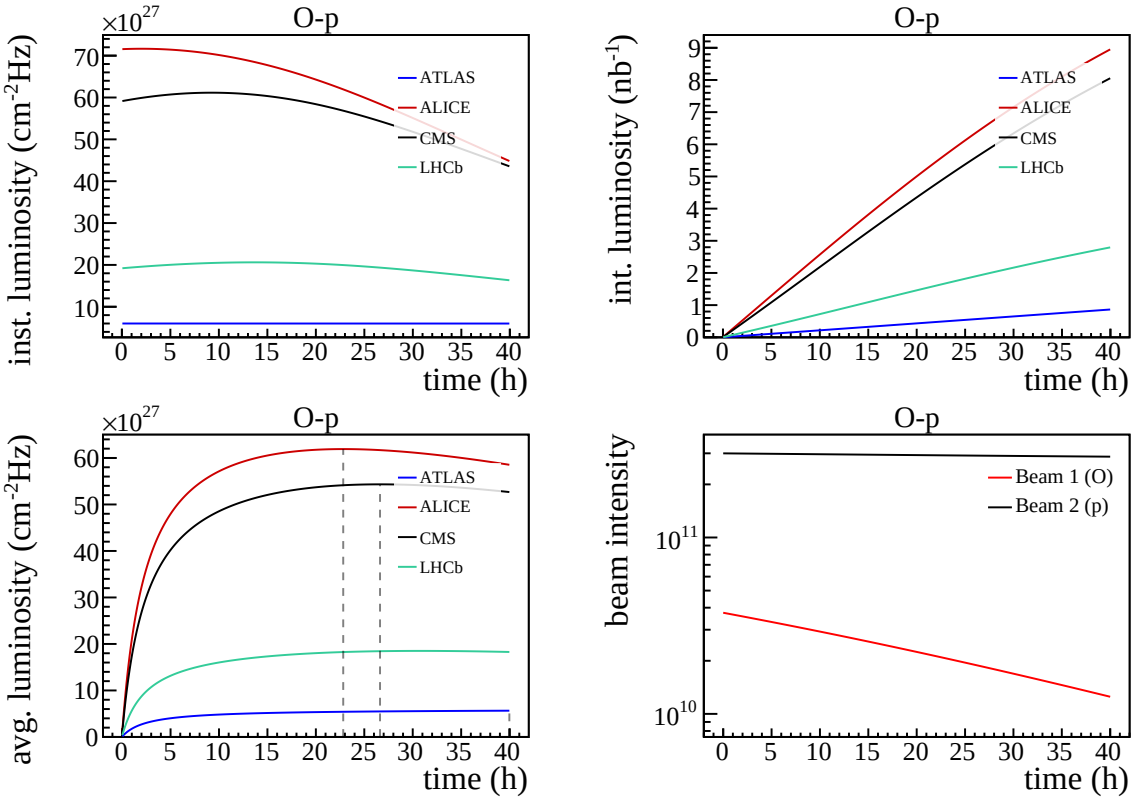

Figure 7.4: Top left: The luminosity evolution for the four LHC experiments. ATLAS is levelled to $\mathcal{L} = 10^{28}\,\mathrm{cm}^{-2}\mathrm{Hz}$ for more than 40 h if desired. The difference between the CMS and ALICE luminosity is due to different crossing angles. Top right: The integrated luminosities versus time. Bottom left: The average luminosities versus time assuming a turnaround time of $T_r = 2.5\,\mathrm{h}$. The dashed lines indicate optimum the fill duration τ_{opt} of ALICE and CMS. Bottom right: Intensity evolution of the oxygen beam (red) and the proton beam (black).

The ATLAS luminosity is strictly levelled to $\mathcal{L} = 6 \times 10^{27}\,\mathrm{cm}^{-2}\mathrm{Hz}$. The peak luminosity among all IPs is achieved in ALICE with $\mathcal{L} = 7.2 \times 10^{28}\,\mathrm{cm}^{-2}\mathrm{Hz}$. The CMS peak luminosity $\mathcal{L} = 6.1 \times 10^{28}\,\mathrm{cm}^{-2}\mathrm{Hz}$ is achieved after 9 h in collisions since radiation damping causes the shrinkage of the bunch volume and thus an increase of the luminosity. The initial luminosity is slightly smaller than that of ALICE due to the larger crossing angle. The LHCb peak luminosity $\mathcal{L} = 2.1 \times 10^{28}\,\mathrm{cm}^{-2}\mathrm{Hz}$ is achieved after 14 h in collisions. This value is significantly smaller than the peak luminosity in CMS and ALICE since the β^* is 3 times larger than in the other experiments and the half crossing angle $\theta/2 = 317\,\mu\mathrm{rad}$ is also much larger. Larger peak luminosities would be achieved if the number of bunches was not artificially increased from 19

bunches per beam to 36 bunches per beam; however, less colliding bunch pairs would increase the time required for LHCf to reach its targeted integrated luminosity since fewer collisions per turn with a pile-up of $\mu = 0.01$ would take place in ATLAS.

ATLAS can be kept levelled for the whole duration of the $40\,\mathrm{h}$ of simulation time. If one assumes a turnaround time of $T_r = 2.5\,\mathrm{h}$, the optimum fill durations of ALICE and CMS are in the range $\tau_{\mathrm{op}} = 23$–$27\,\mathrm{h}$. These numbers have little meaning for a short time period of one week and fills should generally be kept as long as possible; however, it could make sense to not keep fills much longer than $35\,\mathrm{h}$ to optimise the integrated luminosity. In the time range of 25–$30\,\mathrm{h}$, ALICE and CMS would achieve an integrated luminosity between $5\,\mathrm{nb}^{-1}$ and $7\,\mathrm{nb}^{-1}$. LHCb would reach its target of $2\,\mathrm{nb}^{-1}$ in a single fill, and LHCf would require in total two fills of combined roughly $70\,\mathrm{h}$ duration to accomplish its envisaged target of $1.5\,\mathrm{nb}^{-1}$.

7.4 Conclusion

The reduction of the ion size in asymmetric p-A collisions is a viable option to enhance the LHC luminosity production in Run 5 and 6. The effects of moving beam-beam encounters are expected to be fully negligible for all p-A scenarios and the intrinsic momentum shift due to the RF lock at the target energy should generate no noteworthy beta beating. Besides a favourable ratio between hadronic cross section to total cross section, the increased bunch intensities for lighter ions provided by the LHC injector chain is pushing the peak and integrated luminosity substantially. While in a future p-Pb run an integrated NN luminosity of $174\,\mathrm{pb}^{-1}$ ($68\,\mathrm{pb}^{-1}$) can be expected in ATLAS/CMS (ALICE), the integrated NN luminosity is, e.g., a factor 2.2 (1.2) larger in p-Ar operation. Another benefit of colliding smaller sized ion species is a prolonged fill duration τ_{fill}. A longer fill duration makes the collider performance on the scale of a month less susceptible to potential operational issues and machine faults since the average luminosities are only slowly varying around the optimum in long fills. The predicted integrated NN luminosity in symmetric Ar-Ar collisions is in ATLAS/CMS at $1730\,\mathrm{pb}^{-1}$ compared to $213\,\mathrm{pb}^{-1}$ in Pb-Pb collisions. This is an increase by a factor 7.5 [17]. Hence, p-Ar and Ar-Ar operation would benefit the integrated luminosity by a large margin. If the LHC collides ion species lighter than Pb in symmetric A-A and p-A collisions in LHC Run 5 and beyond, a rapid increase of accumulated data can be expected for a variety of ion species.

A potential p-O pilot run in 2023 would significantly help to improve the understanding of the interaction of cosmic rays with Earth's atmosphere and potentially resolve some ambiguities regarding the modelling of cosmic rays. Since the pile-up in ATLAS is not allowed to exceed $\mu = 0.01$, a filling pattern with 36 bunches per beam providing 24 colliding bunch pairs to each experiment is possibly going to be applied. With 24 collisions in ATLAS and a levelling value of $\mathcal{L} = 6 \times 10^{27}\,\mathrm{cm}^{-2}\mathrm{Hz}$, it will take only $70\,\mathrm{h}$ for LHCf to reach the targeted integrated

luminosity of $1.5\,\mathrm{nb}^{-1}$. This time span is equivalent to two fills. LHCb would reach its target of $2\,\mathrm{nb}^{-1}$ in a single fill of a duration of roughly $35\,\mathrm{h}$.

Potential O-O and p-O pilot runs require additional work and investments to ensure safe and reliable operation with oxygen in the LHC injectors. The feasibility of oxygen in the LHC injectors is investigated by a working group with the goal to provide a final verdict regarding the feasibility of accelerating oxygen in the CERN injector complex by 2020.

CHAPTER 8

Conclusion

In Chapter 2, important findings that lead to a better understanding of moving long-range beam-beam encounters were presented. The analysis of the effects of the moving encounters on the beams has shown key differences between the LHC and RHIC: Although the RHIC circumference is smaller than that of the LHC, the lower injection energy of RHIC compared to that of the LHC results in a larger shift per turn d_t of the beam-beam encounter locations if the injection and ramp with asymmetric beams is attempted with unequal revolution frequencies. The larger positional shift d_t causes dipole OKO resonances with a much smaller $|n|$ (see Eq. 2.107) compared to the LHC to intersect the betatron tune footprint. Besides that, the strength of the beam-beam kicks the strong beam applies onto the weak beam is larger in RHIC in Au-D/Al-p operation than in the LHC in Pb-p operation. The common beam pipes in the IR sections of RHIC are short compared to the bunch spacing. This enhances the fluctuations of the coherent kicks[1] and therefore the resulting emittance growth. These fluctuations are smaller in the LHC with longer common beam pipes compared to the bunch spacing. The FCC will not be influenced by moving long-range encounters in p-Pb operation because of the high injection energy and the large circumference.

The developed (simplified) tracking code yielded emittance doubling times of approximately $1\,\mathrm{min}$ or slightly larger for RHIC at injection in Au-D operation. This is an excellent result since growth rates of this magnitude were also observed experimentally. For the nominal LHC in Pb-p operation, emittance doubling times of multiple hundred hours were found. This underlines the unimportance of moving long-range beam-beam encounters in the LHC. IBS remains the much more dominant effect at injection energy. The tracking study also showed

[1] The net dipole kicks remaining after a turn and the tunes feature larger standard deviations.

that the HL-LHC with a bunch spacing of $50\,\mathrm{ns}$ will not face any proton intensity limits up to $N_b = 1.15 \times 10^{11}$ protons per bunch. With these unrealistically high intensities (unlikely to ever be used in p-Pb operation), the vertical emittance doubling time would be $9.4\,\mathrm{h}$; however, the transverse damper of the LHC was neglected in the study. The damper could extend the vertical doubling time to values in the region of $20\,\mathrm{h}$. Such growth rates are fully acceptable. These findings are important since they confirm the experimental observations in the LHC and RHIC, and an assessment of the effects of moving long-range encounters in the HL-LHC and FCC did not exist until this point.

The FMA analysis in Chapter 3 displayed only a very small tune diffusion within the Pb beam in Pb-p operation of the LHC if the Pb beam collides with a proton beam of a much smaller geometric size. The simplified model neglects the non-linear elements of the magnetic lattice; however, the tune diffusion generated by the head-on collisions in the IPs is small and is unlikely to reduce the dynamic aperture generated by the lattice non-linearities noticeably. This is even true for a very large beam-size ratio of $\hat{r} = 2.1$. The Pb-p tune footprint with four head-on collisions and a nominal beam-size ratio of $\hat{r} = 1.7$ is only slightly larger than the tune footprint generated by a single head-on collision in p-p operation. Since stability is observed in p-p collisions, stability in Pb-p collisions is very likely and supported by the Pb-p runs of the LHC in the past. In contrast to the observations made in HERA and the Sp$\bar{\mathrm{p}}$S, a reduced beam lifetime of the beam with the larger geometric size was not concluded for the Pb beam in the LHC.

The beam-evolution study at $E_b = 6.5Z\,\mathrm{TeV}$ in Pb-p collisions in Chapter 4 found that the Pb beams in the LHC are subject to (small) extra loss rates caused by the collisions in the IPs. Estimating these loss rates was only possible by simulating the evolution of all bunches of both beams using ODEs, and the existence of these losses was not known until this study. The presence of such losses is not supported by the FMA conducted in Chapter 3, and parasitic long-range encounters can be excluded from the list of potential sources since only bunches colliding in the IPs are affected. Another important finding was that the IBS growth rates are overestimated for the Pb bunches in the beam-evolution study. The sources for the extra loss rates and overestimated IBS growth rates have not been determined yet.

The hadronic cross section of p-Pb collisions at $\sqrt{s_{\mathrm{NN}}} = 8.16\,\mathrm{TeV}$ was successfully estimated in a study involving BLM signals. The total cross section was found to be $\sigma = (2.32 \pm 0.01\,(\mathrm{stat.}) \pm 0.20\,(\mathrm{sys.}))\,\mathrm{b}$. This value deviates by only $5.4\,\%$ from the predicted total cross section. The hadronic cross section is $\sigma_{\mathrm{had}} = (2.24 \pm 0.01\,(\mathrm{stat.}) \pm 0.21\,(\mathrm{sys.}))\,\mathrm{b}$ after the subtraction of the BFPP and EMD contributions to the total cross section. The theoretical value $\sigma_{\mathrm{had}} = (2.12 \pm 0.01)\,\mathrm{b}$ is well within the uncertainty range. This is an excellent result considering the presence of substantial non-luminous losses in the LHC. The results for the total and hadronic cross section feature large systematic uncertainties mainly caused by the

systematic uncertainties of the luminosities of the experiments. An inexplicable small cross section was obtained from the BLMs at the TCPs. The behaviour at the TCPs requires further analysis. The beam-evolution study in Chapter 4 would benefit from a total cross section $\sigma = (2.32 \pm 0.01\,(\text{stat.}) \pm 0.20\,(\text{sys.}))\,\text{b}$ that is slightly larger than predicted value; however, the extra loss rates that were determined would decrease only slightly.

The prediction of the integrated luminosity in future proton-nucleus runs of the LHC was another key topic throughout this thesis. The p-Pb operation of the LHC in future runs will be significantly enhanced mostly because of the longitudinal slip-stacking in the SPS. Chapter 6 predicts for LHC Run 3 and Run 4 that the increased bunch numbers will lead to integrated luminosities of roughly $30\,\text{nb}^{-1}/\text{d}$ in ATLAS and CMS and $14.2\,\text{nb}^{-1}/\text{d}$ in ALICE. These values are a rough factor 3 larger than in 2016. The ATLAS/CMS peak luminosity is expected to be approximately $\mathcal{L} = 1.7 \times 10^{30}\,\text{cm}^{-2}\text{Hz}$ at the start of a fill, and ALICE is levelled at $\mathcal{L} = 5 \times 10^{29}\,\text{cm}^{-2}\text{Hz}$ for roughly 7 h. The target integrated luminosities of $1.2\,\text{pb}^{-1}$ in ATLAS/CMS and $0.6\,\text{pb}^{-1}$ in ALICE/LHCb for Run 3 and 4 are expected to be achievable within two p-Pb runs (filling scheme with more colliding bunch pairs in LHCb required). The analysis of the TCL collimators has shown that half-gap widths of $15\sigma_{x,\text{Pb}}$ (TCL4/5) and $20\sigma_{x,\text{Pb}}$ (TCL6) suffice to protect the dispersion suppressors of IP1 and IP5 against collision debris. No obvious luminosity limit is expected in future p-Pb runs.

The reduction of the ion size in asymmetric p-A collisions is a viable option to enhance the LHC luminosity production in Run 5 and 6. Chapter 7 analysed the one-month performance in p-A collisions for a variety of ion species. The effects of moving beam-beam encounters are expected to be fully negligible for all considered p-A scenarios and the intrinsic momentum shift due to the RF lock at the target energy should generate no noteworthy beta beating. A future p-Pb run would generate an integrated NN luminosity of $174\,\text{pb}^{-1}$ ($68\,\text{pb}^{-1}$) in ATLAS/CMS (ALICE); however, the integrated NN luminosity is, e.g., a factor 2.2 (1.2) larger in p-Ar collision or 2.0 (1.2) times larger in p-Ca collisions.

A short p-O pilot run to improve the understanding of cosmic-ray physics will possibly take place in 2023 in the LHC. It is expected that there is not enough time for the full commissioning required by Machine Protection; therefore, only 36 bunches per beam providing 24 colliding bunch pairs to each experiment will be stored. ATLAS would be levelled to $\mathcal{L} = 6 \times 10^{27}\,\text{cm}^{-2}\text{Hz}$ that LHCf can take data at low pile-up. It will take only 70 h for LHCf to reach the targeted integrated luminosity of $1.5\,\text{nb}^{-1}$. LHCb would reach its target of $2\,\text{nb}^{-1}$ within 35 h.

Acknowledgement

I would like to thank ...

Dr John M Jowett for the great opportunity to pursue a PhD at CERN. I thank him for always finding the time to answer my questions over the last three years even in situations when time was short. I also owe him deep gratitude for his advice and ideas when I got stuck and did not know how to proceed.

Prof Dr Holger Podlech for accepting me as an external PhD student. I owe him gratitude for his help regarding the preparation of this thesis and his constant willingness to help over the past three years.

Priv.-Doz. Dr. Giuliano Franchetti for preparing the second assessment of this thesis.

Dr Michaela Schaumann for her constant willingness to help and to answer all kind of questions during the past three years.

Dr Tom Mertens for his help to get started and Dr Roderik Bruce for his help towards the end of my time at CERN.

the scientists at Brookhaven National Laboratory for hosting me in February 2019. I am especially grateful to Dr Angelika Drees, Dr Wolfram Fischer, Dr Aljosa Marusic, Dr Guillaume Robert-Demolaize and Dr Steven Tepikian for their help and patience to answer my various questions regarding RHIC.

my colleagues and friends at CERN for the great atmosphere and occasional distractions from work.

my friends in Germany. I always enjoyed coming back home during the last years, although it made it sometimes hard to leave again.

Dr Michael Hauschild and the Wolfgang-Gentner Programme for awarding me a scholarship for the duration of three years at CERN.

Prof Dr Wolfram Helml and Prof Dr Thomas Weis for the opportunity to finish the writing of the thesis at DELTA.

I want to thank my aunt for her constant support over the last three years. I am also grateful to my girlfriend for her support and encouragement. Last but not least, I want to thank my brother for his lifelong support. This thesis is dedicated to him and the memory of my parents.

APPENDIX A

Lie-algebraic treatment of non-linear magnets

The effect of non-linear elements obviously cannot be represented by linear matrices. One way to obtain a time-dependent Hamiltonian for a non-linear accelerator lattice is to extend the Hamiltonian of the unperturbed motion (harmonic oscillator) by the non-linear Hamiltonians containing Dirac delta functions $\delta(s - s_i)$ at the respective locations s_i of the non-linear elements. This time-dependent Hamiltonian, however, is of little use since the solution of the equations of motion is acquired by the piece-wise integration of motion between and at the respective delta functions. One way to obtain a time-independent effective Hamiltonian is to use Lie algebra. The fundamental Poisson brackets of Hamilton dynamics form a Lie algebra. To propagate the phase-space vector of a particle through a non-linear element, the operator $\exp(:h:)$ and is applied to the vector $\mathbf{r}$ [93].[1] The approach of using Lie algebra to treat non-linear elements has the advantage of being symplectic and can be carried out up to arbitrary order of the perturbation. The methods regarding Lie algebra are not explained here but can be found in [93, 94, 196]. In the next section, an effective Hamiltonian for arbitrary multipoles inserted in a linear lattice is derived in support of the calculations in Sec. 2.1.4.3. Furthermore, the effective Hamiltonian for a single octupole (Sec. A.2) and multiple octupoles (Sec. A.3) is derived in support of the tracking algorithm presented in Sec. 2.3.1.

[1] The definition of $:h:$ is given in Sec. 2.1.4.3.

A.1 Multiple arbitrary non-linear elements

The Lie operator of the linear motion of the full turn reads

$$H_0 = -\mu_x J_x - \mu_y J_y \tag{A.1}$$

in normalised coordinates. It already contains the integration with respect to the time-like variable. The Lie operator has the opposite sign with respect to the Hamiltonian. The Lie operator between two non-linear elements is

$$H_0(s_0, s_1) = -(\phi_x(s_1) - \phi_x(s_0))J_x - (\phi_y(s_1) - \phi_y(s_0))J_y\,. \tag{A.2}$$

The Lie operator of any infinitesimal-short multipole is expressible in terms of the Taylor series given in Eq. 2.32

$$H_\mathrm{p}(J_x, J_y, \phi_x, \phi_y) = -\sum_{m,n=-\infty}^{\infty} c_{mn}(J_x, J_y, d_x, d_y)e^{i(m\phi_x+n\phi_y)}\,. \tag{A.3}$$

with

$$c_{mn} = -\frac{1}{4\pi^2}\oint\oint H_\mathrm{p}(J_x, J_y, \phi_x, \phi_y)e^{-i(m\phi_x+n\phi_y)}\mathrm{d}\phi_x\mathrm{d}\phi_y\,. \tag{A.4}$$

The one-turn map is obtained by multiplying the Lie maps rightwards

$$e^{:h:} = e^{:H_0(0,s_1):}e^{:H_\mathrm{p}(s_1):}e^{:H_0(s_1,s_2):}\ldots e^{:H_\mathrm{p}(s_{N-1}):}e^{:H_0(s_{N-1},s_N):}e^{:H_\mathrm{p}(s_N):}e^{:H_0(s_N,C):}\,. \tag{A.5}$$

The goal is to achieve a form

$$e^{:h:} = e^{:H_1:}e^{:H_0:} \tag{A.6}$$

with H_0 being linear unperturbed Hamiltonian and H_1 being the perturbation due the non-linear elements. In this form and assuming $H_1 \ll H_0$, the concatenation is obtained via the Baker-Campbell-Hausdorff (BCH) formula [91, 93]

$$:h: = :H_0 + \left(\frac{:H_0:}{e^{:H_0:}-1}\right)H_1 + \mathcal{O}(H_1^2):\,. \tag{A.7}$$

To achieve this form, different unity operators like $1 = e^{:-H_0(s_m,s_n):}e^{:H_0(s_m,s_n):}$ are plugged into Eq. A.5 to reach

$$e^{:h:} = e^{:\exp(:H(0,s_1):)H_\mathrm{p}(s_1):}e^{:\exp(:H(0,s_2):)H_\mathrm{p}(s_2):}\ldots e^{:\exp(:H(0,s_N):)H_\mathrm{p}(s_N):}e^{:H(0,C):}\,. \tag{A.8}$$

To reach the form shown in Eq. A.6, all terms except the last term have to be concatenated. This is only done up to first order

$$\exp(:h:) = \exp\left(:\sum_{p=1}^{N} e^{:H_0(0,s_p):}H_\mathrm{p}(s_p):\right)\exp(:H_0(0,C):)\,. \tag{A.9}$$

Now, the BCH formula is used to obtain

$$h = H_0(0,C) + \left(\frac{:H_0(0,C):}{e^{:H_0(0,C):}-1}\right)\left(\sum_{p=1}^{N} e^{:H_0(0,s_p):} H_{\mathrm{p}}(s_p)\right) . \tag{A.10}$$

The terms within the sum are

$$\begin{aligned} e^{:H_0(0,s_p):} H_{\mathrm{p}}(s_p) &= -e^{:H_0(0,s_p):} \sum_{m,n=-\infty}^{\infty} c_{mn} e^{i(m\phi_x+n\phi_y)} \\ &= -\sum_{m,n=-\infty}^{\infty} c_{mn}(s_p) e^{i(m\phi_x(s_p)+n\phi_y(s_p))} e^{i(m\phi_x+n\phi_y)} . \end{aligned} \tag{A.11}$$

With that, Eq. A.10 modifies to

$$h = H_0(0,C) + \left(\frac{:H_0(0,C):}{e^{:H_0(0,C):}-1}\right)\left(-\sum_{p=1}^{N}\sum_{m,n=-\infty}^{\infty} c_{mn}(s_p) e^{i(m\phi_x(s_p)+n\phi_y(s_p))} e^{i(m\phi_x+n\phi_y)}\right) . \tag{A.12}$$

The expression in the left parentheses is now executed on the sum on the right

$$\begin{aligned} h = -\mu_x J_x - \mu_y J_y - \sum_{p=1}^{N}\sum_{m,n=-\infty}^{\infty} & c_{mn}(s_p) \frac{m\mu_x + n\mu_y}{2\sin\left(\frac{m\mu_x+n\mu_y}{2}\right)} \\ & \times \exp\left[im\left(\mu_x(s_p) - \frac{\mu_x}{2} + \phi_x\right) + in\left(\mu_y(s_p) - \frac{\mu_y}{2} + \phi_y\right)\right] \end{aligned} \tag{A.13}$$

The Hamiltonian $H = -h$ with arbitrary multipoles finally is

$$\begin{aligned} H = \mu_x J_x + \mu_y J_y + \sum_{mn} & C_{mn} \frac{m\mu_x + n\mu_y}{2\sin\left(\frac{m\mu_x+n\mu_y}{2}\right)} \\ & \times \exp\left[im\left(-\frac{\mu_x}{2} + \phi_x\right) + in\left(-\frac{\mu_y}{2} + \phi_y\right)\right] . \end{aligned} \tag{A.14}$$

The coefficients C_{mn} are obtained by summing over all elements in combination with the respective linear phase advance

$$C_{mn} = \sum_{p=1}^{N} c_{mn}(s_p) e^{i(m\phi_x(s_p)+n\phi_n(s_p))} . \tag{A.15}$$

A.2 Single octupole

In the following, the amplitude detuning resulting from an octupole in one plane is presented. For instructive purposes and for simplicity the detuning of a sextupole not shown here, since the detuning is only of second order. The respective values of the amplitude detuning by sextupoles

can be found in [24]. The Hamiltonian of an infinitesimal short octupole with the integrated strength k_3 in normalised coordinates is

$$H_{\mathrm{oct}} = \frac{k_3}{4}\beta^2\tilde{x}^4\,. \tag{A.16}$$

Assuming an octupole kick followed by a linear transfer, the one-turn Lie map reads

$$e^{:h:} = \exp\left(:-\frac{k_3}{4}\beta_x^2\tilde{x}^4:\right)\exp\left(:-\mu_x\frac{\tilde{x}^2+\tilde{p}^2}{2}:\right) \tag{A.17}$$

$$= \exp\left(:-k_3\beta_x^2J_x^2\cos^4\phi_x:\right)\exp\left(:-\mu_xJ_x:\right) \tag{A.18}$$

$$= \exp\left(:-k_3\beta_x^2J_x^2\frac{1}{8}(3+4\cos(2\phi_x)+\cos(4\phi_x)):\right)\exp\left(:-\mu_xJ_x:\right)\,. \tag{A.19}$$

The angle-independent term commutes with the linear Hamiltonian. Hence, in the limit of a small octupole perturbation, the BCH formula enables the concatenation of the Hamiltonians up to first order in the angle-dependent perturbation

$$h \approx -\mu_xJ_x - \frac{3}{8}k_3\beta_x^2J_x^2 - \frac{1}{8}k_3\beta_x^2J_x^2\frac{:-\mu_xJ_x:}{e^{:-\mu_xJ_x:}-1}(4\cos(2\phi_x)+\cos(4\phi_x)) \tag{A.20}$$

$$H \approx \mu_xJ_x + \frac{3}{8}k_3\beta_x^2J_x^2 + \frac{1}{4}k_3\beta_x^2J_x^2\left(2\mu_x\frac{\cos\left(2\phi_x-\mu_x\right)}{\sin\mu_x}+\mu_x\frac{\cos\left(4\phi_x-2\mu_x\right)}{\sin 2\mu_x}\right) \tag{A.21}$$

Hence, the amplitude detuning is on average

$$\alpha_x = \frac{3}{4}\beta_x^2k_3\,. \tag{A.22}$$

The Hamiltonian breaks down in the vicinity of the resonances and therefore has to be used

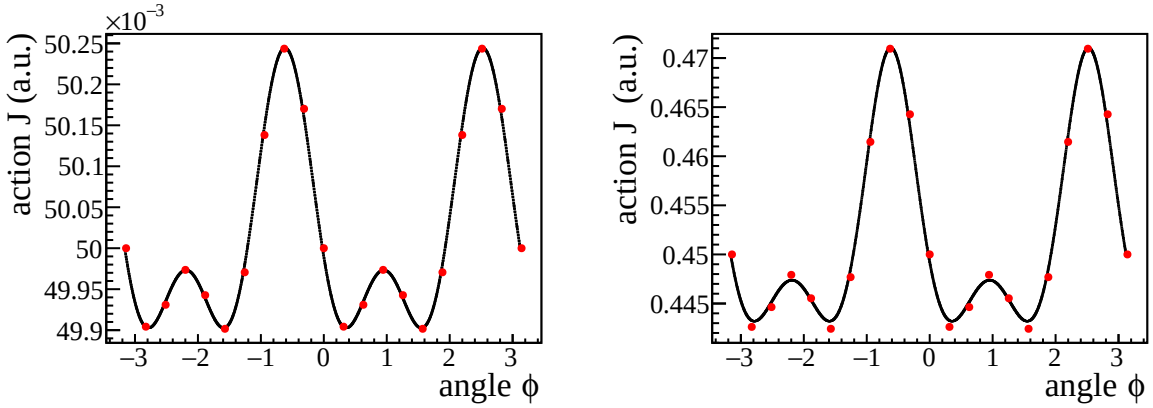

Figure A.1: Left: Comparison between tracking (black) and Hamiltonian representation (red) of a single octupole in an otherwise linear lattice. Right: The same comparison for a factor 9 larger starting action. Small deviations of the Hamiltonian from the tracked data points are observed.

cautiously and only if the tune is far from an octupole resonance. Figure A.1 gives an example of tracking versus Lie algebraic approach. The simple code assumes a single octupole kick and the tracking is performed over 2000 turns in one dimension with a natural betatron tune of $Q = 0.31$. From this example follows that the Hamiltonian acquired via Lie algebra gives excellent agreement for small initial actions, whereas smaller deviations appear for larger initial actions.

A.3 Multiple octupoles

With respect to the Taylor expansion in Eq. A.3, the Fourier coefficients are

$$c_0 = \frac{3}{8} k_3 \beta_x^2 J_x^2 \,, \qquad c_{\pm 2} = \frac{k_3}{4} \beta_x^2 J_x^2 \qquad \text{and} \qquad c_{\pm 4} = \frac{k_3}{16} \beta_x^2 J_x^2 \,. \tag{A.23}$$

With multiple octupoles at positions s_i of strength $k_3(s_p)\beta^2(s_p)$, the coefficients read

$$C_0 = \frac{3}{8} J_x^2 \sum_{p=1}^{N} k_3(s_p) \beta_x^2(s_p) \,, \tag{A.24}$$

$$C_{\pm 2} = \frac{1}{4} J_x^2 \sum_{p=1}^{N} k_3(s_p) \beta_x^2(s_p) \exp(\pm i 2 \phi_x(s_p)) \,, \tag{A.25}$$

$$C_{\pm 4} = \frac{1}{16} J_x^2 \sum_{p=1}^{N} k_3(s_p) \beta_x^2(s_p) \exp(\pm i 4 \phi_x(s_p)) \,. \tag{A.26}$$

The resulting Hamiltonian is

$$H(\phi_x, J_x) = \mu_x J_x + C_0 + C_{\pm 2} \frac{\mu_x \exp \pm (2\phi_x - \mu_x)}{\sin \mu_x} + C_{\pm 4} \frac{2\mu_x \exp \pm (4\phi_x - 2\mu_x)}{\sin 2\mu_x} \,. \tag{A.27}$$

If $k_3(s_p)\beta^2(s_p)$ is constant among all octupoles and the octupoles are uniformly distributed along the phase advance, the Hamiltonian simplifies to

$$H \approx \mu_x J_x + C_0 \,. \tag{A.28}$$

Because of this behaviour, the approximation made in Sec. 2.3.1 is valid if the non-linear elements are well separated along the linear phase advance.

APPENDIX B

Supporting figures

B.1 Supporting figures for Section 2.2.4

Figures B.1–B.6 give the results for the filling patterns that were not explicitly analysed in Sec. 2.2.4. The key parameters of the different filling patterns are listed in the Tables 2.3, 2.4 & 2.5.

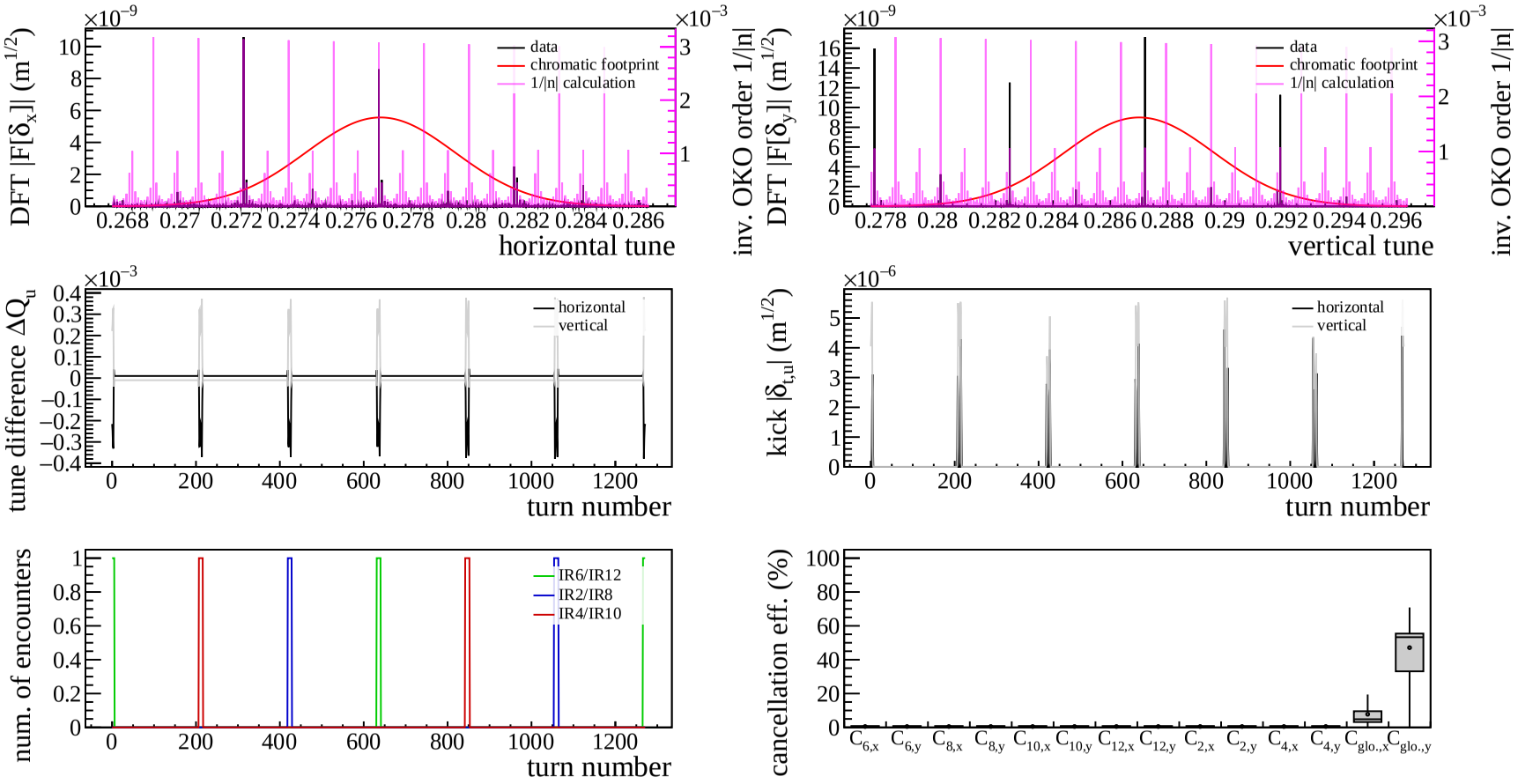

Figure B.1: Top left: Plot of the absolute DFT amplitudes in the horizontal plane $|\mathcal{F}[\delta_x]|$ (see Eq. 2.113) obtained from the IR matrices over 10^6 turns for RHIC with one deuteron bunch (R1). The magenta line indicates the $1/|n|$ approximation and the red line shows the chromatic tune footprint of the Au bunch. Top right: The absolute amplitudes of the DFT in the vertical plane $|\mathcal{F}[\delta_y]|$. Centre left: Plot of the tune shift ΔQ_u obtained from the one-turn matrix over the duration of $2T_m = 1272$ turns (constant tune offset subtracted). Centre right: Plot of the absolute kick strength $|\delta_{t,u}|$ in the vertical and horizontal plane obtained from the one-turn matrix. Bottom left: Number of beam-beam encounters in each IR. Bottom right: The cancellation efficiency of each IR in the horizontal $\mathcal{C}_{\mathrm{IR},x}$ and vertical plane $\mathcal{C}_{\mathrm{IR},y}$. The last two boxes show the global cancellation between the IRs $\mathcal{C}_{\mathrm{glo},u}$.

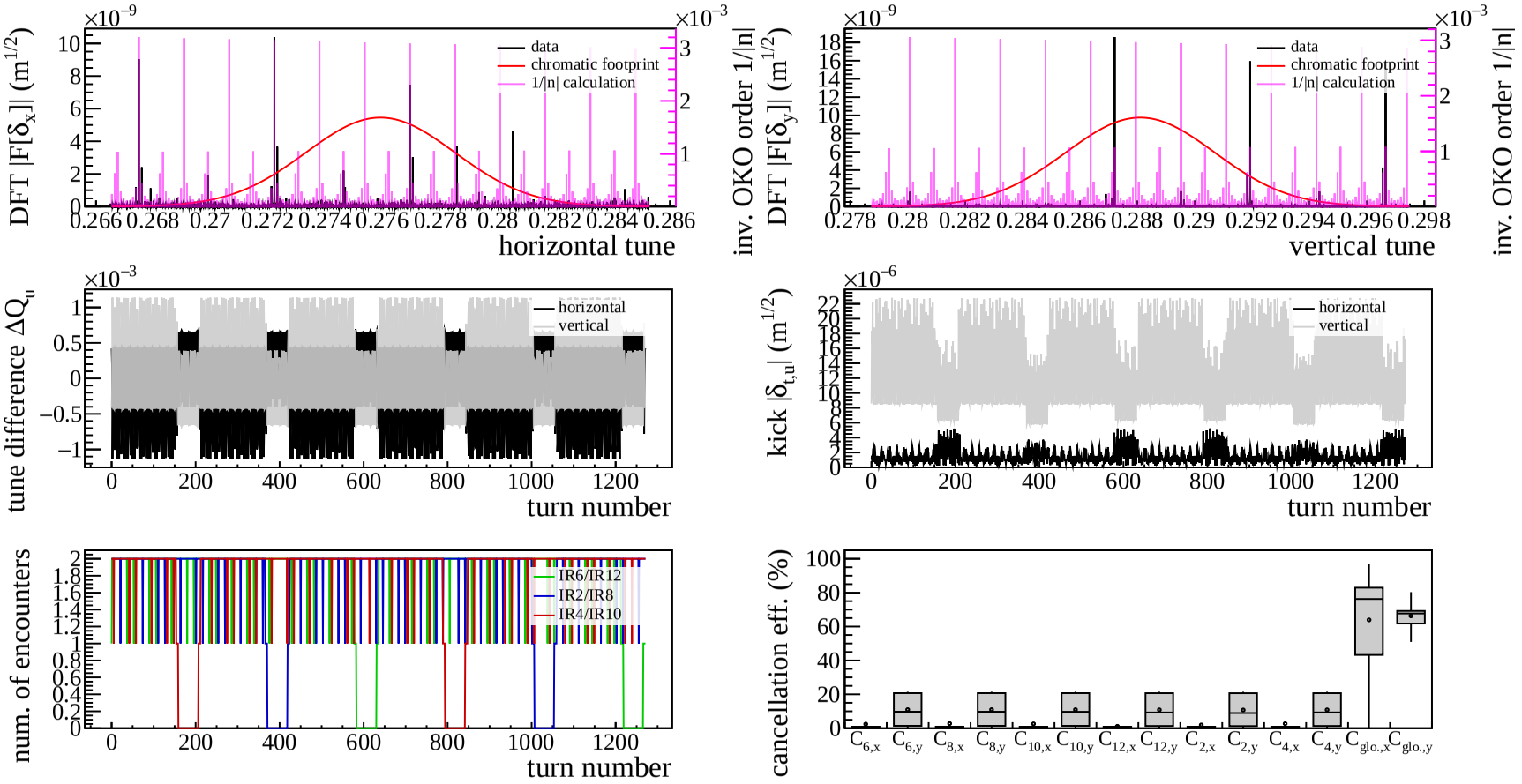

Figure B.2: Top left: Plot of the absolute DFT amplitudes in the horizontal plane $|\mathcal{F}[\delta_x]|$ obtained from the IR matrices over 10^6 turns for RHIC with 110 deuteron bunches (R3). The magenta line indicates the $1/|n|$ approximation and the red line shows the chromatic tune footprint of the Au bunch. Top right: The absolute amplitudes of the DFT in the vertical plane $|\mathcal{F}[\delta_y]|$. Centre left: Plot of the tune shift ΔQ_u obtained from the one-turn matrix over the duration of $2T_m = 1272$ turns (constant tune offset subtracted). Centre right: Plot of the absolute kick strength $|\delta_{t,u}|$ in the vertical and horizontal plane obtained from the one-turn matrix. Bottom left: Number of beam-beam encounters in each IR. Bottom right: The cancellation efficiency of each IR in the horizontal $\mathcal{C}_{\mathrm{IR},x}$ and vertical plane $\mathcal{C}_{\mathrm{IR},y}$. The last two boxes show the global cancellation between the IRs $\mathcal{C}_{\mathrm{glo},u}$.

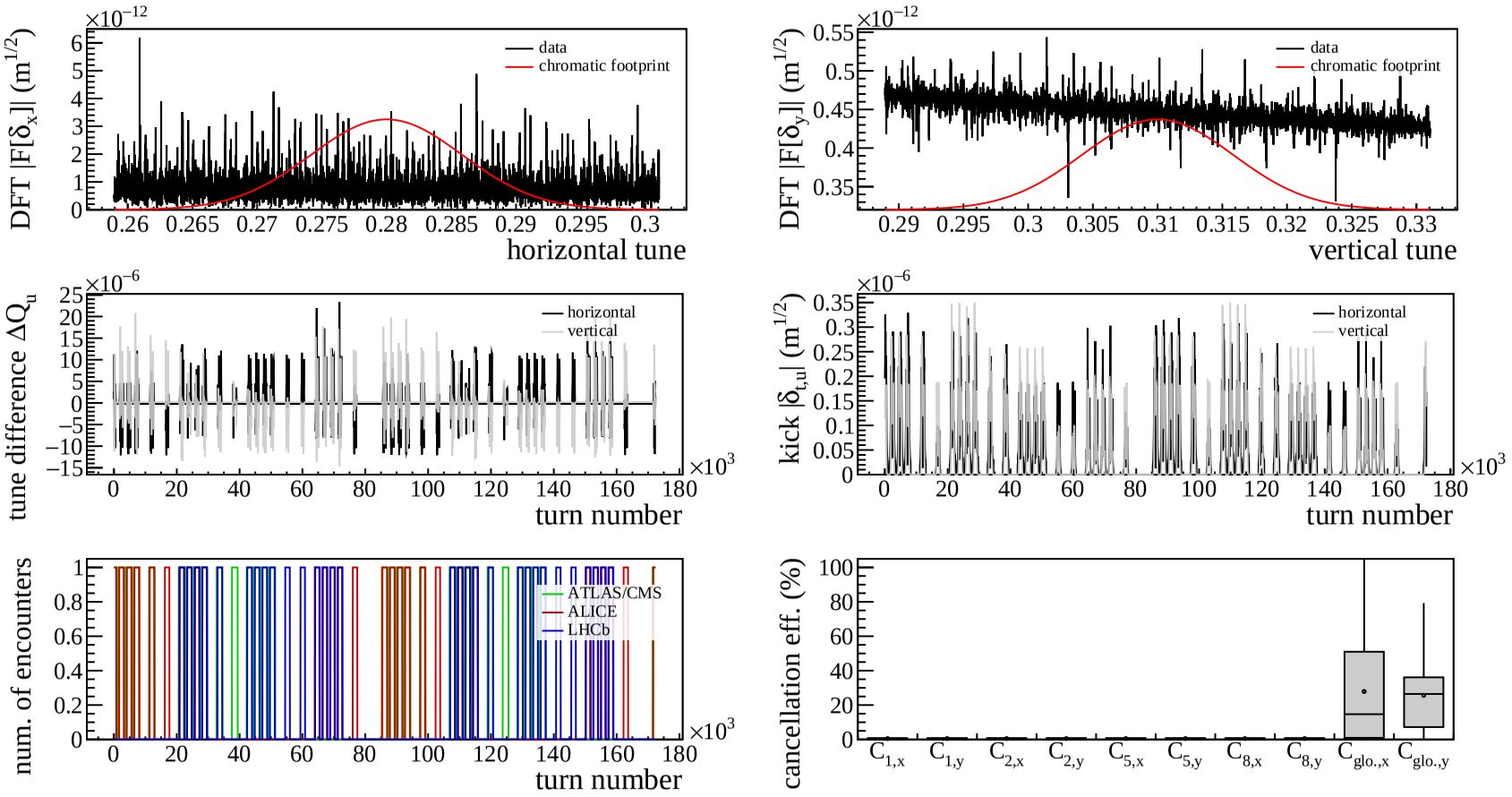

Figure B.3: Top left: Plot of the absolute DFT amplitudes in the horizontal plane $|\mathcal{F}[\delta_x]|$ obtained from the IR matrices over 2×10^5 turns for the LHC for the filling pattern L1 (2012 pilot filling pattern). The red line indicates the chromatic tune footprint of the Pb bunch. Top right: The absolute amplitudes of the DFT in the vertical plane $|\mathcal{F}[\delta_y]|$. Centre left: Plot of the tune shift ΔQ_u obtained from the one-turn matrix over the duration of $2T_m$ turns (constant tune offset subtracted). Centre right: Plot of the absolute kick strength $|\delta_{t,u}|$ in the vertical and horizontal plane obtained from the one-turn matrix. Bottom left: Number of beam-beam encounters in each IR. Bottom right: The cancellation efficiency of each IR in the horizontal $\mathcal{C}_{\mathrm{IR},x}$ and vertical plane $\mathcal{C}_{\mathrm{IR},y}$. The last two boxes show the global cancellation between the IRs $\mathcal{C}_{\mathrm{glo},u}$.

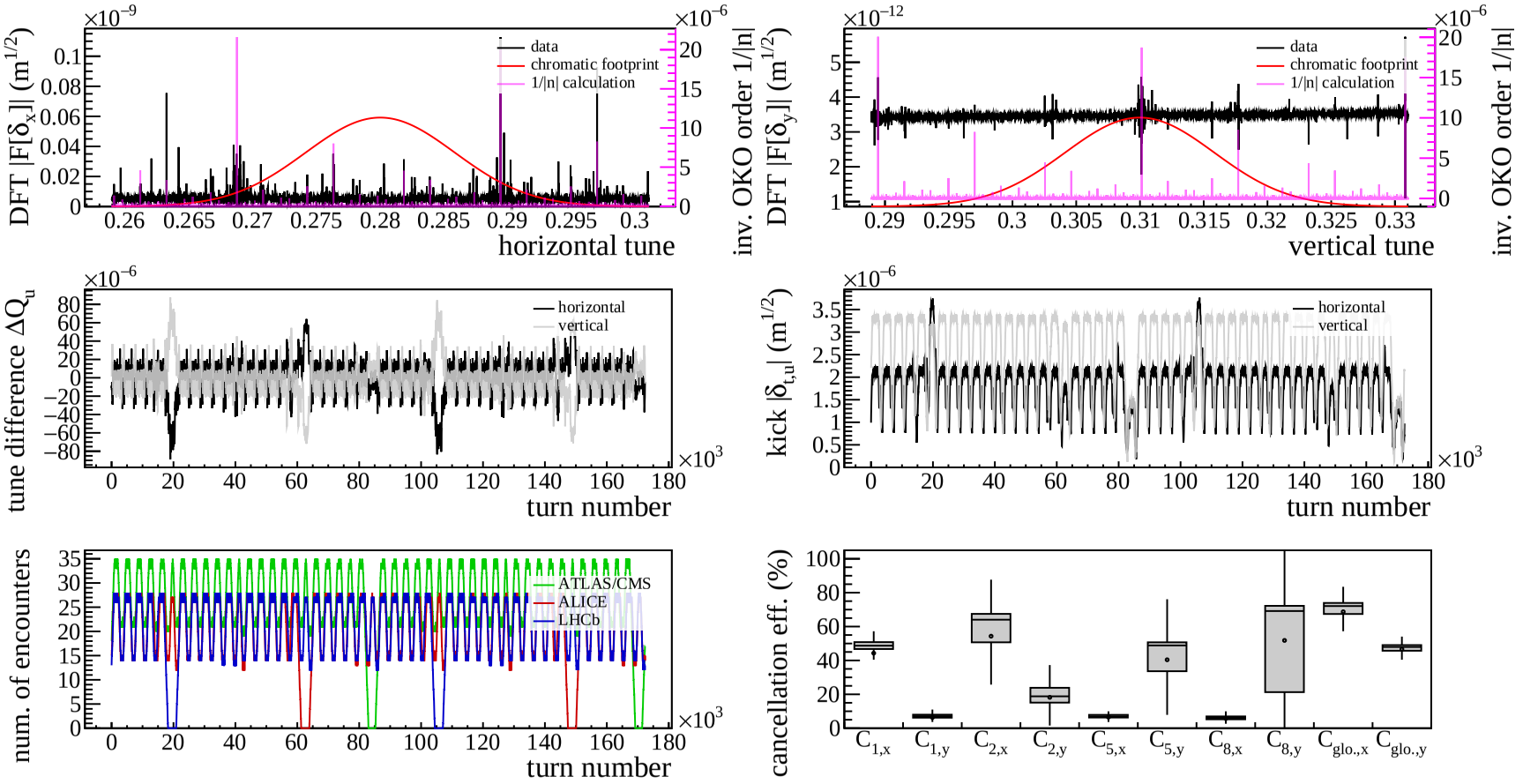

Figure B.4: Top left: Plot of the absolute DFT amplitudes in the horizontal plane $|\mathcal{F}[\delta_x]|$ obtained from the IR matrices over 2×10^5 turns for the LHC with the HL-LHC filling pattern L3. The magenta line indicates the $1/|n|$ approximation and the red line shows the chromatic tune footprint of the Pb bunch. Top right: The absolute amplitudes of the DFT in the vertical plane $|\mathcal{F}[\delta_y]|$. Centre left: Plot of the tune shift ΔQ_u obtained from the one-turn matrix over the duration of $2T_m$ turns (constant tune offset subtracted). Centre right: Plot of the absolute kick strength $|\delta_{t,u}|$ in the vertical and horizontal plane obtained from the one-turn matrix. Bottom left: Number of beam-beam encounters in each IR. Bottom right: The cancellation efficiency of each IR in the horizontal $\mathcal{C}_{\mathrm{IR},x}$ and vertical plane $\mathcal{C}_{\mathrm{IR},y}$. The last two boxes show the global cancellation between the IRs $\mathcal{C}_{\mathrm{glo},u}$.

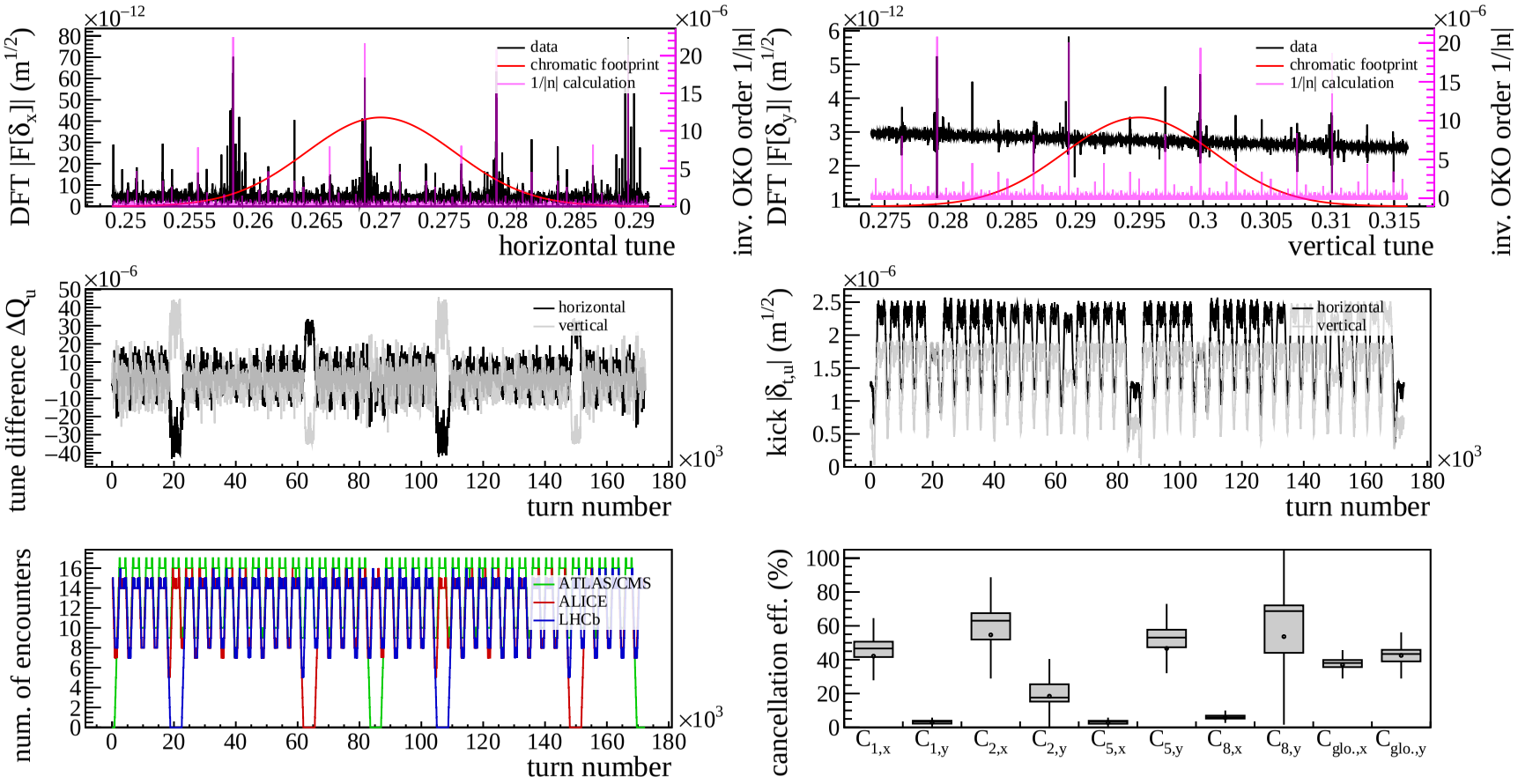

Figure B.5: Top left: Plot of the absolute DFT amplitudes in the horizontal plane $|\mathcal{F}[\delta_x]|$ obtained from the IR matrices over 2×10^5 turns for the HL-LHC and the nominal LHC filling pattern L2. The magenta line indicates the $1/|n|$ approximation and the red line shows the chromatic tune footprint of the Pb bunch. Top right: The absolute amplitudes of the DFT in the vertical plane $|\mathcal{F}[\delta_y]|$. Centre left: Plot of the tune shift ΔQ_u obtained from the one-turn matrix over the duration of $2T_m$ turns (constant tune offset subtracted). Centre right: Plot of the absolute kick strength $|\delta_{t,u}|$ in the vertical and horizontal plane obtained from the one-turn matrix. Bottom left: Number of beam-beam encounters in each IR. Bottom right: The cancellation efficiency of each IR in the horizontal $\mathcal{C}_{\mathrm{IR},x}$ and vertical plane $\mathcal{C}_{\mathrm{IR},y}$. The last two boxes show the global cancellation between the IRs $\mathcal{C}_{\mathrm{glo},u}$.

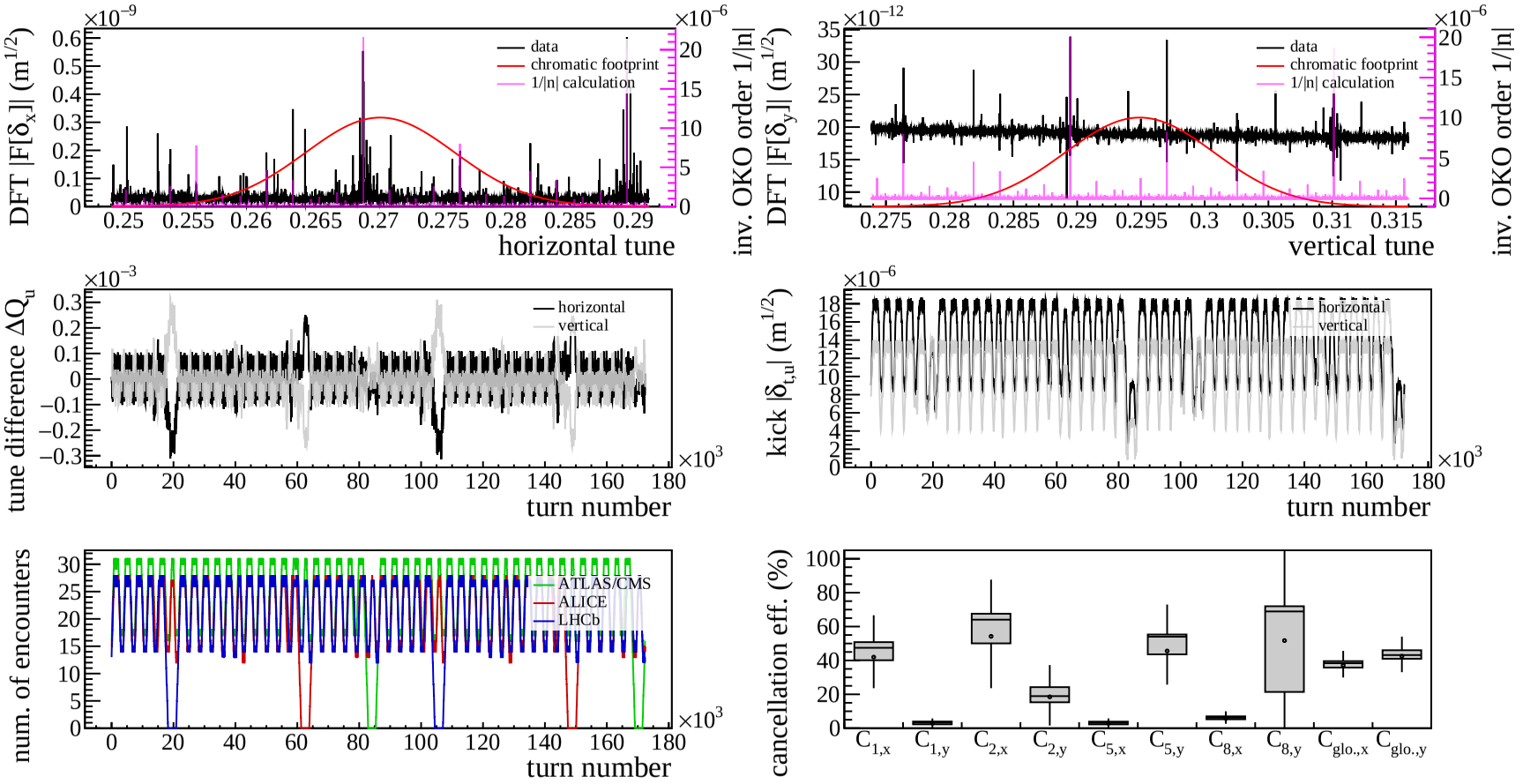

Figure B.6: Top left: Plot of the absolute DFT amplitudes in the horizontal plane $|\mathcal{F}[\delta_x]|$ obtained from the IR matrices over 2×10^5 turns for the HL-LHC for filling pattern L3 with $N_b = 1.15 \times 10^{11}$ protons per bunch. The magenta line indicates the $1/|n|$ approximation and the red line shows the chromatic tune footprint of the Pb bunch. Top right: The absolute amplitudes of the DFT in the vertical plane $|\mathcal{F}[\delta_y]|$. Centre left: Plot of the tune shift ΔQ_u obtained from the one-turn matrix over the duration of $2T_m$ turns (constant tune offset subtracted). Centre right: Plot of the absolute kick strength $|\delta_{t,u}|$ in the vertical and horizontal plane obtained from the one-turn matrix. Bottom left: Number of beam-beam encounters in each IR. Bottom right: The cancellation efficiency of each IR in the horizontal $\mathcal{C}_{\mathrm{IR},x}$ and vertical plane $\mathcal{C}_{\mathrm{IR},y}$. The last two boxes show the global cancellation between the IRs $\mathcal{C}_{\mathrm{glo},u}$.

B.2 Supporting figures for Section 2.3.2

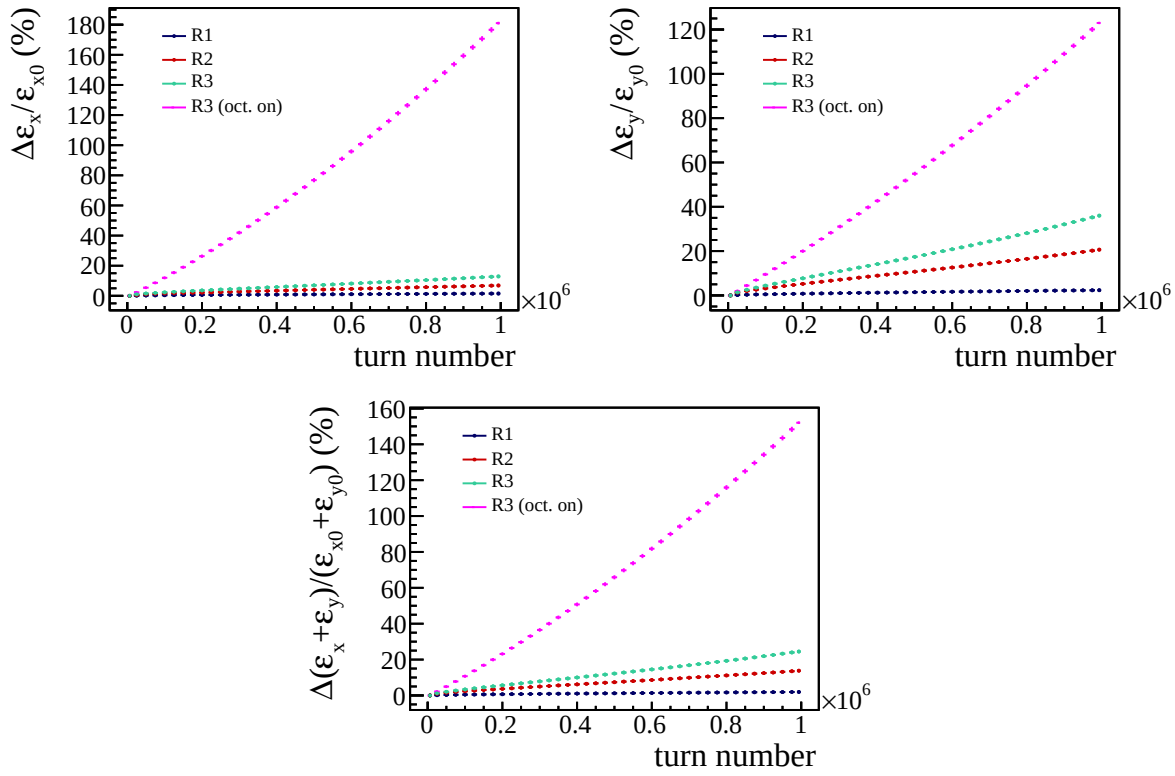

Figure B.7: Top left: Evolution of the relative horizontal emittance change in RHIC over 10^6 turns for the four simulation scenarios without collimation (infinite aperture). Top right: Evolution of the relative change of the vertical emittance. Bottom: Evolution of the relative change of the sum of the transverse emittances.

B.3 Supporting figures for Section 3.3

The Figures B.8–B.11 give the frequency maps for the Pb beam in Pb-p collisions at $E_b = 4Z$ TeV for different beam size ratios between the Pb beam and the proton beam in support of the analogous analysis at $E_b = 6.5Z$ TeV in Sec. 3.3. The detuning by the octupoles is given in Eq. 3.13, i.e., the octupole current is $I_{\mathrm{oct}} = 116$ A. The IP settings are listed in Tab. 4.5 and the bunch parameters are listed in Tab. 3.1. The conclusions for $E_b = 4Z$ TeV and $E_b = 6.5Z$ TeV are the same in the sense that no significant diffusion in neither the bunch core nor in the bunch tails (large transverse actions) is observed in the simplified model presented in Sec. 3.1.1.

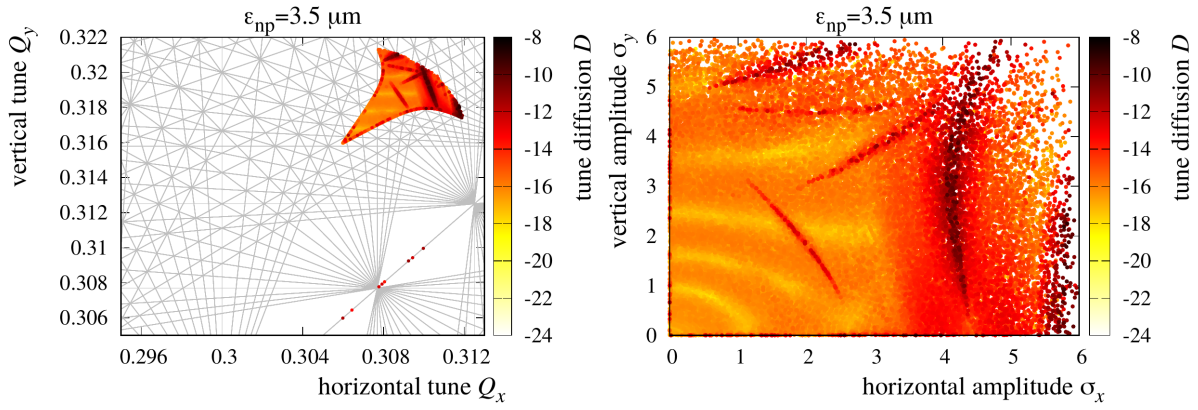

Figure B.8: Left: Frequency map of the Pb beam at $E_b = 4Z$ TeV with proton emittances of $\varepsilon_{np} = 3.5\,\mu$m ($\hat{r} \approx 1.1$). Resonance lines up to 20th order are given in grey. Right: Plot of the initial absolute transverse amplitudes in units of the beam size.

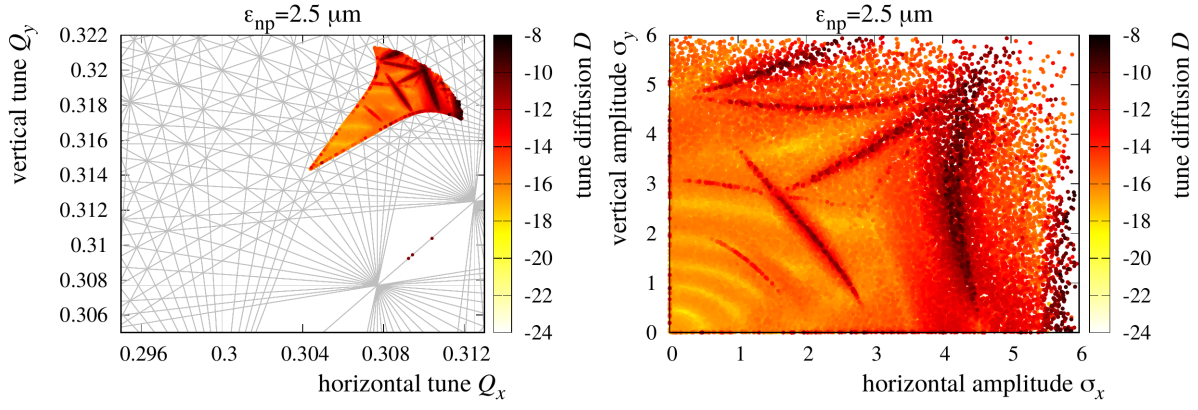

Figure B.9: Left: Frequency map of the Pb beam at $E_b = 4Z$ TeV with proton emittances of $\varepsilon_{np} = 2.5\,\mu$m ($\hat{r} \approx 1.3$). Resonance lines up to 20th order are given in grey. Right: Plot of the absolute transverse amplitudes. No significant tune diffusion is close to the bunch core.

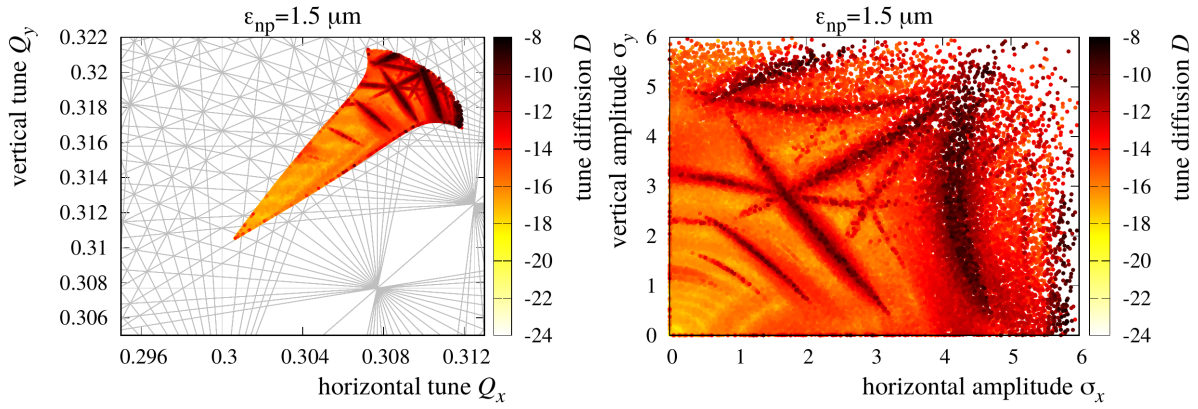

Figure B.10: Left: Frequency map of the Pb beam at $E_b = 4Z\,\mathrm{TeV}$ with proton emittances of $\varepsilon_{np} = 1.5\,\mu\mathrm{m}$ ($\hat{r} \approx 1.7$). Resonance lines up to 20th order are given in grey. Right: Plot of the absolute transverse amplitudes. The bunch core is not effected by any noteworthy diffusion.

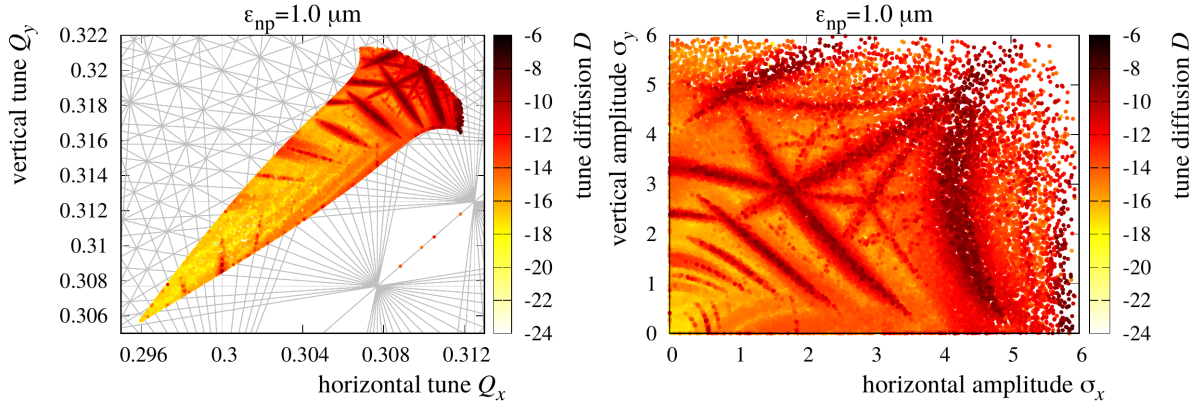

Figure B.11: Left: Frequency map of the Pb beam at $E_b = 4Z\,\mathrm{TeV}$ with proton emittances of $\varepsilon_{np} = 1.0\,\mu\mathrm{m}$ ($\hat{r} \approx 2.1$). Resonance lines up to 20th order are given in grey. Right: Plot of the initial absolute transverse amplitudes.

Bibliography

[1] O. S. Brüning, J. Poole, P. Collier, P. Lebrun, R. Ostojic, S. Myers and P. Proudlock (editors), *LHC design report: Vol. 1 the LHC main ring*, Report CERN-2004-003-V-1, CERN, Switzerland (2004), doi:10.5170/cern-2004-003-v-1.

[2] R. Alemany et al., *p-Pb feasibility test and modifications of LHC sequence and interlocking*, Report CERN-ATS-Note-2012-052 MD, CERN, Switzerland (2012), URL: https://cds.cern.ch/record/1459553.

[3] R. Alemany et al., *First proton-nucleus collisions in the LHC: the p-Pb pilot physics fill*, Report CERN-ATS-Note-2012-094 MD, CERN, Switzerland (2012), URL: https://cds.cern.ch/record/1496101.

[4] J. M. Jowett et al., *Proton-nucleus collisions in the LHC*, in Proceedings of the 4th International Particle Accelerator Conference (IPAC'13), MOODB201, Shanghai, China (2013), URL: http://cds.cern.ch/record/1572994.

[5] J. M. Jowett et al., *The 2016 proton-nucleus run of the LHC*, in Proceedings of the 8th International Particle Accelerator Conference (IPAC'17), TUPVA014, Copenhagen, Denmark (2017), doi:10.18429/jacow-ipac2017-tupva014.

[6] J. Gourber, H. Hereward and S. Myers, *Overlap knock-out resonances at the CERN Intersecting Storage Rings (ISR)*, in Proceedings of the International Conference on Particle Accelerators (PAC'77), 1405, Chicago, USA (1977), URL: https://accelconf.web.cern.ch/AccelConf/p77/PDF/PAC1977_1405.PDF.

[7] S. Myers, *Overlap knock-out resonances with colliding bunched beams in the CERN ISR*, IEEE Transactions on Nuclear Science, **24**, 1405 (1979), doi:10.1109/TNS.1979.4330104.

[8] T. Satogata et al., *Commissioning of RHIC deuteron-gold collisions*, in Proceedings of the International Conference on Particle Accelerators (PAC'03), Portland, USA (2003), doi:10.1109/PAC.2003.1288643.

[9] M. A. Jebramcik and J. M. Jowett, *Moving long-range beam-beam encounters in heavy-ion colliders*, in Proceedings of the 10th International Particle Accelerator Conference (IPAC'19), MOPMP025, Melbourne, Australia (2019), doi:10.18429/jacow-ipac2019-mopmp025.

[10] W. Fischer, *RHIC with asymmetric ion beams*, presentation at workshop on feasibility of p-Pb in the LHC 24.08.2011, CERN, Switzerland (2011).

[11] R. Brinkmann and F. Willeke, *First experience with colliding electron-proton beams in HERA*, in Proceedings of the International Conference on Particle Accelerators (PAC'93), 3742, Washington DC, USA (1993), doi:10.1109/PAC.1993.309774.

[12] K. Cornelis, M. Meddahi and R. Schmidt, *The beam-beam effect in the SPS proton antiproton collider for beams with unequal emittances*, Report CERN-SL-90-73-AP, CERN, Switzerland (1990), URL: https://cds.cern.ch/record/210225.

[13] R. Alemany-Fernández et al., *Performance of the CERN injector chain complex and transmission studies into the LHC during the second proton-lead run*, in Proceedings of the 8th International Particle Accelerator Conference (IPAC'17), TUPVA128, Copenhagen, Denmark (2017), doi:10.18429/JACoW-IPAC2017-TUPVA128.

[14] W. Fischer et al., *Measurement of the total cross section of uranium-uranium collisions at* $\sqrt{s_{\mathrm{NN}}} = 192.8$ *GeV*, Physical Review C, **89**, 014906 (2014), doi:10.1103/PhysRevC.89.014906.

[15] W. Fischer, A. Baltz, M. Blaskiewicz, D. Gassner, K. Drees, Y. Luo, M. Minty and P. Thieberger, *Measurement of the total cross section of gold-gold collisions at* $\sqrt{s_{\mathrm{NN}}} = 200$ *GeV*, in Proceedings of the 7th International Particle Accelerator Conference (IPAC'16), TUPMW039, Busan, Korea (2016), doi:10.18429/JACoW-IPAC2016-TUPMW039.

[16] C. Loizides, J. Kamin and D. d'Enterria, *Improved Monte Carlo Glauber predictions at present and future nuclear colliders*, Physical Review C, **97**, 054910 (2018), doi:10.1103/physrevc.97.054910.

[17] Z. Citron et al., *Future physics opportunities for high-density QCD at the LHC with heavy-ion and proton beams*, Report CERN-LPCC-2018-07, CERN, Switzerland (2019), URL: https://arxiv.org/abs/1812.06772.

[18] M. A. Jebramcik and J. M. Jowett, *Prospects for future asymmetric collisions in the LHC*, Journal of Physics: Conference Series, **1350**, 012003 (2019), doi:10.1088/1742-6596/1350/1/012003.

[19] J. Coupard et al., *LHC Injectors Upgrade, technical design report, Vol. II: ions*, Report CERN-ACC-2016-0041, Geneva, Switzerland (2016), URL: https://cds.cern.ch/record/2153863.

[20] T. Argyropoulos, T. Bohl, A. Lasheen, G. Papotti, D. Quartullo and E. Shaposhnikova, *Momentum slip-stacking in CERN SPS for the ion beams*, in Proceedings of the 10th International Particle Accelerator Conference (IPAC'19), WEPTS039, Melbourne, Australia (2019), doi:10.18429/jacow-ipac2019-wepts039.

[21] M. Martinella, C. Bahamonde Castro, A. Lechner, S. Danzeca, Y. Kadi, M. Brugger and R. Garcia Alia, *Radiation levels in the LHC during the 2015 Pb-Pb and 2016 p-Pb run and mitigation strategy for the electronic systems during HL-LHC operation*, Report CERN-ACC-NOTE-2018-073, CERN, Switzerland (2018), URL: https://cds.cern.ch/record/2647363.

[22] K. Wille, The physics of particle accelerators: an introduction, Oxford University Press (2000), URL: https://cds.cern.ch/record/560708.

[23] H. Wiedemann, Particle accelerator physics, 4th ed., Springer (1993), doi:10.1007/978-3-319-18317-6.

[24] S. Y. Lee, Accelerator physics, 3rd ed., World Scientific Press (2011), doi:10.1142/8335.

[25] CERN, *Report on the design study of Intersecting Storage Rings (ISR) for the CERN Proton Synchrotron*, Report CERN/0542, CERN, Switzerland (1964), URL: https://cds.cern.ch/record/19618.

[26] Brookhaven National Laboratory, *Conceptual design of the Relativistic Heavy Ion Collider (RHIC)*, Report BNL-51932, BNL, USA (1986), URL: https://cds.cern.ch/record/108613.

[27] ATLAS Collaboration, *Observation of a new particle in the search for the Standard Model Higgs boson with the ATLAS detector at the LHC*, Physics Letters B, **716**, 1 (2012), doi:10.1016/j.physletb.2012.08.020.

[28] CMS Collaboration, *Observation of a new boson at a mass of 125 GeV with the CMS experiment at the LHC*, Physics Letters B, **716**, 30 (2012), doi:10.1016/j.physletb.2012.08.021.

[29] BRAHMS Collaboration, *Quark gluon plasma and color glass condensate at RHIC? The perspective from the BRAHMS experiment*, Nuclear Physics A, **757**, 1 (2005), doi:10.1016/j.nuclphysa.2005.02.130.

[30] PHOBOS Collaboration, *The PHOBOS perspective on discoveries at RHIC*, Nuclear Physics A, **757**, 28 (2005), doi:10.1016/j.nuclphysa.2005.03.084.

[31] STAR Collaboration, *Experimental and theoretical challenges in the search for the quark gluon plasma: the STAR Collaboration's critical assessment of the evidence from RHIC collisions*, Nuclear Physics A, **757**, 102 (2005), doi:10.1016/j.nuclphysa.2005.03.085.

[32] PHENIX Collaboration, *Formation of dense partonic matter in relativistic nucleus-nucleus collisions at RHIC: experimental evaluation by the PHENIX Collaboration*, Nuclear Physics A, **757**, 184 (2005), doi:10.1016/j.nuclphysa.2005.03.086.

[33] ALICE Collaboration, *J/Ψ suppression at forward rapidity in Pb-Pb collisions at $\sqrt{s_{\mathrm{NN}}} = 2.76$ TeV*, Physical Review Letters, **109** (2012), doi:10.1103/PhysRevLett.109.072301.

[34] ATLAS Collaboration, *Observation of a centrality-dependent dijet asymmetry in lead-lead collisions at $\sqrt{s_{\mathrm{NN}}} = 2.76$ TeV with the ATLAS detector at the LHC*, Physical Review Letters, **105** (2010), doi:10.1103/PhysRevLett.105.252303.

[35] CMS Collaboration, *Observation and studies of jet quenching in PbPb collisions at $\sqrt{s_{\mathrm{NN}}} = 2.76$ TeV*, Physical Review C, **84**, 024906 (2011), doi:10.1103/PhysRevC.84.024906.

[36] C. A. Salgado et al., *Proton-nucleus collisions at the LHC: scientific opportunities and requirements*, Journal of Physics G, **39**, 015010 (2011), doi:10.1088/0954-3899/39/1/015010.

[37] ATLAS Collaboration, *Evidence for light-by-light scattering in heavy-ion collisions with the ATLAS detector at the LHC*, Nature Physics, **13**, 852 (2017), doi:10.1038/nphys4208.

[38] CERN, *LEP design report: Vol.2 the LEP main ring*, Report CERN-LEP-84-01, CERN, Switzerland (1984), URL: https://cds.cern.ch/record/102083.

[39] ATLAS Collaboration, *The ATLAS experiment at the CERN Large Hadron Collider*, Journal of Instrumentation, **3**, S08003 (2008), doi:10.1088/1748-0221/3/08/s08003.

[40] ALICE Collaboration, *The ALICE experiment at the CERN LHC*, Journal of Instrumentation, **3**, S08002 (2008), doi:10.1088/1748-0221/3/08/s08002.

[41] CMS Collaboration, *The CMS experiment at the CERN LHC*, Journal of Instrumentation, **3**, S08004 (2008), doi:10.1088/1748-0221/3/08/s08004.

[42] LHCb Collaboration, *The LHCb detector at the LHC*, Journal of Instrumentation, **3**, S08005 (2008), doi:10.1088/1748-0221/3/08/s08005.

[43] J. M. Jowett et al., *First run of the LHC as a heavy-ion collider*, in Proceedings of the 2nd International Particle Accelerator Conference (IPAC'11), 1837, San Sebastian, Spain (2011), URL: http://cds.cern.ch/record/1382049.

[44] D. Manglunki et al., *Performance of the CERN heavy ion production complex*, in Proceedings of the 3rd International Particle Accelerator Conference (IPAC'12), THPPP012, New Orleans, USA (2012), URL: https://cds.cern.ch/record/1459464.

[45] J. M. Jowett et al., *The 2015 heavy-ion run of the LHC*, in Proceedings of the 6th International Particle Accelerator Conference (IPAC'16), TUPMW027, Busan, Korea (2016), doi:10.18429/jacow-ipac2016-tupmw027.

[46] J. M. Jowett et al., *The 2018 heavy-ion run of the LHC*, in Proceedings of the 10th International Particle Accelerator Conference (IPAC'19), WEYYPLM2, Melbourne, Australia (2019), doi:10.18429/JACoW-IPAC2019-WEYYPLM2.

[47] M. Schaumann et al., *First Xe-Xe collisions in the LHC*, in Proceedings of the 9th International Particle Accelerator Conference (IPAC'18), MOPMF039, Vancouver, Canada (2018), doi:10.18429/JACoW-IPAC2018-MOPMF039.

[48] M. Schaumann et al., *First partially stripped ions in the LHC ($^{208}Pb^{81+}$)*, in Proceedings of the 10th International Particle Accelerator Conference (IPAC'19), MOPRB055, Melbourne, Australia (2019), doi:10.18429/jacow-ipac2019-moprb055.

[49] CERN, CERN Document Server, URL: https://cds.cern.ch/record/40524.

[50] CERN, CERN Document Server, URL: https://cds.cern.ch/record/2197559.

[51] J.-P. Burnet et al., *Fifty years of the CERN Proton Synchrotron: Volume 1*, Report CERN-2011-004, CERN, Switzerland (2011), doi:10.5170/CERN-2011-004.

[52] J. M. Jowett, B. Auchmann, C. Bahamonde Castro, M. Kalliokoski, A. Lechner, T. Mertens, M. Schaumann and C. Xu, *Bound-free pair production in LHC Pb-Pb operation at $6.37Z$ TeV per Beam*, in Proceedings of the 7th International Particle Acceler-

ator Conference (IPAC'16), TUPMW028, Busan, Korea (2016), doi:10.18429/JACoW-IPAC2016-TUPMW028.

[53] J. M. Jowett and C. Carli, *The LHC as a proton-nucleus collider*, in Proceedings of the 10th European Particle Accelerator Conference (EPAC'06), MOPLS009, Edinburgh, Scotland (2006), URL: http://cds.cern.ch/record/972349.

[54] B. Goddard, E. Carlier, L. Ducimetière, G. Kotzian, J. Uythoven and F. Velotti, *SPS injection and beam quality for LHC heavy ions with* 150 *ns kicker rise time*, in Proceedings of the 7th International Particle Accelerator Conference (IPAC'16), TUPMR048 (2016), doi:10.18429/JACoW-IPAC2016-TUPMR048.

[55] J. M. Jowett, *Colliding heavy ions in the LHC*, in Proceedings of the 9th International Particle Accelerator Conference (IPAC'18), TUXGBD2, Vancouver, Canada (2018), doi:10.18429/jacow-ipac2018-tuxgbd2.

[56] R. Bruce, J. M. Jowett, M. Blaskiewicz and W. Fischer, *Time evolution of the luminosity of colliding heavy-ion beams in BNL Relativistic Heavy Ion Collider and CERN Large Hadron Collider*, Physical Review Special Topics - Accelerators and Beams, **13**, 091001 (2010), doi:10.1103/physrevstab.13.091001.

[57] D. Manglunki et al., *The first LHC p-Pb run: performance of the heavy ion production complex*, in Proceedings of the 4th International Particle Accelerator Conference (IPAC'13), 2648, Shanghai, China (2013), URL: https://cds.cern.ch/record/1568545.

[58] J. M. Jowett, *HL-LHC beam parameters for ions*, presentation at the LHC performance workshop 25.01.2017, Chamonix, France (2017), URL: https://indico.cern.ch/event/580313/.

[59] G. Apollinari (ed.) et al., *High-Luminosity Large Hadron Collider (HL-LHC): technical design report V. 0.1*, Report CERN-2017-007-M, CERN, Switzerland (2017), doi:10.23731/CYRM-2017-004.

[60] F. E. Mills, *Stability of phase oscillations under two applied frequencies*, Report BNL-15936, BNL, USA (1971), URL: http://inspirehep.net/record/1249494/.

[61] D. Boussard and Y. Mizumachi, *Production of beams with high line-density by azimuthal combination of bunches in a synchrotron*, IEEE Transactions on Nuclear Science, **26**, 3623 (1979), doi:10.1109/tns.1979.4330122.

[62] G. Dome, *The SPS acceleration system travelling wave drift-tube structure for the CERN SPS*, Report CERN-SPS-ARF-77-11, CERN, Switzerland (1977), URL: https://cds.cern.ch/record/319440.

[63] Brookhaven National Laboratory, Low-energy RHIC electron cooler (LEReC), White Paper, BNL (2013), URL: https://www.c-ad.bnl.gov/esfd/LE_RHICeCooling_Project/WhitePaper/9_19_13_LEReC_white_paper.pdf.

[64] Brookhaven National Laboratory, *RHIC run overview*, webpage, URL: https://www.agsrhichome.bnl.gov/RHIC/Runs/.

[65] A. Drees, private communication (2019).

[66] W. Fischer et al., *Operational head-on beam-beam compensation with electron lenses in the Relativistic Heavy Ion Collider*, Physical Review Letters, **115**, 264801 (2017), doi:10.1103/PhysRevLett.115.264801.

[67] W. Fischer et al., *Compensation of head-on beam-beam induced resonance driving terms and tune spread in the Relativistic Heavy Ion Collider*, Physical Review Accelerators and Beams, **20**, 091001 (2017), doi:10.1103/PhysRevAccelBeams.20.091001.

[68] M. Blaskiewicz and J. M. Brennan, *Bunched beam stochastic cooling in a collider*, Physical Review Special Topics - Accelerators and Beams, **10**, 061001 (2007), doi:10.1103/physrevstab.10.061001.

[69] M. Blaskiewicz, J. M. Brennan and F. Severino, *Operational stochastic cooling in the Relativistic Heavy-Ion Collider*, Physical Review Letters, **100**, 174802 (2008), doi:10.1103/physrevlett.100.174802.

[70] M. Blaskiewicz, J. M. Brennan and K. Mernick, *Three-dimensional stochastic cooling in the Relativistic Heavy Ion Collider*, Physical Review Letters, **105**, 094801 (2010), doi:10.1103/physrevlett.105.094801.

[71] X. Gu et al., *RHIC Au-Au Operation at 100 GeV in Run 16*, in Proceedings of the North American Particle Accelerator Conference 2016 (NAPAC'16), Chicago, USA (2017), doi:10.18429/jacow-napac2016-mob3co03.

[72] M. Anerella et al., *The RHIC magnet system*, Nuclear Instruments and Methods in Physics Research Section A, **499**, 280 (2003), doi:10.1016/s0168-9002(02)01940-x.

[73] W. W. MacKay et al., *Spin dynamics in AGS and RHIC*, in in Proceedings of the Particle Accelerator Conference 2003, WOAB008 (2003), URL: http://accelconf.web.cern.ch/accelconf/p03/PAPERS/WOAB008.PDF.

[74] C. Liu et al., *RHIC operations with asymmetric collisions in 2015*, Report BNL-108367-2015-IR, BNL, USA (2015), URL: https://www.rhichome.bnl.gov/RHIC/Runs/RhicRun15pA2.pdf.

[75] C. Liu et al., *RHIC operation with asymmetric collisions in 2015*, in Proceedings of the 7th International Particle Accelerator Conference (IPAC'16), TUPMW038, Busan, Korea (2016), doi:10.18429/JACoW-IPAC2016-TUPMW038.

[76] C. Liu et al., *Attempt to accelerate with unequal revolution frequencies in RHIC*, Report BNL-108493-2015-IR, BNL, USA (2015), URL: https://www.bnl.gov/isd/documents/89396.pdf.

[77] C. Liu, private communication (2019).

[78] C. Liu, *Preparations for p-Au run in 2015*, Report BNL-107377-2014-IR, BNL, USA (2014), doi:10.2172/1169564.

[79] European Particle Physics Strategy Update, webpage (2019), URL: https://europeanstrategyupdate.web.cern.ch/open-symposium.

[80] M. Benedikt et al., *Future Circular Collider, Vol. 2 : the lepton collider (FCC-ee)*, Report CERN-ACC-2018-0057, CERN, Switzerland (2018), URL: https://cds.cern.ch/record/2651299.

[81] M. Benedikt et al., *Future Circular Collider,Vol. 3 : the hadron collider (FCC-hh)*, Report CERN-ACC-2018-0058, CERN, Switzerland (2018), URL: https://cds.cern.ch/record/2651300.

[82] M. Schaumann, Heavy-ion performance of the LHC and future colliders, PhD thesis, RWTH Aachen University, Germany (2015), URL: https://cds.cern.ch/record/2065692.

[83] M. Schaumann, *Potential performance for Pb-Pb,p-Pb, and p-p collisions in a future circular collider*, Physical Review Special Topics - Accelerators and Beams, **18**, 091002 (2015), doi:10.1103/physrevstab.18.091002.

[84] R. Versteegen, *Chromatic effects and their correction in off-momentum operation of the LHC for p-Pb collisions*, Report CERN-ATS-Note-2012-102 PERF, CERN, Switzerland (2012), URL: http://cds.cern.ch/record/1500104.

[85] R. Versteegen et al., *Operating the LHC off-momentum for p-Pb collisions*, in Proceedings of the 4th International Particle Accelerator Conference (IPAC'13), TUPFI0421, Shanghai, China (2013), URL: http://cds.cern.ch/record/1594244.

[86] R. Tomás, O. Brüning, M. Giovannozzi, P. Hagen, M. Lamont, F. Schmidt, G. Vanbavinckhove, M. Aiba, R. Calaga and R. Miyamoto, *CERN Large Hadron Collider optics model, measurements, and corrections*, Physical Review Special Topics - Accelerators and Beams, **13**, 121004 (2010), doi:10.1103/PhysRevSTAB.13.121004.

[87] D. Edwards and L. Teng, *Parametrization of linear coupled motion in periodic systems*, IEEE Transactions on Nuclear Science, **20**, 885 (1973), doi:10.1109/TNS.1973.4327279.

[88] I. Borchardt, E. Karantzoulis, H. Mais and H. Ripken, *Calculation of beam envelopes in storage rings and transport systems in the presence of transverse space charge effects and coupling*, Report DESY 87-161, DESY, Germany (1987), URL: https://lib-extopc.kek.jp/preprints/PDF/1988/8802/8802226.pdf.

[89] M. Bassetti and G. Erskine, *Closed expression for the electrical field of a two-dimensional Gaussian charge*, Report CERN-ISR-TH/80-06, CERN, Switzerland (1980), URL: https://cds.cern.ch/record/122227/.

[90] R. Talman, *Multiparticle phenomena and Landau damping*, in Proceedings of Physics of Particle Accelerators: SLAC Summer School 1985, Fermilab Summer School 1984, Stanford, USA (1987), doi:10.1063/1.36371.

[91] W. Herr and T. Pieloni, *Beam-beam effects*, in CAS - CERN Accelerator School: Advanced Accelerator Physics Course, 431 (2016), doi:10.5170/CERN-2014-009.431.

[92] E. W. Weisstein, *Incomplete gamma function (MathWorld–A Wolfram Web Resource)*, URL: http://mathworld.wolfram.com/IncompleteGammaFunction.html.

[93] A. Chao, *Lecture notes on topics in accelerator physics*, Lecture Notes SLAC-PUB-9574, SLAC, USA (2002), URL: http://www.slac.stanford.edu/pubs/slacpubs/9500/slac-pub-9574.pdf.

[94] A. J. Dragt, *Lie methods for nonlinear dynamics with applications to accelerator physics*, Report (2018), URL: http://www.physics.umd.edu/dsat/.

[95] J. M. Jowett, *Parasitic beam-beam effects and separation schemes*, in A. W. Chao, K. H. Mess, M. Tigner and F. Zimmermann (editors), Handbook of Accelerator Physics and Engineering, 2nd ed., World Scientific Press (2013), doi:10.1142/8543.

[96] T. Pieloni, A study of beam-beam effects in hadron colliders with a large number of bunches, PhD thesis, École Polytechnique Fédéral de Lausanna, Switzerland (2008), URL: http://cds.cern.ch/record/1259906.

[97] X. Buffat, Transverse beams stability studies at the Large Hadron Collider, PhD thesis, École Polytechnique Fédéral de Lausanna, Switzerland (2014), URL: http://cds.cern.ch/record/1987672.

[98] K. Hirata, *Coherent betatron oscillation modes due to beam-beam interaction*, Nuclear Instruments and Methods in Physics Research Section A: Accelerators, Spectrometers, Detectors and Associated Equipment, **269**, 7 (1988), doi:10.1016/0168-9002(88)90856-x.

[99] Y. Alexahin and M. Zorzano-Mier, *Excitation of coherent beam-beam resonances for beams with unequal tunes in the LHC*, Report LHC-PROJECT-NOTE-226, CERN, Switzerland (2000), URL: http://cds.cern.ch/record/691835.

[100] Y. Alexahin, *A study of the coherent beam-beam effect in the framework of the Vlasov perturbation theory*, Nuclear Instruments and Methods in Physics Research Section A: Accelerators, Spectrometers, Detectors and Associated Equipment, **480**, 253 (2002), doi:10.1016/s0168-9002(01)01219-0.

[101] A. Chao, Physics of collective beam instabilities in high energy accelerators, Wiley (1993), URL: http://cds.cern.ch/record/246480.

[102] V. A. Lebedev, *Emittance growth due to noise and its suppression with the feedback system in large hadron colliders*, AIP Conference Proceedings, **326**, 396 (1995), doi:10.1063/1.47298.

[103] M. Blaskiewicz, *Emittance growth from electron beam modulation*, Report BNL-90847-2009-IR, BNL, Switzerland (2009), URL: https://www.bnl.gov/isd/documents/80179.pdf.

[104] E. W. Weisstein, *Jacobi-Anger expansion (MathWorld–A Wolfram Web Resource)*, URL: http://mathworld.wolfram.com/Jacobi-AngerExpansion.html.

[105] CERN, SixTrack webpage, URL: http://sixtrack.web.cern.ch/SixTrack/.

[106] E. Forest, F. Schmidt and E. McIntosh, *Introduction to the Polymorphic Tracking Code - Fibre Bundles, Polymorphic Taylor Types and Exact Tracking*, Report (2002), URL: http://madx.web.cern.ch/madx/doc/ptc_report_2002.pdf.

[107] Argonne National Laboratory, *Elegant*, webpage, URL: https://www.aps.anl.gov/Accelerator-Operations-Physics/Software.

[108] J. Laskar, *Introduction to frequency map analysis*, in Hamiltonian Systems with Three or More Degrees of Freedom, 134–150, Springer (1999), doi:10.1007/978-94-011-4673-9_13.

[109] F. Schmidt, *MAD-X PTC integration*, in Proceedings of the 2005 Particle Accelerator Conference, 1272 (2005), URL: https://accelconf.web.cern.ch/accelconf/p05/PAPERS/MPPE012.PDF.

[110] K. Li, *PyHEADTAIL*, presentation at PyHEADTAIL meeting 21.03.2014, CERN, Switzerland (2013), URL: https://indico.cern.ch/event/320542/attachments/618347/850770/PyHEADTAIL-Meeting-ed.pdf.

[111] CERN, PyHEADTAIL webpage, URL: https://github.com/PyCOMPLETE/PyHEADTAIL.

[112] CERN, Batch Service webpage (2019), URL: http://information-technology.web.cern.ch/services/batch.

[113] A. Marusic, private communication (2019).

[114] G. Robert-Demolaize, private communication (2019).

[115] X. Buffat, *Review of ADT impact on emittance growth*, presentation at 118th Hi-Lumi WP2 Meeting 10.04.2018, CERN, Switzerland (2018), URL: https://indico.cern.ch/event/718322/.

[116] M. Syphers, *Beam-beam tune distributions with differing beam size*, Beams-doc-3031 (2008), URL: http://beamdocs.fnal.gov/AD/DocDB/0030/003031/001/BeamsDoc3031.pdf.

[117] Y. Papaphilippou, *Frequency maps of LHC models*, Report LHC-Project-Report-299, CERN, Switzerland (1999), URL: https://cds.cern.ch/record/419551.

[118] J. Laskar, *The chaotic motion of the solar system: A numerical estimate of the size of the chaotic zones*, Icarus, **88**(2), 266 (1990), doi:10.1016/0019-1035(90)90084-m.

[119] CERN, PyNAFF webpage, URL: https://pypi.org/project/PyNAFF/.

[120] S. V. Furuseth and X. Buffat, *Modeling of nonlinear effects due to head-on beam-beam interactions*, Physical Review Accelerators and Beams, **21**(8) (2018), doi:10.1103/physrevaccelbeams.21.081002.

[121] X. Buffat, private communication (2019).

[122] F. Zimmermann, Emittance growth and proton beam lifetime in HERA, PhD thesis, Hamburg University (1993), URL: http://inspirehep.net/record/354381.

[123] O. Brüning and F. Willeke, *Reduction of proton losses in HERA by compensating tune ripple due to power supplies*, Physical Review Letters, **76**, 3719 (1996), doi:10.1103/PhysRevLett.76.3719.

[124] R. Bruce, S. Gilardoni, J. M. Jowett and D. Bocian, *Beam losses from ultra-peripheral nuclear collisions between $^{208}\mathrm{Pb}^{82+}$ ions in the Large Hadron Collider and their alleviation*, Physical Review Special Topics - Accelerators and Beams, **12**, 071002 (2009), doi:10.1103/PhysRevSTAB.12.071002.

[125] R. Bruce, J. M. Jowett, S. Gilardoni, A. Drees, W. Fischer, S. Tepikian and S. R. Klein, *Observations of beam losses due to bound-free pair production in a heavy-ion collider*, Physical Review Letters, **99**, 144801 (2007), doi:10.1103/physrevlett.99.144801.

[126] R. Helm, M. Lee, L. Morton and M. Sands, *Evaluation of synchrotron radiation integrals*, in Proceedings of the International Conference on Particle Accelerators (PAC'73), 900, San Francisco, USA (1973), URL: http://accelconf.web.cern.ch/AccelConf/p73/PDF/PAC1973_0900.PDF.

[127] H. Wiedemann, *Synchrotron radiation in storage rings*, in A. W. Chao, K. H. Mess, M. Tigner and F. Zimmermann (editors), Handbook of Accelerator Physics and Engineering, 2nd ed., World Scientific Press (2013), doi:10.1142/8543.

[128] C. Bernardini, G. F. Corazza, G. D. Giugno, G. Ghigo, J. Haissinski, P. Marin, R. Querzoli and B. Touschek, *Lifetime and Beam Size in a Storage Ring*, Physical Review Letters, **10**, 407 (1963), doi:10.1103/PhysRevLett.10.407.

[129] A. Piwinski, *Intra-beam-scattering*, in Proceedings of the 9th International Conference on High Energy Accelerators, Stanford, USA (1974), doi:10.5170/CERN-1992-001.226.

[130] J. Bjorken and S. K. Mtingwa, *Intrabeam scattering*, Particle Accelerators, **13**, 115 (1983), URL: https://cds.cern.ch/record/140304/.

[131] K. Bane, *A simplified model of intrabeam scattering*, in Proceedings of the 8th European Particle Accelerator Conference (EPAC'02), WEPRI120, Paris, France (2002), URL: http://accelconf.web.cern.ch/AccelConf/e02/PAPERS/WEPRI120.pdf.

[132] S. K. Mtingwa, *A new high energy approximation of intrabeam scattering for flat electron and positron beams*, African Physical Review, **2**, 1 (2008), URL: http://aphysrev.ictp.it/index.php/aphysrev/article/view/71/34.

[133] K. Kubo, S. K. Mtingwa and A. Wolski, *Intrabeam scattering formulas for high energy beams*, Physical Review Special Topics - Accelerators and Beams, **8**, 081001 (2005), doi:10.1103/PhysRevSTAB.8.081001.

[134] M. Hostettler, LHC luminosity performance, PhD thesis, Bern University, Switzerland (2018), URL: https://cds.cern.ch/record/2319396/.

[135] M. A. Furman and M. S. Zisman, *Luminosity*, in A. W. Chao, K. H. Mess, M. Tigner and F. Zimmermann (editors), Handbook of Accelerator Physics and Engineering, 2nd ed., World Scientific Press (2013), doi:10.1142/8543.

[136] M. Hostettler and G. Papotti, *Luminosity lifetime at the LHC in 2012 proton physics*, in Proceedings of the 4th International Particle Accelerator Conference (IPAC'13), 1403, Shanghai, China (2013), URL: http://cds.cern.ch/record/1567672.

[137] T. Pieloni et al., *Observations of two-beam instabilities during the 2012 LHC physics run*, in Proceedings of the 4th International Particle Accelerator Conference (IPAC'13), Shanghai, China (2013), URL: http://cds.cern.ch/record/1581728.

[138] X. Buffat, W. Herr, N. Mounet, T. Pieloni and S. White, *Stability diagrams of colliding beams in the Large Hadron Collider*, Physical Review Special Topics - Accelerators and Beams, **17**, 111002 (2014), doi:10.1103/physrevstab.17.111002.

[139] N. Karastathis, K. Fuchsberger, M. Hostettler, Y. Papaphilippou and D. Pellegrini, *Crossing angle anti-leveling at the LHC in 2017*, in IPAC 2018 (2018), doi:10.18429/JACoW-IPAC2018-MOPMF040.

[140] J. Wenninger and others., *β^* leveling with telescopic ATS squeeze (MD 2410)*, CERN-ACC-NOTE-2017-0052 (2017), URL: http://cds.cern.ch/record/2285184.

[141] A. Gorzawski, D. Mirarchi, G. Papotti, B. M. Salvachua Ferrando, J. Wenninger and T. Pieloni, *Collide and squeeze MD*, Report CERN-ACC-NOTE-2015-0043, CERN, Switzerland (2015), URL: http://cds.cern.ch/record/2115437.

[142] A. Gorzawski, D. Mirarchi, B. Salvachua and J. Wenninger, *Experimental demonstration of β^* leveling at the LHC*, in Proceedings of the 7th International Particle Accelerator Conference (IPAC'16), TUPMW013, Busan, Korea (2016), doi:10.18429/jacow-ipac2016-tupmw013.

[143] ALICE collaboration, *Measurement of visible cross sections in proton-lead collisions at $\sqrt{s_{\mathrm{NN}}} = 5.02$ TeV in van der Meer scans with the ALICE detector*, Journal of Instrumentation, **9**, P11003 (2014), doi:10.1088/1748-0221/9/11/p11003.

[144] R. Bartolini and F. Schmidt, *Normal form via tracking or beam data*, Report CERN-LHC-Project-132, CERN, Switzerland (1997), URL: https://cds.cern.ch/record/333077.

[145] E. Fermi, *Über die Theorie des Stoßes zwischen Atomen und elektrisch geladenen Teilchen*, Zeitschrift für Physik, **29**, 315 (1924), doi:10.1007/BF03184853.

[146] C. von Weizsäcker, *Ausstrahlung bei Stößen sehr schneller Elektronen*, Zeitschrift für Physik, **88**, 612 (1934), doi:10.1007/BF01333110.

[147] E. Williams, *Correlation of certain collision problems with radiation theory*, Kgl. Danske Videnskabernes Selskab Mathematisk-fysiske Meddelelser, **13**, 1 (1935), URL: http://inspirehep.net/record/1377275.

[148] J. D. Jackson, Klassische Elektrodynamik, 5th ed., De Gruyter (2013), doi:10.1515/9783110334470.

[149] A. Aste, *Bound-free pair production cross-section in heavy-ion colliders from the equivalent photon approach*, Europhysics Letters, **81**, 61001 (2008), doi:10.1209/0295-5075/81/61001.

[150] A. Artemyev, V. Serbo and A. Surzhykov, *Double lepton pair production with electron capture in relativistic heavy-ion collisions*, European Physical Journal C, **74**, 2829 (2014), doi:10.1140/epjc/s10052-014-2829-z.

[151] R. Anholt and U. Becker, *Atomic collisions with relativistic heavy ions. IX. Ultrarelativistic collisions*, Physical Review A, **36**, 4628 (1987), doi:10.1103/physreva.36.4628.

[152] H. Meier, Z. Halabuka, K. Hencken, D. Trautmann and G. Baur, *Bound-free electron-positron pair production in relativistic heavy-ion collisions*, Physical Review A, **63**, 032713 (2001), doi:10.1103/PhysRevA.63.032713.

[153] E. W. Weisstein and J. Sondow, *Riemann zeta function (MathWorld–A Wolfram Web Resource)*, URL: http://mathworld.wolfram.com/RiemannZetaFunction.html.

[154] A. Baltz, M. Rhoades-Brown and J. Weneser, *Heavy-ion partial beam lifetimes due to Coulomb induced processes*, Physical Review E, **54**, 4233 (1996), doi:10.1103/PhysRevE.54.4233.

[155] G. Baur and C. Bertulani, *Electromagnetic physics at relativistic heavy ion colliders, for better and for worse*, Nuclear Physics A, **505**, 835 (1989), doi:10.1016/0375-9474(89)90043-2.

[156] S. Klein, *Localized beampipe heating due to e^- capture and nuclear excitation in heavy ion colliders*, Nuclear Instruments and Methods in Physics Research Section A, **459**, 51 (2001), doi:10.1016/S0168-9002(00)00995-5.

[157] S. Klein, *Heavy ion beam loss mechanisms at an electron-ion collider*, Physical Review Special Topics - Accelerators and Beams, **17**, 121003 (2014), doi:10.1103/PhysRevSTAB.17.121003.

[158] P. Hermes et al., *Measured and simulated heavy-ion beam loss patterns at the CERN Large Hadron Collider*, Nuclear Instruments and Methods in Physics Research Section A, **819**, 73 (2016), doi:10.1016/j.nima.2016.02.050.

[159] P. Hermes, Heavy ion collimation at the Large Hadron Collider - simulations and measurements, PhD thesis, Westfälische Wilhelms-Universität Münster, Germany (2016), URL: https://cds.cern.ch/record/2241364.

[160] J. M. Jowett, *Filling schemes, collision schedules and beam-beam equivalence classes*, in F. Zimmermann and J. Poole (editors), Proceedings of the LHC'99 Workshop on Beam-Beam Effects in Large Hadron Colliders, 63–69 (1999), URL: http://cds.cern.ch/record/488278/files/sis-2001-088.pdf.

[161] J. M. Jowett, *Filling schemes for HI2016: 2016 p-Pb run of LHC*, presentation at "Preparation for p-Pb run" meeting 31.08.2016, CERN, Switzerland (2016), URL: https://indico.cern.ch/event/565394/contributions/2284017/attachments/1329049/1996613/HI_Jowett_31Aug2016A.pdf.

[162] C. Wiesner et al., *Asynchronous beam dump tests at LHC*, in Proceedings of the 9th International Particle Accelerator Conference (IPAC'18), MOPMF063, Vancouver, Canada (2018), doi:10.18429/jacow-ipac2018-mopmf063.

[163] C. Barschel, Precision luminosity measurement at LHCb with beam-gas imaging, PhD thesis, RWTH Aachen University, Germany (2014), URL: https://cds.cern.ch/record/1693671.

[164] LHCb collaboration, *Precision luminosity measurements at LHCb*, Journal of Instrumentation, **9**, P12005 (2014), doi:10.1088/1748-0221/9/12/p12005.

[165] J. M. Jowett, R. Alemany-Fernández, M. A. Jebramcik, T. Mertens and M. Schaumann, *Lifetime of asymmetric colliding beams in the LHC*, in Proceedings of the 8th International Particle Accelerator Conference (IPAC'17), TUPVA013, Copenhagen, Denmark (2017), doi:10.18429/JACoW-IPAC2017-TUPVA013.

[166] M. A. Jebramcik, *Luminosity evolution and levelling presets*, presentation at the HI2018 preparation meeting 18.10.2018, CERN, Switzerland (2018), URL: https://indico.cern.ch/event/754026/.

[167] CMS Collaboration, *Measurement of the inelastic cross section in proton-lead collisions at* $\sqrt{s_{\mathrm{NN}}} = 5.02\,TeV$, Physics Letters B, **759** (2016), doi:10.1016/j.physletb.2016.06.027.

[168] C. Barschel, M. Ferro-Luzzi, J.-J. Gras, M. Ludwig, P. Odier and S. Thoulet, *Results of the LHC DCCT calibration studies*, CERN-ATS-Note-2012-026 PERF (2012), URL: https://cds.cern.ch/record/1425904.

[169] CMS Collaboration, *CMS luminosity measurement using 2016 proton-nucleus collisions at* $\sqrt{s_{\mathrm{NN}}} = 8.16\,TeV$, CMS PAS LUM-17-002 (2018), URL: http://cds.cern.ch/record/2628652?ln=en.

[170] E. Torrence, private communication (2018).

[171] European Particle Physics Strategy Update, webpage (2019), URL: https://cafpe.ugr.es/eppsu2019/.

[172] B. Abelev et al., *Technical design report for the upgrade of the ALICE inner tracking system*, Journal of Physics G, **41**, 087002 (2014), doi:10.1088/0954-3899/41/8/087002.

[173] G. Milhano, *Prospects with light ions in Run 5 and heavy ions at HE-LHC*, Presentation at HL/HE-LHC Physics Workshop 01.03.2019, CERN, Switzerland (2019), URL: https://indico.cern.ch/event/783141/.

[174] S. Fartoukh, *An achromatic telescopic squeezing (ATS) scheme for the LHC upgrade*, Report CERN-ATS-2011-161, CERN, Switzerland (2011), URL: https://cds.cern.ch/record/1382077.

[175] S. Fartoukh, *Achromatic telescopic squeezing scheme and application to the LHC and its luminosity upgrade*, Physical Review Special Topics - Accelerators and Beams, **16**, 111002 (2013), doi:10.1103/physrevstab.16.111002.

[176] J. M. Jowett, private communication (2019).

[177] J. M. Jowett, *Ions in the LHC rings*, in Chamonix Workshop 2004 (2004), URL: https://ab-div.web.cern.ch/ab-div/Conferences/Chamonix/chamx2004/PAPERS/1_05_JMJ.pdf.

[178] H. Bartosik, *LIU baseline for ions*, presentation at the LHC performance workshop 25.01.2017, Chamonix, France (2017), URL: https://indico.cern.ch/event/580313/.

[179] J. Wennginer, private communication (2019).

[180] J. Grosse-Oetringhaus, *Particle production and collectivity across system size*, Presentation at HL/HE-LHC Physics Workshop 01.03.2019, CERN, Switzerland (2019), URL: https://indico.cern.ch/event/783141/.

[181] R. Bruce, private communication (2018).

[182] FLUKA team, FLUKA webpage, URL: http://www.fluka.org/fluka.php.

[183] S. Roesler, R. Engel and J. Ranft, *The Monte Carlo event generator DPMJET-III*, in A. Kling, F. J. C. Baräo, M. Nakagawa, L. Távora and P. Vaz (editors), Advanced Monte Carlo for Radiation Physics, Particle Transport Simulation and Applications, 1033–1038, Springer Berlin Heidelberg, Berlin, Heidelberg (2001), doi:10.1007/978-3-642-18211-2_166.

[184] C. Baus and R. Ulrich, Cosmic Ray Monte Carlo webpage (2019), URL: https://github.com/alisw/crmc.

[185] S. Ostapchenko, *Monte Carlo treatment of hadronic interactions in enhanced Pomeron scheme: QGSJET-II model*, Physical Review D, **83**, 014018 (2011), doi:10.1103/physrevd.83.014018.

[186] H. Dembinski, *Proton-oxygen collisions for cosmic ray research: an update*, presentation at Workshop on the physics of HL-LHC, and perspectives at HE-LHC 19.06.2018, CERN, Switzerland (2018), URL: https://indico.cern.ch/event/686494/.

[187] H. Dembinski, *Science case for recording proton-oxygen collisions at the LHC*, presentation at meeting of the LHC Working Group on Forward Physics and Diffraction 20.03.2018, Madrid, Spain (2018), URL: https://indico.cern.ch/event/711754/.

[188] H. Dembinski, *Proton-oxygen collisions at the LHC*, presentation at CFNS workshop on Forward Physics And Instrumentation From Colliders To Cosmic Rays 18.10.2018, Stony Brook, USA (2018), URL: https://indico.bnl.gov/event/4737/.

[189] T. Kövener, private communication (2019).

[190] D. Manglunki et al., *CERN's fixed target primary ion programme*, in Proceedings of the 7th International Particle Accelerator Conference (IPAC'16), TUPMR027, Busan, Korea (2016), doi:10.18429/JACoW-IPAC2016-TUPMR027.

[191] N. Fuster-Martínez, R. Bruce, P. Hermes, J. M. Jowett, D. Mirarchi and S. Redaelli, *Cleaning performance of the collimation system with Xe beams at the Large Hadron Collider*, in Proceedings of the 9th International Particle Accelerator Conference (IPAC'18), MOPMF038, Vancouver, Canada (2018), doi:10.18429/jacow-ipac2018-mopmf038.

[192] D. d'Enterria, private communication (2019).

[193] B. Petersen and F. Moortgat, *Motivation for oxygen in LHC*, presentation at LMC meeting 17.07.2019, CERN, Switzerland (2019), URL: https://indico.cern.ch/event/835697/.

[194] R. Bruce, M. A. Jebramcik, J. M. Jowett, M. Schaumann, J. Wenninger, R. Alemany-Fernández and B. Petersen, *Potential short O-O and p-O runs of LHC*, presentation at LMC meeting 17.07.2019, CERN, Switzerland (2019), URL: https://indico.cern.ch/event/835697/.

[195] LHCf collaboration, *LHCf experiment: technical design report*, Report CERN-LHCC-2006-004, CERN, Switzerland (2006), URL: http://cds.cern.ch/record/926196.

[196] E. Forest, Beam dynamics: A new attitude and framework, Hardwood Academic (1998), URL: https://cds.cern.ch/record/367626.

All URLs and DOIs were successfully accessed on 17 January 2020. Some CERN related URLs are only accessible with a CERN IP address.